Palladium Based Catalysts for Oxygen Reduction in Polymer Electrolyte Membrane Fuel Cells

Newcastle University

A Thesis Submitted By

Georgina Fernández Álvarez

For the Degree of Doctor of Philosophy

School of Chemical Engineering & Advanced Materials
University of Newcastle upon Tyne

August 2010

Abstract

An important issue in low temperature polymer electrolyte membrane fuel cells (PEMFC) is the lack of alternative catalysts to platinum for the oxygen reduction reaction (ORR). The high cost and potential limited availability of platinum restricts its long term use for large scale applications in PEMFC. Consequently, there is a great interest in alternative catalysts to platinum for PEMFC. In this research a systematic study of the synthesis and optimization of carbon-supported palladium and palladium alloy nanoparticle electrocatalysts is reported. The catalysts investigated were Pd, Pd-Au, Pd-Co, Pd-Fe and Pd-Ti supported on carbon black (Vulcan XC-72R). At least two different atomic metal to metal ratios for bimetallic catalysts were investigated. All catalysts were initially evaluated for the ORR by voltammetry in a three-electrode cell.

Different reducing agents, including hydrogen, ethylene glycol (EG), formaldehyde and sodium borohydride were used for the synthesis of Pd nanoparticles. The use of EG led to Pd nanoparticles with the highest ORR activity; this synthetic method was optimised by adjusting the pH of the system. Pd nanoparticles of approximately 6 nm diameter dispersed on carbon black with exchange current densities for the ORR of ca. 1.0×10^{-11} A cm^{-2} were obtained. Two synthetic procedures were chosen for the preparation of bimetallic catalysts: simultaneous co-deposition of both metals on the carbon support and deposition of the second metal on carbon-supported Pd. Pd-Co alloy with atomic ratio Pd:Co 4:1 exhibited improved ORR activity compared to Pd/C after being heat treated at 300 ºC under H_2 flow. The effect of heat treatment under H_2 flow on the ORR activity and physicochemical properties was also studied. Pure Pd particles exhibited sintering after heat treatment; the presence of Au, Co and Fe decreased the degree of sintering and the presence of Ti did not affect Pd particle growth.

Pd and Pd-Co were evaluated in low temperature hydrogen PEMFC, and Pd was tested as cathode catalysts in hydrogen polybenzimidazole (PBI) based high temperature PEMFC, and in direct methanol fuel cells (DMFC). Optimized Pd and Pd-Co catalysts were tested in a hydrogen low temperature PEMFC and the results were compared to those of the state of the art commercial Pt catalyst. With approximately 1.7 times higher metal loading than Pt (still significantly lower cost) the fuel cell with the Pd cathode gave better performance than that with Pt operating with air at 40 ºC. A comparative study of Pd and Pt was carried out in DMFC using different methanol concentrations and under different operating conditions. At methanol concentrations of 5 M and higher, the Pd cathode based cell performed better than that with Pt at 60 ºC with air.

A pseudo one dimensional model for Nafion®-based low temperature hydrogen PEMFC was developed to simulate the influence of cathode catalyst, metal loading, electrode thickness and different operating conditions on the cell voltage and current density output. The model considered mass transport through a thin film electrolyte and through porous media but not gas flow along the channels of the cell. The model closely predicted experimental results at 20 and 40 ºC. Above 40 ºC cell performance did not improve experimentally as was predicted by the model; this lack of improvement was attributed to the decrease of oxygen permeability through Nafion® caused by the lower humidity at higher temperatures. Predicted results showed that enhanced fuel cell performance in the whole current density range could be achieved by increasing metal loading in the cathode whilst maintaining the catalyst layer thickness, which could be practically achieved by increasing the metal content of the carbon-supported catalyst.

Acknowledgments

I read somewhere that this one will be the most widely read page of my entire thesis, people will see here whether they meant something in my life as PhD candidate. I believe there is a big truth in this statement and therefore I would like the people mentioned below to know they all made a real contribution to this piece of work.

I am grateful to my supervisor, Professor Keith Scott, for his continuous guidance and support during the last three years. I would like to thank Dr Jong Hyun Jang, Dr Senthil Kumar Sakkarapalayam-Murugesan and especially Dr Mohamed Mamlouk for their help, guidance and support in the production of this thesis. I would also like to thank the members of the Electron Microscopy and Chemical Analysis services and all the members of staff at CEAM school for their assistance, in particular Dr Kath Liddell, for her crucial help with the X-ray crystallography analyses.

Thanks also to all the members of the research group, who offered me both their help and friendship. Especially I would like to thank Tiago Sousa, Beate Chistgen, Nur Hidayati, Georgios Vlachogia nnopoulos, Amor Larrosa Guerrero, Xu Wang and Xu Wu.

I would like to thank my parents and my brother for the infinite love and support they gave me during the whole process, and my boyfriend, Daniel, for all his patience, love and encouragement. Also thanks to all my family and friends for their constant support.

I dedicate this thesis to my mother, Ada. Thank you for everything.

Table of Contents

List of Figures

List of Tables

Nomenclature

A	Electrode active area for flux (cm^2)
	Pre-exponential factor
a_c	Electrochemical surface area (m_{metal}^2 g^{-1})
b	Tafel slope (mV dec^{-1})
C_S, C_B	Surface and bulk concentrations (mol dm^{-3})
C_{Pt}	Oxygen concentration at platinum surface (mol dm^{-3})
$C_{dissolve}$	Oxygen concentration in the thin film electrolyte (mol dm^{-3})
C_{ref}	Oxygen concentration where i_0^{ref} was measured (mol dm^{-3})
d	Distance between atomic layers in crystals (Å)
D	Diffusion coefficient through the polymer membrane (cm^2 s^{-1})
	Particle diameter (Å)
E	Potential versus Normal Hydrogen Electrode (V)
E_a	Activation energy (kJ mol^{-1})
E^0	Standard reduction potential (V)
E^0_{rev}	Standard cell reversal potential (V)
E_{rev}	Cell reversal potential (V)
F	Faraday constant (C mol^{-1})
ΔG^0	Standard Gibbs free energy (kJ)
H	Henry’s constant (m^3 atm mol^{-1})
i	Current density (mA cm^{-2})
$i_{cross\text{-}over}$	Cross-over current density (mA cm^{-2})
i_k	Kinetic current density (mA cm^{-2})
i_L	Limiting current density (mA cm^{-2})
i_0	Exchange current density (mA cm^{-2})
i_0^{ref}	Exchange current density at reference temperature (A cm^{-2})
j	Current density (mA cm^{-2})
j_0	Reference current density (mA cm^{-2})
k	Reaction rate constant (mol dm-3 s-1)
L_c	Catalyst loading (g_{metal} cm^{-2})

L	Membrane thickness (m)
M	Molecular weight (g mol^{-1})
N_i	Molar flux of species i (mol s^{-1} cm^{-2})
n	Number of electrons involved in a reaction
P_i	Partial pressure of species i (atm)
P^0_i	Reference standard partial pressure of species i (atm)
P^*_{H2O}	Saturation vapor pressure of water at a given temperature (atm)
Q_O	Charge of the oxygen monolayer on smooth Pd (μC cm^{-2})
Q_H	Charge of the hydrogen monolayer on smooth Pt (μC cm^{-2})
R	Gas constant (J K^{-1} mol^{-1})
	Electron/proton transport resistance (Ohm)
S_c	Specific surface area of carbon per unit area
S_{Pt}	Specific surface area of Pt per unit area
S_A	Surface area (m^2 g^{-1})
T	Temperature (K)
T_{ref}	Reference temperature at which i_0^{ref} was measured (K)
t	Time (s)
U_{cell}	Cell potential (V)
X_i	Molar fraction of species i
Z	Thickness of the gas diffusion electrode (m)

Greek Symbols

α	Transfer coefficient
α_a, α_c	Transfer coefficient for anodic and cathodic reactions
γ	Reaction order
η	Overpotential (V)
$\eta_{cross-over}$	Cross over potential loss (V)
θ	Diffraction peak position (radians)
λ	Wavelength (Å)

σ	Conductivity (S cm^{-1})
ω	Rotation speed (rpm)

Acronyms

CV	Cyclic Voltammogram
DMFC	Direct Methanol Fuel Cell
DAB	3-3’-diaminobenzidine
ECSA	Electrochemical Surface Area
EDXA	Energy Dispersive X-ray Analysis
EG	Ethylene Glycol
FWHM	Full width of the peak at half maximum (radians)
GDL	Gas Diffusion Layer
HTPEMFC	High Temperature Polymer Electrolyte Membrane Fuel Cell
IPA	Isophthalic acid
LSV	Linear Sweep Voltammogram
MA	Mass Activity
MEA	Membrane Electrode Assembly
NHE	Normal Hydrogen Electrode
OCP	Open Circuit Potential
ORR	Oxygen Reduction Reaction
PBI	Polybenzimidazole
PEMFC	Polymer Electrolyte Membrane Fuel Cell
PPA	Poly-phosphoric acid
RDE	Rotating Disk Electrode
RH	Relative Humidity
TEM	Transmission Electron Microscopy
XRD	X-ray Diffraction

Catalysts synthesis method

Pd/C-EG	Reduction with ethylene glycol.
Pd/C-EG-300	Reduction with ethylene glycol and treatment in H_2 at 300 ºC.
Pd/C-CH_2O	Reduction with formaldehyde.
Pd/C-CH_2O-300	Reduction with formaldehyde and treatment in H_2 at 300 ºC.
Pd/C-$NaBH_4$	Reduction with sodium borohydride.
Pd/C-$NaBH_4$-300	Reduction with sodium borohydride and treatment in H_2 at 300 ºC.
Pd/C-EG10	Reduction with ethylene glycol at pH 10.
Pd/C-EG11	Reduction with ethylene glycol at pH 11.
Pd/C-EG12	Reduction with ethylene glycol at pH 12.
Pd/C-EG13	Reduction with ethylene glycol at pH 13.
Pd/C-EG11-untr	Reduction with ethylene glycol at pH 11 on as-received Vulcan XC-72R.
Pd/C-EG11-untr-rt	Reduction with ethylene glycol at pH 11 on as-received Vulcan XC-72R and treatment in H_2 at room temperature.
Pd/C-EG11-untr-100	Reduction with ethylene glycol at pH 11 on as-received Vulcan XC-72R and treatment in H_2 at 100 ºC.
Pd/C-EG11-untr-200	Reduction with ethylene glycol at pH 11 on as-received Vulcan XC-72R and treatment in H_2 at 200 ºC.
Pd/C-EG11-untr-300	Reduction with ethylene glycol at pH 11 on as-received Vulcan XC-72R and treatment in H_2 at 300 ºC.
Pd/C-Etek	Pd catalyst purchased from E-Tek.
Pt/C-Etek	Pt catalyst purchased from E-Tek.
PdAu-EG11	Simultaneous reduction with ethylene glycol at pH 11 on as-received Vulcan XC-72R. Nominal atomic ratios Pd:Au 1:1.
PdAu-EG11-300	Simultaneous reduction with ethylene glycol at pH 11 on as-received Vulcan XC-72R and treatment in H_2 at 300 ºC. Nominal atomic ratios Pd:Au 1:1.
Pd_9Au-EG11	Simultaneous reduction with ethylene glycol at pH 11 on as-received Vulcan XC-72R. Nominal atomic ratios Pd:Au 9:1.

Pd$_9$Au-EG11-300	Simultaneous reduction with ethylene glycol at pH 11 on as-received Vulcan XC-72R and treatment in H_2 at 300 ºC. Nominal atomic ratios Pd:Au 9:1.
Pd(Au)-EG11	Reduction of the Au precursor salt with ethylene glycol at pH 11 on Pd/C-EG11. Nominal atomic ratios Pd:Au 1:1.
Pd(Au)-EG11-300	Reduction of the Au precursor salt with ethylene glycol at pH 11 on Pd/C-EG11 and treatment in H_2 at 300 ºC. Nominal atomic ratios Pd:Au 1:1.
Pd$_3$(Au)-EG11	Reduction of the Au precursor salt with ethylene glycol at pH 11 on Pd/C-EG11. Nominal atomic ratios Pd:Au 3:1.
Pd$_3$(Au)-EG11-300	Reduction of the Au precursor salt with ethylene glycol at pH 11 on Pd/C-EG11 and treatment in H_2 at 300 ºC. Nominal atomic ratios Pd:Au 3:1.
PdCo-EG11	Simultaneous reduction with ethylene glycol at pH 11 on as-received Vulcan XC-72R. Nominal atomic ratios Pd:Co 1:1.
PdCo-EG11-300	Simultaneous reduction with ethylene glycol at pH 11 on as-received Vulcan XC-72R and treatment in H_2 at 300 ºC. Nominal atomic ratios Pd:Co 1:1.
Pd$_4$Co-EG11	Simultaneous reduction with ethylene glycol at pH 11 on as-received Vulcan XC-72R. Nominal atomic ratios Pd:Co 4:1.
Pd$_4$Co-EG11-300	Simultaneous reduction with ethylene glycol at pH 11 on as-received Vulcan XC-72R and treatment in H_2 at 300 ºC. Nominal atomic ratios Pd:Co 4:1.
Pd(Co)-EG11	Reduction of the Co precursor salt with ethylene glycol at pH 11 on Pd/C-EG11. Nominal atomic ratios Pd:Co 1:1.
Pd(Co)-EG11-300	Reduction of the Co precursor salt with ethylene glycol at pH 11 on Pd/C-EG11 and treatment in H_2 at 300 ºC. Nominal atomic ratios Pd:Co 1:1.
Pd$_4$(Co)-EG11	Reduction of the Co precursor salt with ethylene glycol at pH 11 on Pd/C-EG11. Nominal atomic ratios Pd:Co 4:1.

Pd_4(Co)-EG11-300	Reduction of the Co precursor salt with ethylene glycol at pH 11 on Pd/C-EG11 and treatment in H_2 at 300 ºC. Nominal atomic ratios Pd:Co 4:1.
PdFe-EG11	Simultaneous reduction with ethylene glycol at pH 11 on as-received Vulcan XC-72R. Nominal atomic ratios Pd:Fe 1:1.
PdFe-EG11-300	Simultaneous reduction with ethylene glycol at pH 11 on as-received Vulcan XC-72R and treatment in H_2 at 300 ºC. Nominal atomic ratios Pd:Fe 1:1.
Pd_3Fe-EG11	Simultaneous reduction with ethylene glycol at pH 11 on as-received Vulcan XC-72R. Nominal atomic ratios Pd:Fe 3:1.
Pd_3Fe-EG11-300	Simultaneous reduction with ethylene glycol at pH 11 on as-received Vulcan XC-72R and treatment in H_2 at 300 ºC. Nominal atomic ratios Pd:Fe 3:1.
PdFe-H_2-500	Simultaneous reduction in H_2 at 500 ºC on as-received Vulcan XC-72R. Nominal atomic ratios Pd:Fe 1:1.
Pd(Fe)-H_2-500	Reduction of the Fe precursor salt in H_2 at 500 ºC on Pd/C-EG11-72R. Nominal atomic ratios Pd:Fe 1:1.
Pd_3Fe-H_2-500	Simultaneous reduction in H_2 at 500 ºC on as-received Vulcan XC-72R. Nominal atomic ratios Pd:Fe 3:1.
Pd_3(Fe)-H_2-500	Reduction of the Fe precursor salt in H_2 at 500 ºC on Pd/C-EG11-72R. Nominal atomic ratios Pd:Fe 3:1.
PdTi-EG11	Simultaneous reduction with ethylene glycol at pH 11 on as-received Vulcan XC-72R. Nominal atomic ratios Pd:Ti 1:1.
PdTi-EG11-300	Simultaneous reduction with ethylene glycol at pH 11 on as-received Vulcan XC-72R and treatment in H_2 at 300 ºC. Nominal atomic ratios Pd:Ti 1:1.
Pd_9Ti-EG11	Simultaneous reduction with ethylene glycol at pH 11 on as-received Vulcan XC-72R. Nominal atomic ratios Pd:Ti 9:1.
Pd_9Ti-EG11-300	Simultaneous reduction with ethylene glycol at pH 11 on as-received Vulcan XC-72R and treatment in H_2 at 300 ºC. Nominal atomic ratios Pd:Ti 9:1.

PdTi-H_2-900	Simultaneous reduction in H_2 at 900 ºC on as-received Vulcan XC-72R. Nominal atomic ratios Pd:Ti 1:1.
Pd(Ti)-H_2-900	Reduction of the Ti precursor salt in H_2 at 900 ºC on Pd/C-EG11-72R. Nominal atomic ratios Pd:Ti 1:1.
Pd_9Ti-H_2-900	Simultaneous reduction in H_2 at 900 ºC on as-received Vulcan XC-72R. Nominal atomic ratios Pd:Ti 9:1.
Pd_9(Ti)-H_2-900	Reduction of the Ti precursor salt in H_2 at 900 ºC on Pd/C-EG11-72R. Nominal atomic ratios Pd:Ti 9:1.

Chapter 1: Introduction

1.1. Overview

Polymer electrolyte membrane fuel cells (PEMFC) are considered good alternatives to internal combustion engines because of their high power density, high energy conversion efficiency and low emission level. Polymer electrolyte membranes used in low temperature PEMFC require water to conduct protons which limits the operation to temperatures below 80 ºC. The technology is currently well developed, however it suffers from several limitations associated with a low temperature of operation: these include low utility of the heat produced during operation, difficult water balance and poor heat transfer characteristics due to the small temperature gradient with the environment.

A major concern with current PEMFC is their high cost compared with internal combustion engines. They typically use platinum catalysts which represents a major part of the fuel cell cost. For instance, for automotive applications, the reported platinum requirements were more than 75 g per vehicle [1]. Considering the average price of platinum in the last five years, ca. $1,200 per troy ounce (Johnson Matthey prices), the cost of the platinum for the fuel cell system will rise to approximately $3,000 per car. These figures represent a clear indicator of the immediate need of finding an alternative material to platinum catalysts for PEMFC if they are to be widely commercialized.

Numerous studies on possible substitutes to platinum can be found in the literature; some replace platinum with alternative less expensive metals. This approach has yielded some competitive alloy catalysts, like Pt-Ni, Pt-Co and Pt-Fe [2-5] for the oxygen reduction reaction (ORR), but the cost is still high. Therefore, the most ambitious approach to this problem is to replace platinum with less expensive materials while maintaining electrocatalytic activity at least equal to that of state of the art Pt catalysts.

Palladium based catalysts have been reported as interesting alternatives for PEMFC [6-9]. Also, considering that the average price of palladium in the last five years was nearly one quarter of the price of platinum, approximately $300 per troy ounce, palladium based catalysts appear as promising candidates to replace platinum.

1.2. Project aim and objectives

The aim of this project is to identify alternative catalysts to platinum for the oxygen reduction reaction in polymer electrolyte membrane fuel cells. The research plan comprised the following objectives:

- Synthesis and physicochemical characterization of palladium-based carbon-supported metal nanoparticles.
- Electrochemical characterization and evaluation of the catalytic activity towards the oxygen reduction reaction of the metal nanoparticles.
- Evaluation of significantly active electrocatalysts as cathode materials in polymer electrolyte membrane fuel cells. Tests were carried out in low and high temperature PEMFC and in direct methanol fuel cells.

All catalysts prepared during this research project were supported on carbon black; Vulcan XC-72R. This support was chosen based on its physicochemical properties: ability to adsorb metal ions on its surface, porosity and high surface area, good electric conductivity and high chemical stability. The employed synthetic method was impregnation followed by reaction with a reducing agent [10-13]. The impregnation method consists of soaking a solution of precursor metal salts into a porous support followed by chemical reduction of the adsorbed salts to form metal particles. Several reducing agents were employed in this study, the main two being ethylene glycol and hydrogen.

The electrochemical method used to evaluate the catalytic activity of the prepared catalyst was cyclic voltammetry which was initially carried out in a 3-electrode cell with a rotating disc electrode. Low temperature polymer electrolyte membrane fuel cell tests were carried out using either H_2 or methanol (direct methanol fuel cell) as fuel and O_2 or air as oxidant. High temperature PEMFC tests were carried out at 120, 150 and 175 ºC using H_2 as fuel and O_2 or air as oxidant.

1.3. Thesis structure

This thesis is divided into nine chapters:

- Chapter 1 provides an overview of current issues with polymer electrolyte membrane fuel cells, together with a summary of the experimental objectives and methodology used in this work.

- Chapter 2 consists of a literature review including low and high temperature hydrogen PEMFC, direct methanol fuel cells, oxygen reduction and Pd based alloys.

- Chapter 3 describes experimental methods and techniques used in this study and details of the experimental procedures used in catalysts synthesis, in electrodes preparation and in fuel cell tests.

- Chapter 4 describes data on physicochemical characterization, electrochemical characterization and activity towards the oxygen reduction reaction of carbon-supported Pd nanoparticles. Characteristics of catalysts prepared by different synthetic procedures, obtained by X-Ray Diffraction (XRD), Energy Dispersive X-Ray Analysis (EDXA) and Transmission Electron Microscopy (TEM) analyses and in a three-electrode cell, are compared and discussed.

- Chapter 5 compares physicochemical and electrochemical characteristics of bimetallic carbon-supported nanoparticles to those of Pd/C. Characteristics of bimetallic catalysts prepared by different synthetic procedures, obtained by XRD, EDXA and TEM analyses and in a three-electrode cell, are compared and discussed.

- In Chapter 6 data from hydrogen polymer electrolyte membrane fuel cell tests is presented and discussed. This chapter includes fuel cell data from low and high temperature PEMFC. Low temperature tests used Pd, Pd-Co and Pt commercial cathodes. High temperature tests compared Pd/C and commercial Pt/C.

- Chapter 7 provides the experimental data obtained from evaluation of the Pd/C cathode catalysts in a direct methanol fuel cell. The effects of the temperature and methanol concentration on cell performance are discussed and the results compared to those of commercial Pt/C.

- In Chapter 8 a model for low temperature hydrogen polymer electrolyte membrane fuel cells developed using thermodynamics, transport and kinetic equations, is presented. The model is used to simulate the influence of cathode catalyst and operating conditions on the cell voltage and current density output.

- Chapter 9 provides conclusions drawn from this study together with recommendations for future work.

In this work a systematic study of the synthesis and optimization of carbon-supported palladium and palladium alloy nanoparticles is reported. A comprehensive comparative study of Pd and Pt catalyst for ORR in polymer electrolyte membrane fuel cells is reported in this piece of work: low and high temperature PEM fuel cells and direct methanol fuel cells.

References

1. Gasteiger, H.A., S.S. Kocha, B. Sompalli, and F.T. Wagner, *Activity benchmarks and requirements for Pt, Pt-alloy, and non-Pt oxygen reduction catalysts for PEMFCs.* Applied Catalysis, B: Environmental, 2005. **56**(1-2): p. 9-35.

2. Xiong, L. and A. Manthiram, *Nanostructured Pt-M/C (M = Fe and Co) catalysts prepared by a microemulsion method for oxygen reduction in proton exchange membrane fuel cells.* Electrochimica Acta, 2005. **50**(11): p. 2323-2329.

3. Xiong, L., A.M. Kannan, and A. Manthiram, *Pt-M (M = Fe, Co, Ni and Cu) electrocatalysts synthesized by an aqueous route for proton exchange membrane fuel cells.* Electrochemistry Communications, 2002. **4**(11): p. 898-903.

4. Salgado, J.R.C., E. Antolini, and E.R. Gonzalez, *Pt-Co/C electrocatalysts for oxygen reduction in H2/O 2 PEMFCs synthesized by borohydride method.* Journal of the Electrochemical Society, 2004. **151**(12).

5. Paulus, U.A., A. Wokaun, G.G. Scherer, T.J. Schmidt, V. Stamenkovic, V. Radmilovic, N.M. Markovic, and P.N. Ross, *Oxygen Reduction on Carbon-Supported Pt-Ni and Pt-Co Alloy Catalysts.* Journal of Physical Chemistry B, 2002. **106**(16): p. 4181-4191.

6. Fernández, J.L., V. Raghuveer, A. Manthiram, and A.J. Bard, *Pd-Ti and Pd-Co-Au Electrocatalysts as a Replacement for Platinum for Oxygen Reduction in Proton Exchange Membrane Fuel Cells.* Journal of the American Chemical Society, 2005. **127**(38): p. 13100-13101.

7. Shao, M.-H., K. Sasaki, and R.R. Adzic, *Pd-Fe Nanoparticles as Electrocatalysts for Oxygen Reduction.* Journal of the American Chemical Society, 2006. **128**(11): p. 3526-3527.

8. Wang, X., N. Kariuki, J.T. Vaughey, J. Goodpaster, R. Kumar, and D.J. Myers, *Bimetallic Pd-Cu Oxygen Reduction Electrocatalysts.* Journal of the Electrochemical Society, 2008. **155**(6): p. B602-B609.

9. Mustain, W.E., K. Kepler, and J. Prakash, *Investigations of carbon-supported CoPd3 catalysts as oxygen cathodes in PEM fuel cells.* Electrochemistry Communications, 2006. **8**(3): p. 406-410.

10. Fernández, J.L., D.A. Walsh, and A.J. Bard, *Thermodynamic Guidelines for the Design of Bimetallic Catalysts for Oxygen Electroreduction and Rapid Screening by Scanning Electrochemical Microscopy. M-Co (M: Pd, Ag, Au)*. Journal of the American Chemical Society, 2004. **127**(1): p. 357-365.

11. Moreira, J., P. del Angel, A.L. Ocampo, P.J. Sebastian, J.A. Montoya, and R.H. Castellanos, *Synthesis, characterization and application of a Pd/Vulcan and Pd/C catalyst in a PEM fuel cell*. International Journal of Hydrogen Energy, 2004. **29**(9): p. 915-920.

12. Salgado, J.R.C., E. Antolini, and E.R. Gonzalez, *Structure and Activity of Carbon-Supported Pt-Co Electrocatalysts for Oxygen Reduction*. Journal of Physical Chemistry B, 2004. **108**(46): p. 17767-17774.

13. Chan, K.-Y., J. Ding, J. Ren, S. Cheng, and K.Y. Tsang, *Supported mixed metal nanoparticles as electrocatalysts in low temperature fuel cells*. Journal of Materials Chemistry, 2004. **14**(4): p. 505-516.

Chapter 2: Literature review

2.1. Introduction

Polymer electrolyte membrane fuel cells (PEMFCs) are usually catalysed by platinum, which makes their production very expensive and hinders their commercialisation. The oxygen reduction reaction (ORR) is the limiting reaction in a PEMFC, due to its slow kinetics and cathodes normally require higher platinum loading than anodes. Therefore there is a clear interest in finding alternative catalysts to platinum for ORR.

Several kinds of catalysts have been considered for the ORR, including tungsten carbides [1-3], molybdenum nitrides [4] and palladium-based catalyst among others. Palladium-based catalysts were the selected materials in this research because the ORR on palladium has been reported to occur by a similar mechanism to that on platinum (Section 2.6) and the price of Pd is approximately one quarter of Pt. Studies of Pd and Pd alloy catalysts by several groups have been reviewed [5-12].

2.2. Low temperature polymer electrolyte membrane fuel cells

A fuel cell is an electrochemical device which converts the chemical energy of a fuel directly into electricity. The first demonstration of a fuel cell was in 1839 by Sir William Robert Grove [13]. In 1800, William Nicholson and Anthony Carlisle described the decomposition of water into hydrogen and oxygen using electricity; Grove went a step further and proposed the combination of the same gases to produce water and electricity. He carried out his idea with a device called a “gas battery”, using oxygen and hydrogen electrochemically generated and an acid electrolyte with platinum electrodes [14].

Although fuel cells are seen as modern devices they have been known for over 150 years. During the 19th century fuel cells had been generally considered as a curiosity and from the early 20th century they became the object of vehement research and development.

During the last decade of the past century the interest in fuel cell development grew, due to an increased concern about the need to reduce CO_2 emissions [13, 14].

The electrochemical reactions taking place in a fuel cell are in principle similar to those in a battery. The main difference between a battery and a fuel cell is that a fuel cell does not store energy internally within the cell; but uses a continuous fuel supply. A fuel cell consists of two electrodes, an anode and a cathode, and an electrolyte, which separates the electrodes and allows ions to flow across it. The fuel is externally supplied to the anode and the oxidant, generally oxygen or air, is supplied to the cathode. At the anode of an acid electrolyte fuel cell the fuel is oxidized, generating protons (positively charged) and electrons. Protons migrate through the electrolyte and react with oxygen at the cathode, while electrons flow from anode to cathode through the external circuit generating an electrical current. The electrolyte does not allow electron transfer, otherwise the electrons would not pass through the external circuit and the function of the cell would be lost.

In fuel cells electrons, protons and oxygen combine at the cathode to form water. Anodic and cathodic reactions occurring in acid electrolyte hydrogen fuel cells are:

$$2H_2 \rightarrow 4H^+ + 4e^- \tag{2.1}$$

$$O_2 + 4H^+ + 4e^- \rightarrow 2H_2O \tag{2.2}$$

The polymer electrolyte membrane (PEM) or proton exchange fuel cell was initially conceived as an acid electrolyte system. It was based on a proton conducting electrolyte. Eventually, the use of acid electrolyte was replaced by the use of a solid polymer electrolyte membrane in which the acid anion is bound to a solid polymer structure. This kind of cells is inherently simple; the membrane is sandwiched between two porous electrodes, which usually use platinum as catalyst, and is mechanically compressed.

Proton conduction inside the membrane occurs by formation of hydrated protons, e.g. H_3O^+ ions, which are mobile [13, 15, 16]. Nafion® (DuPont) is the most popular of the available proton exchange membranes for PEM cells because of its excellent thermal and mechanical stability, and is a member of a class of synthetic polymers with ionic properties called ionomers. Nafion® properties result from incorporating perfluorovinyl ether groups terminated with sulfonate groups onto a tetrafluoroethylene backbone [17]. Nafion® and similar materials depend on water to conduct the protons; therefore they need to be fully hydrated during cell operation. For this reason the operating temperatures are usually below 80 ºC [18].

PEMFC are expensive; and the platinum catalyst makes a major contribution to the cost. For example, in the United States, at the end of 2005 the cost of fuel cell systems was approximately $50 per kW [19]. Automotive applications are one of the target markets of PEMFC; an average car has a power requirement of 50 kW, which means $2500 per car for the fuel cell system alone. In view of a potential increasing price of platinum (nearly doubled since 2005, the need for alternative catalysts to platinum in PEMFCs appears obvious.

2.3. High temperature polymer electrolyte membrane fuel cell

Current low temperature PEM fuel cell technology suffers several limitations. Some of these limitations are due to issues related to hydrogen production, storage, distribution and purity, and many others are caused by the nature of the electrolyte membrane employed. Membrane materials such as Nafion® need to be fully hydrated during cell operation to allow effective proton conductivity. To be fully hydrated operating temperatures lower than 80 ºC are required. This restriction in operating temperature leads to different several technical problems, which have delayed commercialization and require expensive solutions.

Low temperature operation of PEMFCs causes an enlarged impact of poisonous species like carbon monoxide or sulphur species which reduced the catalytic activity [20] and can completely deactivate the catalyst. This requires expensive fuel refining processes. These operating conditions also require complex systems for thermal and water management.

Other challenges include low value of heat energy and low overall efficiency. Operating at high temperatures provides several benefits including enhanced carbon monoxide tolerance and lower humidification issues [18]. Technological developments in high temperature polymer electrolyte membrane fuel cells (HTPEMFC) will also extend the use of alternative fuels in PEM fuel cells, an area experiencing a rapid growth [21, 22].

The current and well developed low temperature PEMFC technology is based on perfluoro sulphonic acid polymer membranes, which require the presence of water to conduct protons. To operate at high temperature a new range of polymer electrolyte membranes, stable and proton conductive in the absence of liquid water, is required. Many attempts have been made to develop a solid polymer electrolyte capable of maintaining high proton conductivity at elevated temperatures without the need of humidification. Some materials have been developed for operation between 100 - 200 ºC. The most broadly used polymer electrolyte is poly[2,2-(*m*-phenylene)-5,5 bibenzimidazole], commonly called polybenzimidazole (PBI). Phosphoric acid doped PBI films have been considered as promising candidates as membranes for high temperature PEMFC [23].

Recent work in high temperature hydrogen PEMFC has been published by Mamlouk and Scott [24]. In this study they investigated the effect of acid and polytetrafluoroethylene (PTFE) content in the catalyst layer, membrane doping level and metal loading of the catalyst. They reported that 40% PTFE in the catalyst layer, 1 mg cm^{-2} phosphoric acid in the cathode and 5.6 molecules of acid per repeat polymer unit (PRU) were favourable for fuel cell operation. Peak powers of 0.27 and 0.4 W cm^{-2} were achieved with air at 120 and 150 ºC respectively.

2.4. Direct methanol fuel cell

Among liquid organic fuels methanol is a good candidate for direct electrochemical oxidation in terms of reactivity at low temperatures, handling and storage. Methanol-fed polymer electrolyte membrane fuel cells would be convenient because this would avoid many difficulties encountered when operating with hydrogen-fed fuel cells, such as gas storage and reforming. In a direct methanol fuel cell (DMFC), methanol is oxidized to carbon dioxide in the anode, protons cross the electrolyte membrane and combine with oxygen at the cathode to form water. Anodic and cathodic reactions occurring in a polymer acid electrolyte DMFC are:

$$CH_3OH + H_2O \rightarrow CO_2 + 6H^+ + 6e^- \tag{2.3}$$

$$\tfrac{3}{2} O_2 + 6H^+ + 6e^- \rightarrow 3H_2O \tag{2.4}$$

One of the major technical problems of current DMFCs is the methanol crossover, i.e. methanol permeation from the anode compartment through the electrolyte membrane to the cathode compartment. This causes cathode performance losses due to the formation of mixed potentials on the cathode catalyst as well as the decrease in the efficiency of methanol utilization [25]. To avoid mixed potentials in the cathode, caused by the simultaneous methanol oxidation and oxygen reduction reactions taking place, a possible solution would be employing a cathode electrocatalyst selective for the ORR.

Previous studies showed that Ru-based catalysts (e.g. Ru-Se, Ru-Se-Mo and Ru-Se-Rh) have some promising properties, i.e. reasonably high activity for oxygen reduction and high methanol tolerance [26-28]. Another possible candidate to substitute Pt is Pd. Palladium, like platinum, has a four-electron pathway for the oxygen reduction reaction and its activity for ORR is only surpassed by platinum [29]. Additionally, Pd has negligible electrocatalytic activity towards methanol oxidation in acid medium [30].

Lee et al. studied the ORR in acid media in the presence of methanol on Pt, Pd and Pd alloys [30]. They found that the Pt electrode exhibited a large anodic current above ca. 0.75 V vs NHE due to methanol oxidation. This methanol oxidation led to an onset potential ca. 200 mV lower that that observed without methanol in the electrolyte, which was attributed to the formation of a mixed potential on the Pt surface. Pd and Pd alloy electrocatalysts did not show mixed potential in the presence of both oxygen and methanol. Several groups have reported enhanced activity of Pd-Pt catalyst towards selective ORR compared to pure Pt in the presence of methanol [31-33].

2.5. Modeling of low temperature polymer electrolyte membrane fuel cell

Mathematical modeling of fuel cells is useful to help understand the exact effect of operating conditions and material properties on fuel cell performance. Various mathematical models for Nafion$^{®}$ based polymer electrolyte membrane fuel cells (PEMFCs) have been reported in the literature. One of the early phenomenological models for a PEMFC with Nafion$^{®}$ membrane was developed by Bernardi and Verbrugge [34]. Mathematical models were used to plot temperature distribution and liquid saturation maps [35], to study current distributions and reactants concentration [36], to describe multi-component transport through flow channels and diffusion layers [37] and or for modeling mass transport throughout porous electrodes [38].

Scott et al. used a one dimensional model for polybenzimidazole membrane fuel cells, the Butler-Volmer equation to describe electrode kinetics and multi-component Stefan Maxwell equations together with Darcy’s law to describe mass transport [39]. This model fitted experimental data but failed to predict limiting current with air operation. In a similar way, Hu et al. reported two other one and two dimensional models for simulation of polarization curves at different stages of an ageing test [8, 40], however, these failed to predict mass transport limitations when the cell was operated with air.

These models assumed that mass transport occurred only through the porous media and thus failed to predict mass transport limitations with air operation and consequently over estimated the cell performance at high current densities. This was similar to the single phase mass transport observation discussed earlier in Nafion based PEMFC models. In practice a thin film of electrolyte covers the catalyst nanoparticles and it is necessary to consider mass transport also through this phase. Reactants need to dissolve in this phase and diffuse through it to reach the catalytic sites; diffusion through the polymer electrolyte is slower compared to that through the porous media which explains the experimentally observed transport behavior. The thin film effect has been introduced in some models for phosphoric acid fuel cells [41, 42].

2.6. Oxygen reduction reaction

The reduction of oxygen to water has been widely studied because of its importance for many practical systems. The electrochemistry of oxygen is also a good example of catalytic reaction involving adsorption on the catalyst surface. Reduction mechanism and kinetics of the cathodic reduction of oxygen are highly sensitive to the properties of the electrode surface and the presence of other adsorbed species. Mechanism and kinetics of the oxygen reduction reaction (ORR) have been investigated on a great variety of electrode materials and electrolytes. An important driving factor for these studies was the high overpotential for the ORR observed in low temperature fuel cells with aqueous electrolytes.

The reduction of O_2 in aqueous solutions is believed to occur by two overall pathways; the direct 4-electron pathway and the 2-electron peroxide pathway [43]. The direct 4-electron pathway involves several steps leading to the reduction of oxygen into OH^- or water. The peroxide pathway involves the formation of hydrogen peroxide in the solution; this peroxide can decompose in the solution, producing O_2 and H_2O.

In acid media, equations for both pathways would be:

- Direct 4-electron pathway

$$O_2 + 4H^+ + 4e^- \rightarrow 2H_2O \qquad (2.5)$$

- Peroxide pathway

$$O_2 + 2H^+ + 2e^- \rightarrow H_2O_2 \tag{2.6}$$

followed by either

$$H_2O_2 + 2H^+ + 2e^- \rightarrow 2H_2O \tag{2.7}$$

or

$$2H_2O_2 \rightarrow 2H_2O + 2O_2 \tag{2.8}$$

The standard reduction potential calculated from thermodynamic data is, for equation 2.5, 1.229 V vs Normal Hydrogen Electrode (NHE). Each pathway involves several intermediates and reaction steps, thus many possible operating routes have been proposed. The main difference is that in the direct 4-electron pathway none of the intermediates lead to peroxide species in the solution, while in the 2-electron peroxide pathway peroxide species are present in the solution [13, 29].

The pathway followed by the ORR depends on the electrode material. The 4-electron pathway is believed to be predominant when Pt or Pd is used, while the peroxide pathway seems to be preferred by electrodes made of Au [13]. Several models have been proposed to explain the interaction of O_2 with the catalysts surface. The interaction of molecular oxygen with a transition metal can be explained in terms of molecular orbitals. For instance, the bridge-type interactions, believed to occur with Pt, involve a lateral interaction of the π orbitals of the O_2 with *d* orbitals of the transition element. This interaction occurs with back-bonding from the other *d* orbitals of the transition element to the π^* orbitals of the O_2. A strong metal-oxygen interaction results in the weakening of the O-O bond. If the interaction is strong enough it may lead to the dissociative adsorption of O_2 [43].

Because the oxygen reduction mechanism has been reported to be the same for palladium as for platinum [44, 45], the mechanism reported above has been assumed to be the one occurring on the palladium-based electrocatalysts prepared.

2.7. Palladium catalysts

The use of several different non platinum-based catalysts for the ORR in acid electrolyte have been reported, including tungsten carbides [1-3], molybdenum nitrides [4] and palladium-based catalyst [5, 10, 11, 46, 47] among others. In the initial stages of this research project some exploratory studies were carried out with molybdenum nitrides, which were reported to be potential candidates to replace Pt for its applications for fuel cells. However, because data reported in this piece of work corresponds to palladium-based catalyst, this literature review is restricted to Pd-based electrocatalysts.

Palladium is a noble metal with high catalytic activity, and is used in several industrial processes [48]. It is more abundant than platinum in the earth crust and less expensive. In electrocatalysis, palladium based catalysts have demonstrated to be good for use in organic fuel oxidation [49] and are able to store and release substantial amounts of hydrogen [50]. Studies of palladium and palladium alloys catalytic activity for oxygen reduction have been reported since the 1960s [45]. Early preparations of carbon-supported Pd catalyst were reported by Chaston et al. in 1961; they studied the reduction of Pd salts on activated charcoal [51]. Similar publications followed this one, as for instance the ones from Pope at al. and Bond [52, 53].

Moreira et al. reported the preparation of carbon supported palladium catalysts (on activated carbon and Vulcan), by an impregnation method and H_2 reduction at 300 ºC, [12]. Catalyst morphology was characterised by X-ray diffraction (XRD) and electrocatalytic activity was tested by cyclic and linear voltammetry. Catalysts were also tested as cathodes in hydrogen PEMFC; current densities exhibited operating with pure H_2 and O_2 at room temperature (1 mg cm^{-2} Pd/Vulcan in the cathode) were 0.04 and 0.13 A cm^{-2} at 0.5 and 0.3 V respectively. The fuel cell performance was better with Pd/Vulcan than with Pd/C.

2.8. Palladium alloy catalysts

In 2004, Savadogo et al. reported for the first time “extremely active” catalysts for ORR in acid electrolyte based on palladium alloys [54]. Those alloys were prepared by sputtering under vacuum from a palladium target and alloying metal sheets on a glassy carbon support. Catalytic properties of these alloys were tested by cyclic voltammetry (CV) in 0.1M H_2SO_4 at 30 ºC. Results indicated that Pd–Co alloy did not show any significant change in their shape or size during the testing process, therefore the Pd–Co alloy catalyst was stable under the applied conditions. Specific activity reported by Savadogo et al. for palladium-cobalt 28% atomic cobalt was 580 μA cm^{-2} at 0.80 V, considerably higher than for bulk platinum, 250 μA cm^{-2}.

The same year Fernández et al. proposed guidelines for the production of catalyst alloys for ORR in acidic media [6]. They assumed a mechanism where one metal is responsible for the cleavage of the O_2 molecule bond while a second metal assists the reduction of the atomic oxygen adsorbed on the surface of the catalyst. Electrocatalytic activity for ORR of binary and ternary combinations of metals (Pd, Co, Au and Ag) deposited on glassy carbon was evaluated, using scanning electrochemical microscopy (SECM) as a rapid activity screening method. Selected metal combinations were prepared on carbon black using an impregnation method followed by a reduction in H_2 at 350 ºC. The mixture Pd-Co 80:20 weight ratios showed the highest activity, close to that of the commercial Pt catalyst. Nevertheless, when tested in a PEM fuel cell, Pd-Co/C catalyst showed an increased overpotential after 3 hours of continuous operation. With addition of a small amount of Au the catalyst stability improved.

Fernández et al. also reported two electrocatalysts, Pd-Ti and Pd-Co-Au, performing at least equal to Pt catalyst for ORR in current PEMFC [5]. Catalysts were prepared by a reverse micro-emulsion route for the Pd-Co-Au/C and by an impregnation method for the Pd-Ti/C catalyst, both were finally heat treated in a reducing flowing atmosphere (90% Ar and 10% H_2 mixture) at high temperatures. Both catalysts were tested as cathode materials in single PEM cells. Pd-Co-Au/C, heat treated at 750 ºC, and Pd-Ti/C, heat treated at 900 ºC, showed both performances at least equal to those of the commercial Pt/C catalyst at the same metal content. Current densities reported at 0.5 V at 60 ºC, with pure H_2 and O_2 and using 0.2 mg cm^{-2} of metal in the cathode, for commercial Pt/C, Pd-Co-Au/C and Pd-Ti/C were 0.15, 0.16 and 0.10 A cm^{-2}, respectively. Preliminary stability tests were carried out for these two catalysts by polarizing the cell at 200 mA cm^{-2} for 12 hours. The performance of the MEA made with the Pd-Ti/C cathode was essentially stable during the stability tests; however the performance of MEA with the Pd-Co-Au/C cathode degraded. These materials were considered to be worth further investigations due to their significantly lower cost and their relative abundance compared to that of Pt. However, further studies for fuel cell applications of these materials have not been reported by Fernández et al. A more extensive physicochemical characterization study was published in 2009 [55].

Studies of Pd deposited on a TiO_2-Ti support were recently reported by Fu et al. [56]. Highly ordered TiO_2 nanotubes were fabricated on a pure titanium support, Pd was then electrochemically deposited on this support. The ORR activity was investigated in acid media in a three-electrode cell and the electrocatalytic activity was found to be lower than that of commercial Pt/C. This lower ORR current was attributed to a lower active area (a consequence of larger Pd particle size) and the lower electrical conductivity of TiO_2 compared to carbon. However this catalyst was cheaper than the commercial Pt/C and the TiO_2-Ti support is more stable than carbon in PEMFC operating conditions.

A comparative study of Pd-Co-Au catalysts prepared by two different methods was presented by Raghuveer et al. [8]. Catalysts were synthesized by a reverse microemulsion method, followed by heat treatment in a reducing atmosphere, and by impregnation followed by reduction using sodium borohydride. Catalysts were characterized by XRD and transmission electron microscopy. The catalyst prepared by reverse microemulsion method presented a single phase Pd-Co-Au alloy after being heat treated at 500 ºC, while the catalyst prepared by borohydride reduction needed temperatures of 900 ºC to form a single metal phase. Average particle sizes measured from TEM images after heat treatments at 900 ºC were 46 and 35 nm for borohydride and microemulsion methods, respectively. Catalytic activities for ORR were tested in PEM fuel cells at 60 ºC and the catalyst prepared by reverse microemulsion showed higher current densities. Current densities at 0.5 V were 0.03, 0.05 A cm^{-2} for borohydride and microemulsion methods, respectively. The difference in current densities was attributed to the difference in particle sizes and consequent differences in surface area.

In 2007, Mustain et al. published a comparative study of commercial platinum catalyst and carbon supported Pd-Co alloy for ORR in PEMFCs [7]. CoPd$_x$/C was prepared by a low temperature aqueous method, reducing salts with sodium bicarbonate and exposing them to a H$_2$/Air flow. The catalytic activity was studied between 30 and 60 ºC in a 5 cm^2 single PEM fuel cell with Nafion® membrane. The best performance was showed by the catalyst with a nominal atomic ratio 1:3, CoPd$_3$/C, comparable with the commercial Pt/C. Current densities of ca. 0.5 A cm^{-2} at 0.5 V were reported for both Pt/C and Pd$_3$Co/C cathodes. CoPd$_3$/C showed excellent chemical stability, with the open circuit potential and the current density at 0.8 V decreasing by only 3 and 10% respectively over 25 h.

Also Pd-Co alloy, this time at a nominal atomic ratio of 65% Pd to 35% Co, was studied for the ORR by Zhang et al. [11]. They studied the effect of reducing agent and H$_2$ treatment temperature on catalyst morphology and activity towards ORR. They used three reducing agents, ethylene glycol, sodium borohydride and formaldehyde and heat treatments in the range 300-700 ºC. Catalytic activities were measured with a RDE in 0.5 M H$_2$SO$_4$ at room temperature. They concluded that 300 ºC was the optimal hydrogen treatment temperature for all three Pd-Co catalyst. After heat treatment the sample prepared using ethylene glycol showed the smallest particle size, approximately 5 nm, the highest electrochemical surface area, and the highest ORR activity of all three Pd-Co catalysts.

Shao and et al. investigated the oxygen reduction reaction on Pd based alloys [9]. Alloys were prepared from commercial crystals, annealed at high temperatures by induction heating. It was found that the activity of Pd$_2$Co/C alloy catalyst nanoparticles synthesized was comparable to that of commercial platinum catalysts, which agrees with the results of

Mustain, Savadogo and Zhang previously reported [7, 11, 54]. In 2007 Shao et al. also reported carbon-supported Pd-Fe alloy nanoparticles with very high activity for the oxygen reduction reaction. Pd_3Fe on Vulcan was prepared by reduction of $FeCl_3$ on commercial Pd/C at 500 ºC in H_2 flow. The ORR activity of these catalysts in acid electrolyte was higher than the activity of the state of the art commercial Pt/C electrocatalyst. In half cell tests with a rotating disc electrode, with 10 µg cm^{-2} of metal, current densities reported at 0.8 V were 5.0 and 4.5 mA cm^{-2} for Pd_3Fe/C and Pt/C respectively.

Wang et al. [47] prepared a series of carbon supported palladium-copper catalysts with different molar ratios by co-impregnation and subsequent reduction in hydrogen atmosphere. It was concluded that the highest activity was shown by the catalysts with atomic ratio Pd:Cu approximately 1:1. In 2009 Fouda-Onana et al. [57] reached the same conclusion, the alloy with Pd:Cu 1:1 atomic ratio had the best activity for ORR. This last study was carried out with Pd-Cu alloys fabricated by sputtering on glassy carbon. Nickel and tin have also been found to enhance the electrocatalytic activity of palladium towards the reduction of molecular oxygen in acid media [58, 59]; however the stability of these materials in operating fuel cell conditions is low.

Many studies of bimetallic catalysts for ORR looked at the deposition of a metallic monolayer on a different metal or alloy. Nilekar et al. studied the deposition of a Pt monolayer on different noble metals; the highest activity towards oxygen reduction was recorded when Pt was deposited on palladium and the amount of Pt used could be further reduced by partially substituting it by a late transition metal [60]. Zhou et al studied the ORR at bare and Pt covered single crystal Pd_2Co (111) and found that activity of Pt on annealed Pd_2Co (111) was higher than on pure Pt [61]. This same group studied the catalytic activity of a monolayer of Pt on Pd_3Fe with a monolayer of segregated Pd [62], a layer formed on the surface of Pd_3Fe when it was annealed at high temperatures. It was found that although Pd_3Fe suffers ORR activity losses ORR due to potential cycling, Pd_3Fe is an excellent substrate for Pt monolayer catalysts for ORR.

Table 2-1 summarises reported electrochemical characteristics of some catalysts with reported ORR activities close to commercial Pt, which could potentially be employed in PEMFC applications. Fernández et al. claimed that carbon-supported Pd-Co-Au exhibited higher performance than commercial Pt/C operating in a H_2 PEMFC at 0.5 V [5]. However, some lack of stability was also reported. In the same publication it was also claimed that the performance of the Pd-Tu cathode was "essentially equal" to that of commercial carbon-supported Pt. At the beginning of this PhD project efforts were made to reproduce their work in order to use it as a stepping stone for the development of new palladium-based catalysts for ORR in low and high temperature PEMFC and possibly DMFC. Unfortunately, after several attempts the performance claimed in their publications could not be matched. By contrary, it was found that reported synthetic methods led to catalysts with ORR activity significantly lower than that of commercial Pt, especially Pd-Ti, which exhibited very low ORR activity (see Appendix A). Shao et al. also claimed the obtainment of a palladium based catalysts for the ORR which performed better than commercial Pt/C, Pd_3Fe/C [9]. Again this work was investigated with the intention to add further developments, however the ORR activity of catalysts prepared according to their synthetic method was dramatically below their claims (see Section 5.4.3).

Table 2-1: Significant publications on palladium-based catalysts for ORR for PEMFC applications.

Catalyst	Fuel Cell Output	Operating Conditions	Reference
Pd-Co-Au/C	0.16 A cm^{-2} (single cell)	0.5 V, 60 ºC, H_2/O_2 0.2 mg cm^{-2} cathode	[5]
Pd-Ti/C	0.10 A cm^{-2} (single cell)	0.5 V, 60 ºC, H_2/O_2 0.2 mg cm^{-2} cathode	[5]
Pt/C	0.15 A cm^{-2} (single cell)	0.5 V, 60 ºC, H_2/O_2 0.2 mg cm^{-2} cathode	[5]
Pd_5Co/C	0.15 A cm^{-2} (single cell)	0.5 V, 60 ºC, H_2/O_2 0.2 mg cm^{-2} cathode	[7]
Pt/C	0.15 A cm^{-2} (single cell)	0.5 V, 60 ºC, H_2/O_2 0.2 mg cm^{-2} cathode	[7]
Pd_3Fe/C	5.0 mA cm^{-2} (cathode)	0.8 V, room temperature 1600 rpm, 10 µg cm^{-2} of metal	[9]
Pt/C	4.5 mA cm^{-2} (cathode)	0.8 V, room temperature 1600 rpm, 10 µg cm^{-2} of metal	[9]

2.9. Conclusions

Palladium, like platinum, is a noble metal that is active for the ORR although its activity and stability are lower. Two main properties of palladium-based alloy catalysts are their ability to catalyze a four-electron ORR and their tolerance to methanol, which is particularly desirable for application in DMFC cathodes. For these reasons, together with its lower price compared with Pt, palladium based catalysts have been the subject of significant research in recent years.

It was reported that alloying of Pd with small amounts of other metals such as cobalt, gold and iron increased its activity towards the ORR. Some of the reported catalysts however require further improvement in terms of stability. In addition there is scope to investigate further combinations of Pd with other noble and non-noble metals.

Palladium and gold form a uniform alloy with a face-centered cubic crystal structure at any atomic ratio at temperatures below ca. 1280 ºC. Palladium and cobalt form a uniform alloy with a face-centered cubic crystal structure when the Pd to Co atomic ratio is 1 to 1 or higher, at temperatures lower than ca. 1300 ºC. The study of these two bimetallic systems would aid the understanding of the behavior of ternary alloys, necessary to improve their electrochemical properties.

Shao et al. used experimental data and Density Functional Theory calculations to correlate the electrocatalytic activity of different metal alloys and monolayers with their electronic properties. Dependence of the activity towards the ORR on the binding energy between oxygen and the d-band center of the metal overlayer was established. The Pd overlayer on $Pd_3Fe(111)$ was claimed to be more active than Pt due to its moderate bond with oxygen which equilibrates the O-O bond-breaking, and the removal of O and OH (unlike pure Pd and Pt surfaces which bind oxygen strongly making the removal of the adsorbed reaction intermediates difficult, and therefore slowing the ORR kinetics). The Pd overlayer on PdFe(111) was reported to have lower ORR activity than on $Pd_3Fe(111)$.

Palladium and titanium form a uniform alloy with a face-centered cubic crystal structure when the Pd to Ti atomic ratio is ca. 9 to 1 or higher, at temperatures lower than approximately 1700 ºC. The activity towards the ORR of Pd has been claimed to be influenced by the presence of TiO_2. The effect of different amounts of Ti in the Pd lattice and of adjacent TiO_2 particles on the ORR activity is to be studied.

It has also been reported that the performance of certain ternary Pd based catalysts surpassed the activity of state of the art commercial Pt/C electrocatalysts. Preparation and characterization of polycrystalline Pd-Fe alloys with different atomic ratios would contribute to the understanding of the Pd-Fe system and this would be employed in future preparation of ternary catalysts.

References

1. Ota, K., A. Ishihara, S. Mitsushima, K. Lee, Y. Suzuki, N. Horibe, T. Nakagawa, and N. Kamiya, *Improvement of cathode materials for polymer electrolyte fuel cell.* Journal of New Materials for Electrochemical Systems, 2005. **8**(1): p. 25-35.

2. Lee, K., A. Ishihara, S. Mitsushima, N. Kamiya, and K.-i. Ota, *Stability and electrocatalytic activity for oxygen reduction in WC + Ta catalyst.* Electrochimica Acta, 2004. **49**(21): p. 3479-3485.

3. Meng, H. and P.K. Shen, *Tungsten Carbide Nanocrystal Promoted Pt/C Electrocatalysts for Oxygen Reduction.* Journal of Physical Chemistry B, 2005. **109**(48): p. 22705-22709.

4. Zhong, H., H. Zhang, G. Liu, Y. Liang, J. Hu, and B. Yi, *A novel non-noble electrocatalyst for PEM fuel cell based on molybdenum nitride.* Electrochemistry Communications, 2006. **8**(5): p. 707-712.

5. Fernández, J.L., V. Raghuveer, A. Manthiram, and A.J. Bard, *Pd-Ti and Pd-Co-Au Electrocatalysts as a Replacement for Platinum for Oxygen Reduction in Proton Exchange Membrane Fuel Cells.* Journal of the American Chemical Society, 2005. **127**(38): p. 13100-13101.

6. Fernández, J.L., D.A. Walsh, and A.J. Bard, *Thermodynamic Guidelines for the Design of Bimetallic Catalysts for Oxygen Electroreduction and Rapid Screening by Scanning Electrochemical Microscopy. M-Co (M: Pd, Ag, Au).* Journal of the American Chemical Society, 2004. **127**(1): p. 357-365.

7. Mustain, W.E., K. Kepler, and J. Prakash, *CoPdx oxygen reduction electrocatalysts for polymer electrolyte membrane and direct methanol fuel cells.* Electrochimica Acta, 2006. **52**(5): p. 2102-2108.

8. Raghuveer, V., P.J. Ferreira, and A. Manthiram, *Comparison of Pd-Co-Au electrocatalysts prepared by conventional borohydride and microemulsion methods for oxygen reduction in fuel cells.* Electrochemistry Communications, 2006. **8**(5): p. 807-814.

9. Shao, M.H., T. Huang, P. Liu, J. Zhang, K. Sasaki, M.B. Vukmirovic, and R.R. Adzic, *Palladium Monolayer and Palladium Alloy Electrocatalysts for Oxygen Reduction.* Langmuir, 2006. **22**(25): p. 10409-10415.

10. Shao, M.-H., K. Sasaki, and R.R. Adzic, *Pd-Fe Nanoparticles as Electrocatalysts for Oxygen Reduction.* Journal of the American Chemical Society, 2006. **128**(11): p. 3526-3527.

11. Zhang, L., K. Lee, and J. Zhang, *Effect of synthetic reducing agents on morphology and ORR activity of carbon-supported nano-Pd-Co alloy electrocatalysts.* Electrochimica Acta, 2007. **52**(28): p. 7964-7971.

12. Moreira, J., P. del Angel, A.L. Ocampo, P.J. Sebastian, J.A. Montoya, and R.H. Castellanos, *Synthesis, characterization and application of a Pd/Vulcan and Pd/C catalyst in a PEM fuel cell.* International Journal of Hydrogen Energy, 2004. **29**(9): p. 915-920.

13. Vielstich, W., H. Gasteiger, and A. Lamm, *Handbook of fuel cells : fundamentals, technology and applications*. 2003, Chichester: Wiley. 4 v.

14. *Fuel cells: Collecting History with the World Wide Web*. 2001: Smithsonian Institution.

15. Blomen, L.J.M.J. and M.N. Mugerwa, *Fuel cell systems*. 1993, New York: Plenum Press. xix, 614.

16. Larminie, J., A. Dicks, and Knovel (Firm), *Fuel cell systems explained*. 2nd ed. 2003, Chichester, West Sussex: J. Wiley. xxii, 406.

17. Heitner-Wirguin, C., *Recent advances in perfluorinated ionomer membranes: Structure, properties and applications.* Journal of Membrane Science, 1996. **120**(1): p. 1-33.

18. Scott, K. and A.K. Shukla, *Polymer electrolyte membrane fuel cells: Principles and advances.* Re-views in Environmental Science and Biotechnology, 2004. **3**(3): p. 273-280.

19. Bar-On, I., R. Kirchain, and R. Roth, *Technical cost analysis for PEM fuel cells.* Journal of Power Sources, 2002. **109**(1): p. 71-75.

20. Li, Q., R. He, J.-A. Gao, J.O. Jensen, and N.J. Bjerrum, *The CO Poisoning Effect in PEMFCs Operational at Temperatures up to 200 ºC.* Journal of the Electrochemical Society, 2003. **150**(12): p. A1599-A1605.

21. Scott, K.a.A.K.S., *Direct Methanol Fuel Cells: Fundamentals, Problems and Perspectives., in Modern aspects of electrochemistry*, ed. R.E. white. 2007, New York: Springer.

22. Scott, K., A.K. Shukla, C.L. Jackson, and W.R.A. Meuleman, *A mixed-reactants solid-polymer-electrolyte direct methanol fuel cell.* Journal of Power Sources, 2004. **126**(1-2): p. 67-75.

23. Ma, Y.L., J.S. Wainright, M.H. Litt, and R.F. Savinell, *Conductivity of PBI membranes for high-temperature polymer electrolyte fuel cells.* Journal of the Electrochemical Society, 2004. **151**(1).

24. Mamlouk, M. and K. Scott, *Phosphoric acid-doped electrodes for a PBI polymer membrane fuel cell.* International journal of energy reasearch, 2010.

25. *Electrocatalysis of Direct Methanol Fuel Cells*, ed. H. Liu and J. Zhang. 2009, Weinheim: WILEY-VCH.

26. Cheng, H., Yuan, W., Scott, K. , *The influence of a new fabrication procedure on the catalytic activity of ruthenium-selenium catalysts.* Electrochimica Acta, 2006. **52**(2): p. 466-473.

27. Hilgendorff, M., Diesner, K., Schulenburg, H., Bogdanoff, P., Bron, M., Fiechter, S., *Preparation Strategies towards Selective Ru-Based Oxygen Reduction Catalysts for Direct Methanol Fuel Cells* Journal of New Materials for Electrochemical Systems, 2002. **5**(2): p. 71-81.

28. Schulenburg, H., Hilgendorff, M., Dorbandt, I., Radnik, J., Bogdanoff, P., Fiechter, S., Bron, M., Tributsch, H., *Oxygen reduction at carbon supported ruthenium-selenium catalysts: Selenium as promoter and stabilizer of catalytic activity.* Journal of Power Sources, 2006. **155**(1): p. 47-51.

29. Kinoshita, K. and Electrochemical Society., *Electrochemical oxygen technology*. The Electrochemical Society series. 1992, New York: Wiley. xiv, 431.

30. Lee, K., O. Savadogo, A. Ishihara, S. Mitsushima, N. Kamiya, and K.I. Ota, *Methanol-tolerant oxygen reduction electrocatalysts based on Pd-3D transition metal alloys for direct methanol fuel cells.* Journal of the Electrochemical Society, 2006. **153**(1).

31. Li, H., Q. Xin, W. Li, Z. Zhou, L. Jiang, S. Yang, and G. Sun, *An improved palladium-based DMFCs cathode catalyst.* Chemical Communications, 2004(23): p. 2776-2777.

32. Joo, J.B., Y.J. Kim, W. Kim, N.D. Kim, P. Kim, Y. Kim, and J. Yi, *Methanol-tolerant PdPt/C alloy catalyst for oxygen electro-reduction reaction.* Korean Journal of Chemical Engineering, 2008. **25**(4): p. 770-774.

33. Kim, I.T., H.K. Lee, and J. Shim, *Synthesis and characterization of Pt-Pd catalysts for methanol oxidation and oxygen reduction.* Journal of Nanoscience and Nanotechnology, 2008. **8**(10): p. 5302-5305.

34. Bernardi, D.M. and M.W. Verbrugge, *A Mathematical Model of the Solid-Polymer-Electrolyte Fuel Cell.* Journal of The Electrochemical Society, 1992. **139**(9): p. 2477-2491.

35. Hottinen, T., M. Noponen, T. Mennola, O. Himanen, M. Mikkola, and P. Lund, *Effect of ambient conditions on performance and current distribution of a polymer electrolyte membrane fuel cell.* Journal of Applied Electrochemistry, 2003. **33**(3): p. 265-271.

36. Mennola, T., M. Noponen, M. Aronniemi, T. Hottinen, M. Mikkola, O. Himanen, and P. Lund, *Mass transport in the cathode of a free-breathing polymer electrolyte membrane fuel cell.* Journal of Applied Electrochemistry, 2003. **33**(11): p. 979-987.

37. Guvelioglu, G.H. and H.G. Stenger, *Computational fluid dynamics modeling of polymer electrolyte membrane fuel cells.* Journal of Power Sources, 2005. **147**(1-2): p. 95-106.

38. Sun, Y.-P. and K. Scott, *An analysis of the influence of mass transfer on porous electrode performance.* Chemical Engineering Journal, 2004. **102**(1): p. 83-91.

39. Scott, K., S. Pilditch, and M. Mamlouk, *Modelling and experimental validation of a high temperature polymer electrolyte fuel cell.* Journal of Applied Electrochemistry, 2007. **37**(11): p. 1245-1259.

40. Hu, J., H. Zhang, Y. Zhai, G. Liu, J. Hu, and B. Yi, *Performance degradation studies on PBI/H3PO4 high temperature PEMFC and one-dimensional numerical analysis.* Electrochimica Acta, 2006. **52**(2): p. 394-401.

41. Cutlip, M.B., S.C. Yang, and P. Stonehart, *Simulation and optimization of porous gas-diffusion electrodes used in hydrogen oxygen phosphoric acid fuel cells--II development of a detailed anode model.* Electrochimica Acta, 1991. **36**(3-4): p. 547-553.

42. Yang, S.C., M.B. Cutlip, and P. Stonehart, *Simulation and optimization of porous gas-diffusion electrodes used in hydrogen/oxygen phosphoric acid fuel cells--I. Application of cathode model simulation and optimization to PAFC cathode development.* Electrochimica Acta, 1990. **35**(5): p. 869-878.

43. Yeager, E., *Dioxygen electrocatalysis: mechanisms in relation to catalyst structure.* Journal of Molecular Catalysis, 1986. **38**(1-2): p. 5-25.

44. Sawyer, D.T. and R.J. Day, *Kinetics for oxygen reduction at platinum, palladium and silver electrodes.* Electrochimica Acta, 1963. **8**(8): p. 589-594.

45. Damjanovic, A. and V. Brusic, *Oxygen reduction at Pt-Au and Pd-Au alloy electrodes in acid solution.* Electrochimica Acta, 1967. **12**(9): p. 1171-1184.

46. Mustain, W.E., K. Kepler, and J. Prakash, *Investigations of carbon-supported CoPd3 catalysts as oxygen cathodes in PEM fuel cells.* Electrochemistry Communications, 2006. **8**(3): p. 406-410.

47. Wang, X., N. Kariuki, J.T. Vaughey, J. Goodpaster, R. Kumar, and D.J. Myers, *Bimetallic Pd-Cu Oxygen Reduction Electrocatalysts.* Journal of the Electrochemical Society, 2008. **155**(6): p. B602-B609.

48. Papageorgopoulos, D.C., M. Keijzer, J.B.J. Veldhuis, and F.A. de Bruijn, *CO Tolerance of Pd-Rich Platinum Palladium Carbon-Supported Electrocatalysts.* Journal of the Electrochemical Society, 2002. **149**(11): p. A1400-A1404.

49. Machida, K. and M. Enyo, *In situ x-ray diffraction study of hydrogen entry into palladium and palladium-gold alloy electrodes during anodic formaldehyde oxidation.* Journal of the Electrochemical Society, 1987. **134**(6): p. 1472-4.

50. Lewis, F.A., *The Palladium-Hydrogen System*. 1967. 178 pp.

51. Chaston, J.C., E.J. Sercombe, and V.I.O.P. 122-125, *Palladium-on-Charcoal Catalysts: some effects of variables on hydrogenation activity.* Platinum Metals Review, 1961. **5**(4): p. 122-125.

52. Bond, G.C., *Small Particles of the Platinum Metals.* Platinum Metals Review, 1975. **19**(4): p. 126-134.

53. Pope, D., W.L. Smith, M.J. Eastlake, and R.L. Moss, *The structure and activity of supported metal catalysts. VI. Measurement of dispersion in palladium-charcoal catalysts.* Journal of Catalysis, 1971. **22**(1): p. 72-84.

54. Savadogo, O., K. Lee, K. Oishi, S. Mitsushima, N. Kamiya, and K.I. Ota, *New palladium alloys catalyst for the oxygen reduction reaction in an acid medium.* Electrochemistry Communications, 2004. **6**(2): p. 105-109.

55. Sun, Y.M., M. Alpuche-Aviles, A.J. Bard, J.P. Zhou, and J.M. White, *Preparation and characterization of Pd-Ti electrocatalyst on carbon supports for oxygen reduction.* Journal of Nanoscience and Nanotechnology, 2009. **9**(2): p. 1281-1286.

56. Fu, Y., Z.D. Wei, S.G. Chen, L. Li, Y.C. Feng, Y.Q. Wang, X.L. Ma, M.J. Liao, P.K. Shen, and S.P. Jiang, *Synthesis of Pd/TiO2 nanotubes/Ti for oxygen reduction reaction in acidic solution.* Journal of Power Sources, 2009. **189**(2): p. 982-987.

57. Fouda-Onana, F., S. Bah, and O. Savadogo, *Palladium-copper alloys as catalysts for the oxygen reduction reaction in an acidic media I: Correlation between the ORR kinetic parameters and intrinsic physical properties of the alloys.* Journal of Electroanalytical Chemistry, 2009. **636**(1-2): p. 1-9.

58. Solorza-Feria, O., V. Collins-Martinez, R.G. Gonzalez-Huerta, A. Lopez-Ortiz, and D. Delgado-Vigil, *Oxygen reduction kinetics of ball-milling synthesis Pd electrocatalysts in acid medium.* Journal of New Materials for Electrochemical Systems, 2009. **12**(2-3): p. 63-67.

59. Miah, M.R., M.T. Alam, T. Okajima, and T. Ohsaka, *Electrochemically fabricated tin-palladium bimetallic electrocatalyst for oxygen reduction reaction in acidic media.* Journal of the Electrochemical Society, 2009. **156**(10): p. B1142-B1149.

60. Nilekar, A.U., Y. Xu, J. Zhang, M.B. Vukmirovic, K. Sasaki, R.R. Adzic, and M. Mavrikakis, *Bimetallic and ternary alloys for improved oxygen reduction catalysis.* Topics in Catalysis, 2007. **46**(3-4): p. 276-284.

61. Zhou, W.P., M.B. Vukmirovic, K. Sasaki, and R.R. Adzic. *Oxygen reduction reaction on a Pt monolayer on a $Pd_2Co(111)$ single crystal surface*. in *ECS Transactions*. 2008.

62. Zhou, W.P., X. Yang, M.B. Vukmirovic, B.E. Koel, J. Jiao, G. Peng, M. Mavrikakis, and R.R. Adzic, *Improving electrocatalysts for O2 reduction by fine-tuning the Pt-support interaction: Pt monolayer on the surfaces of a Pd3Fe(111) single-crystal alloy.* Journal of the American Chemical Society, 2009. **131**(35): p. 12755-12762.

Chapter 3: Research methodology

3.1. Introduction

In this chapter methods and techniques employed in the physicochemical and electrochemical characterization of electrocatalysts are briefly described. It also includes the detailed description of experimental set up used to carry out different electrochemical tests and different synthetic procedures employed in the preparation of electrocatalysts. Electrochemical characterization of the electrocatalysts was initially carried out using a three-electrode cell. Cyclic voltammetry was the main electrochemical method used to characterise the catalysts. A few selected catalysts were further tested in low and high temperature hydrogen PEMFC and DMFC.

The crystalline structure of carbon-supported palladium and palladium-based catalysts was characterised using X-Ray Diffraction (XRD). Transmission Electron Microscopy was employed to study particle size and particle distribution on the carbon support. Energy Dispersive X-ray analysis was used to quantify the metal content of the electrocatalysts. Particle sizes and distance between atomic layers in crystals were calculated from the XRD data using Scherrer and Bragg equations, respectively.

3.2. Three-electrode cell

In the study of the oxygen reduction reaction, the cathodic reaction must be the rate determining reaction. At the counter electrode (the anode) water was oxidized to oxygen and protons. The area of the counter electrode was larger than that of the cathode to ensure that the anode reaction was not limiting. The three-electrode cell used in this study is shown schematically in Figure 3-1.

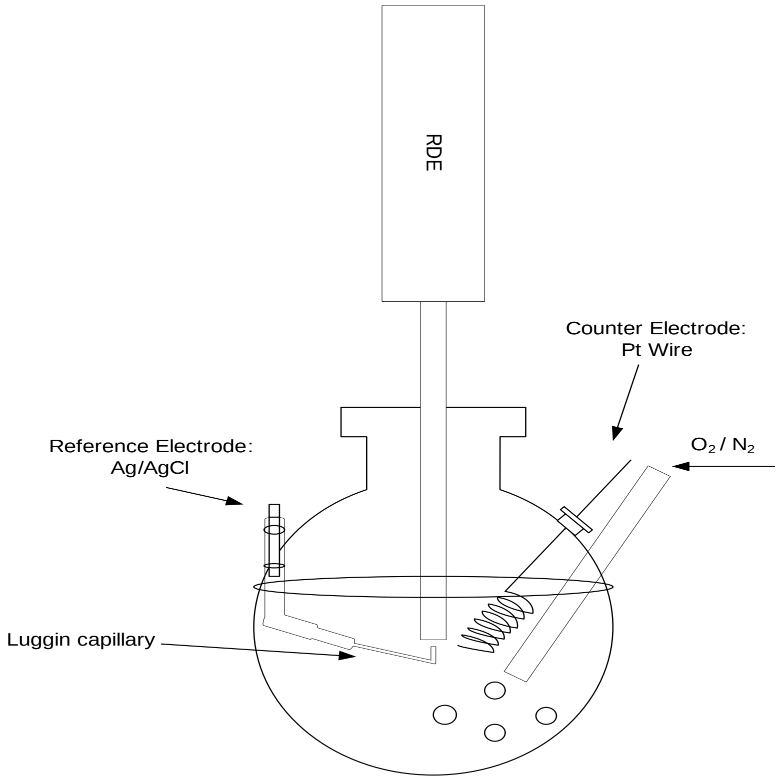

Figure 3-1: Schematic diagram of the half cell experimental setup.

The electrolyte, 0.1 dm^3 (L) of 0.5 mol dm^{-3} H_2SO_4, was saturated either with N_2 or O_2 before carrying out electrochemical measurements. To ensure the electrolyte was fully saturated with either N_2 or $O_{2,}$ the desired gas was bubbled into the solution at a flow rate of ca. 40 cm^3 min^{-1} for 0.5 hours before running each test. Gas flow was controlled manually with a N_2 or O_2 flow meter (Platon (RM&C), U.K); gas flow rates lower than 20 cm^3 min^{-1} were used while tests were carried out.

The half cell consists of a Rotating Disc Electrode (RDE), from Radiometer Analytical, as a working electrode. The RDE tip was made of glassy carbon, 3 mm in diameter. Different rotation speeds were used when ORR activities were studied. The reference electrode employed was a Silver Chloride Saturated KCl electrode (+0.197 V vs Normal Hydrogen Electrode), and the counter electrode was a coiled platinum wire, 23 cm long and 0.5 mm diameter. A Luggin capillary held the reference electrode to minimise the IR potential losses across the electrolyte. The tip of the Luggin capillary was situated approximately 1 mm from the working electrode.

The electrode was prepared by depositing a drop of catalyst ink onto the glassy carbon tip of the RDE. Catalysts inks were prepared by mixing 30.3 mg of carbon supported catalysts with 4 mL of water-ethanol (33% volume of ethanol) solution containing 0.38% of Nafion®. This mixture was mixed in the ultrasonic bath for ca. 0.3 hours, then immediately an ink drop of 4 µL was located on the glassy carbon tip of the RDE. The drop was allowed to dry in air and the electrode was then introduced in the oven under an air atmosphere for 3 minutes at 100 ºC. The catalyst loading on the electrode was 86 µg cm^{-2} for all different catalysts tested. Electrochemical data was collected with a BAS Epsilon potentiostat.

3.3. Low temperature polymer electrolyte membrane fuel cell

Membrane electrode assemblies (MEAs) were prepared by hot pressing membrane and electrodes together at 130 ºC for 3 min applying a load of ca. 50 kg cm^{-2}. Nafion® 112 (DuPont) was used as the electrolyte membrane; the received membrane was boiled in 2% hydrogen peroxide for approximately 0.5 hours, rinsed with deionized water and then boiled in 1M H_2SO_4 for 1 hour before being thoroughly washed with deionized water. Pt/C purchased from E-Tek was used as anode material in each case.

The electrodes were prepared as follows. Catalyst inks were prepared by mixing in an ultrasonic bath the carbon-supported catalyst with Nafion® in a water-ethanol (66% volume of ethanol) solution for 0.5 hours. The amount of Nafion® in the catalyst ink was 20% of the catalyst weight. Metal loadings were 0.2 mg cm^{-2} of Pt in the anode and 0.6 mg cm^{-2} of Pt, Pd, Pd_4Co or Pd_9Ti in the cathode. The catalyst layer was sprayed on a commercial gas diffusion layer, a low temperature microporous layer (GDL LT 1200-W, from E-Tek).

The fuel cell setup used to test the MEAs is shown schematically in Figure 3-2. The cell body was made of graphite with 1 cm x 1 cm parallel flow fields. The temperature of the cell was controlled by cartridge heaters inserted into the cell body. Operation temperatures were 20, 40 and 60 ºC. The relative humidity was measured at different operating conditions using a humidity and temperature transmitter (Vaisala HUMICAP®, Finland). H_2 was used as a fuel and either air or oxygen was used as an oxidant. The hydrogen passed through a home-made humidifier kept at a temperature 10 ºC higher than the cell operation temperature. Air and oxygen were used directly without further humidification. Flow rates were controlled manually by appropriate flow meters (Platon (RM&C), U.K). Gases were fed at atmospheric pressure.

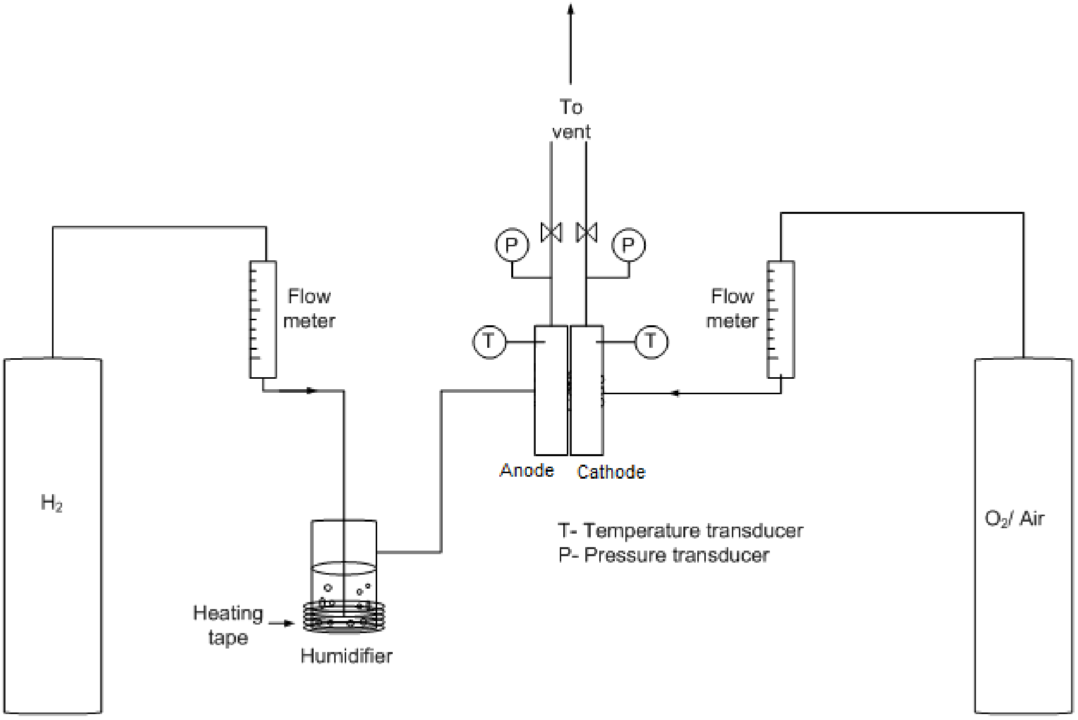

Figure 3-2: Schematic diagram of the low temperature PEM fuel cell experimental setup.

MEA conductivity was measured using a Gill AC frequency response analyzer (ACM instruments, U.K) in the range of 10 to 200 kHz with amplitude of 15 mV.

3.4. High temperature polymer electrolyte membrane fuel cell

Membrane Electrode Assemblies (MEA) for High Temperature Polymer Electrolyte Membrane (HTPEM) fuel cell tests were prepared using home-made polybenzimidazole membrane (PBI) and gas diffusion electrodes suitable for high temperature operation.

3.4.1. Polybenzimidazole membrane preparation

For the preparation of the membrane, PBI powder (from Between Lizenz GmbH, Germany) was dissolved in N,N'-dimethylacetamide (DMAc) at a temperature of 250°C in an autoclave. The autoclave was purged with nitrogen and the temperature gradually increased to 250°C whilst the pressure was increased to 6 bars. The temperature was then held for 5 hours and the solution was kept under magnetic stirring to allow the polymer to dissolve. A 2% weight lithium chloride solution was added to the solution as a stabiliser [1]. The solution was allowed to cool and then was filtered to remove any un-dissolved polymer. The membrane was casted by pouring the solution on an optically flat glass and kept in the oven between 90 and 110 ºC for 12 hours to produce a 40 to 60 μm thick membrane. Membranes were then further dried at 200 ºC for 2 hours to remove any traces of DMAc. Membrane was finally boiled in de-ionised water for 1 hour to remove any possible traces of solvent and lithium chloride.

Pure PBI has a very low conductivity [2], therefore it requires doping with phosphoric acid to facilitate proton conduction. The higher the doping level the higher the conductivity, however, its mechanical properties deteriorate dramatically by increasing the doping level [3]. The doping process was carried out by immersing the membrane in an 11.5% weight phosphoric acid solution for 5 days at room temperature. After doping, the membrane was dried under vacuum at 110°C until it was a constant weight. The doping level was calculated from the weight gain of the membrane before and after doping; it was between 5.5 and 6 molecules of acid per repeat polymer unit.

3.4.2. Membrane electrode assembly preparation and testing

Membrane electrode assemblies (MEAs) were prepared by hot pressing the membrane together with the electrodes at 130 ºC for 3 min applying a load of ca. 50 kg cm^{-2}. The electrodes were prepared as follows using catalysts inks. The catalyst ink was prepared by mixing the carbon-supported catalyst in a water:ethanol 3:1 mixture containing 40 and 20% weight PTFE for the cathode and anode inks, respectively, for 30 minutes. The required amount of PA acid was added afterwards to the surface of the catalyst layer using a micro-pipette. Metal loadings were 0.2 mg cm^{-2} of Pt in the anode and 0.3 mg cm^{-2} of metal in the cathode. 20% weight Pt/C purchased from E-Tek was used as anode material in each case. The catalyst layer was sprayed on a commercial wet proofed gas diffusion layer, (H2315 C1 from Freudenberg, Germany).

The cell used for the HTPEMFC tests was built of titanium, and was gold plated in the area in contact with the MEA as the oxide formation in this surface increases the contact resistance. The fuel cell had 1 cm x 1 cm gold plated parallel flow fields. The cell temperature was controlled by thermostatically managed cartridge heaters inserted into the cell body. Feeding gases were passed through a home-made humidifier before entering the cell at room temperature. Flow rates were controlled manually by an appropriate flow meter (Platon (RM&C), U.K).

3.5. Direct methanol fuel cell

Membrane electrode assemblies (MEAs) were prepared, as for low and high temperature PEMFCs, by hot pressing membrane and electrodes at 130 ºC for 3 min, applying a load of ca. 50 kg cm^{-2}. The electrodes were prepared as follows using catalysts inks. Metal loadings were 2 mg cm^{-2} PtRu in the anode and 2 mg cm^{-2} of Pd or Pt in the cathode. Catalysts used were commercial carbon-supported PtRu 60% weight (E-Tek) for the anode and commercial carbon-supported Pt 20% weight (E-Tek) or home-made Pd/C 20% weight. Nafion® 117 was used as the electrolyte membrane; the received material was boiled in 2% hydrogen peroxide for 30 minutes, rinsed with deionized water and then boiled with 1M H_2SO_4 for 1 hour before being thoroughly washed with deionized water. Catalyst layers were sprayed on a commercial commercial wet proofed gas diffusion layer, (CX196, from Freudenberg, Germany). The catalyst ink was prepared by mixing in an ultrasonic bath the carbon-supported catalyst with a water:ethanol Nafion® solution for 30 minutes. The amount of Nafion® in the catalyst ink was 15% of the catalyst weight.

The fuel cell setup used to test the MEAs is shown schematically in Figure 3-3. The cell body was made of two graphite blocks each with 3 cm x 3 cm parallel flow fields. The temperature of the cell was controlled by heating pads located at both sides of the cell body. Operating temperatures were 20, 40 and 60 ºC. Aqueous 1M methanol solution was pumped into the anode at a rate of ca. 7 mL min^{-1} using a Watson Marlow 101U/R pump. Air or oxygen was fed to the cathode side at a rate of approximately 300 mL min^{-1}. Gas flow rate was controlled manually by appropriate flow meters (Platon (RM&C), U.K) and was fed at atmospheric pressure.

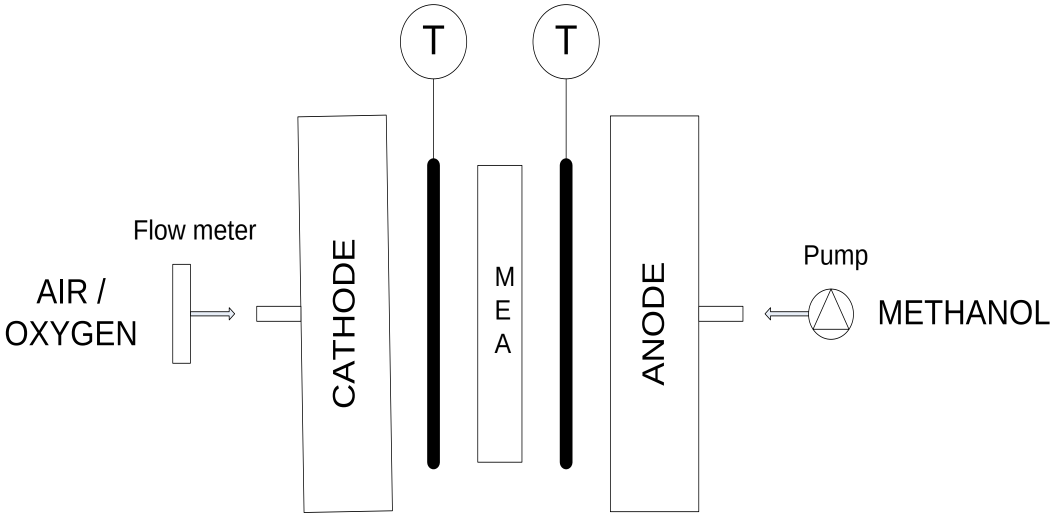

Figure 3-3: Schematic diagram of the direct methanol fuel cell experimental setup.

3.6. Cyclic voltammetry and Tafel analysis

3.6.1. Cyclic voltammetry

The electrochemical behavior of a system can be obtained by recording the current-time curves at different potentials. Information can be obtained in a single experiment, by sweeping the potential with time and recording the current-potential curve. This method is known as Linear Sweep Voltammetry (LSV). By switching the direction of the scan at a certain potential (switching potential) and carrying out the reverse experiment of the LSV the so called Cyclic Voltammetry (CV) is obtained. CV is one of the most commonly used methods for the study of electrochemical systems. The cyclic voltammogram of a given electrode without any active species in the electrolyte results in a current-potential curve characteristic for the electrode material used [4, 5]. Cyclic voltammetry was the main electrochemical method used to characterise the synthesized catalysts.

Cyclic voltammetry in oxygen free electrolyte was used to characterise short term stability of catalysts, to quantify the electrochemical surface area (ECSA) and, together with XRD analysis, to determine whether a new metal phase was formed in the study of alloy catalysts. As previously mentioned the cyclic voltammogram of a given electrode without active species in the electrolyte is characteristic for each electrode material. Therefore, the modification of the electrode material, for instance by alloying it with another metal, would lead to a change in the current-potential curve recorded. Short term stability and electrochemical surface area studies are both based on the surface area of the catalysts determined from the cyclic voltammogram.

For palladium electrodes, in contrast with platinum, the charge of a monolayer of adsorbed hydrogen is difficult to determine due to the ability of bulk palladium to absorb hydrogen [6, 7]. Therefore, the electrochemical surface area was calculated from the charge of the monolayer of chemisorbed oxygen, which was estimated from the area of the palladium oxide reduction peak. The charge of the oxygen monolayer (Q_O) for a smooth palladium electrode is twice as large as the hydrogen monolayer (Q_H) in platinum, $Q_H = ½\ Q_O$ ($Q_H = 210\ \mu C\ cm^{-2}$) [6, 8, 9]. When the values of the electrochemical surface area (the area of the Pd-O reduction peak) decreased by a significant fraction with each successive potential cycle the catalyst was said not to have short term stability.

Electrochemical surface area (ECSA) was quantified from slow scan voltammograms, at scan rate 5 mV s^{-1}. Electrode conditioning consisted of ten cycles at scan rate 50 mV s^{-1}, after this slow voltammograms were recorded. Different potential ranges were selected depending on the scan rate. Initial 10 cyclic voltammetries in N_2 saturated electrolyte were performed between 0.04 and 1.24 V vs Normal Hydrogen Electrode (NHE); when the scan rate was 5 mV s^{-1} the potential range was between 0.07 and 1.24 V vs NHE. Open circuit potential of the cell was taken as initial potential, ca. 0.8 V, the first and second switching potentials were 1.24 and 0.04 or 0.07 V, respectively, and the final potential was 1.24 V.

The activity towards the ORR was evaluated by CV in O_2 saturated electrolyte. A cyclic voltammogram was recorded in O_2 saturated 0.5 M H_2SO_4 electrolyte at scan rate 1 mV s^{-1}. The open circuit potential (OCP) of the cell was measured when the electrode was immersed in the O_2 saturated electrolyte. The first scan or LSV was recorded by holding the electrode at a potential 50 mV higher than the OCP for 10 s and then, immediately after, sweeping the potential at 1 mV s^{-1} towards lower potentials, to 0.25 V. The second scan or backward LSV started from 0.25 V sweeping the potential at 1 mV s^{-1} up to the OCP potential plus 50 mV. All parameters reported were obtained from the backward LSV.

3.6.2. Tafel analysis

The kinetic current density or current density in absence of mass transport effect, i_k, is a function of the exchange current density, i_0, this relationship can be expressed by the Butler-Volmer equation as [10]:

$$i_k = i_0\left(\exp\left(\frac{-\alpha_c F}{RT}\eta\right) - \exp\left(\frac{\alpha_a F}{RT}\eta\right)\right) \tag{3.1}$$

Where i_k is the overall current density, i_0 is the exchange current density (in A m^{-2}) η is the overpotential, and α is the transfer coefficient.

The relationship between the overall current density, i, and the currents with and without mass transport effects is expressed by the well known Koutecky-Levich equation (Equation 3.2):

$$\frac{1}{i} = \frac{1}{i_k} + \frac{1}{i_l} \tag{3.2}$$

Koutecky-Levich equation can be solved for the kinetic current and expressed as:

$$i_k = \frac{i_L \times i}{i_L - i} \tag{3.3}$$

Substituting Equation 3.3 in the Butler-Volmer equation:

$$\frac{i_L \times i}{i_L - i} = i_0\left(\exp\left(\frac{-\alpha_c F}{RT}\eta\right) - \exp\left(\frac{\alpha_a F}{RT}\eta\right)\right) \tag{3.4}$$

For large negative overpotentials the second term, exp(αaFη/RT), becomes negligible and Equation 3.4 becomes the Tafel form:

$$\frac{i_L \times i}{i_L - i} = i_0\left(\exp\left(\frac{-\alpha F}{RT}\eta\right)\right) \tag{3.5}$$

Rearranging Equation 3.5:

$$\eta = \frac{RT}{\alpha F}\ln i_0 - \frac{RT}{\alpha F}\ln\left(\frac{i_L \times i}{i_L - i}\right) \tag{3.6}$$

The relationship between overpotential and current densities at high overpotentials when the system is not mass transfer affected is given by Tafel as:

$$\eta = a + b\log\left(\frac{i_L \times i}{i_L - i}\right) \tag{3.7}$$

From Equations 3.6 and 3.7 we obtain the empirical Tafel constants:

$$a = \frac{2.3RT}{\alpha F}\log i_0 \tag{3.8}$$

$$b = \frac{-2.3RT}{\alpha F} \tag{3.9}$$

Plots of log i vs η are known as Tafel plots, they are useful tools to evaluate kinetic parameters. Tafel plots generate a linear region of slope b. From b the transfer coefficient, α, can be calculated using Equation 3.9. When the linear region is extrapolated to zero overpotential log i_0 is obtained.

Data points for Tafel analysis of the kinetically controlled region were taken from the near-steady-state voltammograms, with linear sweep voltammetries at scan rate 1 mV s^{-1}. To determine Tafel data parameters (Equation 3.7) $\log(i_L x i/i_L - i)$ vs η data were plotted. Tafel parameters were obtained by adjusting the straight line to the linear region of the plot (minimum correlation coefficient of 0.995).

3.7. Rotating disc electrode and Koutecky-Levich plots

The Rotating Disc Electrode (RDE) provides a well defined hydrodynamic regime when used in the study of the kinetics of electrode reactions. The use of RDE allows passing a controllable flow of electrolyte (containing dissolved oxygen) over the catalysts later on the electrode. It was employed in the three electrode cell experiments. The RDE employed in this study was an EDI101 from Radiometer Analytical, and consisted of a flat glassy carbon disc embedded in a rod of PTFE. Rotation speeds of 400, 900, 1600, 2500 and 3600 rpm were selected to evaluate the kinetics and the mass transport effects.

The relationship between the overall current density and the currents with and without mass transport effects is expressed by the previously cited Koutecky-Levich equation (Equation 3.2).

The Koutecky-Levich equation can be also expressed as:

$$\frac{1}{i} = \frac{1}{i_k} + \frac{1}{B\sqrt{\omega}} \qquad (3.10)$$

Where ω is the rotation speed and B is a constant dependent on the oxygen diffusivity, concentration and on the viscosity of the electrolyte [4]. Koutecký-Levich plots were obtained representing i^{-1} vs $\omega^{-1/2}$, where i is the overall current density and ω is the rotation speed, at a given potential value. The extrapolation of the linear region of the plots to infinite rotation speed allowed the determination of the kinetic current i_k.

Activity for ORR of Pd/C catalysts was analyzed using the Koutecky-Levich plots. From this analysis current densities in the absence of mass transport, i_k, were obtained. Current densities measured at five different rotation speeds, 400, 900, 1600, 2500 and 3600 rpm, were presented for five different potential values. Data was obtained from slow scan voltammograms, linear sweep voltammetries at scan rate 5 mV s^{-1}.

3.8. X-ray diffraction analyses

X-Ray Diffraction (XRD) crystallography was used to determine the crystal structure of the catalysts, thus determining the formation of alloy. Changes in the crystal structure compared to pure Pd were use to determinate whether or not an alloy was formed. Data obtained from XRD diffractograms was used to calculate distances between atomic layers in crystals and estimate the size of metal nanoparticles.

A broad peak at a 2θ value around 25º, due to the carbon support [11], was present in every spectrum. Data from diffraction peak corresponding Pd (220) crystal face, which was considered not to be influenced by the presence of carbon, was employed in calculations. Diffraction peaks of Pd (111), Pd (220) and Pd (331) might overlap with the diffraction peak of the carbon support, therefore Pd (220) peak was chosen to evaluate the size of supported Pd particles [12, 13].

X-ray diffraction analyses were carried out using a PANanalytical X'Pert Pro diffractometer fitted with an X'Celerator and peak positions were analysed using the X'Pert Data Viewer software. The radiation was Cu K-alpha, with λ = 1.54180 Å. Analyses were performed by the Chemical Analysis Unit at Newcastle University.

The crystallite size, referred to as particle size, was calculated from the XRD data using Scherrer equation [14]:

$$D = k \times \lambda / FWHM \times \cos\theta \tag{3.11}$$

Where *D* is the particle diameter, in Å, *k* is the shape factor (k =0.89 for spherical particles), *FWHM* is the full width of the peak at half maximum, *λ* is the wavelength applied in the characterization and θ is the position at the maximum of diffraction. Both *FWHM* and θ are expressed in radians.

The Pd-Pd bond distance, or nearest neighbour distance in the lattice, was calculated using Braggs equation [14]:

$$2d \times \sin\theta = n \times \lambda \tag{3.12}$$

Where *d* is the distance between atomic layers in crystals, expressed in Å, and *n* is an integer (n =1).

3.9. Energy Dispersive X-Ray Analysis

Energy Dispersive X-Ray Analysis (EDXA) was used for the elemental analysis of the samples. This technique was used to quantify the overall metal content in carbon supported catalysts and to determine the atomic metal to metal ratio for bimetallic electrocatalysts. This analytical technique relies on the investigation of interactions between electromagnetic radiation and matter, analyzing X-rays emitted by the sample, which are characteristic of each atomic structure, and therefore of each element [15].

Carbon supported metal nanoparticles were located in aluminium supports for the analysis. The EDXA analyzer was a Rontec Edwin. Analyses were performed by the Chemical Analysis Unit at Newcastle University.

3.10. Transmission electron microscopy analysis

Transmission Electron Microscopy (TEM) analysis were used to study particle size and particle distribution on the carbon support. Carbon and metal particles have different capacity to absorb electrons. This difference provides a contrast in the images which allows the metal nanoparticles on the carbon support to be located. Metal particles appear darker than carbon in TEM images [16].

Catalyst powder was suspended in deionised water; this mixture was located on 200 mesh copper grids (Gilder Grids Ltd.) and dried on air. Images were obtained from a Philips CM100 TEM with Compustage attached to a high resolution digital camera. Analyses were performed by the Electron Microscopy Research Services at Newcastle University.

3.11. Catalysts preparation

3.11.1. Preparation of carbon-supported Pd nanoparticles

Electrocatalysts were prepared by reduction of the palladium precursor, ammonium tetrachloropalladate (II), using different reducing agents; ethylene glycol (EG), formaldehyde and sodium borohydride. The reduction with EG, using the polyol method [17], was carried out under N_2 flow to minimise the number of oxidized species in the catalysts [18]. Synthesis with the other two reducing agents was carried out under air. Further catalyst preparations were carried out using the polyol method and maintaining an alkaline pH, in order to optimise the synthesis method. The carbon support used was Vulcan XC-72R (Cabot), which was pre-treated in order to create acidic functionalities on the carbon surface. These acid groups would increase the hydrophilic character of the carbon and lead to a more uniform distribution of the Pd nanoparticles on the carbon surface. Pre-treatment consisted of refluxing the carbon for 16 hours at 120 ºC in a solution containing 7 mol dm^{-3} (M) of HNO_3 [12]. Prior to metal deposition, pre-treated carbon was thoroughly washed with deionised water until the pH was close to neutral.

3.11.2. Preparation using ethylene glycol as a reducing agent

Reduction of the palladium salt with ethylene glycol (EG) was carried out at five different conditions. For the first procedure there was no pH control during the addition of the palladium salt; the salt was dissolved in a 4:1 mixture of ethylene glycol and 0.1 M aqueous NaOH solution. For the other four procedures the pH was adjusted to a certain value (10, 11, 12 or 13) and kept constant during the addition of the aqueous Pd salt solution. The pH was measured using a Jenway 3310 pH meter. Pd nanoparticles were also deposited on untreated Vulcan XC-72R using EG at pH 11.

In the preparation, 40 cm^3 (mL) of ethylene glycol (Aldrich, 99.8%), were mixed with 0.3 g of pre-treated Vulcan XC-72R under magnetic stirring and nitrogen flow. The pH of the solution was adjusted, if applicable, with drops of 1 M NaOH (Aldrich, 98%) solution. 20 $cm^3$of an aqueous solution containing 0.203 g of $(NH_4)_2PdCl_4$ (Aldrich, 99.995%) were added drop wise whilst maintaining a constant pH. The mixture was heated to 110 ºC and refluxed for 3 hours. The system was continuously stirred overnight at room temperature.

The overall reduction of the palladium salt by ethylene glycol is shown in Equation 3.13. This reaction is believed to yield palladium metal and CO_2 adsorbed on the surface of the metal particles [19]. This adsorbed CO_2 may be further oxidized to CO_2. The intermediate products of the ethylene glycol oxidation would be aldehydes, which are not very stable and would oxidize to glycolic and oxalic acid. The two carboxylic acids would be further oxidized to CO_2.

$$C_2H_6O_2 + 3Pd^{2+} \rightarrow 2CO_2 + 3Pd + 6H^+ \tag{3.13}$$

In each case, the carbon-supported palladium catalyst was separated by centrifuging and extensively washed with water and acetone. The catalyst was dried at 100 ºC in air overnight and the resulting solid was ground with a mortar. These materials were called Pd/C-EG, Pd/C-EG10, Pd/C-EG11, Pd/C-EG12 and Pd/C-EG13 corresponding to no pH control, pH 10, pH 11, pH 12 and pH 13 respectively. The Pd prepared on untreated carbon was called Pd/C-EG11-untr. Part of each catalyst was further treated at 300 ºC under H_2 flow for 1 hour [11] and those materials were called Pd/C-EG-300, Pd/C-EG10-300, Pd/C-EG11-300, Pd/C-EG12-300, Pd/C-EG13-300 and Pd/C-EG11-untr-300.

3.11.3. Preparation using formaldehyde as a reducing agent

Pre-treated Vulcan XC-72R, 0.3g, was dispersed in 40 cm^3 of water containing 0.14 g of $NaCO_3$ (Aldrich, 99.5%). The dispersion was heated to 80 ºC with continuous stirring. 20 cm^3 of an aqueous solution of $(NH_4)_2PdCl_4$, containing the necessary amount of salt to prepare 20 % weight Pd on carbon, was added drop wise to the carbon dispersion. Afterwards 1.1 equivalents of formaldehyde from a 37 wt % solution in H_2O (ACS reagent, Aldrich) were added to the mixture [20]. The mixture was stirred continuously at 80 ºC for 1 hour and at room temperature overnight. Equation 3.14 illustrates the reduction of the noble metal precursor salt by formaldehyde [21].

$$CH_2O + Pd^{2+} \rightarrow CO + Pd + 2H^+ \qquad (3.14)$$

The carbon supported Pd catalyst was separated by centrifuging and extensively washed with water. The catalyst was dried at 100 ºC in air overnight and the resulting solid was ground with a mortar. This catalyst was called Pd/C-CH_2O. Part of the catalyst was further treated at 300 ºC under H_2 flow at for 1 hour [11] and this material was called Pd/C-CH_2O-300.

3.11.4. Preparation using sodium borohydride as a reducing agent

Pre-treated Vulcan XC-72R, 0.3 g, was dispersed in 40 cm^3 of water. The suspension was kept under magnetic stirring and heated to 80 ºC. The pH was adjusted to 11 with drops of 1 M NaOH. An aqueous solution of $(NH_4)_2PdCl_4$, containing enough palladium salt to prepare 20 % weight Pd on carbon, was added drop wise to the suspension. The pH was not controlled after the addition of the Pd salt solution. 20 mL of an aqueous sodium borohydride solution, containing 2 eq. of $NaBH_4$ (Aldrich, 99%), was added drop wise to the mixture. The reaction system was kept at 80 ºC for 1 hour and stirred continuously overnight at room temperature [11]. The reduction in alkaline media of the palladium precursor salt to Pd metal is illustrated in Equation 3.15 [22].

$$BH_4^- + 2Pd^{2+} + 6OH^- \rightarrow 2Pd + BO_3^{3-} + 2H_2 + 3H_2O \quad (3.15)$$

The carbon supported Pd catalyst was separated by centrifuging and extensively washed with water. The catalyst was dried at 100 ºC in air overnight and the resulting solid was ground with a mortar. This catalyst was called Pd/C-$NaBH_4$. Part of the catalyst was further treated at 300 ºC under H_2 flow for 1 hour and this material was called Pd/C-$NaBH_4$-300.

3.11.5. Preparation of carbon-supported bimetallic nanoparticles

Catalysts were prepared by reduction of the precursor salts on Vulcan XC-72R, using either ethylene glycol (EG) or hydrogen as reducing agent. A portion of the catalysts prepared by EG reduction were treated at 300 ºC under H_2 to study the effect of heat treatment. Precursors used for Pd, Au, Co, Fe and Ti were ammonium tetrachloropalladate (II) (99.995%, Sigma-Aldrich), gold (III) chloride trihydrate (99.99%, Sigma-Aldrich), cobalt (II) nitrite hexahydrate (98%, Sigma-Aldrich), iron (III) chloride hexahydrate (98%, Fluka) and titanium (IV) propoxide (98%, Sigma-Aldrich), respectively.

At least two different atomic ratios were selected for each bimetallic combination; 1:1, 3:1 and 9:1 for Pd-Au, 1:1 and 4:1 for Pd-Co, 1:1 and 3:1 for Pd-Fe and 1:1 and 9:1 for Pd-Ti. Also two different synthetic procedures were chosen for preparations; simultaneous co-deposition of both metals on the carbon support and deposition of the second metal on carbon-supported Pd, Pd/C. The Pd/C was prepared by EG reduction at pH 11 following the procedure described in chapter 4. All catalysts prepared by co-deposition were initially prepared with a 20% weight metal content; catalysts prepared on Pd/C were prepared on Pd/C 20% weight, therefore the metal content was higher.

Palladium-gold and palladium-cobalt catalysts were exclusively synthesized by EG reduction. Catalysts prepared were named PdAu-EG11, PdAu-EG11-300, Pd_9Au-EG11 and Pd_9Au-EG11-300 when they were prepared by co-deposition of both precursors, and Pd(Au)-EG11, Pd(Au)-EG11-300, $Pd_3(Au)$-EG11 and $Pd_3(Au)$-EG11-300 when they were prepared on Pd/C. Pd-Co catalysts were called PdCo-EG11, PdCo-EG11-300, Pd_3Co-EG11 and Pd_3Co-EG11-300 when prepared by co-deposition, and Pd(Co)-EG11, Pd(Co)-EG11-300, $Pd_3(Co)$-EG11 and $Pd_3(Co)$-EG11-300 when prepared on Pd/C.

Palladium-iron and palladium-titanium catalysts were initially prepared following the co-deposition procedure by EG reduction; PdFe-EG11, PdFe-EG11-300, Pd_3Fe-EG11, and Pd_3Fe-EG11-300 and PdTi-EG11, PdTi-EG11-300, Pd_9Ti-EG11 and Pd_9Ti-EG11-300 respectively. The second collection of these bimetallic catalysts was prepared by reducing its precursor salts in H_2 at high temperature, following both the co-deposition and deposition on Pd/C procedures. The temperature of the furnace was 500 ºC for Pd-Fe [23] and 900 ºC for Pd-Ti [24]. Catalysts were named PdFe-H_2-500, Pd_3Fe-H_2-500, Pd(Fe)-H_2-500 and $Pd_3(Fe)$-H_2-500, and PdTi-H_2-900, Pd(Ti)-H_2-900, Pd_9Ti-H_2-900 and $Pd_9(Ti)$-H_2-900 for palladium-iron and palladium-titanium bimetallic catalysts, respectively.

Reductions by EG were carried out using the polyol method [17] under N_2 flow to minimise the number of oxidized species in the catalyst [18]; the pH of the reaction system was kept constant at 11, which was concluded in the previous chapter to be the optimum pH value for the synthesis of carbon-supported Pd nanoparticles. The carbon support used was Vulcan XC-72R, which was used as received. A typical synthesis using ethylene glycol as a reducing agent was described in section 3.11.2.

Pd-Fe and Pd-Ti catalysts prepared by reduction in H_2 atmosphere were synthesized as follows. Precursor salts (the necessary amount to prepare catalysts with 20 % metal content) were dissolved in deionised water. Carbon black, 0.3 g per 60 mL of water, was suspended in the solution. The solvent was evaporated overnight at 60 ºC under continuous stirring. The dried solid was placed in a boat and treated in the furnace under H_2 flow, 40 mL min^{-1}, during 2 hours at 500 and 900 ºC for Pd-Fe and Pd-Ti respectively. For catalysts prepared on Pd/C, the latter was suspended in a solution containing the second metal salt. The amount of either iron or titanium precursor was calculated based on the selected atomic ratio between the palladium and the second metal.

Table 3-1 summarises atomic ratios of Pd to metal, and synthetic methods selected for the preparation of bimetallic catalysts. The key to the synthetic methods is given below. Each carbon-supported catalyst was separated from the reaction solution by centrifuging and was extensively washed with water and acetone. Catalysts were dried at 100 ºC in air overnight. The resulting solid was ground with a mortar and a portion of each catalyst was treated at 300 ºC under H_2.

Table 3-1: Nominal atomic ratios and synthetic methods used in the preparation of bimetallic catalysts.

Catalyst	**Atomic ratio**	**Synthetic method**
Pd-Au	1:1	EG-pH11, EG-pH11-300, Pd/C + EG-pH11, Pd/C + EG-pH11-300
	3:1	EG-pH11, EG-pH11-300
	9:1	Pd/C + EG-pH11, Pd/C + EG-pH11-300
Pd-Co	1:1	EG-pH11, EG-pH11-300, Pd/C + EG-pH11, Pd/C + EG-pH11-300
	4:1	EG-pH11, EG-pH11-300, Pd/C + EG-pH11, Pd/C + EG-pH11-300
Pd-Fe	1:1	EG-pH11, EG-pH11-300, H_2-500, Pd/C + H_2-500
	3:1	EG-pH11, EG-pH11-300, H_2-500, Pd/C + H_2-500
Pd-Ti	1:1	EG-pH11, EG-pH11-300, H_2-900, Pd/C + H_2-900
	9:1	EG-pH11, EG-pH11-300, H_2-900, Pd/C + H_2-900

The meaning of each synthetic method is the following: “EG-pH11”, reduction with ethylene glycol at pH 11;“Pd/C + EG-pH11”, reduction with ethylene glycol at pH 11 using Pd/C as support; “-300”, heat treatment in H_2 at 300 ºC; “H_2-500” and “H_2-900”, reduction in H_2 at 500 ºC and 900 ºC, respectively; "Pd/C + H_2-500" and "Pd/C + H_2-900", reduction in H_2 at 500 ºC and 900 ºC using Pd/C as support, respectively (see also Nomenclature).

References

1. Sandor, R.B.C., NC), Thornburg, Theodore S. (Harrisburg, NC), *Polybenzimidazole solutions*. 1991, Hoechst Celanese Corporation (Charlotte, NC): United States.

2. Hoel, D. and E. Grunwald, *High protonic conduction of polybenzimidazole films [3]*. Journal of Physical Chemistry, 1977. **81**(22): p. 2135-2136.

3. Li, Q., R. He, J.O. Jensen, and N.J. Bjerrum, *PBI-Based Polymer Membranes for High Temperature Fuel Cells - Preparation, Characterization and Fuel Cell Demonstration.* Fuel Cells, 2004. **4**(3): p. 147-159.

4. Bard, A.J., *Electrochemical Methods: Fundamentals and Applications*. 2nd edition ed. 2001: John Wiley & Sons, Inc.

5. Vielstich, W., H. Gasteiger, and A. Lamm, *Handbook of fuel cells : fundamentals, technology and applications*. 2003, Chichester: Wiley. 4 v.

6. Breiter, M.W., *Dissolution and adsorption of hydrogen at smooth Pd wires at potentials of the alpha phase in sulfuric acid solution.* Journal of Electroanalytical Chemistry, 1977. **81**(2): p. 275-284.

7. Mallát, T., É. Polyánszky, and J. Petró³, *Electrochemical study of palladium powder catalysts.* Journal of Catalysis, 1976. **44**(3): p. 345-351.

8. Lee, K., O. Savadogo, A. Ishihara, S. Mitsushima, N. Kamiya, and K.-i. Ota, *Methanol-Tolerant Oxygen Reduction Electrocatalysts Based on Pd-3D Transition Metal Alloys for Direct Methanol Fuel Cells.* Journal of the Electrochemical Society, 2006. **153**(1): p. A20-A24.

9. Suo, Y., L. Zhuang, and J. Lu, *First-principles considerations in the design of Pd-alloy catalysts for oxygen reduction.* Angewandte Chemie - International Edition, 2007. **46**(16): p. 2862-2864.

10. Scott, K., S. Pilditch, and M. Mamlouk, *Modelling and experimental validation of a high temperature polymer electrolyte fuel cell.* Journal of Applied Electrochemistry, 2007. **37**(11): p. 1245-1259.

11. Zhang, L., K. Lee, and J. Zhang, *Effect of synthetic reducing agents on morphology and ORR activity of carbon-supported nano-Pd-Co alloy electrocatalysts.* Electrochimica Acta, 2007. **52**(28): p. 7964-7971.

12. Guha, A., W. Lu, T.A. Zawodzinski Jr, and D.A. Schiraldi, *Surface-modified carbons as platinum catalyst support for PEM fuel cells.* Carbon, 2007. **45**(7): p. 1506-1517.

13. Wu, C., H. Zhang, and B. Yi, *Hydrogen generation from catalytic hydrolysis of sodium borohydride for proton exchange membrane fuel cells.* Catalysis Today, 2004. **93-95**: p. 477-483.

14. Cullity, B.D., *Elements of X-Ray Diffraction*. 1978: Addison-Wesley.

15. Garratt-Reed, A.J., *Energy Dispersive X-ray Analysis in the Electron Microscope*. 2003, London: BIOS Scientific Publishers.

16. Heidenreich, R.D., *Fundamentals of transmission electron microscopy* 1964, New York: Interscience Publishers.

17. Larcher, D. and R. Patrice, *Preparation of metallic powders and alloys in polyol media: A thermodynamic approach.* Journal of Solid State Chemistry, 2000. **154**(2): p. 405-411.

18. Li, H., G. Sun, Y. Gao, Q. Jiang, Z. Jia, and Q. Xin, *Effect of Reaction Atmosphere on the Electrocatalytic Activities of Pt/C and PtRu/C Obtained in a Polyol Process.* Journal of Physical Chemistry C, 2007. **111**(42): p. 15192-15200.

19. Bock, C., C. Paquet, M. Couillard, A. Botton Gianluigi, and R. MacDougall Barry, *Size-selected synthesis of PtRu nano-catalysts: reaction and size control mechanism.* Journal of the American Chemical Society, 2004. **126**(25): p. 8028-37.

20. Umeda, M., M. Kokubo, M. Mohamedi, and I. Uchida, *Porous-microelectrode study on Pt/C catalysts for methanol electrooxidation.* Electrochimica Acta, 2003. **48**(10): p. 1367-1374.

21. Ohtani, B., S. Ikeda, H. Nakayama, and S.I. Nishimoto, *Shape- and size-selective photocatalytic reactions by layered titanic acid powder suspended in deaerated aqueous alcohol solutions.* Physical Chemistry Chemical Physics, 2000. **2**(22): p. 5308-5313.

22. Lee, D., S. Hwang, and I. Lee, *One-step preparation and characterization of PtRu (1:1)/C electrocatalysts by polyol method for polymer electrolyte fuel cells.* Journal of Power Sources, 2006. **160**(1): p. 155-160.

23. Shao, M.-H., K. Sasaki, and R.R. Adzic, *Pd-Fe Nanoparticles as Electrocatalysts for Oxygen Reduction.* Journal of the American Chemical Society, 2006. **128**(11): p. 3526-3527.

24. Fernández, J.L., V. Raghuveer, A. Manthiram, and A.J. Bard, *Pd-Ti and Pd-Co-Au Electrocatalysts as a Replacement for Platinum for Oxygen Reduction in Proton Exchange Membrane Fuel Cells.* Journal of the American Chemical Society, 2005. **127**(38): p. 13100-13101.

Chapter 4: Characterization of carbon-supported Pd nanoparticles

4.1. Introduction

The activity of carbon-supported palladium nanoparticles for the oxygen reduction reaction (ORR) in acid electrolyte is reported in this chapter. Catalysts' crystal structure, particle size and particle distribution on the carbon support were characterised by X-ray diffraction analysis and transmission electron microscopy. Their electrochemical characteristics were investigated by cyclic voltammetry in 0.5 M H_2SO_4.

Palladium nanoparticles were prepared on pre-treated Vulcan XC-72R. The carbon support was subjected to acid treatment in order to modify the hydrophilic character of the carbon surface [1]. Synthetic conditions which led to be best catalyst for ORR were repeated on as-received Vulcan XC-72R, this new catalyst was also studied for comparison.

An impregnation-reduction method was used for preparation of carbon-supported palladium nanoparticles. Metal precursors were impregnated on the carbon support from an aqueous solution and subsequently reduced. Three different reducing agents were initially selected: ethylene glycol [2], formaldehyde [3] and sodium borohydride [4] Ethylene glycol was chosen as a reducing agent, and the catalyst synthesis was optimized by adjusting the pH of the system. All catalysts were physicochemically and electrochemically characterized in order to determine the influence of the synthesis method on their particle size, distribution and activity for the ORR.

The effect of heat treatment, under a reducing atmosphere (H_2), on the catalyst particle size was also studied. The effect of temperature in the range from room temperature to 300 ºC was also studied for a specific catalyst.

4.2. Physicochemical characterization of carbon-supported Pd nanoparticles

4.2.1. EDXA and TEM characterization of carbon-supported Pd nanoparticles

For all three catalysts prepared without pH control, the Pd contents estimated by EDXA analyses were 21.7%, 18.7% and 19.1% by weight, for Pd/C-EG, Pd/C-CH_2O and Pd/C-$NaBH_4$, respectively. According to the preparation procedure, complete deposition of Pd precursor on the carbon would lead to a 20% weight palladium catalysts. Deviations from the nominal value may be due to either carbon loss or incomplete Pd deposition on the carbon surface. No further studies on the amount of Pd deposited on the carbon were carried out for Pd/C-EG, Pd/C-CH_2O and Pd/C-$NaBH_4$.

Palladium contents for catalysts prepared by ethylene glycol reduction in basic media were all greater than 20%. Average palladium weight percentages obtained from EDXA analysis were between 24 and 34% (Table 4-1). This suggested an increase in carbon loss when the reduction was carried out in the basic pH region. Since the pre-treated Vulcan XC-72R employed in the synthesis had its surface functionalized with oxygen containing groups with a different acidic characteristic [1], the alkalinity of the reaction system could have favored the suspension, and subsequent loss, of the carbon support. TEM images showed that not all the carbon had Pd nanoparticles deposited on its surface. Therefore, it may be possible that during the washing stage some carbon particles, mainly those without Pd nanoparticles, were removed. The catalyst supported on untreated carbon black and prepared by EG reduction at pH 11, Pd/C-EG11-untr, had a palladium content of 22.5%, closer to the nominal 20% by weight, which indicates a smaller carbon loss during the preparation stages. This would support the hypothesis stated above that the pre-treated carbon was more likely than the untreated to be removed during the washing process.

Table 4-1: Particle size, ECSA and metal content for carbon-supported palladium catalysts.

Catalyst	**Particle size (nm)**	**ECSA (m^2 g^{-1})**	**Metal content (% weight)**
Pd/C-EG	10.7	6.1	21.7
Pd/C-EG-300	21.8	2.0	21.7
Pd/C-CH_2O	5.2	9.6	18.7
Pd/C-CH_2O-300	18.1	3.1	18.7
Pd/C-$NaBH_4$	11.7	4.4	19.1
Pd/C-$NaBH_4$-300	18.8	2.4	19.1
Pd/C-EG10	5.8	11.7	26.5
Pd/C-EG11	5.7	15.4	34.1
Pd/C-EG12	7.7	10.6	29.2
Pd/C-EG13	5.8	15.3	23.6
Pd/C-EG11-untr	7.3	14.6	22.5
Pd/C-EG11-untr-rt	10.4	-	22.5
Pd/C-EG11-untr-100	11.2	-	22.5
Pd/C-EG11-untr-200	14.1	-	22.5
Pd/C-EG11-untr-300	16.5	-	22.5
Pd/C Etek	3.5	15.7	19.9
Pt/C Etek	3.4	55.3	19.8

Catalysts were examined by transmission electron microscopy. Every sample showed agglomeration of metal particles. Figure 4-1A shows a TEM image of Pd/C-EG11. Carbon-supported platinum catalyst was also prepared using EG reduction at pH 11. Particles sizes of approximately 3.5 nm and a good distribution of the platinum nanoparticles on the carbon support were obtained (Figure 4-1B). All palladium catalysts exhibited significant agglomeration, for this reason particle size and particle size distribution could not be studied from the TEM images. However, some individual particles were measured from the TEM pictures and the observed size matched the sizes obtained from the X-ray diffraction spectra. The least severe agglomeration was observed for Pd/C-EG11.

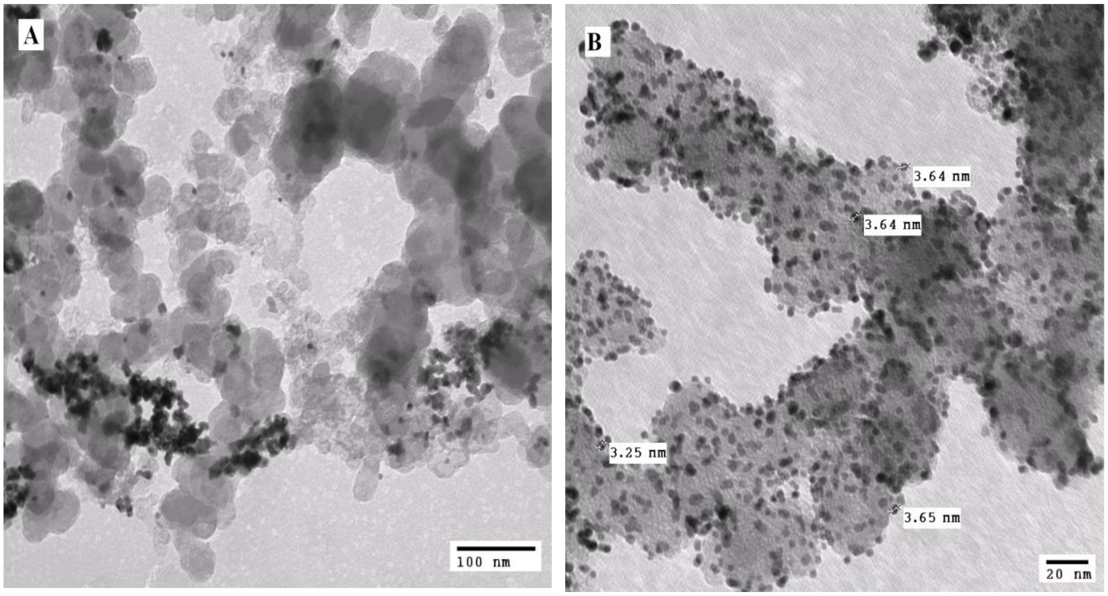

Figure 4-1: TEM pictures of A) Pd/C-EG11 and B) Pt/C-EG11.

4.2.2. XRD characterization of carbon-supported Pd nanoparticles

The average Pd-Pd bond distance, *d*, was calculated for each carbon-supported palladium catalyst prepared. Pd-Pd bond for Pd/C was found to have an average value of 0.2751 nm; the associated error was ± 0.0003 nm. This value matched the International Centre for Diffraction Data (ICDD) data for palladium [5].

All carbon-supported palladium catalysts were characterised by X-Ray diffraction spectrophotometry. The broad peak at a 2θ value around 25º in each spectra was due to the carbon support [4]. All samples showed peaks matching those of palladium face-centered cubic (fcc) lattice. Diffraction patterns corresponding to palladium oxides were not observed in any case. A portion of each prepared catalyst was heat treated under H_2 atmosphere at 300 ºC to study the effect on the Pd nanoparticles. Every palladium catalyst treated under H_2 at 300 ºC exhibited larger Pd nanoparticles after this treatment. Particle sizes are shown in Table 4-1.

Particle size and Pd-Pd bond distance, or nearest neighbour distance in the lattice, were calculated from the XRD data using Scherrer (equation 3.11) and Bragg (equation 3.12) equations [6], respectively. Peak (220), which was considered to not be influenced by the presence of carbon, was used for calculations. Diffraction peaks of Pd (111), Pd (220) and Pd (331) might overlap with diffraction peaks of the carbon support, therefore the Pd (220) peak was chosen to evaluate the size of supported Pd particles [1, 7], values of which are shown in Table 4-1.

Figure 4-2 shows XRD patterns corresponding to carbon-supported palladium catalysts initially prepared using three different reducing agents, both before and after treatment in H_2 at 300 ºC. Smallest particles were obtained using formaldehyde as the reducing agent. Particle sizes for Pd/C-EG and Pd/C-$NaBH_4$ were similar to each other and much larger than those of Pd/C-CH_2O, as can be seen from a simple comparison of spectra peaks; peaks corresponding to the face-centered cubic lattice of Pd were wider and shorter for Pd/C-CH_2O, which indicates smaller particles. When catalysts were treated at 300 ºC under H_2, particle growth was observed in every catalyst; peaks for treated catalysts were higher and narrower. Larger growth was experienced by smaller palladium nanoparticles. Those of Pd/C-CH_2O increased from 5 nm diameter before heat treatment to 18 nm after, and particles in Pd/C-EG and Pd/C-$NaBH_4$ increased from 11 and 12 to 22 and 19 nm, respectively. Commercial Pd/C from Etek was also characterized; it exhibited the smallest Pd nanoparticles of all electrocatalysts characterized (3.5 nm) and suffered the biggest sintering when heat treated under H_2 (16 nm after treatment).

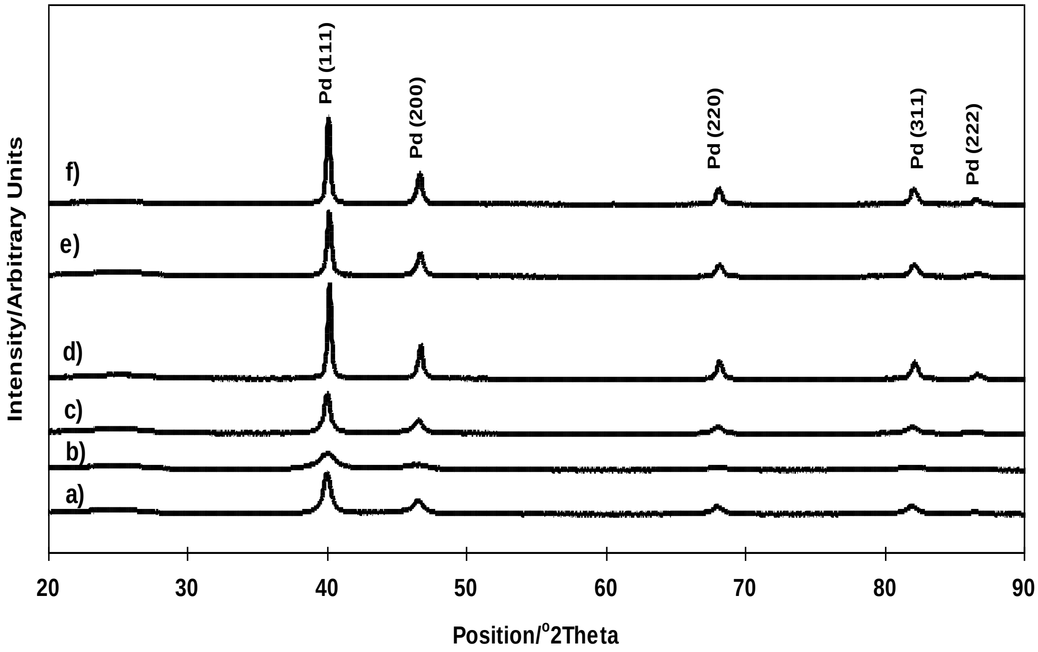

Figure 4-2: XRD patterns of carbon-supported palladium catalysts. a) Pd/C-EG b) Pd/C-CH_2O c) Pd/C-$NaBH_4$ d) Pd/C-EG-300 e) Pd/C-CH_2O-300 f) Pd/C-$NaBH_4$-300.

Figure 4-3 shows XRD patterns for catalysts prepared by ethylene glycol reduction with pH control. All peaks presented similar dimensions, therefore similar particle size. All carbon-supported palladium nanoparticles prepared by ethylene glycol reduction in basic media were smaller than those prepared without pH control. Thus, it could be concluded that the synthesis of Pd/C was strongly influenced by the pH of the reaction mixture. The reduction of the palladium precursor salt in basic media led to smaller Pd particles and, within the pH range from 10 to 13, no significant differences in size were observed. Pd/C-EG11-untr, prepared by EG reduction at pH 11 on as-received Vulcan XC-72R, also had particle size close to all catalysts prepared on pre-treated carbon in basic conditions.

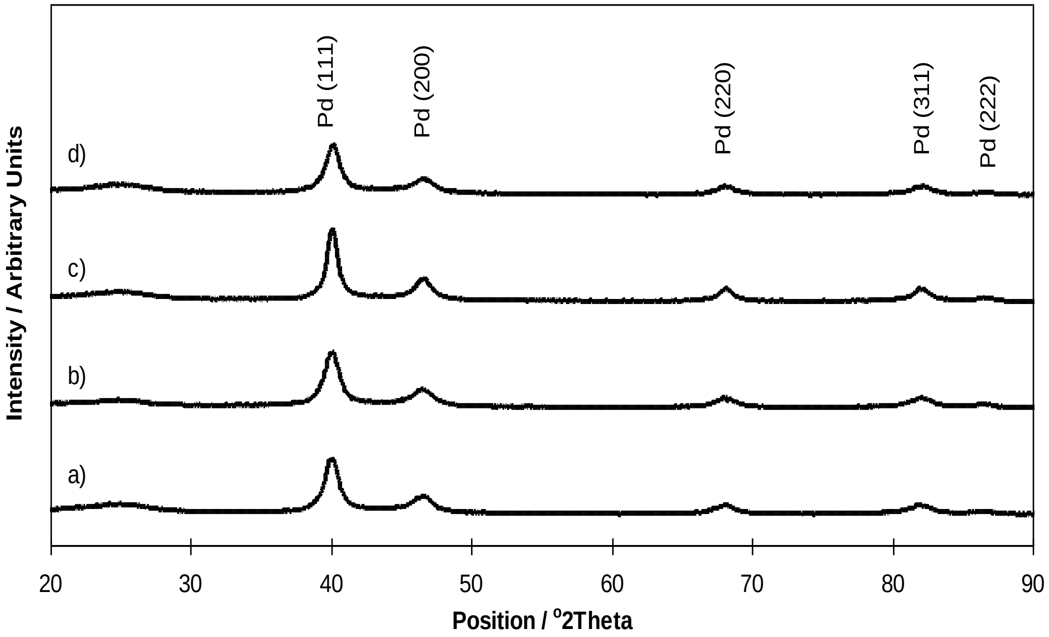

Figure 4-3: XRD patterns of carbon-supported palladium catalysts. a) Pd/C-EG10 b) Pd/C-EG11 c) Pd/C-EG12 d) Pd/C-EG13.

When catalysts prepared by ethylene glycol reduction with pH control were treated at 300 ºC under H_2 they all exhibited particle growth. To study the effect of temperature on the sintering of Pd nanoparticles small amounts of Pd/C-EG11 were treated under hydrogen at 100, 200 and 300 ºC. XRD spectra of these catalysts are shown on Figure 4-4. Particle size increased with increasing treatment temperature (Table 4-1). At 100 ºC the Pd particle size increased from 6 to 11 nm, at 200 ºC to 14 nm and at 300 ºC to 17 nm. XRD data indicated the presence of a single Pd metallic phase with a face-centered cubic structure. Temperature treatment did not affect the metallic phase but clearly induced Pd particle growth, as it was evident from the sharpening of the diffraction peaks (smaller full width at half maximum of the peak leads to larger particle size according to Scherrer equation). This particle growth with temperature has been previously reported in nitrogen by Canton et al. [8] and in hydrogen by Jiang et al. [9].

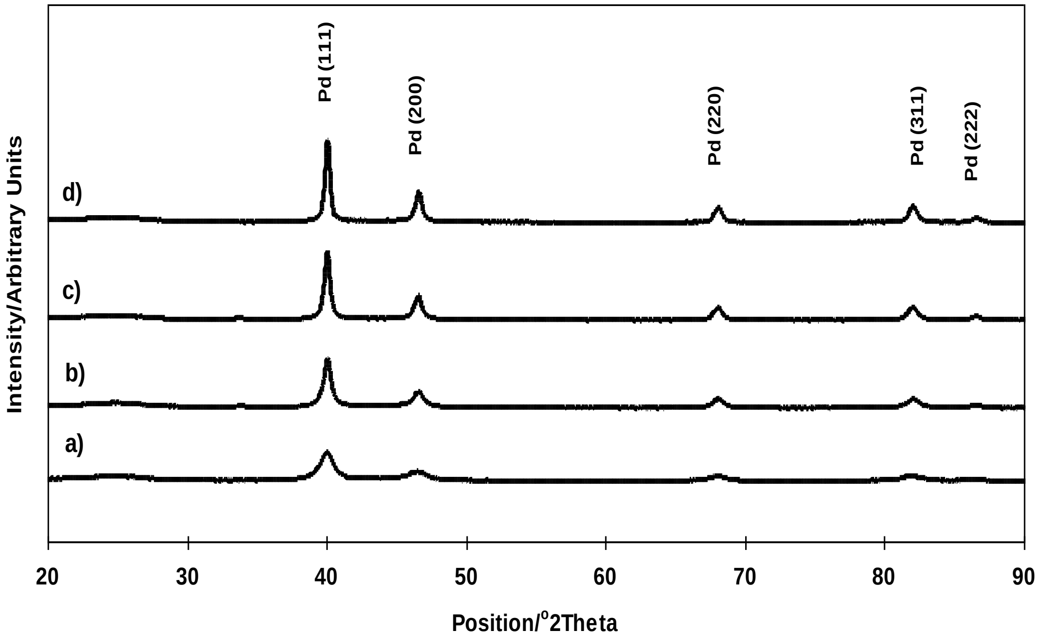

Figure 4-4: XRD patterns of carbon-supported Pd catalysts. a) Pd/C-EG11 b) Pd/C-EG11-100 c) Pd/C-EG11-200 d) Pd/C-EG11-300.

4.3. Electrochemical characterization of carbon-supported Pd nanoparticles

The electrochemical properties of prepared palladium catalysts were characterised by cyclic voltammetry in acid electrolyte. Cyclic voltammograms (CVs) were recorded in N_2 saturated 0.5 M H_2SO_4 solution at room temperature. The open circuit potential of the half cell, ca. 0.8 V vs NHE, was used as starting potential for the voltammetry.

Figure 4-5 shows the cyclic voltammogram of carbon-supported commercial Pt catalyst. On the positive sweep, only current corresponding to the double layer charging current was recorded in the potential range from ca. 0.30 to 0.82 V vs NHE. Above ca. 0.75 V oxygen chemisorptions started. In the negative potential sweep, reduction of the oxide layer started at potentials close to 0.90 V, the oxide reduction peak was located at ca. 0.74 V. From ca. 0.50 V to 0.30 V only the double layer charging current was observed in the cathodic sweep. When the electrode potential was below ca. 0.3 V a cathodic current was recorded. This current was due to hydrogen adsorption on the platinum surface. At potentials below ca. 0.02 V H_2 gas evolved. After the scan reversion H_2 molecules and the layer of chemisorpted hydrogen were oxidized again [10].

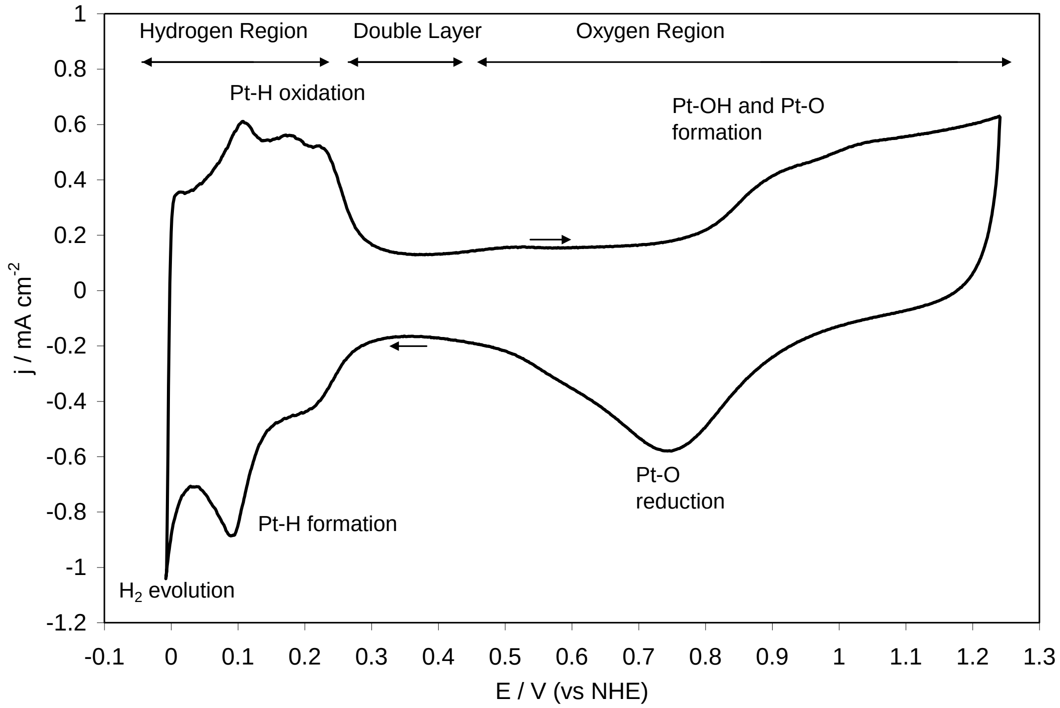

Figure 4-5: Cyclic voltammogram of Pt/C from E-Tek in N_2 saturated 0.5 M H_2SO_4 solution at room temperature, scan rate 10 mV s^{-1}.

A typical CV of the prepared Pd/C catalysts deposited on glassy carbon is shown in Figure 4-6. The initial potential was the open circuit potential, ca. 0.8 V, and scans were performed between potentials of 1.24 and 0.07 V, respectively; and the final potential was 1.24 V. On the positive sweep, only current corresponding to the double layer charging current was recorded in the potential range from ca. 0.3 to 0.75 V vs NHE. Oxidation of the palladium surface started at ca. 0.75 V and a small peak at ca. 1.04 V was also observed; these results matched previous observations by Burke et al. [11, 12]. In the negative potential sweep oxide reduction started at ca. 0.83 V with the peak positions located at ca. 0.72 V. From ca. 0.55 V to 0.3 V only the double layer charging current was observed in the cathodic sweep. When the electrode potential was below ca. 0.3 V a cathodic current was recorded. Burke et al. [12] and Breiter [13] attributed this current to, initially, hydrogen adsorption on the palladium surface and, at lower potentials, to the dissolution of hydrogen in the bulk of the palladium.

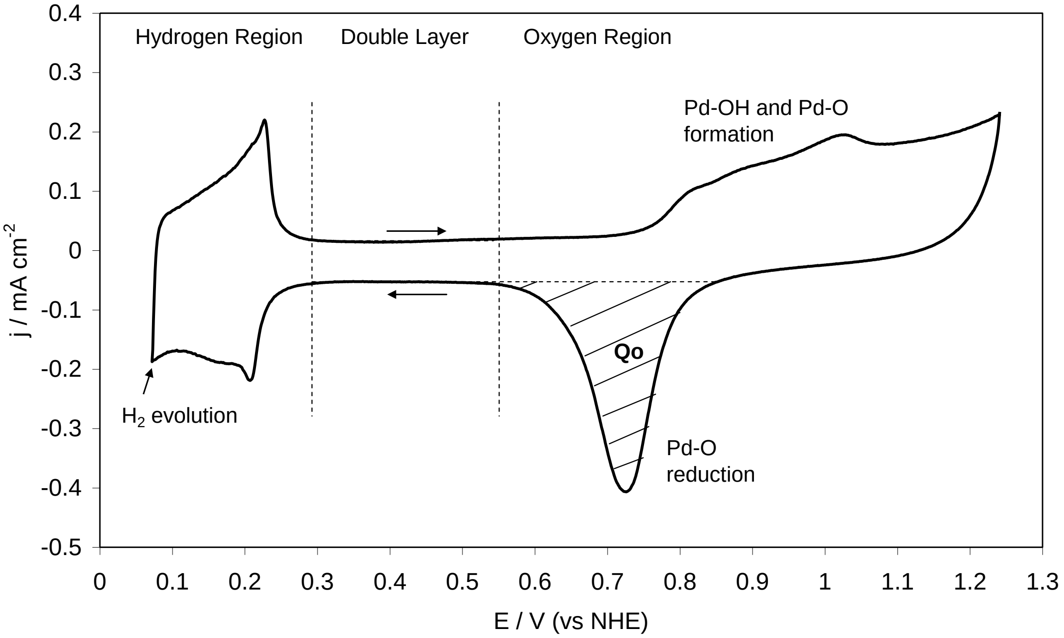

Figure 4-6: Cyclic voltammogram of Pd/C-EG11-untr in N_2 saturated 0.5 M H_2SO_4 solution at room temperature, scan rate 5 mV s^{-1}.

4.3.1. Palladium electrochemical dissolution in acid electrolyte

Palladium dissolution in sulphuric acid solution was reported to start at potentials close to 0.96 V in the anodic sweep by Rand et al. [14]. Thus, peaks corresponding to its anodic dissolution could not be discriminated from the oxygen adsorption peaks in the voltammogram at a scan rate 5 mV s^{-1}. After the initial fast cycling to condition the electrodes, none of the prepared carbon-supported palladium catalysts presented evidence of dissolution. Nevertheless, the dissolution rate depends on the metal surface area; therefore catalysts with smaller metal particles, which mean higher surface area per gram of metal, would dissolve faster. Evidence of dissolution was seen in the fast scan cyclic voltammograms recorded for the commercial Pd/C, which had a particle diameter of approximately half the diameter of the Pd/C-EG11-untr (3.5 compared to 7 nm, respectively). Figure 4-7 shows voltammograms corresponding to 80 cycles at scan rate 50 mV s^{-1} of a commercial Pd/C (Etek) electrode. A dissolution peak at ca. 0.96 V could not be differentiated, but the loss of electrochemical surface area was dramatic, which could be appreciated after each single cycle. Palladium dissolution during the electrode conditioning, also called electrochemical activation, of palladium nanoparticles in 0.5 M H_2SO_4 was also reported by Solla-Gullón et al. [15].

Whilst voltammograms in N_2 saturated 0.5 M H_2SO_4 were recorded, N_2 was being bubbled into the electrolyte. The stirring caused by these bubbles in the solution would remove some dissolved metal from the vicinity of the electrode surface; this together with the large volume of electrolyte, would cause a low re-deposition rate at lower potentials in the cathodic sweep. Re-deposition of dissolved Pd was reported by Rand et al. to occur at potentials close to 0.7 V in the cathodic sweep [14]. Therefore, due to the small re-deposition rate of Pd, the current generated by this would not have been large enough to be discriminated from the oxygen desorption peak, at ca. 0.7 V.

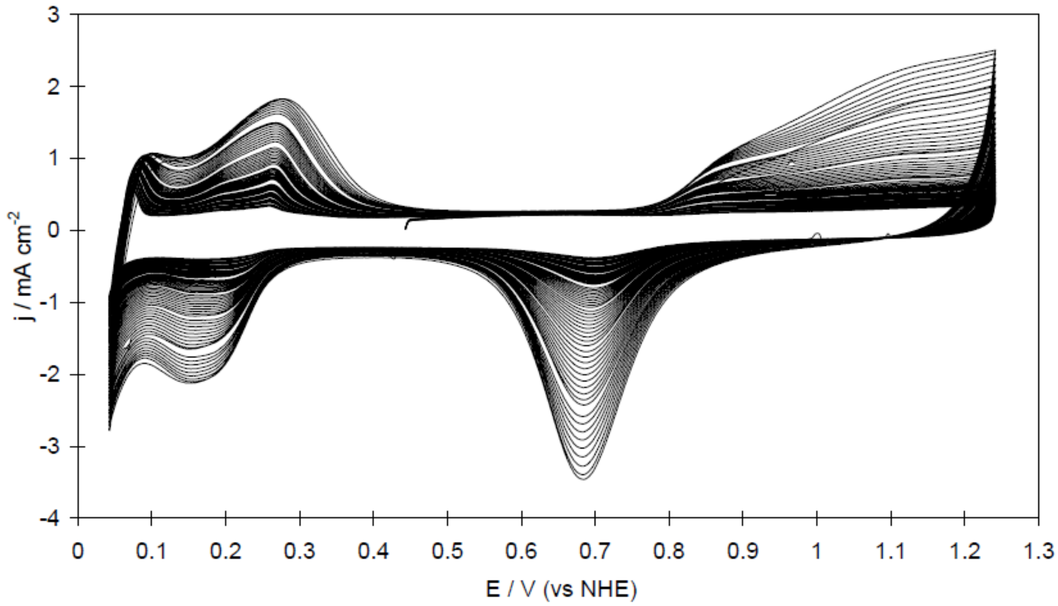

Figure 4-7: Cyclic voltammogram of commercial Pd/C (Etek) in N_2 saturated 0.5 M H_2SO_4 solution at room temperature, scan rate 50 mV s^{-1}. The plot shows the first 80 potential cycles of the electrode.

The electrode conditioning consisted of ten cycles between 0.04 and 1.24 V vs NHE using a scan rate of 50 mV s^{-1}. All Pd/C catalysts presented a stable voltammogram after the ten cycles, but the commercial Pd/C (Etek) did not. Nonetheless, the slow scan cyclic voltammogram of the commercial Pd/C, recorded straight after the conditioning, was used for comparison despite its instability.

4.3.2. Quantification of the electrochemical surface area

In contrast to platinum, it was difficult to determine the charge of a monolayer of adsorbed hydrogen on a Pd catalyst due to the capacity of palladium to absorb hydrogen [13, 16]. Therefore, quantification of the electrochemical surface area (ECSA) was made using the oxygen desorption peaks as explained in Chapter 3.

There was a large difference in the ECSA for the commercial Pd/C catalyst compared to those of catalysts prepared without pH control. This can be easily seen in Figure 4-8 from the difference in the palladium oxide reduction peak sizes. For commercial Pd/C catalyst ECSA was 16 m^2 g^{-1}, whilst for Pd/C-CH_2O, Pd/C-EG and Pd/C-$NaBH_4$ calculated values were 10, 6 and 4 m^2 g^{-1}, respectively. Electrochemical surface area values were in agreement with palladium particle sizes calculated from the XRD diffractograms, smaller particles lead to higher surface areas.

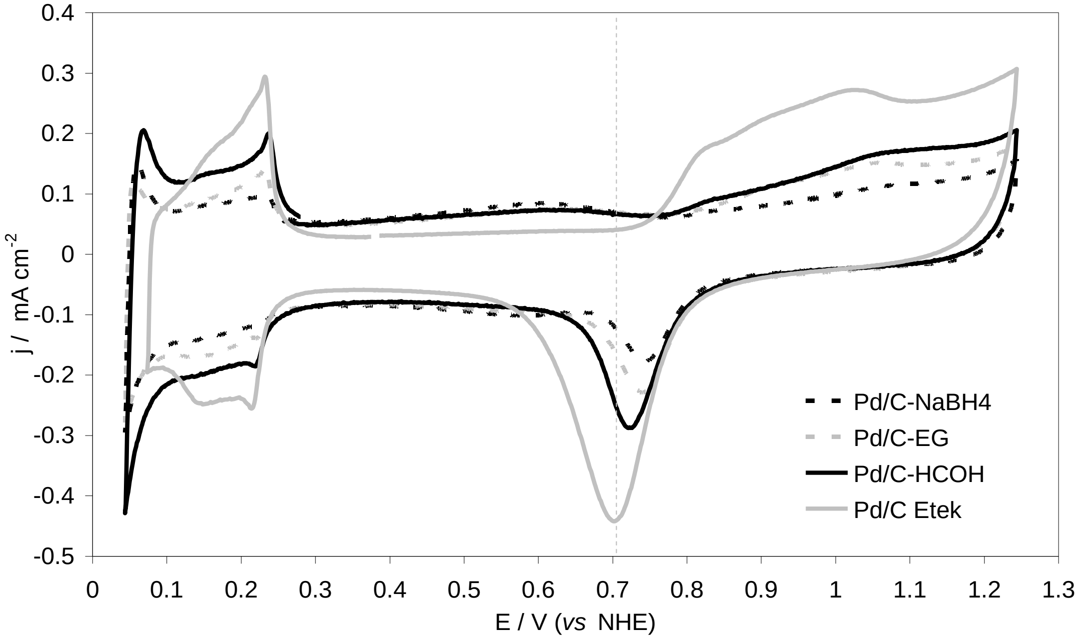

Figure 4-8: Cyclic voltammograms of Pd/C catalysts prepared using three different reducing agents, EG, CH_2O and $NaBH_4$.

In Figure 4-8 it can be seen that the maximum of the oxide reduction peak is positioned at different potentials for different Pd catalysts. Potential values were approximately 0.70 V for Pd/C Etek, 0.72 V for Pd/C-CH_2O and 0.74 V for Pd/C-EG and Pd/C-$NaBH_4$ vs NHE. The shift in potentials was believed to be related to the size of the palladium particles; smaller palladium particles exhibit the maximum current of the oxide reduction peak at lower potentials. This behavior has been previously reported by Zeng et al. for carbon-supported platinum nanoparticles [17]. The Pt oxide reduction peak was reported to shift progressively to negative potentials with a decrease in the size of platinum particles. Mukerjee et al. attributed this behavior to stronger adsorption of the OH groups in smaller particles, caused by an increase in low coordination sites with the decrease of the particle diameter [18].

As reported above, Pd/C-CH_2O, Pd/C-EG and Pd/C-$NaBH_4$ gave ECSA values of 10, 6 and 4 m^2 g^{-1}, and their particle sizes were 5, 11 and 12 nm, respectively. Pd/C-CH_2O gave the highest ECSA, however its activity towards ORR was low, as discussed in Section 4.4. Pd/C-$NaBH_4$ had both low ECSA and activity for ORR. Pd/C-EG gave an ECSA value intermediate between Pd/C-CH_2O and Pd/C-$NaBH_4$, and the highest ORR activity out of the three catalysts. Thus, ethylene glycol was chosen as the reducing agent for future synthesis.

The particle size obtained for Pd-EG, initially prepared without monitoring the pH, was approximately 11 nm. Pd or palladium alloy particles of approximately 5 nm size were reported by Zhang et at, Mujerkee et al, and Li et al. among others [4, 19-21]. Therefore, efforts in this study were to find an optimum pH for the reduction of ammonium tetrachloropalladate by ethylene glycol; thus additional four Pd/C catalysts were prepared by ethylene glycol reduction. The pH was restricted to the basic region, with four values, between 10 and 13 pH units, chosen. Cyclic voltammograms in O_2 solution for those four catalysts are compared in Figure 4-9.

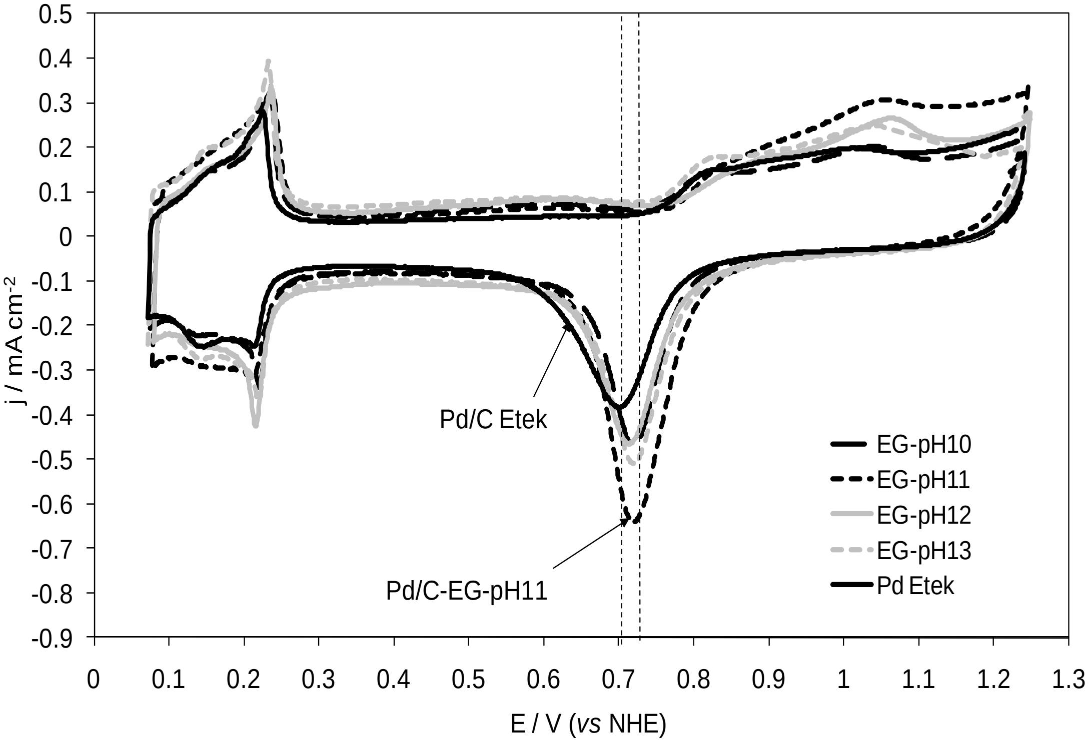

Figure 4-9: Cyclic voltammograms of Pd/C catalysts prepared by EG reduction at five different pH values in a range from 10 to 13 pH units.

As discussed earlier in this chapter, shifts in the position of the palladium reduction peak seemed to be related to size of the palladium nanoparticles; catalysts with smaller particles produced oxide reduction peaks at lower potentials. All four catalysts prepared by EG reduction in basic conditions presented a shift in the position of the palladium reduction peak to lower potentials compared to Pd/C-EG, ca. 20 mV lower, at 0.72 V. This agreed with XRD observations, from which the particle size calculated was approximately 6 nm, smaller than the 11 nm of Pd/C-EG. Cyclic voltammograms in N_2 saturated solution were also compared with that of a piece of Pd foil used as the electrode (Figure 4-10). Pd foil showed its palladium reduction peak was at 0.74 V, potential value higher than the observed for nanoparticles as was expected, providing further evidence of the dependence of the position of the palladium reduction peak upon the particle size.

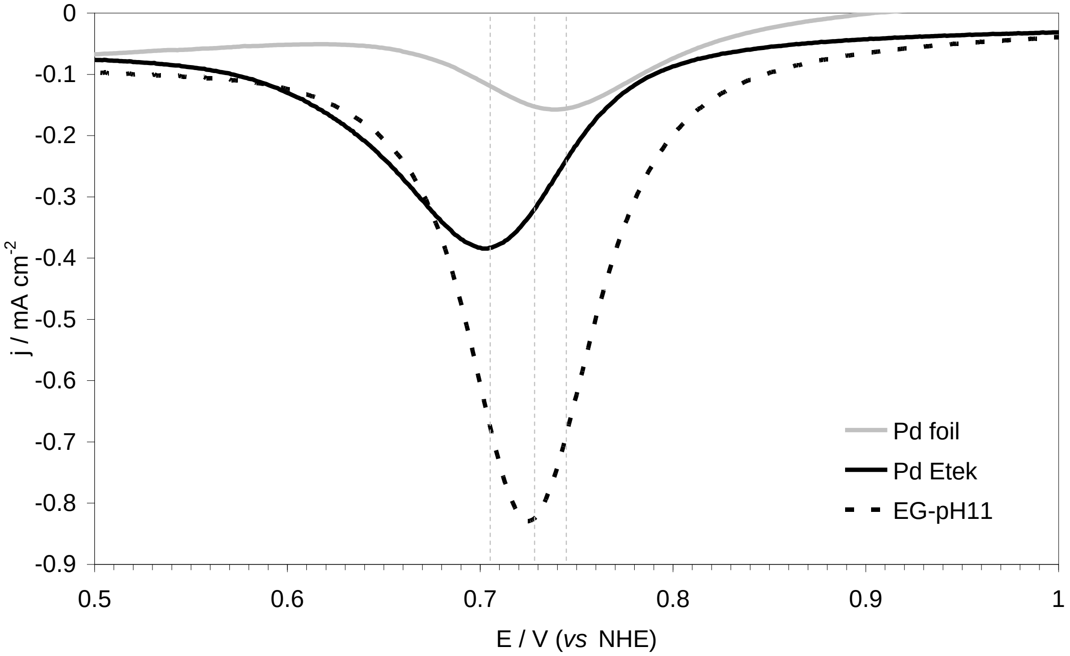

Figure 4-10: Cyclic voltammograms of Pd/C-EG11, commercial Pd/C and a Pd foil electrode.

ECSA calculated from the charge of the monolayer of chemisorbed oxygen was more than double for catalysts prepared by EG reduction in alkaline conditions compared to Pd/C-EG (as expected from their smaller particle sizes). Electrochemical surface areas corresponding to Pd/C-EG10, Pd/C-EG11, Pd/C-EG12 and Pd/C-EG13 were 12, 15, 11 and 15 m^2 g^{-1}, respectively (Table 4-1). The smallest ECSA was calculated for Pd/C-

EG12, which had the largest particle size of 8 nm compared to 6 nm for the other three. The two catalysts with highest active areas were prepared at pH 11 and 13. This information, together with the distribution of the nanoparticles on the carbon surface and the kinetic parameters obtained from the study of the ORR, led to the selection of the synthesis method for carbon-supported nanoparticles for the ORR reaction in acid electrolyte.

Carbon-supported palladium nanoparticles were also prepared on as-received Vulcan XC-72R using ethylene glycol as a reducing agent at pH 11 (Pd/C-EG11-untr). The ECSA calculated for Pd/C-EG11-untr was 15 m^2 g^{-1}, the same ECSA value that the catalyst prepared on pre-treated carbon (Table 4-1). Voltammograms of Pd/C-EG11-untr and Pd/C-EG11 in oxygen free electrolyte are compared in Figure 4-11. The double layer charging current and the area of the oxide reduction peak were larger for the catalyst supported on pre-treated carbon due to the presence of functional groups on its surface and the higher metal content (see Table 4-1), respectively. The hydrogen sorption-desorption and the oxidation-reduction reactions of the Pd nanoparticles occurred at the same potentials for both catalysts. Neither the physicochemical characteristics of the Pd nanoparticles nor the activity towards ORR, as discussed in Section 4.4, of Pd/C-EG11-untr catalyst showed significant differences to those for the Pd/C-EG11.

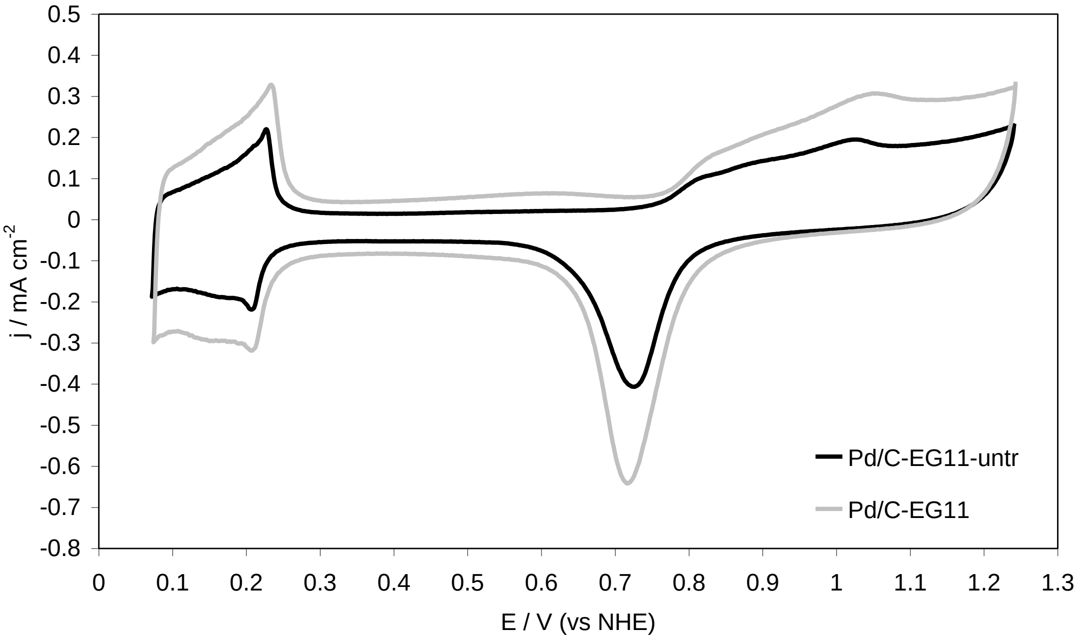

Figure 4-11: Cyclic voltammograms of Pd/C catalysts prepared by EG reduction at pH 11 using two different carbon supports, Vulcan XC-72R as-received and Vulcan XC-72R pretreated with HNO_3.

Particle size values estimated from XRD diffractograms indicated that catalyst heat treatment, under H_2 flow at 300 ºC, increased the size of Pd particles in every catalyst prepared. The decrease in the ECSA is a direct consequence of the particle size growth, and this decrease could be clearly observed when comparing voltammograms of the treated and untreated catalysts. Figure 4-12, Figure 4-13 and Figure 4-14 show voltammograms of catalysts prepared without pH control before and after heat treatment.

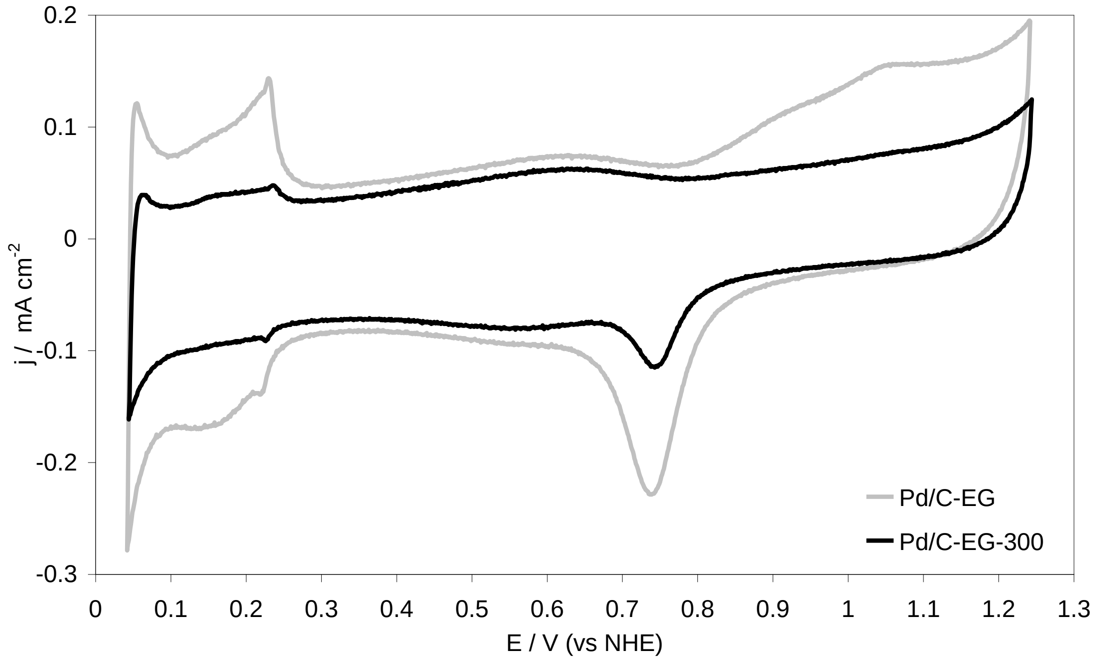

Figure 4-12: Cyclic voltammograms of Pd/C-EG and Pd/C-EG-300, before and after heat treatment.

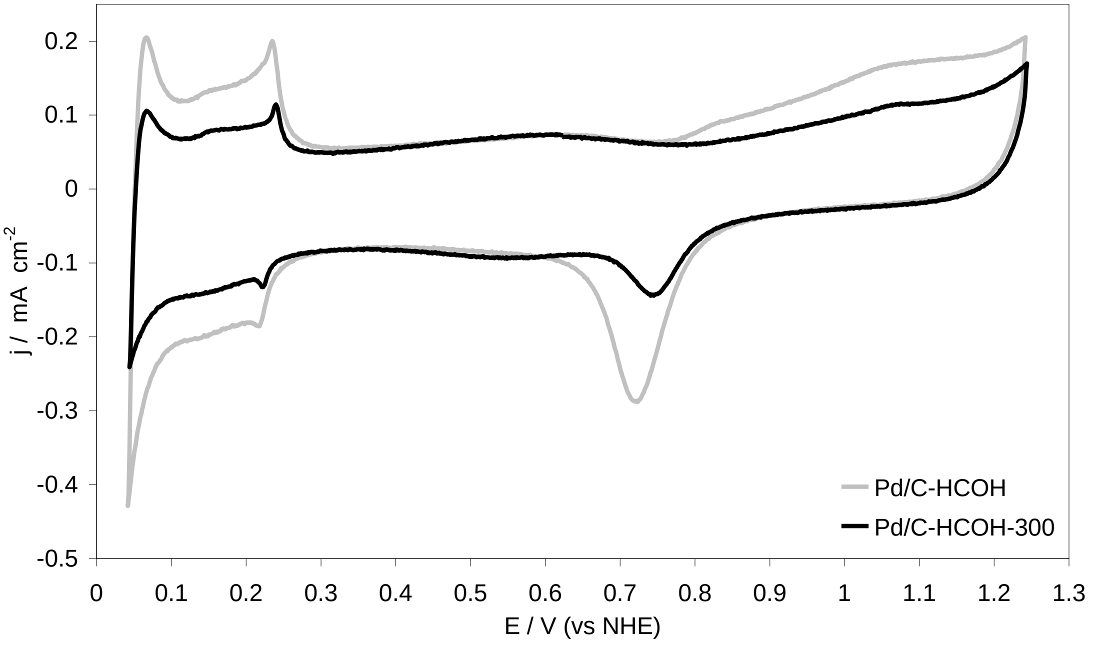

Figure 4-13: Cyclic voltammograms of Pd/C-CH_2O and Pd/C-CH_2O-300, before and after heat treatment.

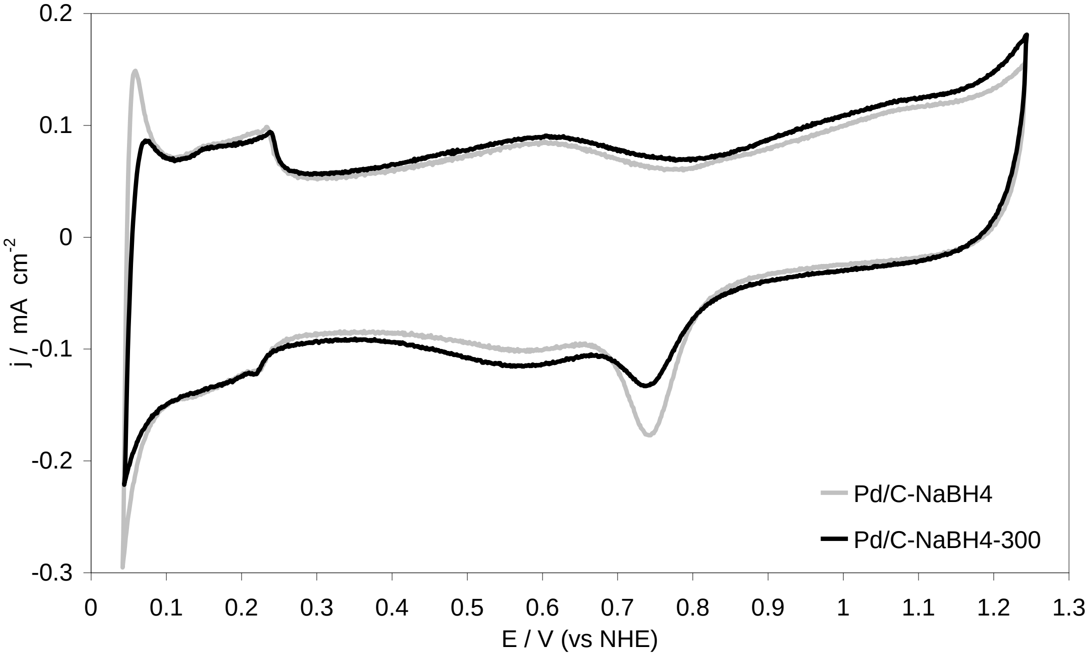

Figure 4-14: Cyclic voltammograms of Pd/C-NaBH$_4$ and Pd/C-NaBH$_4$-300, before and after heat treatment.

In the three sets of voltammograms a decrease in the area under the palladium oxide reduction peak was observed after treating it at 300 ºC in H$_2$. ECSA values before and after the treatment for Pd/C-EG11, Pd/C-NaBH$_4$ and Pd/C-CH$_2$O were 6 and 2 m^2 g^{-1}, 4 and 3 m^2 g^{-1} and 10 and 2 m^2 g^{-1}, respectively (Table 4-1). The reduction in ECSA was more severe in catalysts prepared using EG and CH$_2$O (Figure 4-12 and Figure 4-14), with smaller particle sizes before treatment. This agrees with the conclusions drawn from XRD analyses (Section 4.2.2).

4.4. Activity towards the oxygen reduction reaction of carbon-supported Pd nanoparticles

The ORR activity of the palladium catalysts was evaluated from their Tafel slopes, exchange current densities and mass activity (MA), reported as current per mass of the metal in ampere per gram of palladium (A g^{-1} Pd).

To determine the ORR activity the following protocol was established. A cyclic voltammogram (CV) was recorded in O_2 saturated 0.5 M H_2SO_4 electrolyte at a scan rate 1 mV s^1. Once the electrode was immersed in the O_2 saturated electrolyte, the open circuit potential (OCP) of the cell was measured. The first scan or LSV was recorded by holding the electrode at a potential 50 mV higher than the OCP for 10 s and then, immediately after, sweeping the potential at 1 mV s^{-1} towards lower potentials, to 0.25 V (forward scan). The second LSV was recorded straight after the forward scan, starting from 0.25 V and sweeping the potential at 1 mV s^{-1} up to the OCP potential plus 50 mV (backward scan). All the parameters reported were obtained from the backward LSV.

Both forward and backward linear sweep voltammograms for Pd/C-EG11-untr are shown in Figure 4-15. Hysteresis appeared between the forward and backward potential sweeps. Currents in the anodic scan were larger than those in the prior cathodic scan at potentials above ca. 0.7 V. This behavior is widely known for platinum electrodes and it is demonstrated to be caused by the different oxide coverage of the electrode during the anodic and cathodic scans [22]. Gottesfeld et al. stated that a platinum electrode in O_2 saturated 0.5 M H_2SO_4 at room temperature has an oxide-free surface to approximately 0.9 V during the anodic scan and a surface partially covered by oxide to approximately 0.5 V during the cathodic scan [23]. Studies reported by Sleightholme et al. have also shown that the oxygen coverage of the Pd surface depends on the electrode potential and previous operating conditions (history of the electrode) [24]. Therefore, by analogy with platinum [25], the difference between both scans in a palladium electrode was probably due to different oxide coverage of the metal surface. The PdO standard reduction potential is lower than PtO, 0.92 V compared to 0.98 V (Poubaix diagrams [26]), therefore the potentials at which the palladium electrode would be oxide-free would be lower than for a platinum electrode. Since the aim of this work was to study the ORR on palladium surface, not on palladium oxide, the backward LSV was chosen because it was understood to be the one with the minimum oxide coverage.

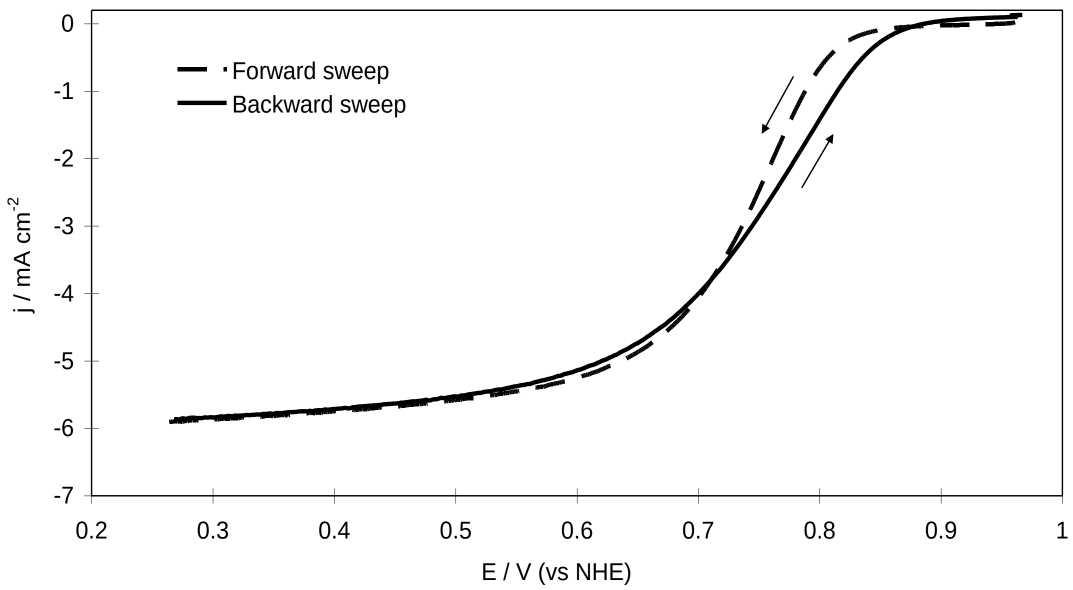

Figure 4-154: Linear sweep voltammograms of Pd/C-EG11-untr in O_2 saturated 0.5M H_2SO_4 solution at room temperature, scan rate 1 mV s^{-1} and 2500 rpm.

Figure 4-16 compares voltammograms in oxygen saturated electrolyte of the Pd/C catalysts initially prepared using three different reducing agents and the commercial Pd Etek catalyst. The voltammogram corresponding to commercial Pt/C is also plotted for comparison. Onset potentials for Pd/C-$NaBH_4$, Pd/C-CH_2O and Pd/C-EG were 0.86, 0.86 and 0.84 V, respectively. All three onset potentials were at least 0.1 V lower than the Pt commercial catalysts, 0.96 V vs NHE.

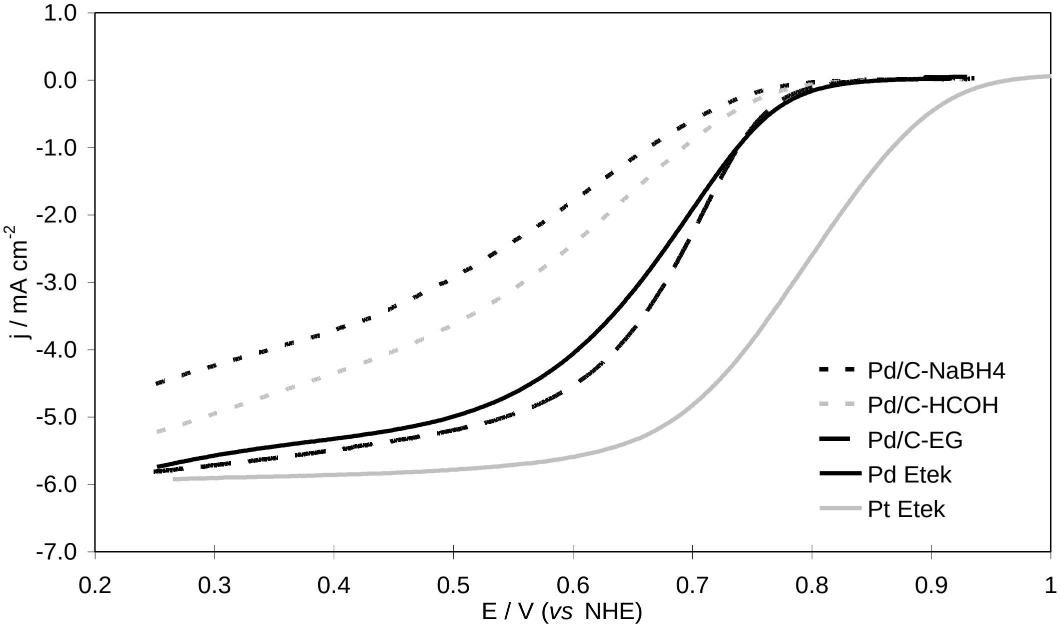

Figure 4-16: Linear sweep voltammograms of Pd/C catalysts Pd/C-EG, Pd/C-CH_2O and Pd/C-$NaBH_4$.

Mass activities of Pd/C-$NaBH_4$, Pd/C-CH_2O and Pd/C-EG were compared at 0.75 V, where current densities were significant for all catalysts. The highest mass activity (MA) at 0.75 V was exhibited by Pd/C-EG, 7 A g^{-2} Pd (Table 4-2), which was close to the MA of Pd/C from Etek (9 A g^{-2} Pd) but still only approximately 15% of the MA of Pt/C from Etek, 45 A g^{-2} Pd. The higher MA of Pd/C-EG compared to Pd/C-CH_2O or Pd/C-$NaBH_4$ could be attributed to a better distribution of the metal nanoparticles on the carbon surface (therefore higher surface area), a consequence of the use of this milder reducing agent. Similar behavior was reported for palladium-cobalt catalysts by Zhang et al. [4].

Table 4-2: Tafel slope, transfer coefficient, exchange current density and onset potential for different carbon-supported Pd catalysts.

Catalyst	**Onset potential (V *vs* NHE)**	**Tafel slope (mV dec^{-1})**	**Transfer coefficient**	**Exchange current density (A cm^{-2})**	**Mass activity at 0.75V (A g^{-1} Pd)**
Pd/C-EG	0.86	62	0.93	6.0 x 10^{-12}	7.2
Pd/C-EG-300	0.83	60	0.96	8.5 x 10^{-12}	2.9
Pd/C-CH$_2$O	0.86	62	0.93	2.2 x 10^{-12}	3.9
Pd/C-NaBH$_4$	0.84	62	0.94	2.7 x 10^{-12}	2.4
Pd/C-EG10	0.88	60	0.96	9.7 x 10^{-12}	16.4
Pd/C-EG11	0.89	59	0.98	7.7 x 10^{-12}	19.6
Pd/C-EG12	0.89	60	0.96	1.0 x 10^{-11}	15.7
Pd/C-EG13	0.87	62	0.93	8.6 x 10^{-12}	15.7
Pd/C-untr	0.89	59	0.98	1.0 x 10^{-11}	29.7
Pd/C Etek	0.86	64	0.90	5.2 x 10^{-12}	8.8
Pt/C Etek	0.96	64 128	0.91 0.45	1.4 x 10^{-10} 6.1 x 10^{-8}	45.3

Figure 4-17 shows LSVs for the Pd/C catalysts prepared using EG as a reducing agent and controlling the pH of the system. In every case the onset potential increased by between 20 and 30 mV with respect to the catalyst prepared using EG without controlling the pH of the system. Measured onset potentials were 0.88, 0.89, 0.89 and 0.87 V for Pd/C-EG10, Pd/C-EG11, Pd/C-EG12 and Pd/C-EG13, respectively. Although there were no significant differences in onset potentials between these four catalysts, highest onset potentials recorded were for Pd/C-EG11 and Pd/C-EG12, 0.89 V. This was believed to be due to the higher metal content of these two catalysts, 34 and 29% weight, respectively. Mass activities, measured at 0.75V, were all more than double of the MA for Pd/C-EG, and were all in the range between 16 and 20 A g^{-2}: Pd/C-EG11 being the highest at 20 A g^{-2} Pd. This value was twice the MA of Pd/C from Etek, 9 A g^{-2} Pd, and nearly thrice that of the MA of Pd/C-EG, but was much lower than 45 A g^{-2} of Pt/C from Etek.

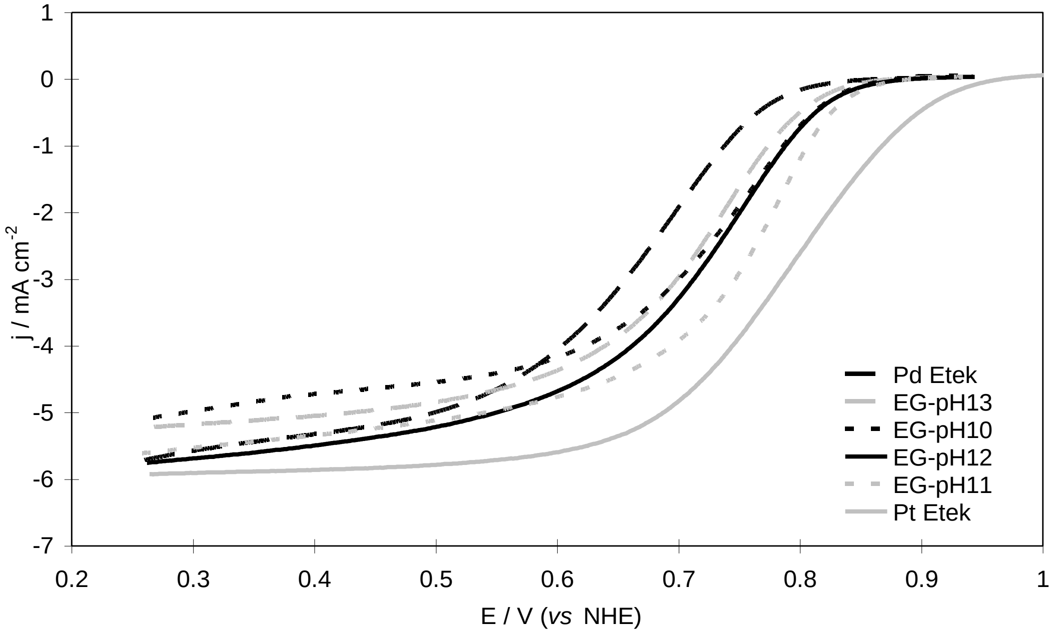

Figure 4-17: Linear sweep voltammograms of Pd/C catalysts Pd/C-EG10, Pd/C-EG11, Pd/C-EG12 and Pd/C-EG13.

Mass activity of Pd/C-EG11 and Pd/C-untr were also measured at 0.80 V in order to compare them with the available literature. Values were 7.8 and 9.4 A g^{-1} for Pd/C-EG11 and Pd/C-untr, respectively. Mass activity values for carbon-supported Pd nanoparticles have been reported in the same range, 8.4 A g^{-1} Pd at 0.8 V, by Wang et al. [27]. On the other hand, mass activity values over one order of magnitude larger than ours, ca. 230 A g^{-1} at 0.80 V, have been reported by Shao et al. using a thinner catalysts layer (10 μg cm^{-2}) [28]. Different activities for different catalyst layer thickness illustrate the strong influence of the thickness of the catalyst layer in fuel cells and this effect is discussed in Chapter 6.

All palladium catalysts prepared by EG reduction in basic media presented improved mass activities compared to the palladium catalyst prepared by EG reduction without pH control. The distribution of metal particles on the carbon surface was better and the diameter of palladium nanoparticles was smaller when alkaline conditions were used during the synthesis. Higher distribution meant less agglomeration of the Pd nanoparticles and lead to catalysts with higher active area; therefore higher mass activities were recorded. The better distribution of palladium particles at basic pH was already discussed in the section 4.3.2.

Tafel analysis of data points in the kinetically controlled region were taken from the near-steady-state linear sweep voltammogramms at scan rate 1 mV s^{-1}. Data was corrected for mass transport effects, using the correction parameter $i \times i_L / (i_L - i)$ (where i represents the current density at any potential and i_L the limiting current density) [29].

Tafel plots were linear, with a minimum correlation coefficient of 0.995, over one order of magnitude of the current density. In Figure 4-19A Tafel plots for Pd/C Etek, Pd/C-EG, Pd/C-CH_2O and Pd/C-$NaBH_4$ are compared and Figure 4-19B shows Tafel plots for Pd/C catalysts prepared by ethylene glycol reduction at different controlled pH values of the system for Pd/C-EG10, Pd/C-EG11, Pd/C-EG12 and Pd/C-EG13. All plots were parallel and all carbon-supported palladium catalysts exhibited Tafel slopes (b) ranging from 59 to 64 mV $decade^{-1}$. In the case of the Pt catalysts two Tafel slopes were observed. The slope in the low current density region, between ca. 0.88 and 0.94 V, was 64 mV $decade^{-1}$ and the slope in the high current density region, between ca. 0.72 and 0.87, was 128 mV $decade^{-1}$. A non linear region was observed in the high current density region for the palladium catalysts, as can be seen in Figure 4-18.

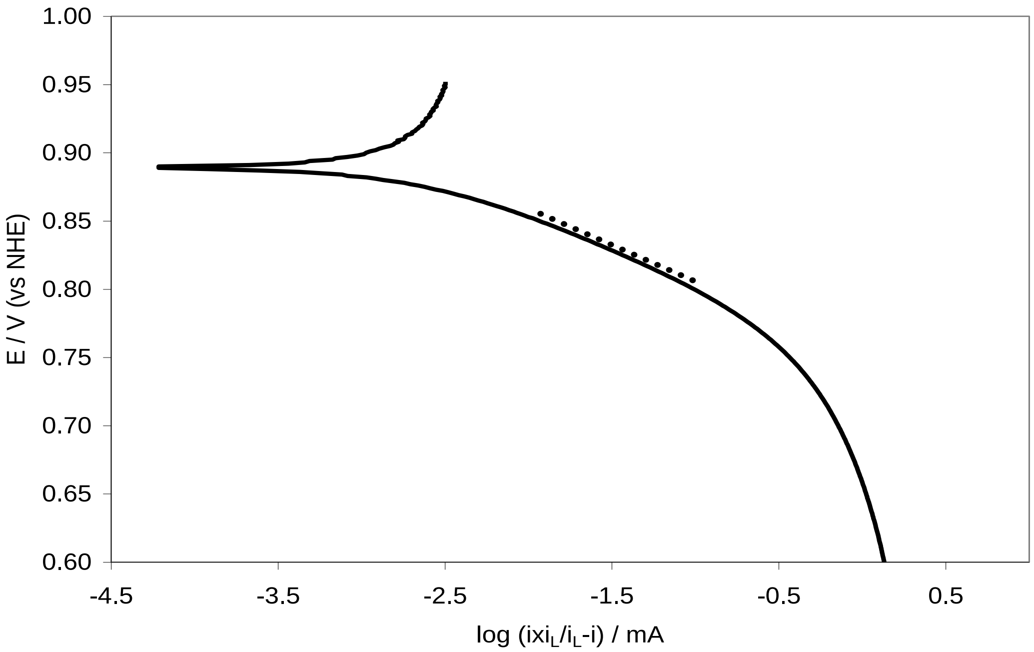

Figure 4-18: Tafel plot for the Pd/C catalysts Pd/C-EG11.

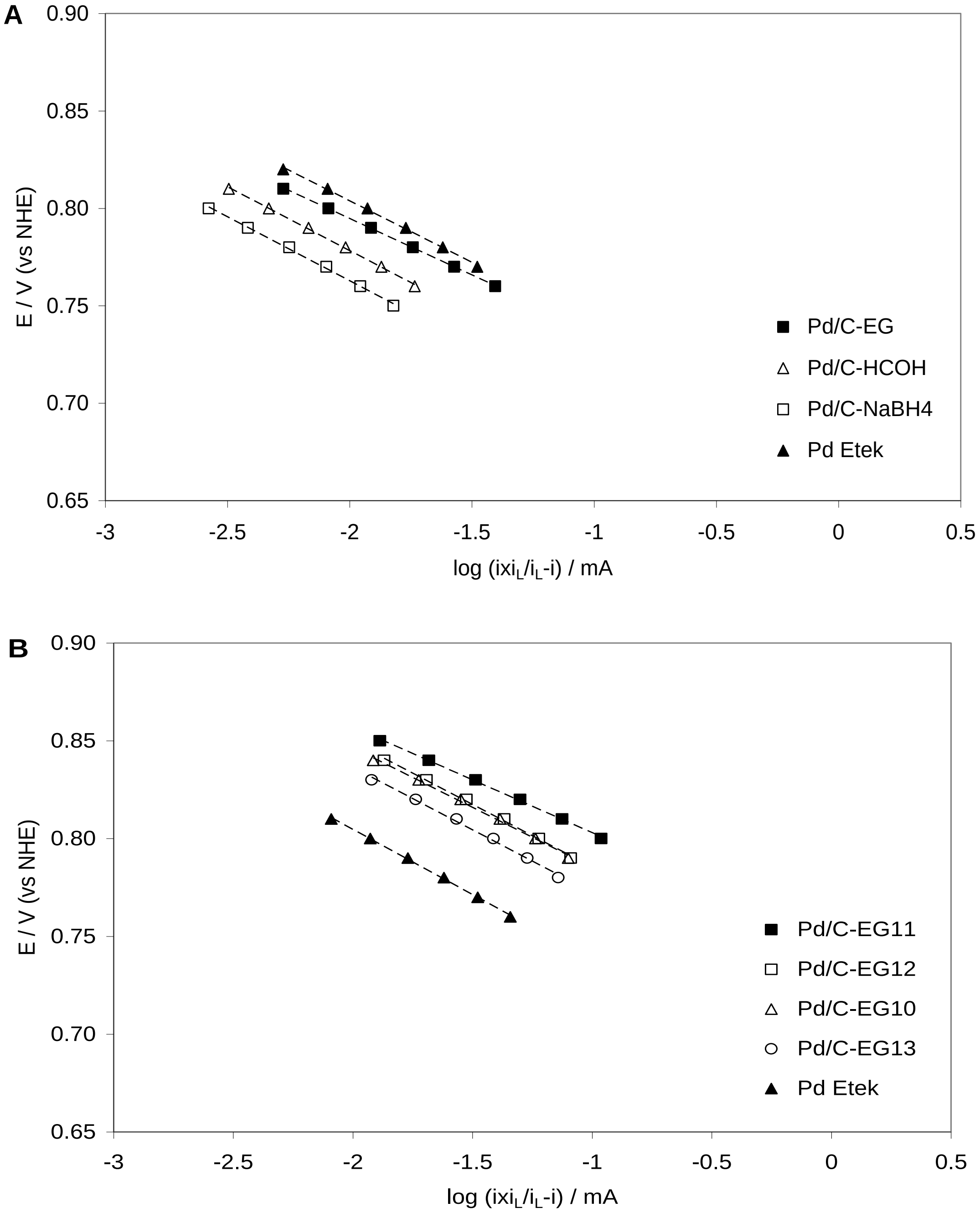

Figure 4-19: Tafel plots for Pd/C catalysts A) Pd/C-EG, Pd/C-CH_2O and Pd/C-$NaBH_4$ B) Pd/C-EG10, Pd/C-EG11, Pd/C-EG12 and Pd/C-EG13.

Tafel slopes of ca. 60 to 70 mV decade^{-1} have been previously reported for Pd and Pd alloys in 0.5 M H_2SO_4 by Zhang, Gnanamutu, Hoare, Mustain, Savadogo and Tilak among others [4, 30-34]. Damjanovic et al. reported that the mechanism of the ORR on a palladium electrode is the same that the one taking place on a platinum electrode, since both electrodes exhibited the same Tafel slope for the ORR. They also reported that the low Tafel slope value for a platinum electrode, 60 mV decade^{-1}, corresponds to the oxygen reduction taking place on a oxide-covered platinum electrode [25]. Thus, it was concluded that all Tafel slopes reported in this piece of work for palladium catalysts correspond to ORR on oxide-covered palladium electrodes. Tafel plots, potential versus logarithm of current density, are shown in Figure 4-19.

Exchange current densities were obtained by extrapolating the Tafel line to the equilibrium potential. The equilibrium potential value used was 1.21 V after correcting the standard reduction potential for oxygen concentration, using the solubility value of O_2 in 0.5 M H_2SO_4 (1.02 x 10^{-3} mol dm^{-3} [35]) and the Nernst equation. Exchange current densities for Pd/C-EG, Pd/C-CH_2O and Pd/C-$NaBH_4$, were 6.0 x 10^{-12}, 2.2 x 10^{-12} and 2.7 x 10^{-12} A cm^{-2}, respectively (Table 4-2). Exchange current densities for Pd/C-EG10, Pd/C-EG11, Pd/C-EG12 and Pd/C-EG13 were 9.7 x 10^{-12}, 7.7 x 10^{-12}, 1.0 x 10^{-11} and 8.6 x 10^{-12} A cm^{-2}, respectively. Exchange current densities of catalysts synthesized monitoring the pH were the same order of magnitude as values reported for palladium by Gnanamuthu et al. and by Tilak et al. (10^{-11} A cm^{-2}) [30, 34], but over an order of magnitude lower that the value reported by Savadogo et al. for palladium (2.2 x 10^{-10} A cm^{-2}) [33]. All palladium catalysts prepared using ethylene glycol, had an exchange current density of ca. 10^{-11} A cm^{-2}. The other two catalysts, Pd/C-CH_2O and Pd/C-$NaBH_4$, exhibited exchange current densities closer to 10^{-12} A cm^{-2}. This would indicate that physicochemical characteristics of palladium nanoparticles synthesized using formaldehyde or sodium borohydride are less favorable than those synthesized using ethylene glycol.

The ORR activity of catalysts reduced in a hydrogen atmosphere, i.e. Pd/C-EG-300 was studied. A decrease in mass activity compared to Pd/C-EG was observed (7 to 3 A g^{-1} at 0.75V). This decrease was believed to be due to the loss of catalyst surface area caused by particle growth during heat treatment. The exchange current density for Pd/C-EG-300 (8.5 x 10^{-12} A cm^{-2} Pd) was not significantly different to the other Pd/C synthesized using ethylene glycol. Because all heat treated catalysts suffered a loss of ECSA compared to the untreated catalyst, ORR activity studies for other treated catalysts were not carried out.

Activity towards the oxygen reduction reaction of Pd/C-EG11-untr was also evaluated. Pd/C-EG11 and Pd/C-EG11-untr presented similar particle sizes, calculated for the XRD patterns, and similar ECSA, calculated from the cyclic voltammograms in N_2 saturated electrolyte. Therefore it was not surprising that the onset potentials and exchange current densities were also very close for Pd/C-EG11 and Pd/C-EG11-untr: OCP was 0.89 V for both and i_0 was 8 x 10^{-12} and 1 x 10^{-11} A cm^{-2}, respectively. However, the current density at 0.75 V was higher for Pd/C-EG11-untr, which led to higher mass activity, 30 A g^{-2} Pd. The slight increase in the current density at 0.75 V together with the decrease in carbon lost (discussed in Section 4.2.1) and the simplicity of the synthesis, led to the selection of Pd/C-EG11 as the catalyst of choice for further investigations. Thus, pre-treatment of the carbon support with HNO_3 was no longer carried out for practical reasons. The carbon treatment was highly time consuming; the carbon would be allowed to reflux in a nitric acid solution overnight, the product was washed up to twenty times with deionized water until reaching a pH close to neutral and subsequently separated by centrifugation. The carbon treated this way was allowed to dry overnight at 100 ºC and ground afterwards. Approximately one gram of treated carbon was obtained at the end of the process.

Figure 4-20 shows anodic LSVs for Pd/C-EG11-untr at five different rotation speeds, 400, 900, 1600, 2500 and 3600 rpm (tests carried out from lower to higher rotation speeds). Forward and backward linear sweep voltammograms were successively recorded for each rotation speed in the potential range 0.25 to 0.95 V, starting with 400 rpm and ending with 3600 rpm. For the rotation speed 400 rpm the cathodic potential sweep is also plotted (dotted line). The inset in Figure 4-20 shows the onset potential region, in which it can be seen that the variability in onset potential within the five voltammograms was only 2 mV. Therefore it could be concluded that the palladium nanoparticles were stable in the conditions applied and further investigations were carried out.

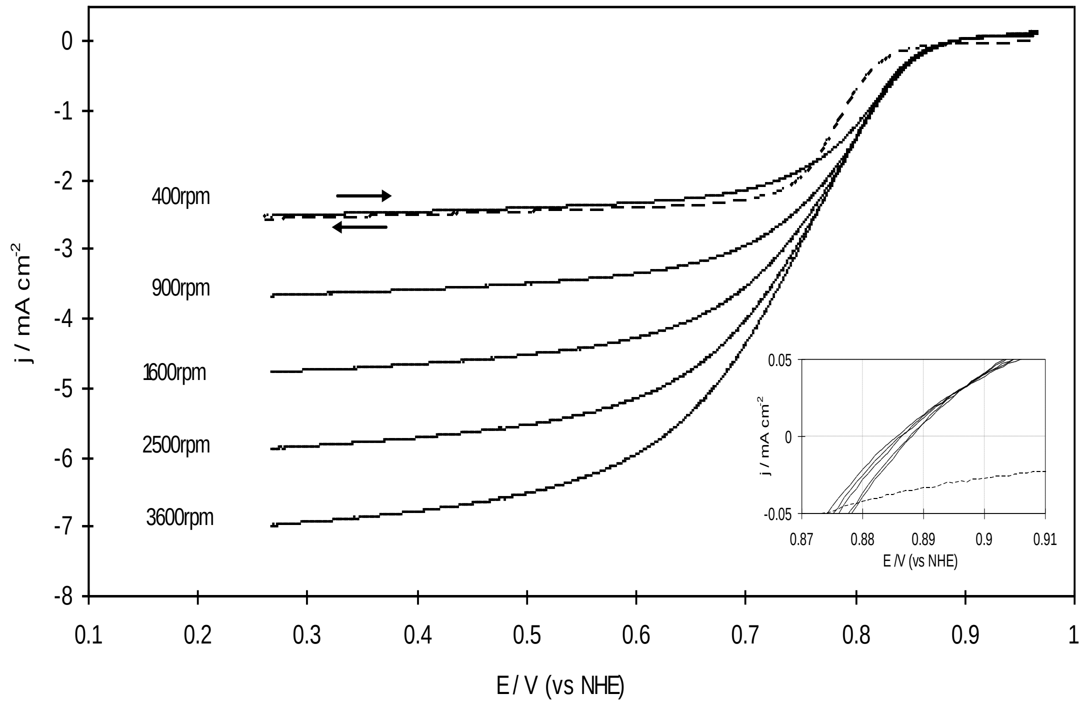

Figure 4-20: Linear sweep voltammograms of Pd/C-untr at different rotation speed.

Linear sweep voltammograms at different rotation speeds were analyzed using the Koutecky-Levich equation: $1/i = 1/i_k + 1/i_L$ [36]. In this equation i_k is the kinetic current and i_L is the mass-transport controlled current. Koutecký-Levich plots are plots of i^{-1} vs $\omega^{-1/2}$, where i is the overall current density and ω is the rotation speed, were produced for some of the catalysts. In a plot of i vs ω, the overall current will tend to a limit, i_k, when the rotating speed tends to ∞. The kinetic current, i_k, is defined as the current is absence of any mass-transport effect. When i^{-1} is plotted vs $\omega^{-1/2}$, the plot should be linear and it can be extrapolated to infinite rotation speed, $\omega^{-1/2} = 0$, to obtain i_k^{-1} [36]. Koutecký-Levich plots for Pd/C-EG11-untr are shown in Figure 4-21. Current values were taken from the linear sweep voltammograms, current values at five different rotation speeds and at five different potentials, 0.67, 071, 075, 079 and 0.82 V.

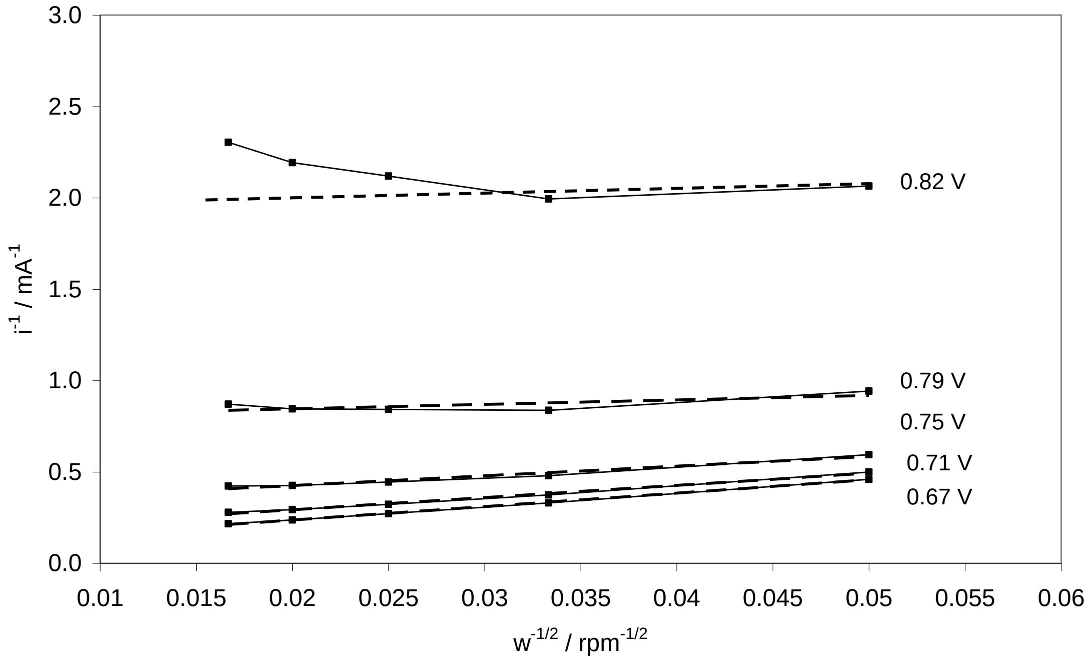

Figure 4-21: Koutecký-Levich plots for Pd/C-untr.

A plot of the logarithm of the kinetic currents obtained from Koutecký-Levich plots vs potential was built to evaluate the Tafel slope in this new potential range (Figure 4-22). The Tafel slope from Koutecký-Levich plots (potential range ca. 0.70 to 0.80 V) was 101 mV decade^{-1}, significantly different from the slope estimated from mass-transport corrected Tafel plots (range 0.80 to 0.85 V), of 59 mV decade^{-1}. This change in the slope, by analogy with Pt, was attributed to a change in the surface coverage of the chemisorbed oxygen-containing species: the oxygen coverage changes with the potential and this coverage influences the oxygen adsorption, as explained by Tarasevich (cited by Tammevesky [37] and Mamlouk [38]) and Parthasarathy [39]. The oxygen coverage in the potential range 0.70 to 0.80 V was different to the coverage in the kinetic region (potential range 0.80 to 0.85 V) as was previously discussed in Section 4.3.1; therefore different Tafel slopes would be observed in these two potential regions.

The straight line fitted to produce a Tafel equation from data obtained from Koutecký-Levich plots (Figure 4-22), had a correlation coefficient of only 0.987, which is lower than the minimum of 0.995 obtained in traditional Tafel plots. The change in Tafel slope at high current was shown in Figure 4-18 and was confirmed by Koutecký-Levich plots.

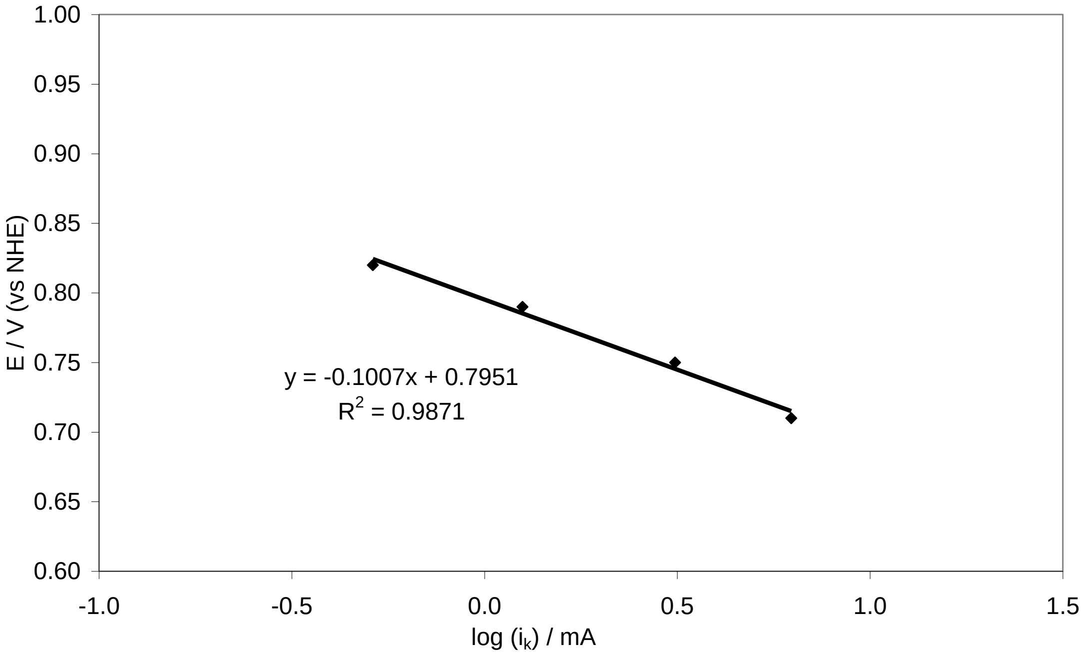

Figure 4-22: Kinetic current vs potential plots for Pd/C-untr.

4.5. Conclusions

Palladium nanoparticles supported on pre-treated Vulcan XC-72R were initially synthesized using an impregnation method followed by a reduction with three different reducing agents: ethylene glycol, formaldehyde and sodium borohydride. The pH of the system was not controlled in any of these three syntheses. Ethylene glycol yielded the catalyst with higher activity towards the ORR per unit of mass (mass activity) and so ethylene glycol was chosen as the reducing agent.

Different syntheses were carried out using ethylene glycol as the reducing agent in order to identify the most favourable pH to carry out the reduction. The aim was to obtain palladium particles well dispersed on the carbon support and with an optimum particle size for the ORR. Palladium nanoparticles which provided both high ORR activity and stability were obtained (optimum particle size); however further research on particle distribution on the carbon surface would be necessary. It was found that reduction of ammonium tetrachloropalladate (II) at basic pH, between 10 and 13 pH units, yielded Pd particles of approximately 6 nm. The pH, within this alkaline region, had no apparent effect on the Pd particle size. Exchange current densities estimated for Pd/C catalysts prepared by EG reduction were all similar, in the interval 7.7 x 10^{-12} to 1.0 x 10^{-11} A cm^{-2} Pd. Therefore, it was concluded that the particle size, within the studied range, did not influence the ORR activity of Pd nanoparticles prepared by EG reduction.

On the other hand, the pH of the reaction system induced a change in the dispersion of palladium nanoparticles on the carbon surface. Dispersion of the Pd nanoparticles was higher in basic pH, as indicated by higher ECSA and mass activity values. TEM analysis showed particle agglomeration for all the Pd/C catalysts analysed. The least severe agglomeration was observed for Pd/C-EG11, this was as evidenced by its mass activity (20 A g^{-2} Pd) higher than mass activities of Pd/C-EG, Pd/C-EG10, Pd/C-EG12 or Pd/C-EG13. A pH value of 11 was chosen in further catalyst preparations by EG reduction, both for Pd or palladium-based bimetallic catalysts.

All carbon-supported palladium catalysts exhibited only one Tafel slope, this one being in the low current density region, with values ranging from 59 to 64 mV $decade^{-1}$. In the high current density region a constantly changing Tafel slope was observed. This change in Tafel slope was believed to be due to the change of the oxygen coverage of the catalyst surface with the potential.

Carbon-supported palladium nanoparticles were also prepared on as-received Vulcan XC-72R using ethylene glycol as reducing agent at pH 11. Characterization of this catalyst (Pd/C-untr) showed that its particle size of 7 nm with an ECSA of 15 m^2 g^{-1}, and exchange current density of 1.0 x 10^{-11} A cm^{-2} Pd, were similar to those calculated for Pd/C-EG11. Future preparations were carried out on as-received Vulcan XC-72R.

Heat treatment in H_2 at 300 ºC caused particle growth on all carbon-supported palladium nanocatalysts. The extension of the sintering increased with increasing temperature in the range from room temperature to 300 ºC, and it was more severe for smaller palladium particles. Heat treatment caused an important loss of ECSA in each catalyst and therefore a decrease in its mass activity. Heat treatment did not affect the activity towards ORR of the Pd catalyst; kinetic parameters calculated for Pd/C-EG-300 did not differ significantly from those of Pd/C-EG.

To conclude, palladium nanoparticles suitable to be used as cathode catalysts in PEMFC were obtained. By using ethylene glycol as the reducing agent at pH 11, ammonium tetrachloropalladate (II) yielded Pd nanoparticles of approximately 6 nm which provided both high ORR activity and stability. Further research on particle distribution on the carbon surface would possibly lead to an increase in the electrochemical surface area and therefore the mass activity of this catalyst.

References

1. Guha, A., W. Lu, T.A. Zawodzinski Jr, and D.A. Schiraldi, *Surface-modified carbons as platinum catalyst support for PEM fuel cells.* Carbon, 2007. **45**(7): p. 1506-1517.

2. Li, H., G. Sun, Y. Gao, Q. Jiang, Z. Jia, and Q. Xin, *Effect of Reaction Atmosphere on the Electrocatalytic Activities of Pt/C and PtRu/C Obtained in a Polyol Process.* J. Phys. Chem. C Full Journal Title:Journal of Physical Chemistry C, 2007. **111**(42): p. 15192-15200.

3. Umeda, M., M. Kokubo, M. Mohamedi, and I. Uchida, *Porous-microelectrode study on Pt/C catalysts for methanol electrooxidation.* Electrochim. Acta Full Journal Title:Electrochimica Acta, 2003. **48**(10): p. 1367-1374.

4. Zhang, L., K. Lee, and J. Zhang, *Effect of synthetic reducing agents on morphology and ORR activity of carbon-supported nano-Pd-Co alloy electrocatalysts.* Electrochim. Acta Full Journal Title:Electrochimica Acta, 2007. **52**(28): p. 7964-7971.

5. *International Centre for Diffraction Data*. Available from: http://www.icdd.com/.

6. Cullity, B.D., *Elements of X-Ray Diffraction*. 1978: Addison-Wesley.

7. Wu, C., H. Zhang, and B. Yi, *Hydrogen generation from catalytic hydrolysis of sodium borohydride for proton exchange membrane fuel cells.* Catalysis Today, 2004. **93-95**: p. 477-483.

8. Canton, P., C. Meneghini, P. Riello, A. Balerna, and A. Benedetti, *Thermal evolution of carbon-supported Pd nanoparticles studied by time-resolved X-ray diffraction.* Journal of Physical Chemistry B, 2001. **105**(34): p. 8088-8091.

9. Jiang, L., A. Hsu, D. Chu, and R. Chen, *Size-dependent activity of palladium nanoparticles for oxygen electroreduction in alkaline solutions.* Journal of the Electrochemical Society, 2009. **156**(5): p. B643-B649.

10. Vielstich, W., H. Gasteiger, and A. Lamm, *Handbook of fuel cells : fundamentals, technology and applications*. 2003, Chichester: Wiley. 4 v.

11. Burke, L.D. and D.T. Buckley, *Anomalous oxidation reactions at noble metal surfaces at low potentials: with particular reference to palladium.* Journal of the Electrochemical Society, 1996. **143**(3): p. 845-854.

12. Burke, L.D. and J.K. Casey, *Examination of the electrochemical behavior of palladium electrodes in acid.* Journal of the Electrochemical Society, 1993. **140**(5): p. 1284-1291.

13. Breiter, M.W., *Dissolution and adsorption of hydrogen at smooth Pd wires at potentials of the alpha phase in sulfuric acid solution.* Journal of Electroanalytical Chemistry, 1977. **81**(2): p. 275-284.

14. Rand, D.A.J. and R. Woods, *A study of the dissolution of platinum, palladium, rhodium and gold electrodes in 1 M sulphuric acid by cyclic voltammetry.* Journal of Electroanalytical Chemistry, 1972. **35**(C): p. 209-218.

15. Solla-Gullón, J., V. Montiel, A. Aldaz, and J. Clavilier, *Synthesis and electrochemical decontamination of platinum-palladium nanoparticles prepared by water-in-oil microemulsion.* Journal of the Electrochemical Society, 2003. **150**(2): p. E104-E109.

16. Mallát, T., É. Polyánszky, and J. Petró, *Electrochemical study of palladium powder catalysts.* Journal of Catalysis, 1976. **44**(3): p. 345-351.

17. Zeng, J., J.Y. Lee, and W. Zhou, *Activities of Pt/C catalysts prepared by low temperature chemical reduction methods.* Appl. Catal., A Full Journal Title:Applied Catalysis, A: General, 2006. **308**: p. 99-104.

18. Mukerjee, S. and J. McBreen, *Effect of particle size on the electrocatalysis by carbon-supported Pt electrocatalysts: An in situ XAS investigation.* Journal of Electroanalytical Chemistry, 1998. **448**(2): p. 163-171.

19. Li, H., G. Sun, Q. Jiang, M. Zhu, S. Sun, and Q. Xin, *Synthesis of highly dispersed Pd/C electro-catalyst with high activity for formic acid oxidation.* Electrochem. Commun. Full Journal Title:Electrochemistry Communications, 2007. **9**(6): p. 1410-1415.

20. Grigoriev, S.A., P. Millet, and V.N. Fateev, *Evaluation of carbon-supported Pt and Pd nanoparticles for the hydrogen evolution reaction in PEM water electrolysers.* J. Power Sources Full Journal Title:Journal of Power Sources, 2008. **177**(2): p. 281-285.

21. Luo, C., Y. Zhang, and Y. Wang, *Palladium nanoparticles in poly(ethyleneglycol): the efficient and recyclable catalyst for Heck reaction.* Journal of Molecular Catalysis A: Chemical, 2005. **229**(1-2): p. 7-12.

22. Damjanovic, A. and V. Brusic, *Electrode kinetics of oxygen reduction on oxide-free platinum electrodes.* Electrochimica Acta, 1967. **12**(6): p. 615-628.

23. Gottesfeld, S., I.D. Raistrick, and S. Srinivasan, *Oxygen Reduction Kinetics on a Platinum RDE Coated with a Recast Nafion Film.* Journal of the Electrochemical Society, 1987. **134**(6): p. 1455-1462.

24. Sleightholme, A.E.S., *Electrochemical studies of fuel cell catalysts*, in *Chemistry*. 2007, Imperial College: London.

25. Damjanovic, A., *Mechanism of oxygen reduction related to electronic structure of gold-palladium alloy.* Journal of Physical Chemistry, 1967. **71**(8): p. 2741-2742.

26. Pourbaix, M., *Atlas of Electrochemical Equilibria in Aqueous Solutions*. 2nd ed. 1974, Houston: National Association of Corrosion Engineers.

27. Wang, X., N. Kariuki, D. Myers, and R. Kumar, *V.C.6 Non-Platinum Electrocatalysts.* DOE Hydrogen Program, 2006. FY 2006 Annual Progress Report: p. 791-793.

28. Shao, M.-H., K. Sasaki, and R.R. Adzic, *Pd-Fe Nanoparticles as Electrocatalysts for Oxygen Reduction.* Journal of the American Chemical Society, 2006. **128**(11): p. 3526-3527.

29. Parthasarathy, A., C.R. Martin, and S. Srinivasan, *Investigations of the O2 reduction reaction at the platinum Nafion interface using a solid-state electrochemical cell.* Journal of the Electrochemical Society, 1991. **138**(4): p. 916-921.

30. Gnanamuthu, D.S. and J.V. Petrocelli, *A Generalized Expression for the Tafel Slope and the Kinetics of Oxygen Reduction on Noble Metals and Alloys.* Journal of The Electrochemical Society, 1967. **114**(10): p. 1036-1041.

31. Hoare, J.P., *Oxygen Overvoltage on Bright Palladium in Acid Solutions.* Journal of The Electrochemical Society, 1965. **112**(11): p. 1129-1133.

32. Mustain, W.E., K. Kepler, and J. Prakash, *CoPdx oxygen reduction electrocatalysts for polymer electrolyte membrane and direct methanol fuel cells.* Electrochimica Acta, 2007. **52**(5): p. 2102-2108.

33. Savadogo, O., K. Lee, K. Oishi, S. Mitsushima, N. Kamiya, and K.I. Ota, *New palladium alloys catalyst for the oxygen reduction reaction in an acid medium.* Electrochemistry Communications, 2004. **6**(2): p. 105-109.

34. Tilak, B.V., K. Tari, and C.L. Hoover, *Metal Anodes an Hydrogen Cathodes: Their Activity towards* O_2 *Evolution and* ClO_3^{2-} *Reduction Reactions.* Journal of the Electrochemical Society, 1988. **135**(6): p. 1386-1392.

35. Gubbins, W., *The Solubility and Diffusivity of Oxygen in Electrolytic Solutions.* 1965.

36. Bard, A.J., *Electrochemical Methods: Fundamentals and Applications*. 2nd edition ed. 2001: John Wiley & Sons, Inc.

37. Tammeveski, K., M. Arulepp, T. Tenno, C. Ferrater, and J. Claret, *Oxygen electroreduction on titanium-supported thin Pt films in alkaline solution.* Electrochimica Acta, 1997. **42**(19): p. 2961-2967.

38. Mamlouk, M., *Investigation of High Temperature Polymer Electrolyte Membrane Fuel Cells*, in *Chemical Engineering and Advanced Materials*. 2008, Newcastle University: Newcastle upon Tyne.

39. Parthasarathy, A., S. Srinivasan, A.J. Appleby, and C.R. Martin, *Temperature dependence of the electrode kinetics of oxygen reduction at the platinum/nafion(R) interface - a microelectrode investigation.* Journal of the Electrochemical Society, 1992. **139**(9): p. 2530-2537.

Chapter 5: Characterization of carbon-supported bimetallic Pd-M nanoparticles

5.1. Introduction

Physicochemical characterization and catalytic activity towards the oxygen reduction reaction (ORR) in acid media of carbon-supported bimetallic nanoparticles are discussed in this chapter. Electrocatalysts are divided into four groups: palladium-gold, palladium-cobalt, palladium-titanium and palladium-iron. At least two different atomic ratios were selected for each bimetallic combination. Two synthetic procedures were chosen for the preparations: simultaneous co-deposition of both metals on the carbon support and deposition of the second metal on carbon-supported Pd; Pd/C prepared by the EG reduction at pH 11 as described in the previous chapter. The effect of heat treatment in H_2 at different temperatures is also discussed in this chapter.

The first bimetallic combination, palladium-gold, was chosen to establish the basis for future study of palladium-based ternary electrocatalysts, despite the poor ORR activity reported in the literature for Pd-Au alloys [1, 2]. Ternary metal combinations based on palladium, like Pd-Co-Au [3], have been claimed to be as active as commercial carbon-supported nanoparticles. Therefore, it was decided to study the synthetic method, physicochemical properties and ORR activity of Pd-Au bimetallic catalysts with different metal ratios. To study the influence of the introduction of Au in the Pd lattice three different Pd to Au atomic ratios, ranging from a gold rich to a 10% atomic Au alloy, were chosen.

Palladium-cobalt and palladium-iron alloys have been reported to have electrocatalytic activities for the ORR higher than that of pure palladium [4-6]. Studies by Suo et al. of adsorption energies of monoatomic oxygen in alloys with different degree of alloy supported the experimental data [7]. In this chapter the effect of different synthetic methods and atomic ratios has been studied for Pd-Co and Pd-Fe electrocatalysts.

Pd_4Co alloy was reported to be very active towards the oxygen reduction reaction for different groups [8, 9], this work was replicated in order to understand the system for future third metal additions. The system Pd:Co 1:1 was also studied because of the obvious advantage of the low cost of Co. Pd overlayers on $Pd_3Fe(111)$ and the Pd overlayer on PdFe(111) were reported to have high ORR activity [10]. In this chapter the preparation and characterization of polycrystalline Pd_3Fe and PdFe are discussed.

Palladium-titanium catalysts were also prepared by different synthetic methods and using different atomic ratios. Fernández et al [3] reported the bimetallic combination Pd-Ti with atomic ratio 1 to 1 to be highly active towards the oxygen reaction. The preparation of a Pd-Ti 1 to 1 atomic ratio was attempted and the results are discussed in this chapter. The effect of small amounts of Ti in the Pd lattice, 9 to 1 Pd to Ti, on the ORR activity is also discussed.

The aim of the experiments discussed in this chapter was to screen a number of bimetallic electrocatalysts. The influence of different factors on the catalyst structure and ORR activity was studied: the reducing agent, temperature, the deposition order and the atomic ratio of both metals.

5.2. Physicochemical characterization of carbon-supported bimetallic nanoparticles

The average *d* value (Pd-Pd bond distance) for Pd/C was calculated after applying the Bragg equation to twenty carbon-supported Pd catalysts. The Pd-Pd bond for Pd/C was found to have an average value of 0.2751 nm, the associated error was ± 0.0003 nm. In the study of the following bimetallic catalysts, it was decided to consider as a proof of alloy formation, a *d* value outside the interval 0.2751 ± 0.0006 nm. This interval was calculated by adding 200% of the error to the Pd/C *d* value.

5.2.1. Physicochemical characterization of palladium-gold catalysts

Metal content and Pd to Au atomic ratio obtained from EDXA characterizations for each palladium-gold catalyst are shown in Table 5-1. Total metal content of catalysts prepared by simultaneous co-deposition of Pd and Au was aimed at 20% weight; catalysts prepared on 20% weight Pd/C would therefore have higher metal content. Table 5-1 also lists for each catalyst the particle size and, the Pd-Pd bond distance (estimated from XRD patterns) and electrochemical surface area (ECSA) (estimated from slow scan cyclic voltammograms). XRD patterns for palladium-gold catalysts are compared in this section. Palladium-gold phase diagram [11] shows that both metals alloy at any atomic ratio forming a face-centered cubic crystal system.

Table 5-1: Particle size, electrochemical surface area, Pd-Pd bond distance and metal content for palladium-gold electrocatalysts**.**

Catalyst	Particle size (nm)	ECSA ($m^2\ g^{-1}$)	Pd-Pd bond	Metal content (% weight)	Atomic ratio

			distance (nm)		(Pd:Metal)
PdAu-EG11	2.7	-	0.2852	4.8 Pd, 12.4 Au	1:1.4
PdAu-EG11-300	9.5	-	0.2833	4.8 Pd, 12.4 Au	1:1.4
Pd$_9$Au-EG11	-	11.4	-	14.2 Pd, 3.7 Au	1: 0.14
Pd$_9$Au-EG11-300	-	4.9	-	14.2 Pd, 3.7 Au	1: 0.14
Pd(Au)-EG11	6.0 Pd, 18.8 Au	3.7	0.2751	11.2 Pd, 28.4 Au	1:1.4
Pd(Au)-EG11-300	10.2 Pd, 21.4 Au	0.6	0.2746	11.2 Pd, 28.4 Au	1:1.4
Pd$_3$(Au)-EG11	6.4 Pd, 13.4 Au	8.4	0.2749	17.8 Pd, 13.0 Au	1:0.4
Pd$_3$(Au)-EG11-300	8.9 Pd, 14.3 Au	3.0	0.2747	17.8 Pd, 13.0 Au	1:0.4
Pd-EG11-untr	7.3	14.6	0.2751	22.5	-
Pt-Etek	3.4	55.3	-	19.8	-

Figure 5-1 shows XRD patterns of all four catalysts synthesized without heat treatment in H_2. Both catalysts prepared by depositing gold on Pd/C, Pd(Au)-EG11 and Pd$_3$(Au)-EG11, showed diffraction patterns corresponding to pure Pd and pure Au phases, no alloy was present in the samples. This was confirmed by the Pd-Pd bond distance calculated from the Bragg equation; the Pd (220) diffraction peak, for Pd(Au)-EG11 and Pd$_3$(Au)-EG11 was 0.2751 and 0.2749 nm, respectively. The Pd-Pd bond distance did not differ significantly from the value calculated for Pd/C, 0.2751 nm (Table 5-1).

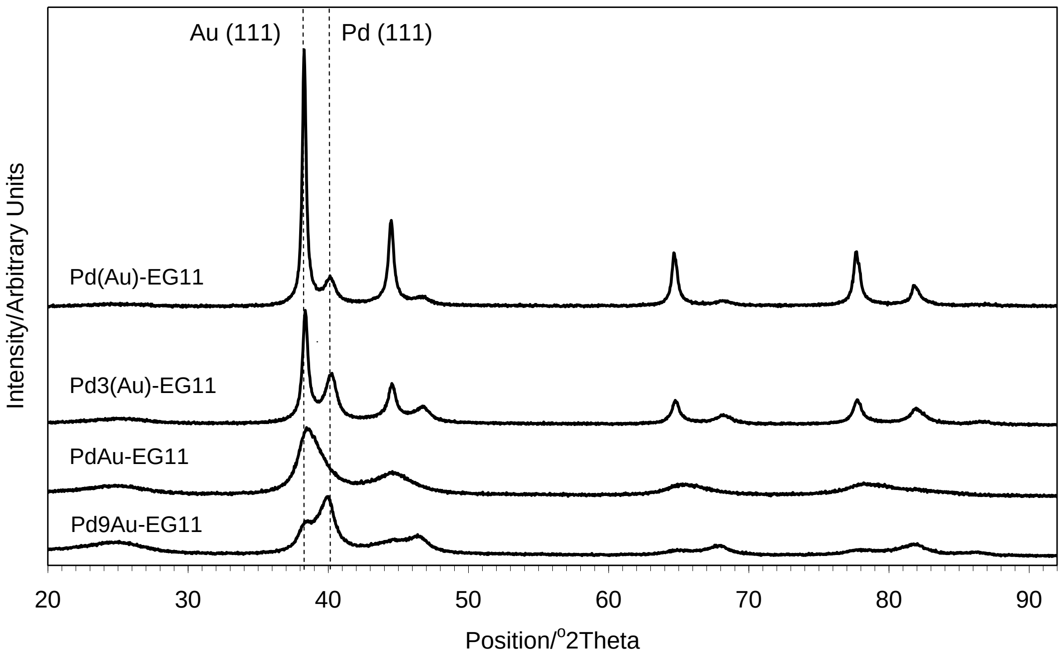

Figure 5-1: X-ray diffraction patterns of carbon-supported Pd-Au catalysts.

However, when catalysts were prepared by the co-deposition method (PdAu-EG11 and Pd_9Au-EG11) complete phase segregation was not observed, solid solution of both metals was present. When metals were co-deposited with atomic ratio 1:1.4, PdAu-EG11, an asymmetric diffraction peak located between diffraction angles for pure Pd and pure Au and with its maximum close to the gold diffraction angle was observed. The asymmetry of the peak suggests a concentration gradient in the solid solution and the position of the maximum suggests the presence of a pure gold phase; no peak at the palladium diffraction angle was present. When co-deposition was made at atomic ratio 1:0.14, Pd_9Au-EG11, both Pd and Au diffraction peaks, as well as an intermediate peak, were observed. These patterns suggest the presence of several metal phases; Pd, Au and a solid solution of both with a concentration gradient. The Pd-Pd bond distance of 0.2852 nm calculated for PdAu-EG11, confirms the presence of alloy by departure from the Pd/C value of ca. 0.01 nm. The palladium lattice expanded due to the replacement of part of Pd with Au. The Pd-Pd bond distance for Pd_9Au-EG11 could not be calculated due to the overlapping of peaks.

Figure 5-2 shows palladium gold catalysts heat treated in H_2 at 300 ºC. When catalysts were prepared by deposition of gold on Pd/C, Pd(Au)-EG11-300 and Pd_3(Au)-EG11-300, no Pd-Au alloy was formed after heat treatment in H_2. XRD patters showed two separated peaks corresponding to pure Pd and pure Au phases. This was confirmed by the lack of difference of the Pd-Pd bond values between Pd/C and Pd(Au)-EG11-300 and Pd_3(Au)-EG11-300, which were 0.7546 and 0.7547 nm, respectively. Therefore, no alloy was obtained in any of palladium-gold electrocatalysts prepared by depositing gold on Pd/C. The only observed difference between the XRD patterns of catalysts untreated, Pd(Au)-EG11 and Pd_3(Au)-EG11, and catalysts heat treated, Pd(Au)-EG11-300 and Pd_3(Au)-EG11-300, was a growth in the Pd particle size. The estimated diameter of the Pd particles increased from 6 to 10 nm and only from 6 to 9 nm when atomic ratios were 1:1.4 and 1:0.4 Pd to Au, respectively (see Table 5-1).

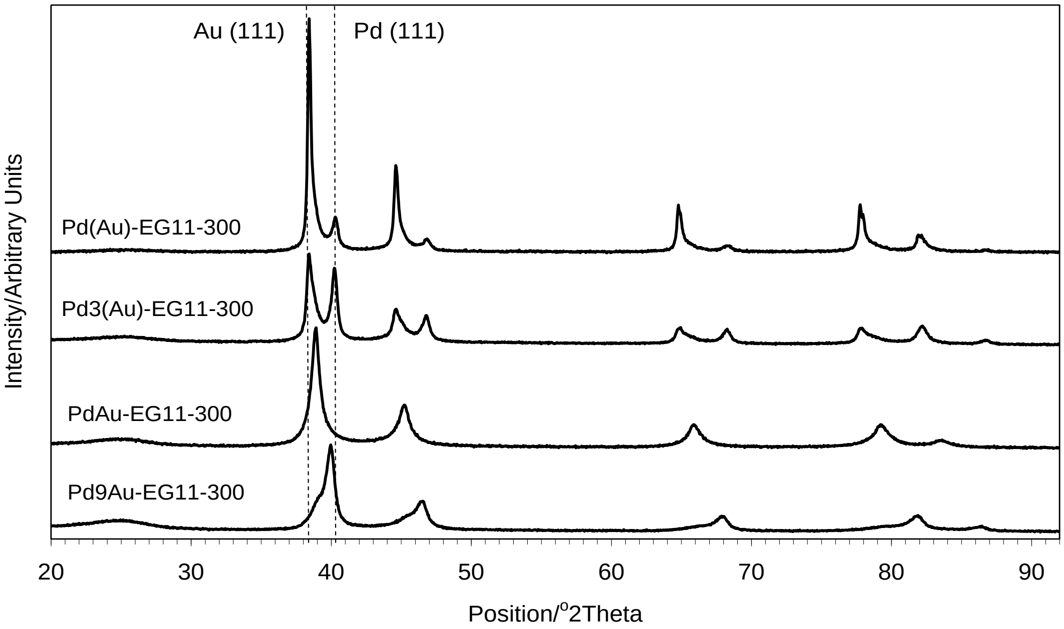

Figure 5-2: X-ray diffraction patterns of carbon-supported Pd-Au catalysts heat treated in H_2 at 300 ºC.

In contrast to electrocatalysts prepared on Pd/C, materials prepared by the co-deposition method, PdAu-EG11-300 and Pd_9Au-EG11-300, showed changes in metal phases after heat treatment. When co-deposited metals at atomic ratios Pd to Au 1 to 1.4, were heat treated in H_2, the asymmetric diffraction peak (PdAu-EG11) turned into a symmetrical peak with its maximum at a diffraction angle between Au and Pd positions. Diffractograms showed a typical face-centered cubic pattern with diffraction angles shifted to lower positions compared to those of Pd/C, which indicated the formation of a Pd-Au alloy. The Pd-Pd bond distance calculated for PdAu-EG11-300 was 0.2833 nm, significantly larger than for Pd/C. The palladium lattice expanded due to the replacement of part of the Pd with Au. At an atomic ratio of 1:0.14 the diffraction peaks were shifted from the Pd and Au positions; overlapped peaks appeared on intermediate positions. This suggests the presence of Pd-Au solid solution with different metal proportions. No peaks at palladium or gold diffraction angles were present. Therefore, no pure Pd or Au phases were present either on PdAu-EG11-300 or Pd_9Au-EG11-300. The Pd-Pd bond distance for Pd_9Au-EG11-300 could not be calculated due to the overlapping of the peaks.

The particle size calculated for PdAu-EG11 (Table 5-1) of approximately 3 nm, was not accurate due to the asymmetry of the diffraction peak, which was likely to be the combination of two diffraction peaks, corresponding to Pd-Au solid solutions with different metal ratios. The asymmetry of the peak, which was likely to be caused by peak overlapping, could lead to a measured larger full width at half maximum (FWHM), and therefore to calculate a smaller crystallite size. The particle size was however still used for comparison. Since the diffractograms for Pd_9Au-EG11 and Pd_9Au-EG11-300 presented overlapped peaks, FWHM could not be measured and particle sizes could not be estimated by the Scherrer equation.

The effect of heat treatment in H_2 at 300 ºC on the catalysts was a growth in the Pd particles in every case. However, this growth was smaller than the increase in the particle size observed for pure palladium particles when subjected to the same treatment. The effect of Au can be observed by comparing the effect of heat treatment of PdAu-EG11 with Pd/C from E-Tek. For PdAu-EG11 the estimated particle size was 3 nm, which increased to 10 nm after heat treatment; Pd/C from E-Tek had Pd nanoparticles of approximately 3.5 nm when received, particle size increased to 16 nm after heat treatment. Therefore, it could be suggested that introduction of Au in the Pd lattice reduced the extent of sintering when treated at high temperature in presence of H_2. A similar effect was observed in catalysts prepared on Pd/C, Pd(Au)-EG11 and Pd_3(Au)-EG11, where Pd particles increased from 6 to 10 nm and only from 6 to 9 nm, respectively. This increase was considerably smaller than the rise observed for Pd/C prepared by EG reduction (6 to 17 nm) as shown in the previous chapter. The depression in the sintering degree due to the presence of a second element in the Pd lattice was previously reported in the literature with other metals such as Fe [12]. The Au particle size did not exhibit significant changes in any case.

5.2.2. Physicochemical characterization of palladium-cobalt catalysts

Table 5-2 lists the metal content for each palladium-cobalt catalyst. The total content of catalysts prepared by simultaneous co-deposition of Pd and Co was close to 20% metal weight, whilst catalysts prepared on Pd/C had higher metal content. The palladium-cobalt phase diagram [11] shows that both metals alloy, forming a face-centered cubic crystal system, when the Pd atomic content is higher than 52%.

Table 5-2: Particle size, electrochemical surface area, Pd-Pd bond distance and metal content for palladium-cobalt electrocatalysts.

Catalyst	**Particle size (nm)**	**ECSA (m^2 g^{-1})**	**Pd-Pd bond distance (nm)**	**Metal content (% weight)**	**Atomic ratio (Pd:Metal)**
PdCo-EG11	7.7	12.2	0.2753	12.4 Pd, 6.3 Co	1:0.9
PdCo-EG11-300	8.4	9.0	0.2739	12.4 Pd, 6.3 Co	1:0.9
Pd_4Co-EG11	7.3	13.5	0.2748	19.7 Pd, 2.0 Co	1:0.2
Pd_4Co-EG11-300	9.6	10.3	0.2747	19.7 Pd, 2.0 Co	1:0.2
Pd(Co)-EG11	7.7	10.0	0.2748	20.4 Pd, 6.9 Co	1:0.6
Pd(Co)-EG11-300	7.9	7.8	0.2743	20.4 Pd, 6.9 Co	1:0.6
Pd_4(Co)-EG11	6.9	12.2	0.2746	23.8 Pd, 2.2 Co	1:0.2
Pd_4(Co)-EG11-300	9.9	9.1	0.2746	23.8 Pd, 2.2 Co	1:0.2
Pd-EG11-untr	7.3	14.6	0.2751	22.5	-
Pt-Etek	3.4	55.3	-	19.8	-

Figure 5-3 shows XRD patterns of Pd-Co catalysts synthesized without heat treatment in H_2. No shift in Pd peak positions were observed before heat treatment in any catalyst, which suggests that heat treatment is necessary to form a Pd-Co alloy. This was confirmed by the Pd-Pd bond distance for all untreated catalysts (Table 5-2), for PdCo-EG11, Pd_4Co-EG11, Pd(Co)-EG11 and Pd_4(Co)-EG11 which were 0.5753, 0.5748, 0.5748 and 0.5746 nm, respectively. All of them could be considered to have a crystal lattice like pure palladium. No diffraction peaks corresponding to pure Co crystals were revealed in the XRD patterns. The peak for the crystal face (111) of face-centered cubic cobalt would be at a diffraction angle of 44.2º: no signal at this angle appeared in the diffractograms as can be seen in Figure 5-3. This behavior agrees with the results reported by Zhang et al. [6], who found that reducing Pd and Co salts on carbon required heat treatment to form a single-phase Pd–Co alloy.

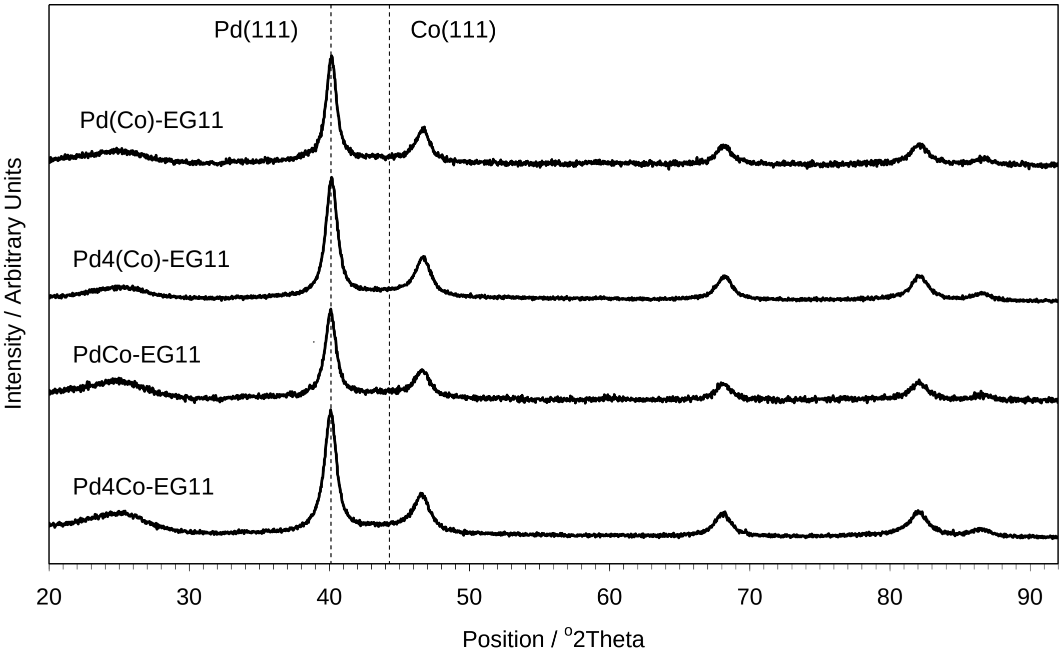

Figure 5-3: X-ray diffraction patterns of carbon-supported Pd-Co catalysts prepared by ethylene glycol reduction.

Figure 5-4 shows the XRD patterns of Pd-Co catalysts synthesized after heat treatment in H_2. After heat treatment, both PdCo-EG11-300 and Pd(Co)-EG11-300 showed the typical face-centered cubic pattern with diffraction angles shifting to higher positions compared to those of Pd/C. Pd-Pd bond distances were 0.2739 and 0.2743 nm, respectively. Shift in the position of diffraction peaks towards higher angles indicates the formation of a Pd-Co alloy. The palladium lattice contracts due to the replacement of some of Pd atoms with Co. Shifts in the peak position in catalysts with low Co content, Pd_4Co-EG11-300 and Pd_4(Co)-EG11-300, could not be considered significant because the difference in the average Pd-Pd bond distance value for all Pd/C was not larger than 0.0006 nm. Distances were 0.2747 and 0.2745 nm, respectively. The lack of confirmation of the alloy presence was probably due to the small magnitude of the increase in the diffraction angle, caused by a very small amount of Co introduced in the palladium lattice.

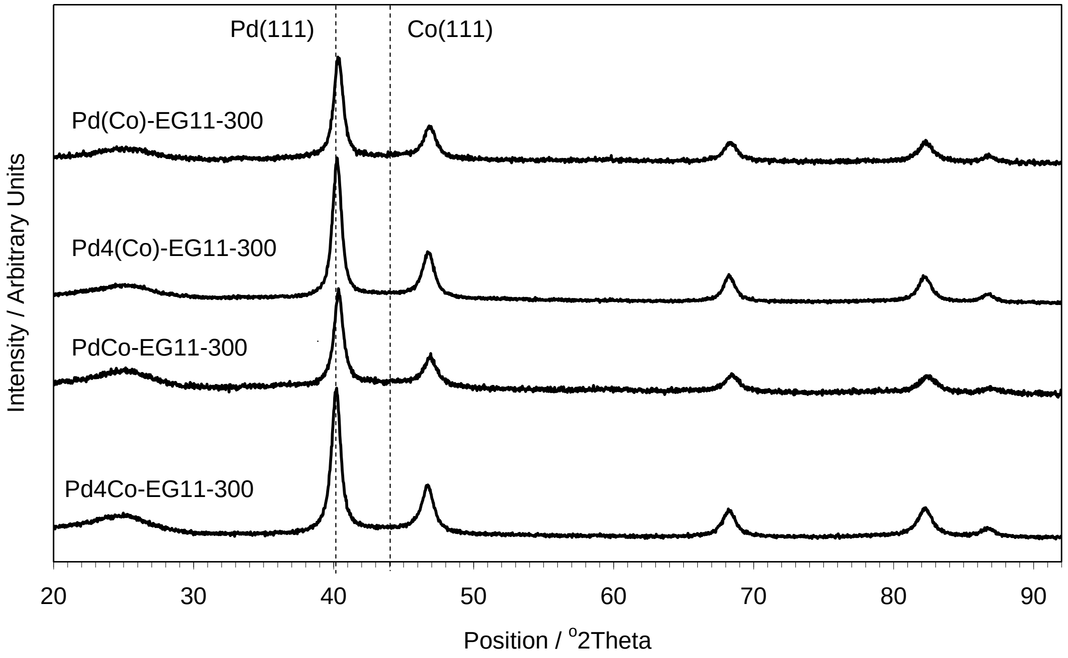

Figure 5-4: X-ray diffraction patterns of carbon-supported Pd-Co catalysts after heat treatment in H_2 at 300 °C.

Particle sizes calculated from the XRD patterns for Pd(Co)-EG11 and Pd_4(Co)-EG11, were similar to each other (8 and 7 nm, respectively) and equal to the values estimated for PdCo-EG11 and Pd_4Co-EG11 (8 and 7 nm, respectively). From the latter observation it could be concluded that the amount of Co salt present when the Pd salt was reduced in EG did not affect the crystallite size of the reduced Pd.

The study of the particle size after heat treatment in H_2 at 300 °C showed that heat treatment had the same effect on catalysts prepared by co-deposition and catalysts prepared on-Pd/C. Catalysts with low Co content, Pd_4Co-EG11 and Pd_4(Co)-EG11, suffered a larger particle growth, from ca. 7 to 10 nm in both cases; catalysts with higher Co content, PdCo-EG11 and Pd(Co)-EG11, had an average particle size of ca. 8 nm, both before and after heat treatment (Table 5-2). For pure Pd the increase in the particle size was much more extreme; particles for Pd/C-EG11 were calculated to be approximately 7 nm and for Pd/C-EG11-300 were approximately 17 nm, as reported in the previous chapter. The presence of Co seemed to depress the sintering degree of Pd particles, and the higher the atomic ratio the smaller the particle growth. This finding, i.e. the depression of particle growth when a second metal is present, agrees with earlier observations by Tarasevich et al. [12] for Pd-Fe catalysts.

5.2.3. Physicochemical characterization of palladium-iron catalysts

The metal content for each palladium-iron catalyst is shown in Table 5-3. The total metal content of catalysts prepared by simultaneous co-deposition of Pd and Fe was aimed at 20% weight; catalysts prepared on Pd/C had a higher metal content.

Table 5-3: Particle size, electrochemical surface area, Pd-Pd bond distance and metal content for palladium-iron electrocatalysts.

Catalyst	**Particle size (nm)**	**ECSA (m^2 g^{-1})**	**Pd-Pd bond distance (nm)**	**Metal content (% weight)**	**Atomic ratio (Pd:Metal)**
PdFe-EG11	11.1	6.8	0.2749	13.6 Pd, 4.7 Fe	1:0.7
PdFe-EG11-300	11.4	4.6	0.2745	13.6 Pd, 4.7 Fe	1:0.7
Pd_3Fe-EG11	8.6	10.6	0.2747	18.8 Pd, 3.1 Fe	1:0.3
Pd_3Fe -EG11-300	10.1	8.7	0.2742	18.8 Pd, 3.1 Fe	1:0.3
PdFe-H_2-500	7.1	4.9	0.2729	9.9 Pd, 5.9 Fe	1:1.1
Pd(Fe)-H_2-500	7.4	5.8	0.2729	22.9 Pd, 10.2 Fe	1:0.9
Pd_3Fe-H_2-500	8.0	10.8	0.2729	15.8 Pd, 2.7 Fe	1:0.3
Pd_3(Fe)-H_2-500	9.0	7.2	0.2727	25.9 Pd, 4.2 Fe	1:0.3
Pd-EG11-untr	7.3	14.6	0.2751	22.5	-
Pt-Etek	3.4	55.3	-	19.8	-

No palladium-iron catalyst prepared by reduction with ethylene glycol showed any shift in the position of the XRD diffractions patterns, compared to Pd/C (Figure 5-5), before heat treatment at 300 ºC in H_2 atmosphere. This was confirmed by their Pd-Pd bond distances (Table 5-3) for PdFe-EG11, and Pd_3Fe-EG11 which were 0.5749 and 0.5747 nm, respectively. This suggested the no palladium-iron alloy was formed, at least in an extent identifiable by XRD.

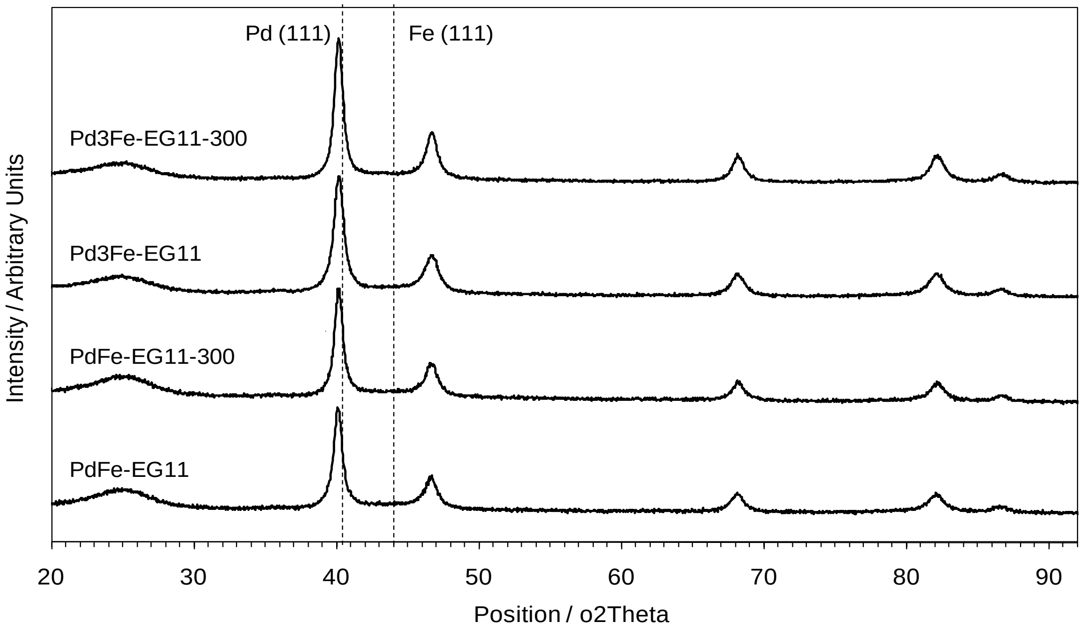

Figure 5-5: X-ray diffraction patterns of carbon-supported Pd-Fe catalysts prepared by EG reduction.

Although ethylene glycol reduction at 110 ºC did not prove to be able to introduce iron atoms in the palladium lattice, a high background (high baseline) can be seen in the diffractograms (Figure 5-6), which indicates the presence of the transition metal in the sample. This high background was caused by the fluorescence scattering occurring when the Cu radiation hits the Fe atoms [13]. The EDXA analysis (Table 5-3) confirmed the presence of Fe. PdFe-EG11 and Pd_3Fe-EG11 had an iron content of 40 and 23% atomic ratio, respectively. The lack of shift in the Pd patterns and the absence of Fe or iron oxide peaks in the diffractograms can be explained by the presence of Fe in an amorphous form.

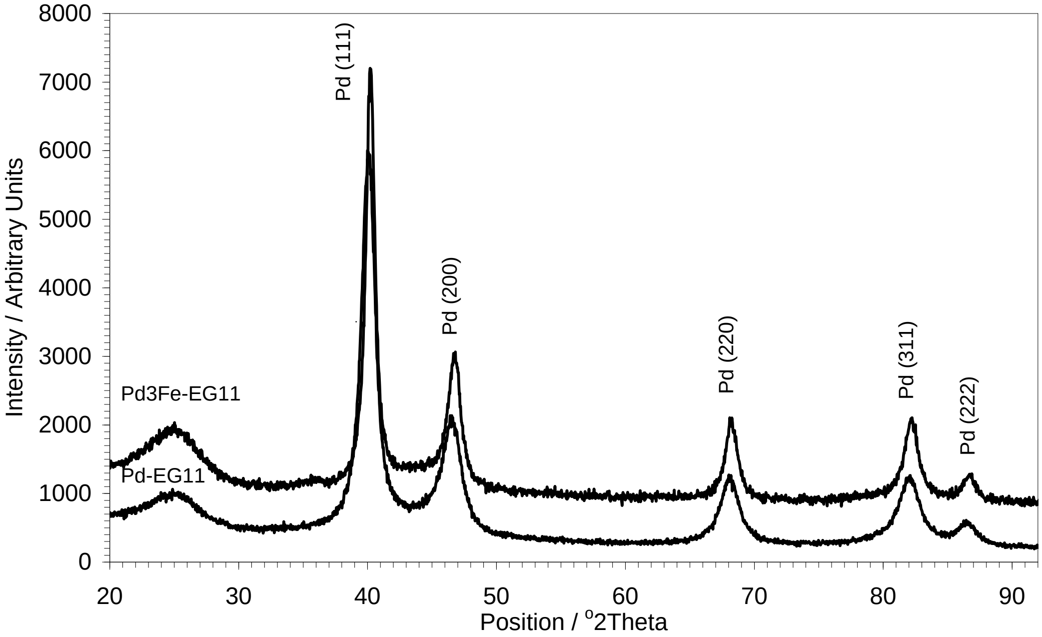

Figure 5-6: Comparison of X-ray diffraction patterns of PdFe-EG11 and Pd-EG11 catalysts.

When palladium-iron catalyst prepared by reduction with ethylene glycol were treated in H_2 at 300 ºC, small differences were seen in the position of the peaks in the XRD diffractions patterns. Pd-Pd bond distance values calculated from the Bragg equation were 0.2745 and 0.2742 nm for PdFe-EG11-300 and Pd_3Fe-EG11-300, respectively. According to the criteria previously established for consideration of an alloy, the Pd-Pd bond distance should be outside the interval 0.2751 ± 0.0006 nm; the bond distance of PdFe-EG11-300 (0.2745 nm) was included in that interval, and therefore we could not affirm that an alloy was obtained. However, the slow scan cyclic voltammogram differed slightly from the voltammogram expected for Pd/C, as discussed in the following section. However, the bond distance in Pd_3Fe-EG11-300 was significantly different compared to Pd/C. Although it has been reported that temperatures higher than 300 ºC were necessary to form a Pd-Fe alloy [12, 14], the bond distance proved that Fe atoms were introduced into the palladium lattice. This value of 0.2742 nm was similar to the Pd-Pd distances reported by Shao et al. for Pd_2Fe/C and PdFe/C [14]. Although it is believed that part of the palladium had Fe introduced in its lattice, because of the decrease in the Pd-Pd bond distance, the presence of any of these metal phases could not be proved. Only the presence of iron oxide could be confirmed from the cyclic voltammograms, further analysis would be necessary to determine the presence of iron in its reduced form.

All Pd-Fe catalysts prepared by reduction in H_2 at 500 ºC showed a typical face-centered cubic pattern with diffraction angles clearly shifted to higher positions compared to those of Pd/C (Figure 5-7). The shift of diffraction peak positions towards higher angles indicates the formation of a Pd-Fe alloy. Since Fe atoms are smaller than Pd, the palladium lattice contracts when part of the palladium is replaced with iron. This was confirmed by the Pd-Pd bond distance of each catalyst showed in Table 5-3: 0.2729, 0.2729, 0.2729 and 0.2727 nm for PdFe-H_2-500, Pd_3Fe-H_2-500, Pd(Fe)-H_2-500 and Pd_3(Fe)-H_2-500, respectively. According to the phase diagram for Pd-Fe [11], an ordered face-centered cubic Pd_3Fe phase forms at ca. 20 to 30% atomic Fe. The bond distance for this phase was reported to be 0.2730 nm by Shao et al. [14], a value similar to that observed in this work.

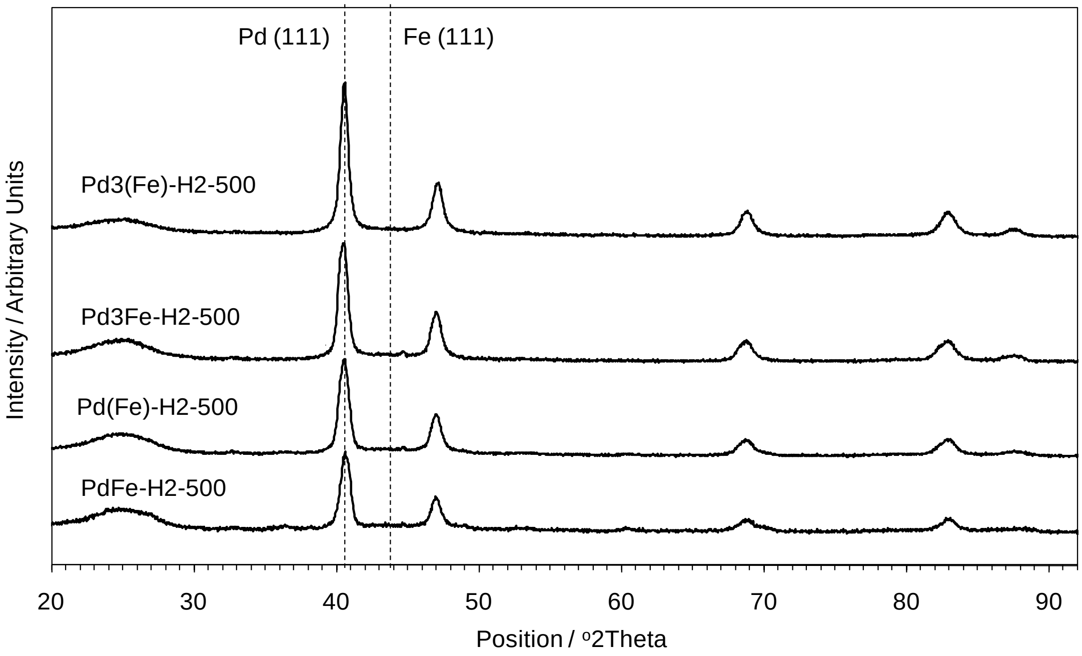

Figure 5-7: X-ray diffraction patterns of carbon-supported Pd-Fe catalysts prepared by reduction in H_2 at 500 ºC.

No patterns for face-centered cubic iron phase, maximum intensity diffraction peak at 43.47º, or any other crystal phase showed in the X-ray diffractograms. Thus it was concluded that any Fe not introduced in the Pd lattice during heat treatment may have remained in the catalyst as an amorphous iron oxide. Previous investigations in the synthesis of Pd-Fe nanoparticles by Tarasevich et al. [12] showed that a fraction of the iron exists on the surface as compounds of hydrated Fe_2O_3.

No differences in XRD patterns were observed between catalysts prepared by simultaneous deposition of Pd and Fe salts and catalysts synthesized on Pd/C. However, difference in the ORR activity were observed as discussed in Section 5.4.3.

Pd-Fe catalysts synthesized by EG reduction presented low variability in their particle sizes, calculated to be between 9 and 11 nm (Table 5-3). It is interesting to note that hardly any sintering was observed after treatment in H_2 at 300 ºC. PdFe-EG11 had 11 nm particles both before and after treatment; Pd_3Fe-EG11 had 9 nm particles before and 11 nm after heat treatment. This behavior differed to that observed for Pd/C, which suffered larger sintering, and agreed with previously observations for Pd-Au and Pd-Co catalysts, which also exhibited smaller sintering than Pd after heat treatment. The presence of a second metal depressed the degree of sintering. Sintering extent decreased with increasing Fe content.

Catalysts prepared by reduction in H_2 at 500 ºC surprisingly had the smaller particle sizes, as they were prepared at higher temperatures. PdFe-H_2-500 and Pd(Fe)-H_2-500 had particles of ca. 7 nm, particles for Pd_3Fe-H_2-500 and Pd_3(Fe)-H_2-500 were 8 and 9 nm, respectively. Larger particles of catalysts with lower Fe content confirmed previous observations for catalysts prepared using EG: the larger the amount of Fe atoms in the palladium lattice the smaller the particle size increase with temperature. The smaller particles in catalysts subjected to higher temperatures during synthesis may be due to a larger proportion on Fe in the Pd lattice, responsible for depressing sintering.

5.2.4. Physicochemical characterization of palladium-titanium catalysts

Table 5-4 shows the metal content, particle size and Pd-Pd bond distance for each palladium-titanium catalyst. The total metal content of catalysts prepared by simultaneous co-deposition of Pd and Ti was aimed at 20% weight; catalysts prepared on Pd/C had higher metal content.

Table 5-4: Particle size, electrochemical surface area, Pd-Pd bond distance and metal content for palladium-titanium electrocatalysts.

Catalyst	Particle size (nm)	ECSA (m^2 g^{-1})	Pd-Pd bond distance (nm)	Metal content (% weight)	Atomic ratio (Pd:Metal)
PdTi-EG11	7.2	10.7	0.2748	14.0 Pd, 3.8 Ti	1:0.7
PdTi-EG11-300	16.3	6.3	0.2747	14.0 Pd, 3.8 Ti	1:0.7
Pd_9Ti-EG11	6.9	15.5	0.2751	20.0 Pd, 1.2 Ti	1:0.14
Pd_9Ti-EG11-300	15.0	7.7	0.2745	20.0 Pd, 1.2 Ti	1:0.14
PdTi-H_2-900	24.6	0.75	0.2748	10.6 Pd, 9.3 Ti	1:1.9
Pd(Ti)-H_2-900	26.7	1.1	0.2747	22.8 Pd, 13.6 Ti	1:1.3
Pd_9Ti-H_2-900	24.6	1.7	0.2747	21.7 Pd, 1.3 Ti	1:0.16
Pd_9(Ti)-H_2-900	22.9	2.9	0.2746	21.9 Pd, 1.3 Ti	1:0.13
Pd-EG11-untr	7.3	14.6	0.2751	22.5	-
Pt-Etek	3.4	55.3	-	19.8	-

No palladium-titanium catalysts prepared by ethylene glycol reduction showed any significant shift in the position of XRD diffractions patterns, compared to Pd/C, before or after heat treatment at 300 ºC in H_2. Thus, no significant changes in the Pd lattice were observed. This was concluded from their Pd-Pd bond distances calculated from the XRD patterns (Table 5-4), for PdTi-EG11, PdTi-EG11-300, Pd_9Ti-EG11 and Pd_9Ti-EG11-300 which were 0.2748, 0.2747, 0.2751 and 0.2745 nm, respectively. Some of the figures, in particular those corresponding to Pd_9Ti-EG11 and Pd_9Ti-EG11-300, could indicate some changes in the lattice; but as it was established that significant changes were those over 200% of the error around the Pd/C (0.2751 ± 0.0006 nm Pd-Pd bond), they were not taken as significant changes.

Figure 5-8 shows the XRD patters of all palladium-titanium catalysts prepared by ethylene glycol reduction. At first sight only the typical face-centered cubic pattern for palladium could be observed, but on closer inspection, the XRD pattern for TiO_2 in its anatase form could be seen in PdTi-EG11 and PdTi-EG11-300, catalysts with higher Ti content (1:0.7 Pd:Ti). The highest intensity diffraction peak for anatase, plane (101), appeared at a diffraction angle at ca. 25.28° [15]; the broad peak generated by the carbon support also appeared at ca. 25°, overlapping the anatase signal. The second peak in intensity of anatase, 35%, is (200) at 48.05°, which was partially overlapped by Pd (200) at 46.66°. Therefore, in catalysts with very low Ti content it was difficult to identify the presence of anatase.

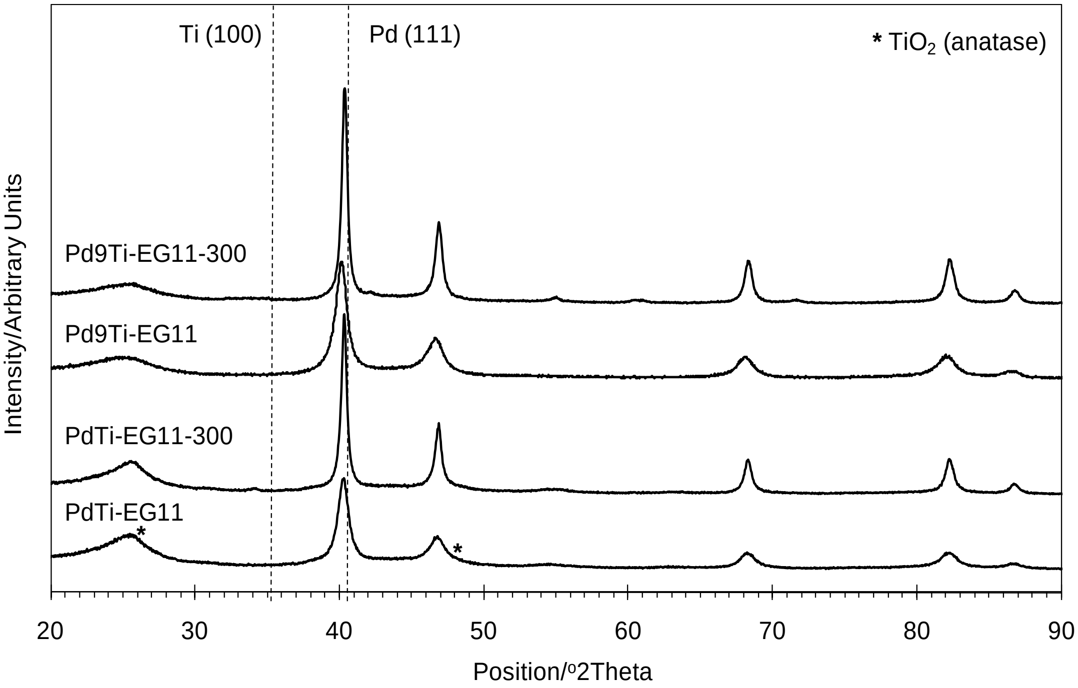

Figure 5-8: X-ray diffraction patterns of carbon-supported Pd-Ti catalysts prepared by ethylene glycol reduction.

Catalysts prepared by reduction in H_2 at 900 ºC, either prepared on Pd/C or with both metals co-deposited exhibited no significant differences in the Pd-Pd bond distance compared to the average Pd/C. Bond distances calculated from XRD patterns (Table 5-4), were 0.2748, 0.2747, 0.2747 and 0.2746 nm for PdTi-H_2-900, Pd(Ti)-H_2-900, Pd_9Ti-H_2-900 and Pd_9(Ti)-H_2-900, respectively. Although no catalysts showed a change in the Pd-Pd bond distance that we could consider meaningful according to selected criteria, the average Pd-Pd bond distance for catalysts synthesized by reduction in H_2 at 900 ºC was 0.2747 nm (lower than that of Pd/C). This may indicate the insertion of some Ti in the Pd lattice. The preparation of Pd-Ti alloy by heat treatment at 900 ºC in a hydrogen atmosphere was already claimed by Fernández et al. [3]. They supported their claim on small shifts in the position of the reflections corresponding to the face-centered cubic lattice of palladium; they also reported the presence of small amounts of anatase. Therefore, the presence of some Pd-alloy could not be completely ruled out.

XRD patterns for PdTi-H_2-900 and Pd(Ti)-H_2-900, with atomic ratios 1:0.16 and 1:0.13 Pd:Ti, are shown in Figure 5-9 and Figure 5-10, respectively. For both catalysts XRD patterns of TiO_2 in its anatase form were obvious. On the other hand, the anatase patterns could not be seen in catalysts with low Ti content, Pd_9Ti-H_2-900 and Pd_9(Ti)-H_2-900, 1:0.16 and 1:0.13 Pd:Ti, respectively. The only difference observed between catalysts synthesized by the different reducing agents with low titanium content was the palladium particles size.

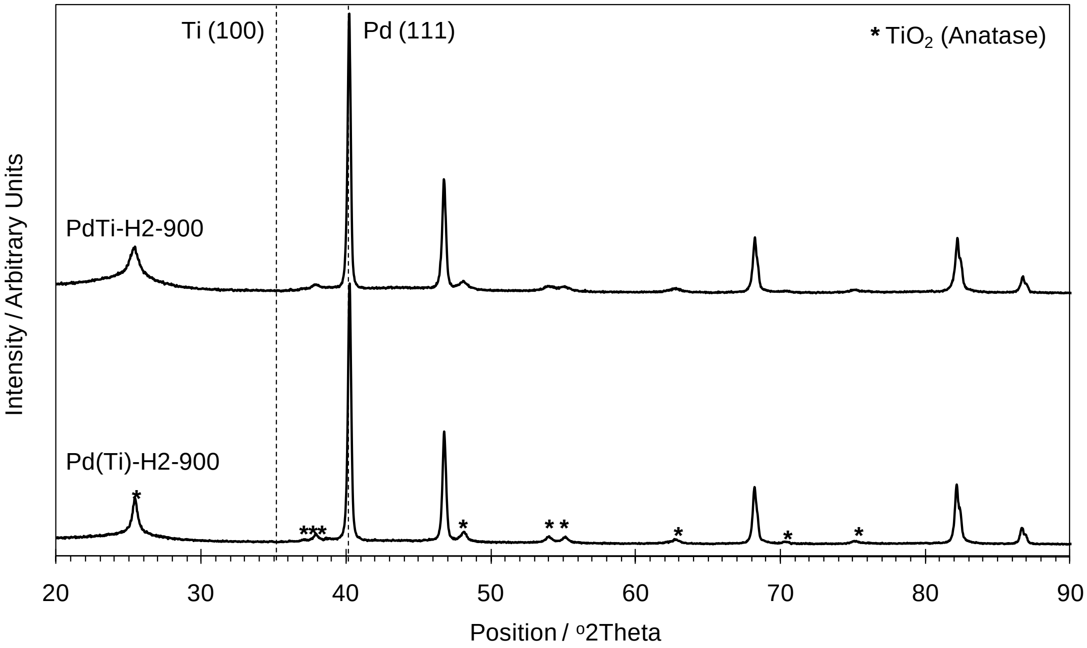

Figure 5-9: X-ray diffraction patterns of carbon-supported Pd-Ti catalysts prepared by reduction in H_2 at 900 °C with atomic ratio Pd:Ti 1:1.

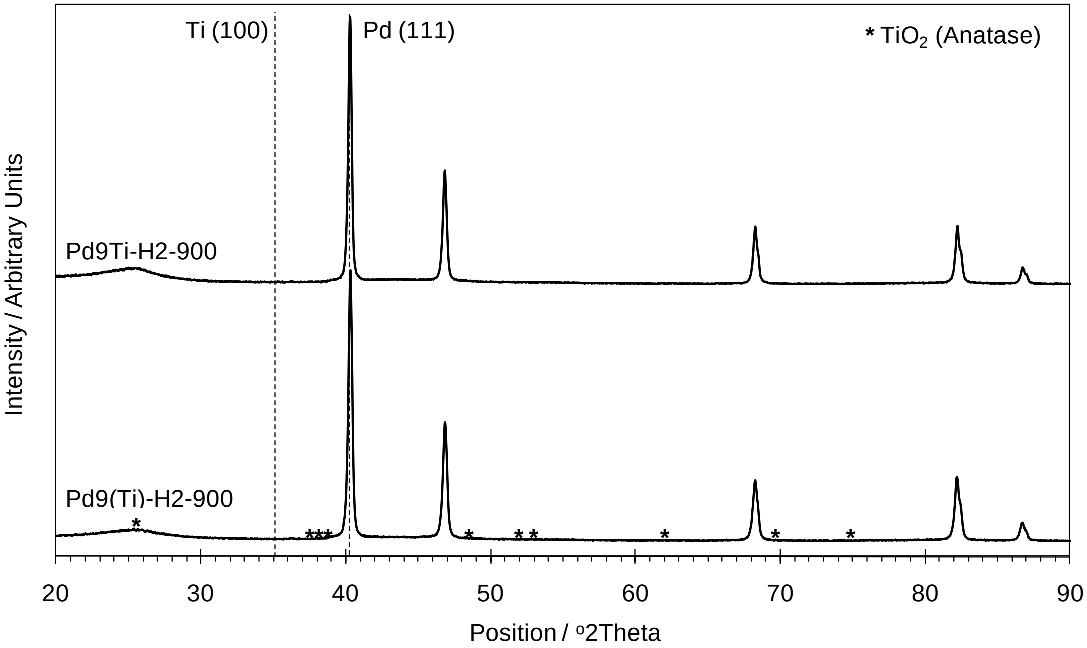

Figure 5-10: X-ray diffraction patterns of carbon-supported Pd-Ti catalysts prepared by reduction in H_2 at 900 °C with atomic ratio Pd:Ti 9:1.

Particle sizes calculated from the Pd (220) peak are shown in Table 5-4. Particle size for catalysts prepared by EG reduction were 7, 16, 7 and 15 nm for PdTi-EG11, PdTi-EG11-300, Pd_9Ti-EG11 and Pd_9Ti-EG11-300, respectively. It was interesting to notice that the presence of titanium or titanium oxide did not depress the sintering of the palladium nanoparticles, during the treatment in H_2 at 300 ºC. The particle growth after treatment, for both low and high titanium content catalysts, had the same magnitude in growth suffered by pure Pd/C discussed in Chapter 4. In the other three sets of bimetallic catalysts, Pd-Au, Pd-Co and Pd-Au, a substantial reduction in the Pd particle growth after heat treatment was observed when the second metal was added. This was not the case for Pd-Ti catalysts.

Palladium titanium catalysts synthesized by H_2 reduction at 900 ºC had very large Pd particles, 25, 27, 25, 23 nm, for PdTi-H_2-900, Pd(Ti)-H_2-900, Pd_9Ti-H_2-900 and Pd_9(Ti)-H_2-900, respectively. The elevated temperature of the reduction produced large Pd crystallites and that led to low surface area, as will be discussed in the following section.

5.3. Electrochemical characterization of carbon-supported bimetallic nanoparticles

The ECSA for every bimetallic combination has been quantified by the charge of the oxygen reduction peak [13, 16], from slow cyclic voltammograms, as explained in chapter 4. Electrochemical surface areas are expressed in $m^2\ g^{-1}$ of metal. Values are tabulated and compared with the ECSA of the previously prepared Pd/C-EG11.

5.3.1. Electrochemical characterization of palladium-gold catalysts

Electrochemical surface area values for palladium-gold catalysts are compared in Table 5-1. ECSA values were calculated from the palladium oxide reduction peak, which has been reported to be linked to oxygen desorption from both Pd and Au surface atoms constituting one phase [17].

For both PdAu-EG11 and PdAu-EG11-300, the ECSA could not be determined due to the dramatic decrease of the palladium oxide reduction peak after the initial fast cycles (Figure 5-11A and B). During the first few potential cycles their electrochemical behaviour was close to this of a pure Pd electrode (Section 4.3). On the positive sweep, only current corresponding to the double layer charging current was recorded in the potential range from ca. 0.30 to 0.80 V vs NHE; oxygen chemisorptions started above ca. 0.80 V. In the negative potential sweep, reduction of the oxide layer started at potentials close to 0.95 V, the oxide reduction peak was located at ca. 0.80 V. From ca. 0.60 V to 0.30 V only the double layer charging current was observed in the cathodic sweep. At a electrode potential below ca. 0.30 V a cathodic current was recorded; this current was attributed to, initially, hydrogen adsorption on the palladium surface and, at lower potentials, to the dissolution of hydrogen in the bulk of the palladium, as previously discussed for the Pd electrode. It was also observed that oxygen and hydrogen adsorption and desorption peaks were less pronounced on the heat treated catalyst (PdAu-EG11-300); this was attributed to a larger amount of gold on the catalyst surface indicating a more uniform alloy. After the initial electrode conditioning of ten cycles in N_2 saturated solution at scan rate 50 mV s^{-1}, the electrode response lost its palladium electrochemical character and the voltammogram exhibited the electrochemical characteristics of a pure gold electrode, where no oxidation or reduction currents could be observed when the potential is cycled between 0.04 and 1.24 V vs NHE [18]. These observations suggest that the electrochemical conditioning of Pd-Au alloy electrodes in acid electrolyte, containing ca. 60% at Au, leads to a gold-like behavior. Similar behavior was previously reported by Damjanovic et al. for gold-rich palladium alloys treated with concentrated hydrochloric acid [19]. Łukaszewski et al. also reported that the voltammograms of Pd-Au alloys suffer significant changes during potential cycling in acid media, this is believed to be due to the selective dissolution of Pd [17].

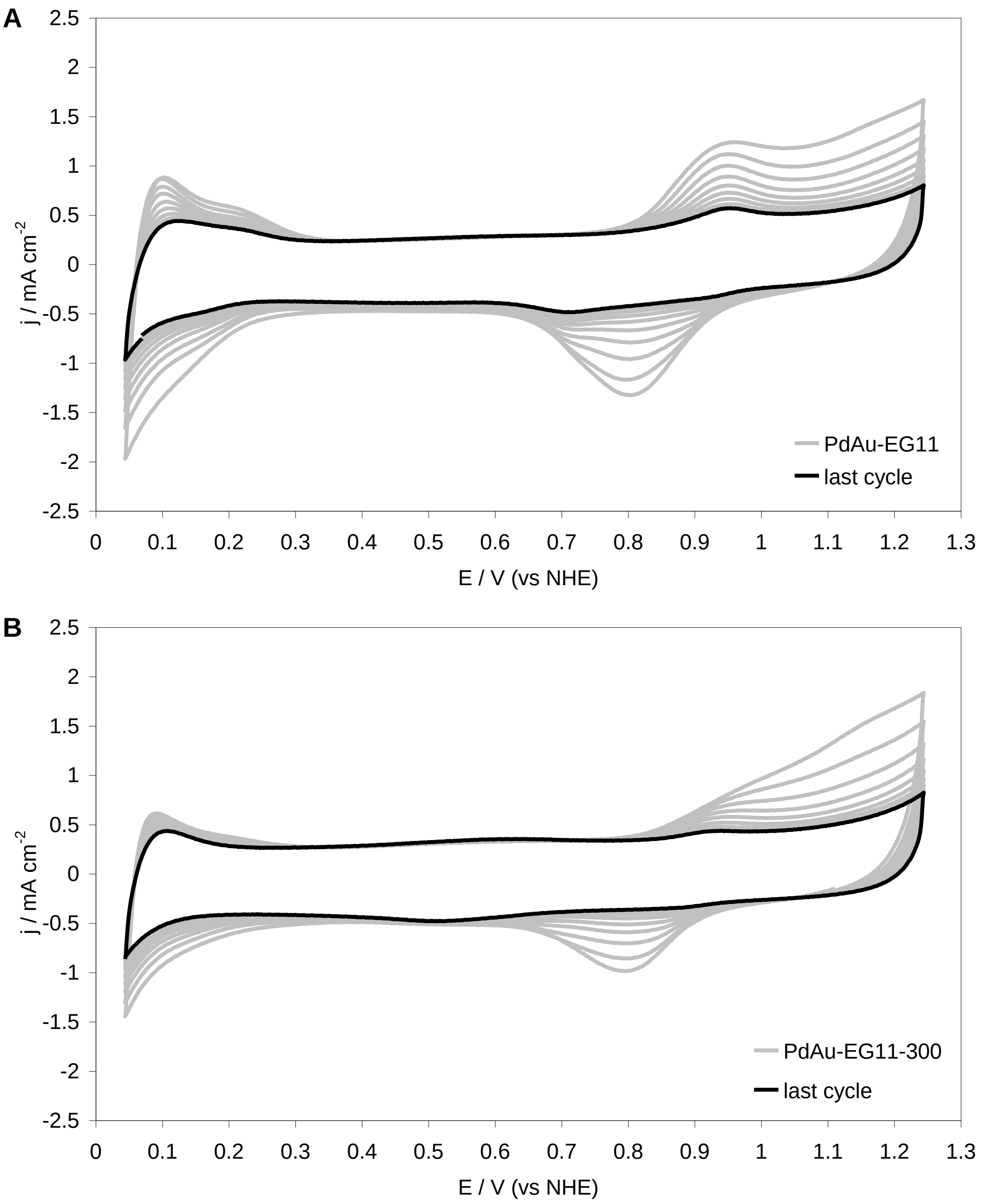

Figure 5-11: Fast scan cyclic voltammograms of carbon-supported Pd-Au catalysts A) PdAu-EG11 and B) PdAu-EG11-300.

Pd anodic dissolution starts at potentials close to 0.96 V in sulphuric acid solution while Au dissolution does not occur at potentials below ca. 1.5 V [20]; therefore the electrode conditioning would cause the dissolution of the Pd from the alloy surface. The stirring caused by the N_2 bubbles and the large electrolyte to catalyst ratio would lead to a very low palladium re-deposition rate at cathodic potentials leaving a gold-rich electrode surface. The study of the ORR on the electrode surface confirmed the hypothesis of the gold rich surface (Section 5.4.1).

When the atomic ratio of Pd:Au was changed from 1:1.4 to 1:0.14 for Pd_9Au-EG11 and Pd_9Au-EG11-300, respectively, the decrease in the area under the palladium oxide reduction peak during the initial fast potential cycles still occurred. However, the extension of this decrease was smaller compared to PdAu-EG11 and PdAu-EG11-300 (Figure 5-12A and B). From the X-ray diffraction patterns it was concluded that in both catalysts several metal phases were present, therefore the decrease in the reduction peak could be due to the dissolution of Pd from the surface of the Pd-Au phase leaving a gold-rich surface. The palladium phase would also suffer dissolution but the decrease in the area would be insignificant in only a few potential cycles. The overall result was a smaller loss in the ECSA than in the catalysts with high Au content. That would agree with the data for catalysts prepared on Pd/C (Figure 5-13 and Figure 5-14), with low degree of Pd-Au alloy formation, presenting a small decrease in the Pd oxide reduction peak during the initial conditioning.

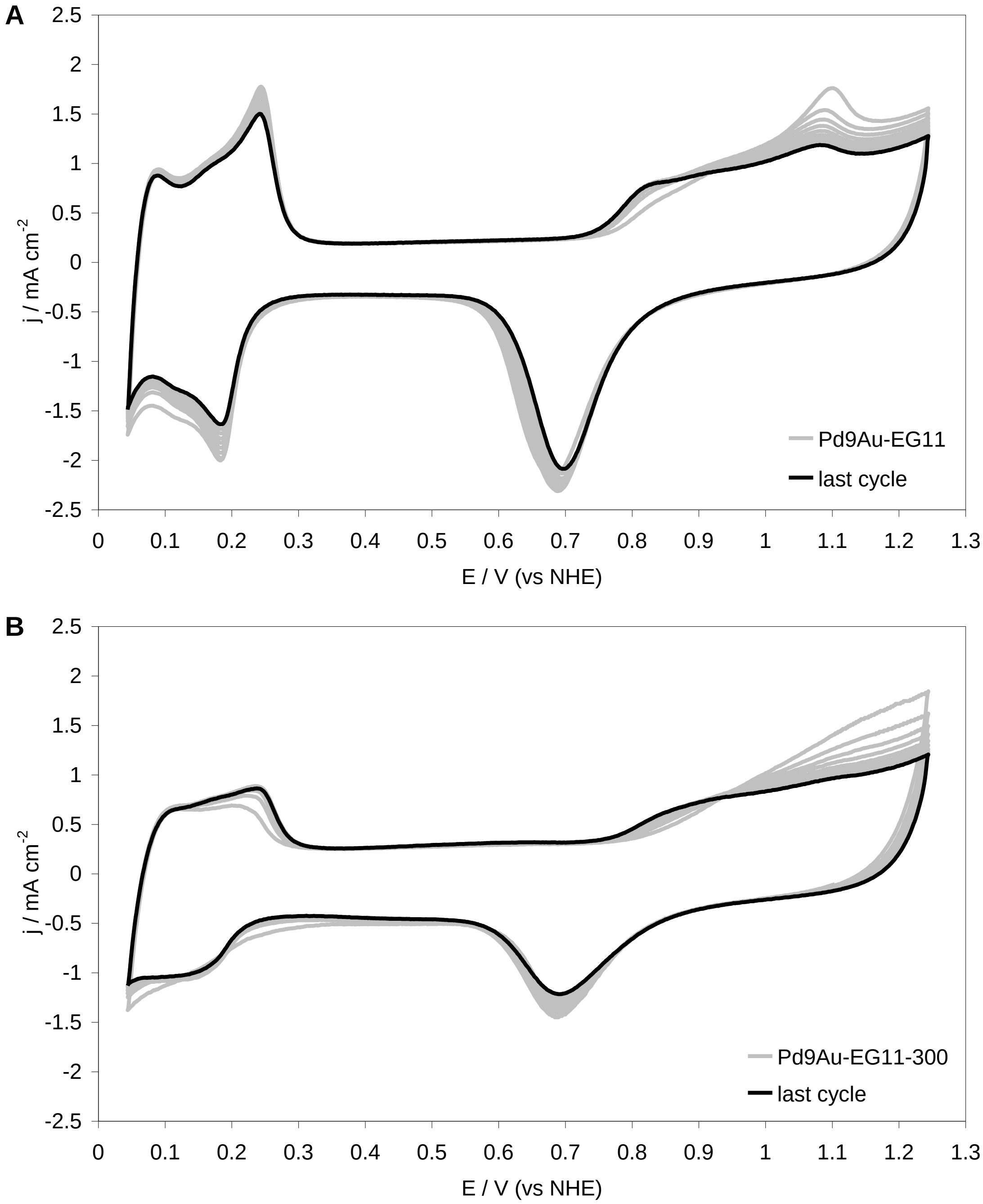

Figure 5-12: Fast scan cyclic voltammograms of carbon-supported Pd-Au catalysts A) Pd_9Au-EG11 and B) Pd_9Au-EG11-300.

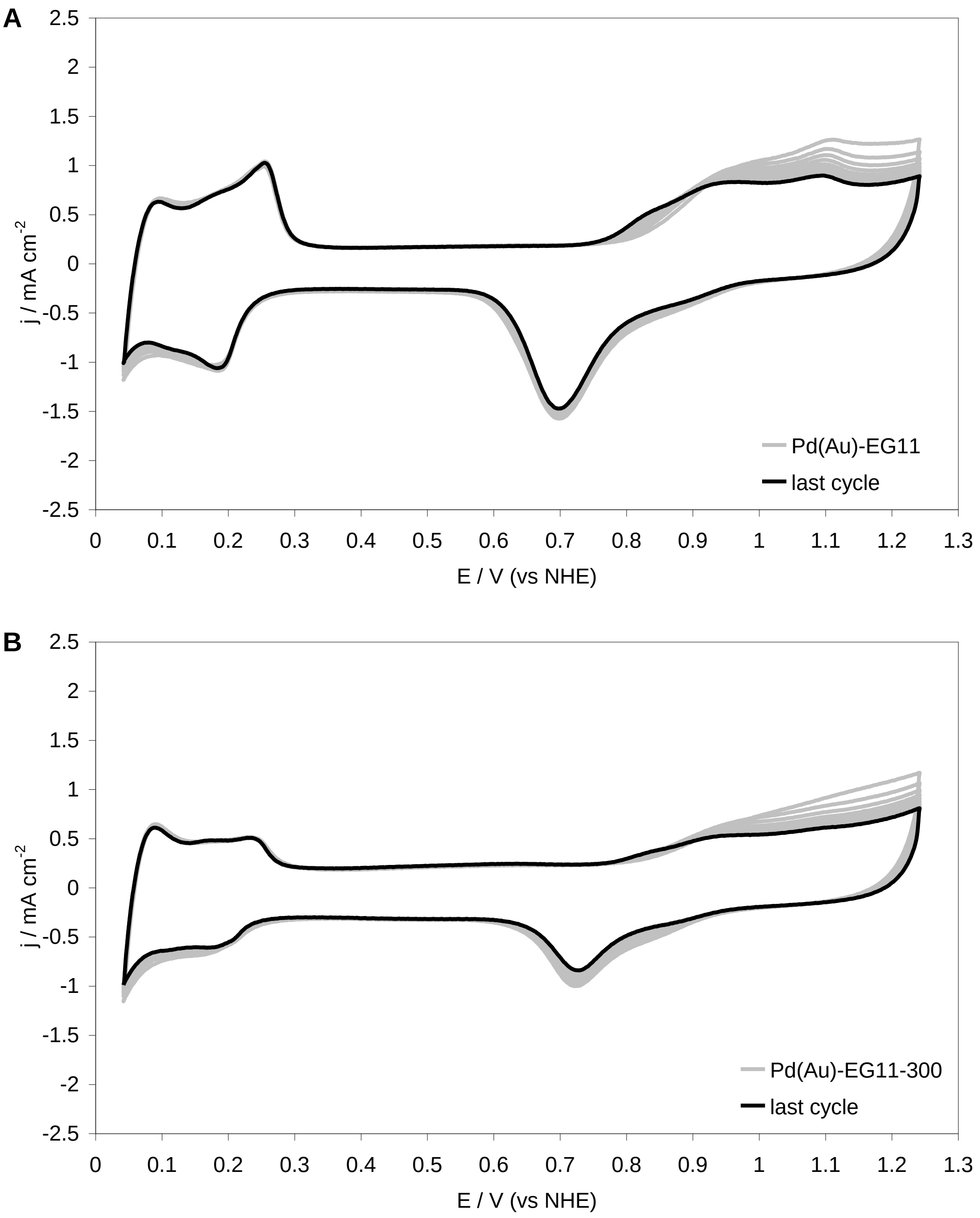

Figure 5-13: Fast scan cyclic voltammograms of carbon-supported Pd-Au catalysts A) Pd(Au)-EG11and B) Pd(Au)-EG11-300.

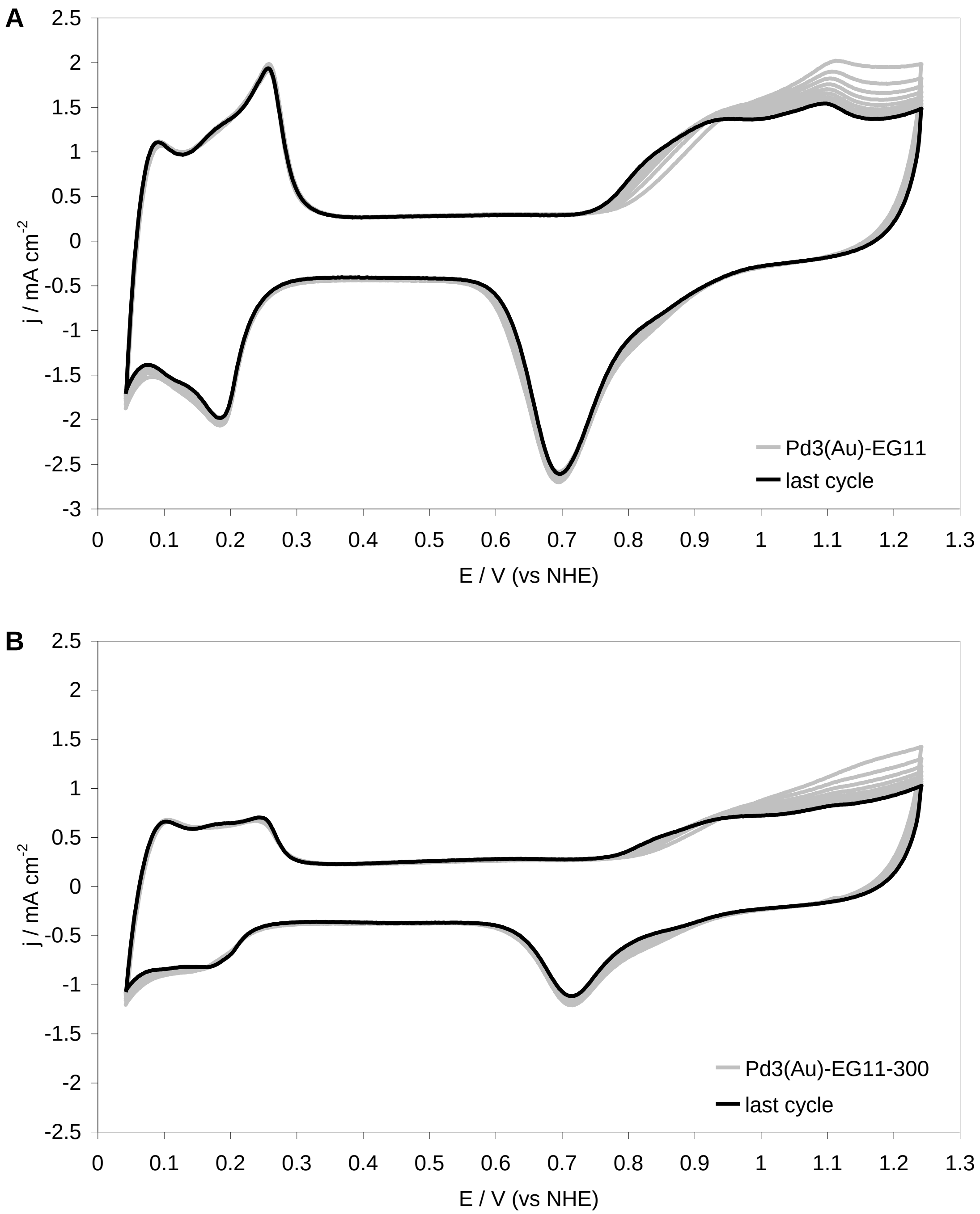

Figure 5-14: Fast scan cyclic voltammograms of carbon-supported Pd-Au catalysts A) Pd_3(Au)-EG11 and B) Pd_3(Au)-EG11-300**.**

ECSA values were calculated from the CVs at a scan rate 5 mV s^{-1}; these voltammetries were recorded after the initial ten fast cycles in each case. Therefore, voltammograms for different electrocatalysts were compared even though some of them had not reached a steady state voltammogram. The slow scan rate voltammograms for Pd-Au catalysts are compared in Figure 5-15A when prepared by co-deposition and Figure 5-15B, when prepared on Pd/C, respectively.

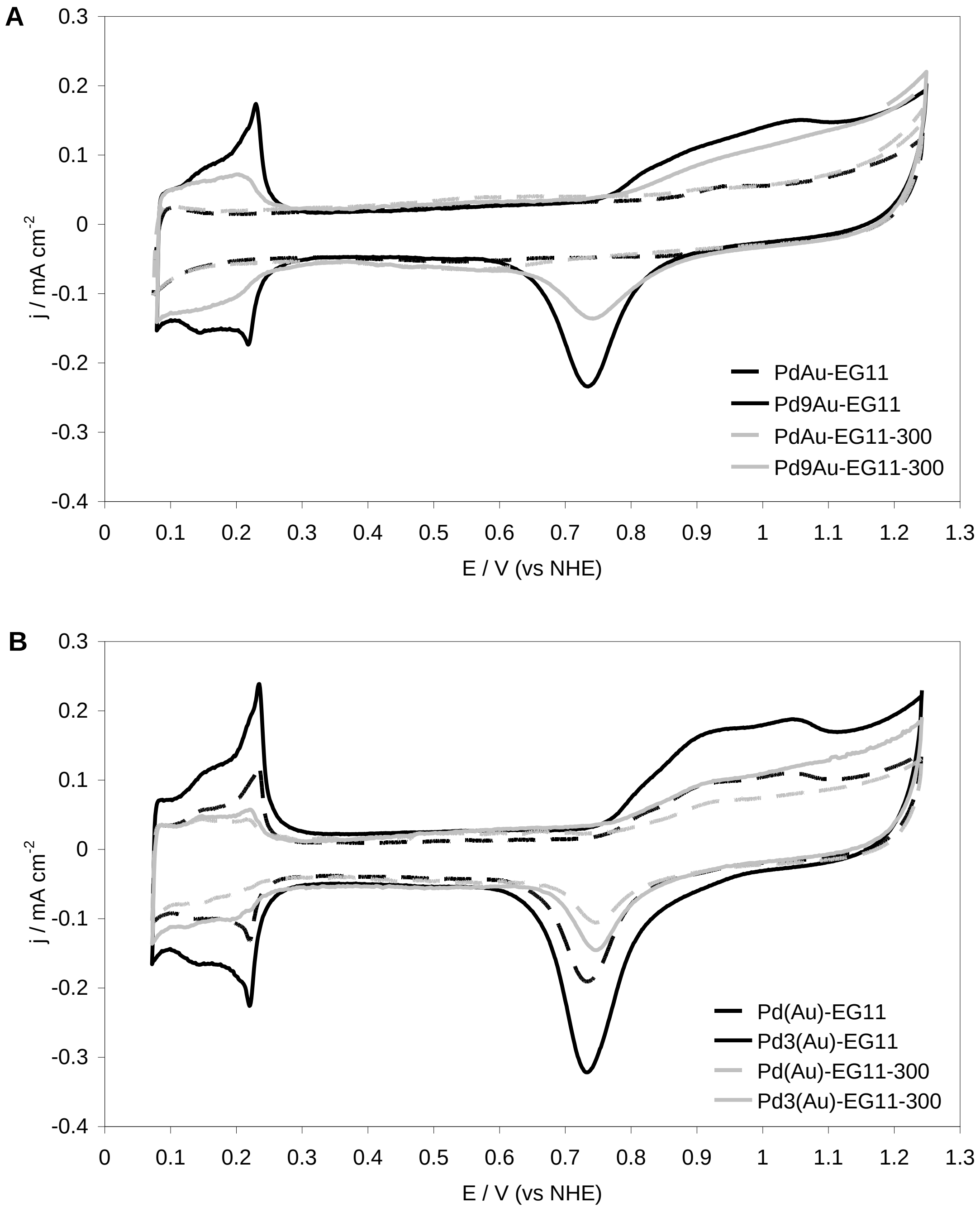

Figure 5-15: Cyclic voltammograms of carbon-supported Pd-Au catalysts prepared A) by co-deposition of Pd and Au salts on carbon and B) on Pd/C.

In Figure 5-15A can be observed that co-deposited electrocatalysts with high gold content (PdAu-EG11 and PdAu-EG11-300) exhibited a gold-like behavior, no oxidation or reduction currents could be observed when the potential is cycled between 0.04 and 1.24 V vs NHE. For low Au content (Pd_9Au-EG11 and Pd_9Au-EG11-300) anodic and cathodeic currents were observed in the oxygen and hydrogen regions; these currents were larger for Pd_9Au-EG11. When Au was deposited on Pd/C (Figure 5-15B) all catalysts exhibited oxygen and hydrogen adsorption/desorption currents; these been larger for catalysts with lower Au content and un-treated. The largest ECSA obtained by the co-deposition method was for Pd_9Au-EG11 (11 m^2 g^{-1}) whilst for catalysts prepared on Pd/C a maximum value of 8 m^2 g^{-1} was obtained for Pd_3(Au)-EG11. For Pd_3(Au)-EG11, particle sizes were approximately 6 nm for Pd and 13 nm for Au. The particle size of Pd_9Au-EG11 could not be estimated due to the overlapping of the peaks in the XRD patterns (Figure 5-1). Therefore the relationship between the particle size and the ECSA could not be discussed.

In every Pd-Au catalyst a large decrease in the ECSA was recorded after heat treatment in H_2 atmosphere. The decrease in area was greater than would be expected by the particle size increase. Pd_9Au-EG11 and Pd_3(Au)-EG11 lost approximately 60% of its ECSA after heat treatment, from 11 to 5 m^2 g^{-1} and 8 to 3 m^2 g^{-1}, respectively. For Pd(Au)-EG11 the decrease was over 80%, from 4 to 0.6 m^2 g^{-1}. The increase in the particle size, discussed in the previous paragraph, could not be the only cause of this large loss of ECSA. Thus, decrease of the ECSA was probably strongly affected by the increase in the degree of alloy. ECSA values were calculated from the oxide reduction peak; this peak does not appear in a gold electrode in the potential range studied. Therefore the more Au is introduced in the Pd lattice the higher the blockage to oxygen adsorption is on its surface and the smaller the area under the oxide reduction peak. Studies of the O_2 adsorption on Pd-Au alloys showed that adsorption is almost zero for Au content higher than 30% [2]. This would explain the extreme decrease in the surface area, of much larger magnitude than the increase in the particle size; the effect observed in the ORR activity was different, as discussed in Section 5.4.1.

A slight shift of the position of the palladium oxide reduction peaks after heat treatment was also observed. The position of the oxide reduction peak shifted with alloy formation due to a change in the catalyst properties. In Section 5.2.1 it was discussed how treatment in a H_2 atmosphere at 300 ºC increased the degree of alloy, to different extents, depending on the catalysts. The oxide reduction peak position shifted from ca. 0.73 to 0.74 V for Pd_9Au-EG11 to Pd_9Au-EG11-300, from ca. 0.73 to 0.745 V for Pd(Au)-EG11 to Pd(Au)-EG11-300 and from ca. 0.73 to 0.74 V for Pd_3(Au)-EG11 to Pd_3(Au)-EG11-300. This shift in the palladium oxide peak position with gold content of the electrode surface was reported by Łukaszewski et al. [17]. The shift in the position would also confirm the above mentioned change in the surface composition, towards a gold-richer surface; causing the dramatic ECSA decrease.

5.3.2. Electrochemical characterization of palladium-cobalt catalysts

Unlike palladium-gold catalysts, ECSA values for palladium-cobalt catalysts did not show dramatic differences with different metal ratios and synthetic methods, and no significant differences could be found within each synthetic method. Values of ECSA are compared in Table 5-2. Slow cyclic voltammetries for all palladium-cobalt catalysts prepared are shown in Figure 5-16. As a general trend, in all the Pd-Co voltammograms only current corresponding to the double layer charging current was observed in the positive sweep in the potential range from ca. 0.25 to 0.80 V vs NHE; oxygen chemisorptions started above ca. 0.80 V. In the negative potential sweep, reduction of the oxide layer started at potentials close to 0.85 V, the oxide reduction peak was located at ca. 0.75 V. From ca. 0.60 V to 0.25 V only the double layer charging current was observed in the cathodic sweep and a cathodic current was recorded from ca. 0.25 V; this current was attributed to hydrogen adsorption dissolution as previously discussed for the Pd electrode.

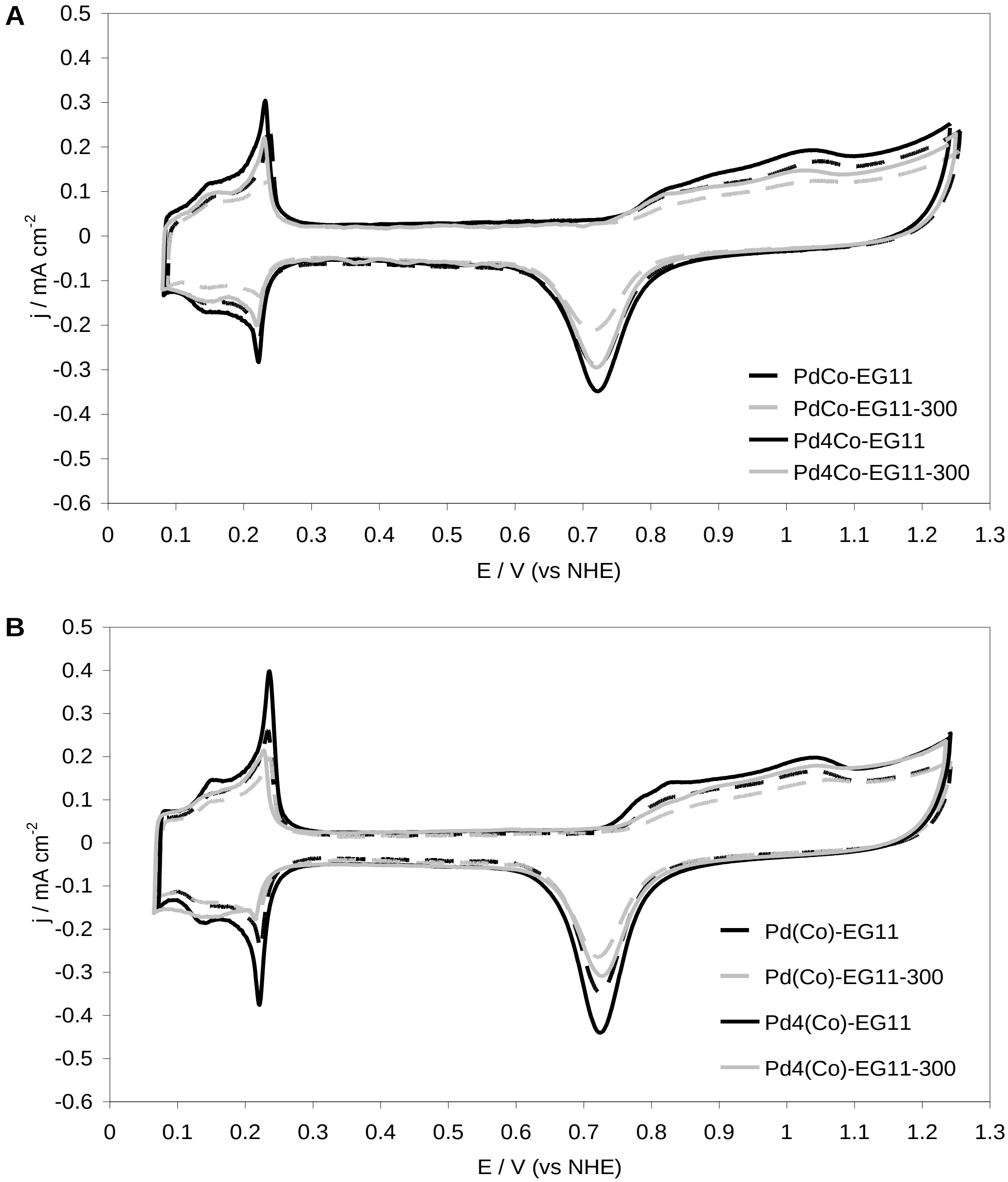

Figure 5-16: Cyclic voltammograms of carbon-supported Pd-Co catalysts prepared A) by co-deposition of Pd and Co salts on carbon and B) on Pd/C.

Catalyst prepared by co-deposition of Pd and Co salts, PdCo-EG11 and Pd_4Co-EG11, presented ECSA values of 12 and 14 m^2 g^{-1} and palladium contents of 12 and 20% weight, respectively. Electrochemical surface area of PdCo-EG11 was ca. 90% of the area of Pd_4Co-EG11, whilst the palladium content of PdCo-EG11 was ca. 60% of Pd_4Co-

EG11. The particle size was similar in both cases, approximately 7.5 nm. This small difference of 10% in their electrochemical surface areas compared to the larger difference of 40% in noble metal content could be explained by the leaching of the un-alloyed Co during electrode conditioning. The leaching of Co would lead to Pd with higher roughness, and this way the electrocatalysts with higher Co content would show the highest ECSA. Leaching of Co in Pd-Co alloys was previously reported [5] although this was not investigated.

Catalysts prepared on Pd/C, Pd(Co)-EG11 and Pd_4(Co)-EG11, exhibited ECSA values of 10 and 12 m^2 g^{-1} and palladium contents of 20 and 24% weight, respectively. Unlike the behavior observed in co-deposited catalysts, for catalysts prepared by depositing Co on Pd/C differences in ECSA of catalysts with different Pd content agreed to differences in Pd contents; both ECSA and Pd content were approximately 20% larger for Pd_4(Co)-EG11. This would support the hypothesis that the leaching of un-alloyed Co increased the ECSA in co-deposited catalysts, as previously suggested. Since in Pd(Co)-EG11 and Pd_4(Co)-EG11 cobalt was deposited on already reduced Pd/C, this Co would have been located on the surface of the carbon or Pd nanoparticles. Therefore its dissolution would not have changed the catalysts ECSA because the dissolution of un-alloyed Co sitting on the Pd/C surface would not affect the catalysts roughness. Therefore we can conclude that a deposition of un-alloyed Co on Pd/C does not affect the ECSA of the catalyst.

The decrease of the ECSA after heat treatment was approximately 25% for each Pd-Co catalyst. However, it is interesting to note that although all four catalysts lost approximately one quarter of the ECSA after heat treatment; the increase in the particle size was larger for catalysts with low cobalt content, as previously discussed in Section 5.2.2. This could be explained for co-deposited catalysts by combining the hypothesis of leaching of un-alloyed Co and the depression of Pd particle sintering due to the presence of Co (the higher the Co:Pd atomic ratio the smaller the particle growth). Catalysts would lose ECSA because alloying stopped the Co leaching, therefore its roughness did not increase during electrode conditioning. This effect would be smaller for low Co content, but the catalysts with lower Co content experienced larger particle growth, which also decreased its surface area. This would have produced an overall similar decrease in the ECSA of PdCo-EG11 and Pd_4Co-EG11.

5.3.3. Electrochemical characterization of palladium-iron catalysts

Slow cyclic voltammetries for PdFe-EG11 and Pd_3Fe-EG11 showed the electrochemical characteristics of a palladium electrode (Section 4.3): oxygen chemisorptions started above ca. 0.8 V in the positive sweep and in the negative potential sweep reduction of the oxide layer started close to 0.8 V, the oxide reduction peak was located at ca. 0.7 V. However, it is interesting to comment on the voltammograms recorded whilst conditioning the electrode (Figure 5-17). During the first cathodic potential sweep a large reduction peak, commencing at ca. 0.53 V and with its maximum at ca. 0.36 V, appeared in both cases. The corresponding oxidation peak, in the following anodic sweep at ca. 0.75 V, had a much smaller area in both cases. In the second cycle both reduction and oxidation peaks could barely be seen and they were not present in the third cycle. That was believed to be due to all the iron in the electrode being oxidized to a soluble form. The dissolved iron would probably have had some influence in the ORR activity of the catalysts; this issue is discussed in Section 5.4.3.

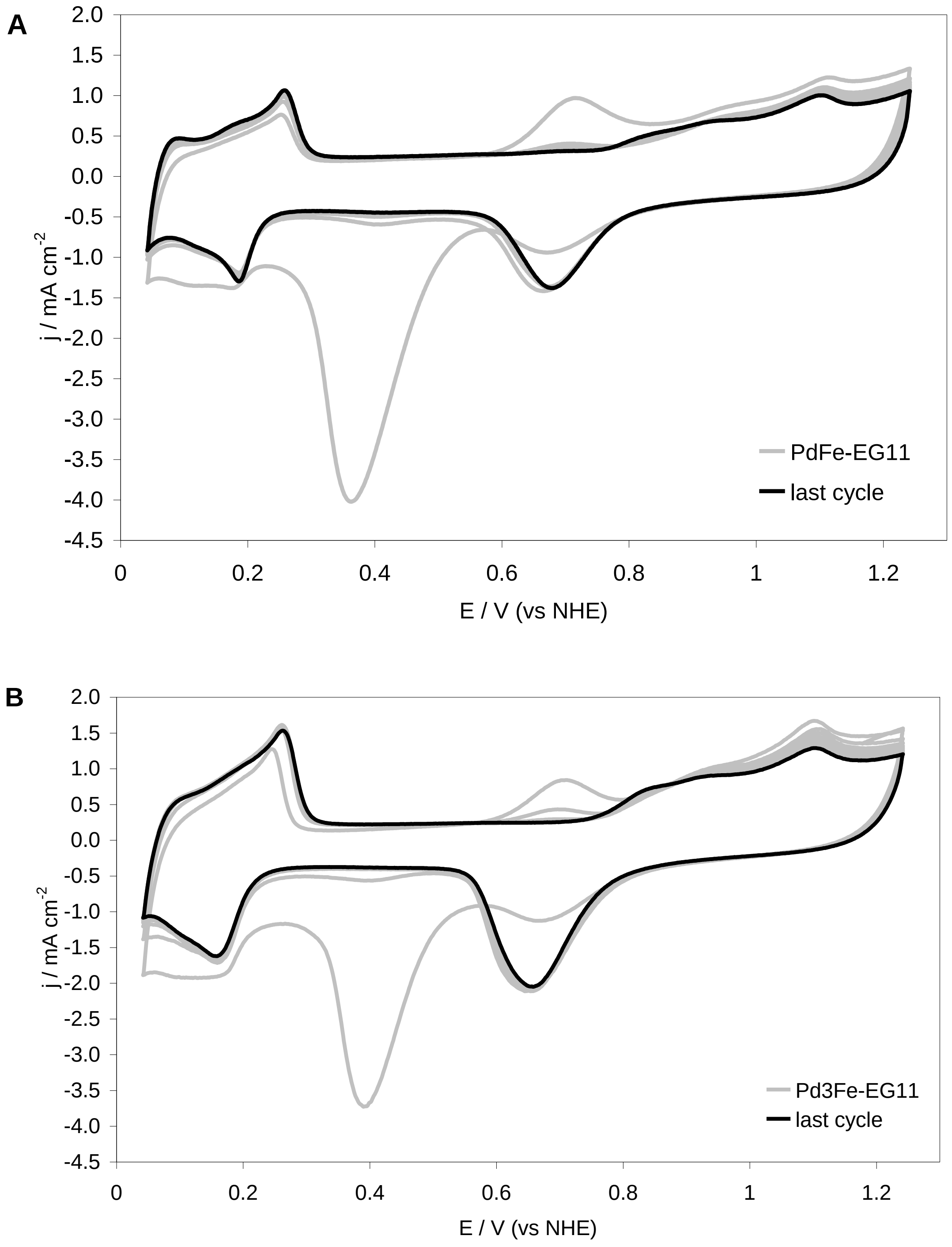

Figure 5-17: Fast scan cyclic voltammograms of carbon-supported Pd-Fe catalysts A) PdFe-EG11 and B) Pd_3Fe-EG11.

This reduction current is believed to be due to the reduction of iron species present in the electrode in an oxidized form. According to the Pourbaix diagram for iron in aqueous solution, the reduction of Fe_2O_3 at pH 1 starts at ca.0.52 V vs NHE [21], which matches the position of the discussed reduction peak. Therefore the Fe_2O_3 in the electrocatalysts would be reduced to Fe^{2+} enabling the electrode to go into the solution. Due to the large volume of electrolyte compared to the amount of catalysts only a very small fraction would redeposit during the following anodic sweep. The area under the iron oxide reduction peak was larger for PdFe-EG11 than for Pd_3Fe-EG11, indicating a larger amount of iron in the electrode, which agrees with the EDXA analyses.

After treating PdFe-EG11 and Pd_3Fe-EG11 under a H_2 flow at 300 ºC a small decrease in the area of the iron oxide reduction peak was observed in both cases, although the behavior during fast CV cycling remained the same. Peaks caused by the reduction and re-oxidation of Fe^{3+} disappeared after the first two cycles.

Catalysts synthesized by H_2 reduction at 500 ºC also exhibited the iron oxide reduction peak in the initial cycle of the conditioning. The magnitude of this peak was smaller in any of the catalysts prepared by EG reduction. The smallest amount of amorphous Fe_2O_3 was found to be in Pd_3(Fe)-H_2-500.

The electrochemical surface area of 7 m^2 g^{-1} for PdFe-EG11 was smaller than for Pd_3Fe-EG11, 11 m^2 g^{-1} (Table 5-3). This smaller surface area appeared to be a consequence of the larger particle size of PdFe-EG11, 11 nm compared with the 8 nm of Pd_3Fe-EG11. This would suggest that the presence of $FeCl_3$ somehow affects the deposition of Pd with EG when both salts are present in the solution. Larger amounts of Fe salt in the solution would induce the formation of larger Pd particles.

Approximately one quarter of the ECSA was lost after treatment at 300 ºC under H_2 flow in both Pd-Fe catalysts prepared by EG reduction. A small amount of sintering could be one of the causes of this decrease in ECSA, although no significant particle growth was observed in any catalyst. The introduction of some Fe in the Pd lattice, discussed in the previous section, could have affected the ECSA calculated for PdFe-EG11-300 and Pd_3Fe-EG11-300.

Electrochemical surface areas for Pd-Fe catalysts prepared by H_2 reduction at 500 ºC and co-deposition, PdFe-H_2-500 and Pd_3Fe-H_2-500, were 5 and 11 m^2 g^{-1}, respectively. When prepared on Pd/C, Pd(Fe)-H_2-500 and Pd_3(Fe)-H_2-500, the difference was less, 6 and 7 m^2 g^{-1}, respectively. Surprisingly, differences in the ECSA for catalysts prepared by H_2 reduction at 500 ºC did not correspond to differences in particle size calculated from the XRD; sizes for PdFe-H_2-500 and Pd_3Fe-H_2-500, were 7 and 8 nm and for Pd(Fe)-H_2-500 and Pd_3(Fe)-H_2-500 were 8 and 9 nm, respectively (Table 5-3).

Taking into account that the ECSA was calculated per gram of metal and since no significant disparity existed between PdFe-H_2-500 and Pd_3Fe-H_2-500 particle sizes, the fact that Pd_3Fe-H_2-500 had approximately double the ECSA could be explained by its larger Pd content; 16% weight versus the 10% weight in PdFe-H_2-500. The difference in the Pd content would also explain why the ECSA of Pd(Fe)-H_2-500 was smaller than the ECSA of Pd_3(Fe)-H_2-500, since the Pd contents measured by EDXA were 23% and 26%, respectively.

Interestingly, slow scan cyclic voltammetries for catalysts prepared by ethylene glycol reduction presented different electrochemical characteristics before and after heat treatment at 300 ºC in H_2 (Figure 5-18A). As previously mentioned, voltammetry at a scan rate 5 mV s^{-1} for PdFe-EG11 and Pd_3Fe-EG11 produced the electrochemical characteristics of a palladium electrode; the palladium oxide reduction peak was at ca. 0.72 V vs NHE. After heat treatment, PdFe-EG11-300, which showed the smallest change, gave a small reduction peak at potentials close to 0.7 V vs NHE, which seemed to be overlapped with the Pd oxide reduction peak. This small peak is believed to be caused by the introduction of a small amount of Fe atoms in the Pd lattice; introduction which could not be confirmed from XRD analyses, as discussed in the previous section. More obvious was the change in the electrochemical behavior of Pd_3Fe-EG11-300; the whole Pd oxide reduction peak exhibited a shift of ca. 15 mV towards lower potentials. This shift was believed to be caused by the introduction, to a larger extension than in the PdFe-EG11-300, of Fe atoms in the Pd lattice. This hypothesis is supported by Pd-Pd bond distances calculated from the X-ray diffraction angles, which were significantly different from pure Pd. The influence of this change in the ORR activity is discussed in Section 5.4.3.

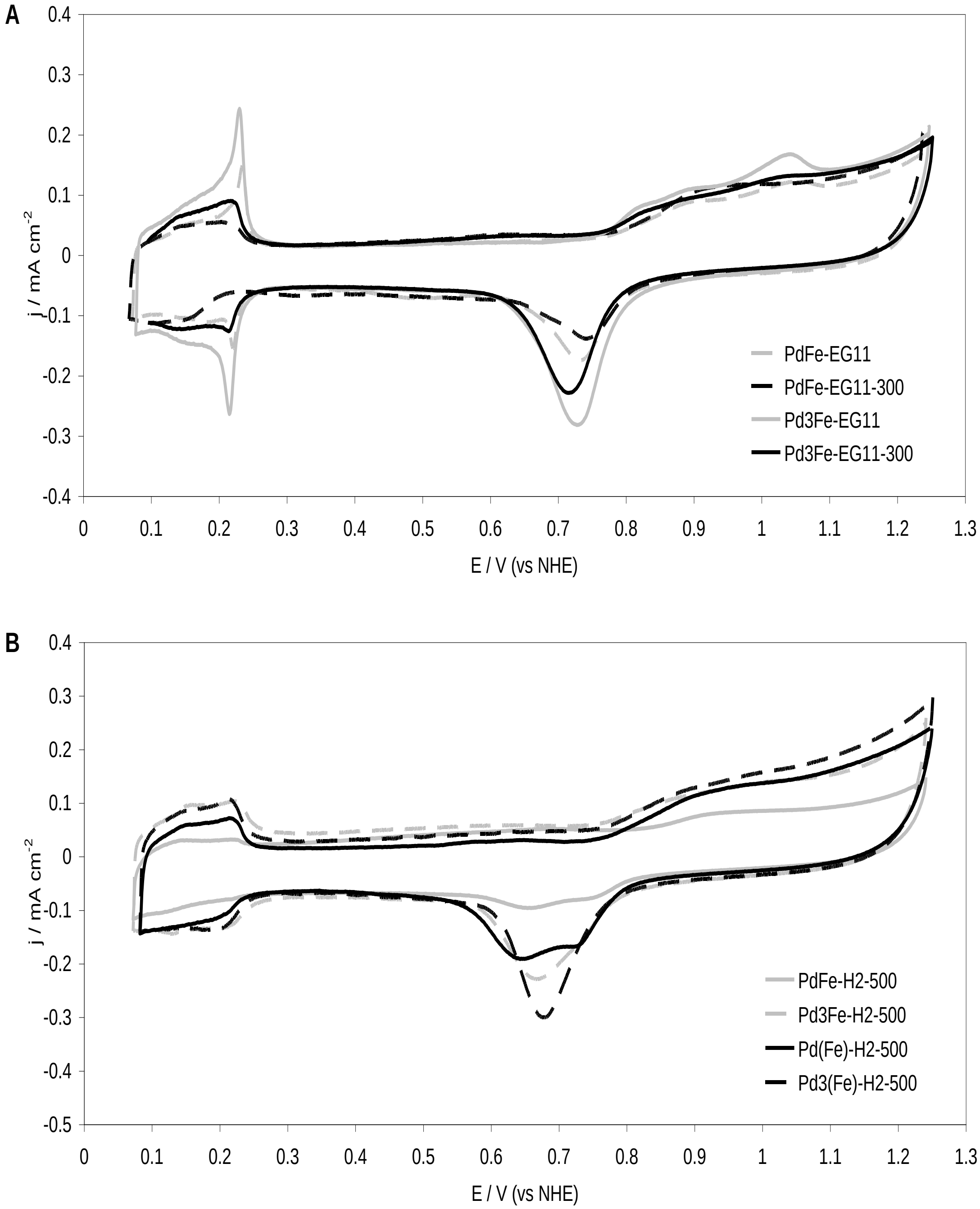

Figure 5-18: Cyclic voltammograms of carbon-supported Pd-Fe catalysts prepared A) by ethylene glycol reduction and B) by reduction in H_2 at 500 ºC.

Slow scan voltammetries of catalysts prepared by H_2 reduction at 500 ºC all presented different characteristics to Pd/C (Figure 5-18B). Catalysts with high iron content, PdFe-H_2-500 and Pd(Fe)-H_2-500, presented two peaks in the cathodic sweep, one at ca. 0.72 and the other at ca. 0.65 V vs NHE. These two peaks were not resolved in the fast scan rate voltammograms. The peak at 0.72 V would be due to reduction of palladium oxide, the peak at 0.65 V would then correspond to the reduction of the Pd-Fe alloy. No slow scan voltammograms in N_2 saturated solution were found in the literature for comparison. Catalysts with low iron content Pd_3Fe-H_2-500 and Pd_3(Fe)-H_2-500, showed a single broad peak at ca. 0.68 V vs NHE which is believed to be a combination of the two peaks observed in catalysts with higher Fe content. The Pd-Fe alloy oxide reduction peak would be masked by the palladium oxide reduction peak due to the large amount of Pd in the catalyst. Shifts in the oxide reduction to lower potentials for Pd-Fe compared with Pd where also reported by Shao et al. [14].

5.3.4. Electrochemical characterization of palladium- titanium catalysts

The shape of all slow cyclic voltammograms in a N_2 saturated electrolyte of Pd-Ti catalysts, both prepared by ethylene glycol reduction (Figure 5-19A) or by reduction in H_2 at 900 ºC (Figure 5-19B), exhibited the electrochemical behavior of a pure Pd electrode (Section 4-3). On the positive sweep oxygen chemisorptions started above ca. 0.8 V. In the negative potential sweep, reduction of the oxide layer started at potentials of ca. 0.8 V and the oxide reduction peak was located at ca. 0.7 V. From ca. 0.6 V to 0.3 V only the double layer charging current was observed in the cathodic sweep. At an electrode potential below ca. 0.3 V a cathodic current was recorded which was attributed to hydrogen adsorption and dissolution. Titanium oxide electrodes reported in the literature [22] do not present reduction or oxidation peaks in the selected potential range. Therefore its presence could not be determined by these voltammograms.

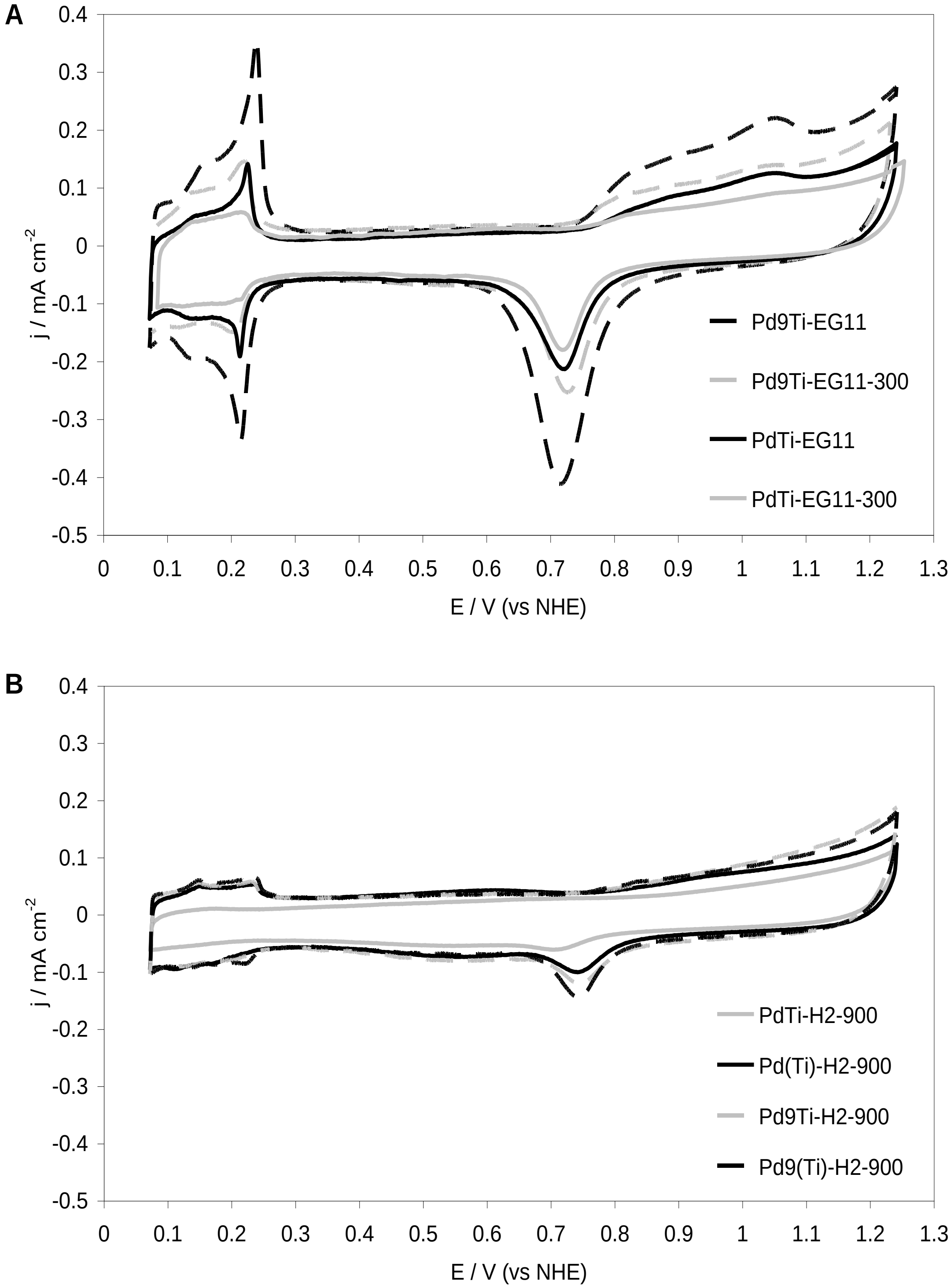

Figure 5-19: Cyclic voltammograms of carbon-supported Pd-Ti catalysts prepared A) by ethylene glycol reduction and B) by reduction in H_2 at 900 °C.

However, it is interesting to note that the palladium oxide reduction peak of Pd_9Ti-EG11-300 was slightly shifted to higher potentials compared to Pd_9Ti-EG11 (Figure 5-19A). Since the Pd-Pd bond distance presented the lowest value of all palladium-titanium catalysts (although not considered significant) as shown in the physicochemical characterization, it is believed that this shift may be linked to the introduction of small amounts of Ti in the Pd lattice. No data from the literature could be found to support this hypothesis; nevertheless, as discussed in the following section, important differences in the ORR activity were observed between Pd_9Ti-EG11 and Pd_9Ti-EG11-300.

Carbon supported Pd-Ti materials produced by both reducing methods presented a dramatic difference in the ECSA. This is believed to be caused by the extreme temperatures, 900 ºC, used in the reduction with H_2 with hydrogen flow. High temperatures and hydrogen atmosphere cause sintering of Pd nanoparticles, provoking a loss in the electrochemical surface area of the catalysts. Values were calculated from slow voltammograms (Figure 5-19) and are shown in Table 5-4.

Pd_9Ti-EG11 presented the highest ECSA, 16 m^2 g^{-1}, which can be easily seen in Figure 5-19A, followed by PdTi-EG11 with 11 m^2 g^{-1}. If ECSAs for PdTi-EG11 and Pd_9Ti-EG11 were calculated using the Pd content, instead of the total metal content, the values would be 14 and 16 m^2 g^{-1} Pd, respectively, which is the same value obtained for Pd/C, 15 m^2 g^{-1} (Table 5-4) within the experimental error. Particle sizes for both PdTi-EG11 and Pd_9Ti-EG11 were also equal, ca. 7 nm, and equal to the particle size of Pd/C prepared by the same method. Therefore we can conclude that the presence of titanium oxide did not affect the morphology of palladium nanoparticles when prepared by ethylene glycol reduction.

After treatment under H_2 flow at 300 ºC, both PdTi-EG11 and Pd_9Ti-EG11 behaved in a similar way. The ECSA suffered a significant decrease in both cases, over 40% and 50% for PdTi-EG11-300 and Pd_9Ti-EG11-300, respectively. The decrease can be explained by the particle size growth after heat treatment as previously mentioned. The effect of TiO_2 on the activity towards ORR will be discussed in the following section.

Cyclic voltammetries for Pd-Ti catalysts prepared by reduction at 900 ºC in H_2 are compared in Figure 5-19B. The largest ECSA calculated belonged to Pd_9(Ti)-H_2-900 and was just below 3 m^2 g^{-1}; the smallest was for PdTi-H_2-900, 0.75 m^2 g^{-1}. These small active surface areas are believed to be due to particularly large particles. Particle sizes are in the range of 23 to 27 nm (Table 5-4). The smallest ECSA recorded for Pd-Ti and bimetallic catalysts was that for PdTi-H_2-900, under 0.8 m^2 g^{-1}. The low Pd content, ca. 10% weight, combined with the large particle size, 25 nm, were believed to be the cause of this small value.

5.4. Activity towards the oxygen reduction reaction of carbon-supported bimetallic nanoparticles

5.4.1. Evaluation of palladium-gold catalysts

Onset potentials, exchange current density and Tafel slopes for palladium-gold catalysts were compared with the same parameters for Pd/C-EG11, Pt/C from E-Tek and Au electrodes data from the literature (Table 5-5).

Table 5-5: Onset potential, Tafel slope, transfer coefficient, exchange current density and mass activity for carbon-supported palladium-gold catalysts.

Catalyst	**Onset potential (V *vs* NHE)**	**Tafel slope (mV dec^{-1})**	**Transfer coefficient**	**Exchange current density (A cm^{-2})**	**Mass activity at 0.75V (A g^{-2} Pd)**
PdAu-EG11	0.76	103	0.56	-	0.4
PdAu-EG11-300	0.67	91	0.64	-	0.4
Pd$_9$Au-EG11	0.85	59	0.98	1.2 x 10^{-12}	8.5
Pd$_9$Au-EG11-300	0.84	56	1.05	3.9 x 10^{-13}	4.5
Pd(Au)-EG11	0.85	58	1.00	1.5 x 10^{-12}	13.9
Pd(Au)-EG11-300	0.85	57	1.01	2.3 x 10^{-12}	5.0
Pd$_3$(Au)-EG11	0.87	63	0.92	1.2 x 10^{-11}	18.3
Pd$_3$(Au)-EG11-300	0.86	63	0.92	8.7 x 10^{-12}	8.1
Pt-Etek	0.96	64 128	0.91 0.45	1.4 x 10^{-10} 6.1 x 10^{-8}	45.3
Pd-EG11-untr	0.89	59	0.98	1.0 x 10^{-11}	29.7
Au [23]	0.70	100	0.58	10^{-13}	-
Au/C [24]	-	106	0.55	-	-

The most dramatic difference in ORR activity, compared to Pd/C, was presented by Pd-Au catalysts prepared by co-deposition with high Au content (Figure 5-20): PdAu-EG11 and PdAu-EG11-300. Both of them presented onset potentials much lower than Pd/C of 0.76 and 0.67 V, respectively. These values were close to the value of 0.70 V reported in the literature for pure Au [23]. Tafel slopes (Figure 5-21), of 103 and 91 mV decade^{-1}, respectively, were also similar to the slopes reported in the literature for pure gold electrodes in acid electrolyte (100 and 106 mV decade^{-1} for Au and Au/C, respectively, in diluted sulphuric acid [23, 24]). After the initial conditioning the electrodes behaved like Au.

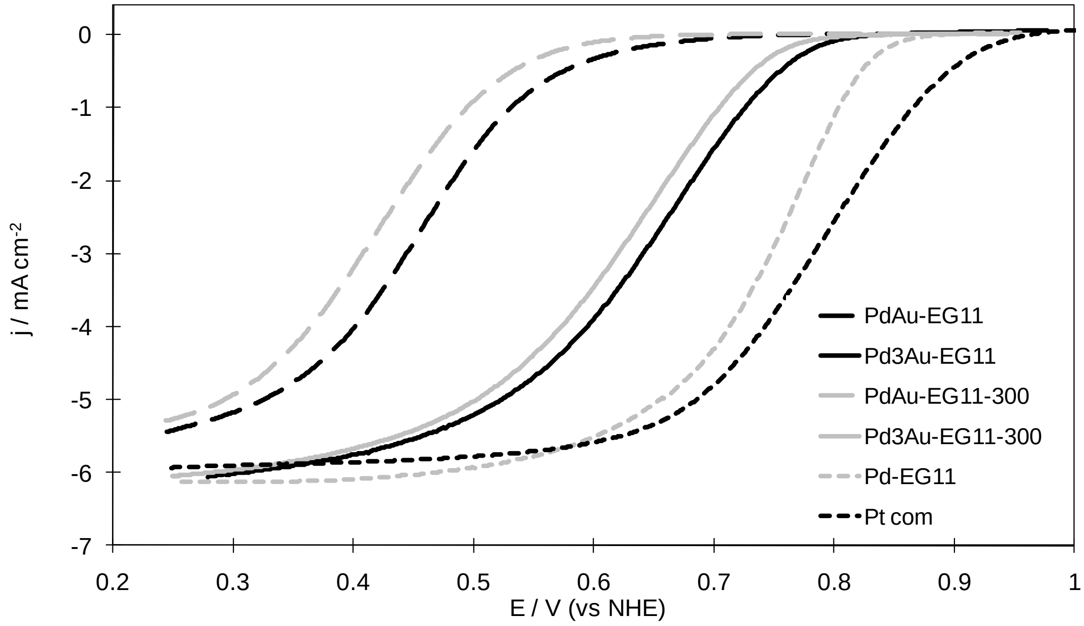

Figure 5-20: Linear sweep voltammograms of carbon-supported Pd-Au catalysts prepared by co-deposition of Pd and Au salts on carbon.

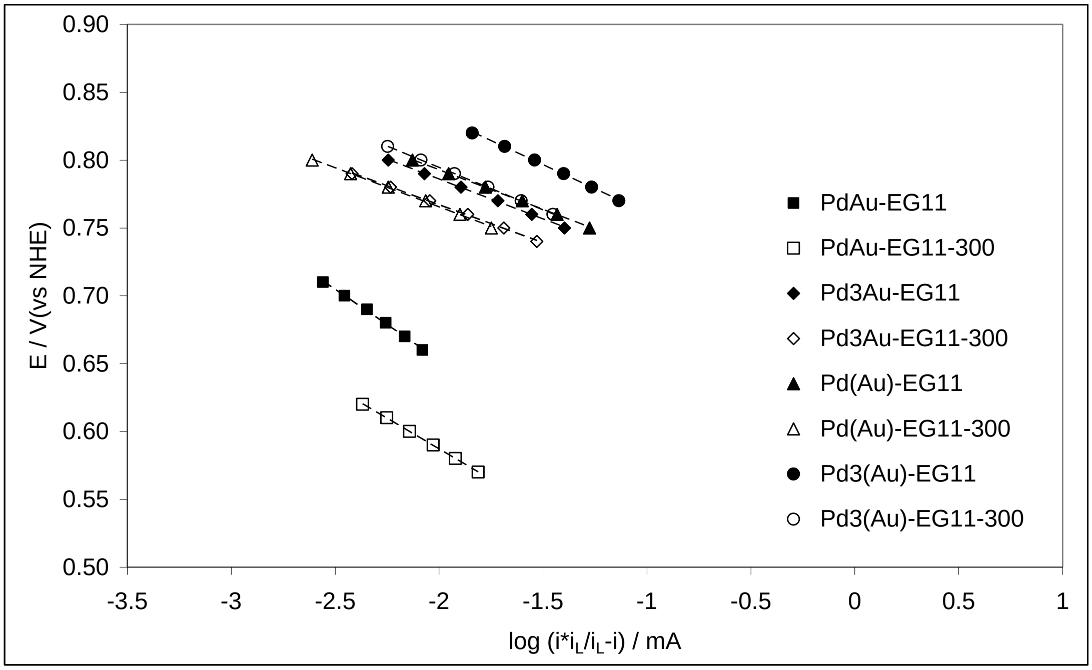

Figure 5-21: Tafel plots for palladium-gold catalysts.

The behavior of catalysts synthesized by co-deposition with more than 50% atomic Au content agreed with data reported by Damjanovic et al [19], who observed a gold-like behavior on Pd-Au alloy electrodes containing more that 50% atomic Au. Damjanovic et al. [19] suggested that the change in Tafel slope from 60 to 100 mV decade^{-1}, in Pd-Au alloys with more than 50% atomic Au, was due to a mechanism change caused by a change in the electronic structure of the alloy. Exchange current densities were not calculated for these two catalysts because data for their ECSAs could not be obtained from the slow scan cyclic voltammograms, as discussed in the previous section.

Every other palladium-gold catalyst prepared, (Pd_9Au-EG11, Pd_9Au-EG11-300, Pd(Au)-EG11, Pd_3(Au)-EG11, Pd(Au)-EG11-300 and Pd_3(Au)-EG11-300), gave onset potentials and Tafel slopes closer to Pd/C-EG11, although the onset potential was lower in every case. Onset potentials were 0.85, 0.84, 0.85, 0.87, 0.85 and 0.86 V vs NHE for Pd_9Au-EG11, Pd_9Au-EG11-300, Pd(Au)-EG11, Pd_3(Au)-EG11, Pd(Au)-EG11-300 and Pd_3(Au)-EG11-300. Their Tafel slopes values were all within the range 60 ± 4 mV decade^{-1}.

Pd_9Au-EG11 and Pd_9Au-EG11-300 (Figure 5-20) exhibited onset potentials of 0.85 and 0.84 V; 40 and 50 mV lower than Pd/C, respectively. Pd_9Au-EG11 showed an i_0 value one order of magnitude lower than Pd/C (see Table 5-5). XRD patterns for this catalyst indicated the presence of several metal phases; Pd, Au and a solid solution of both with a concentration gradient. The partial solution of Au in the Pd lattice could be held responsible for the decrease in the i_0 in Pd_9Au-EG11. The alloy formation could cause the electrochemical characteristics of the electrode to shift towards gold-like behavior [19], as previously discussed for PdAu-EG11 and PdAu-EG11-300. This would be supported by the one order of magnitude decrease in the exchange current density, when the catalyst was treated in H_2 at 300 ºC. As discussed in the physicochemical characterization, heat treatment caused an increase in the extent of the alloy and no pure Pd phase was longer present. Therefore, the exchange current density would differ even more than that for Pd/C.

Pd(Au)-EG11 and Pd_3(Au)-EG11 (Figure 5-22) showed onset potentials of 0.85 and 0.87 V, 40 and 20 mV lower than Pd/C, respectively. The i_0 for catalysts at atomic ratio Pd:Au 1:0.4 was 1.2 x 10^{-11} A cm^{-2}, very similar to Pd/C, whilst the exchange current density for catalysts at atomic ratio Pd:Au 1:1.4 was one order of magnitude lower, 1.5 x 10^{-12} A cm^{-2}. The decrease in the ORR activity, specially noticed in the catalysts at atomic ratio Pd:Au 1:1.4, was believed to be due to the influence of the gold particles deposited on Pd/C, since not Pd-Au alloy was formed according to the XRD patterns. The larger the amount of Au nanoparticles introduced in the catalysts the closer the ORR activity to a gold electrode.

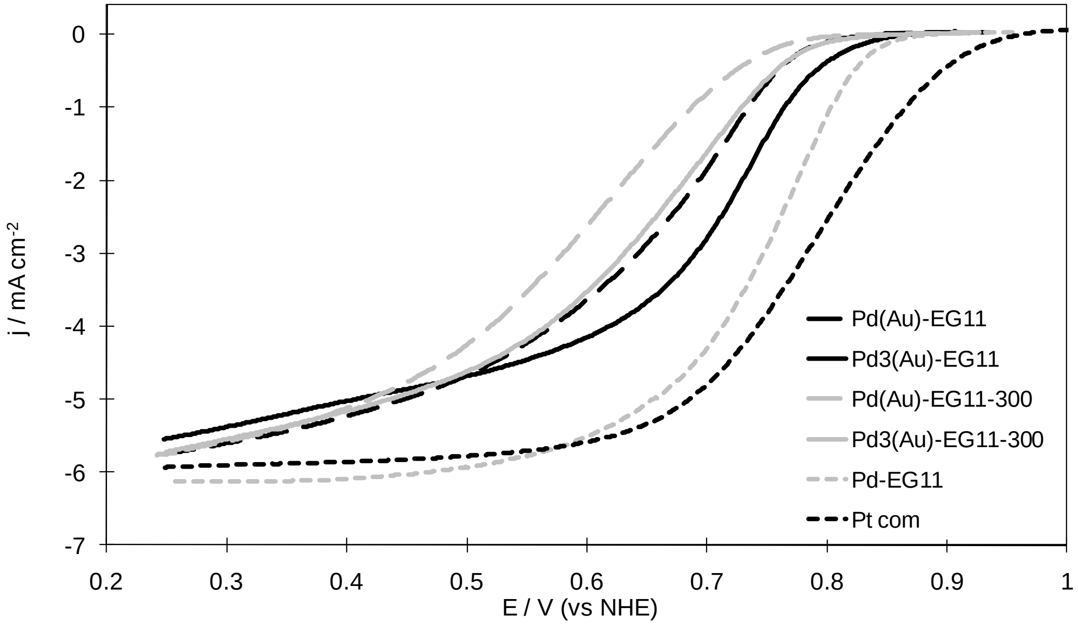

Figure 5-22: Linear sweep voltammograms of carbon-supported Pd-Au catalysts prepared on Pd/C.

When Pd(Au)-EG11 and Pd_3(Au)-EG11 were treated in H_2 at 300 ºC, neither the exchange current density nor the onset potential changed significantly (Table 5-5). Onset values for treated catalysts, Pd(Au)-EG11-300 and Pd_3(Au)-EG11-300 (Figure 5-22), were 0.85 and 0.86 V and i_0 was 2.3 x 10^{-12} and 8.7 x 10^{-12} A cm^{-2}, respectively. This confirmed the information obtained from X-ray diffraction analyses, which showed that no Pd-Au alloy was formed. However, a small extension of alloy was believed to have occurred, based on both the extreme decrease of the ECSA compared to the particle size increase and the shift in the palladium oxide reduction peak, as previously discussed.

After heat treatment a decrease in the mass activity was observed in every case. Mass activities decreased from 9 to 5, 14 to 5 and 18 to 8 A g^{-2} Pd for Pd_9Au-EG11, Pd(Au)-EG11 and Pd_3(Au)-EG11 after heat treatment, respectively. This behavior was expected since heat treatment caused particle growth and that would lead to smaller surface area. Onset potentials and i_0 values for Pd(Au)-EG11 and Pd_3(Au)-EG11 did not show significant changes.

As discussed in the previous paragraph, the more Au introduced in the Pd lattice the lower the oxygen adsorption on its surface and therefore the smaller the area under the oxide reduction peak. However this was found to be contradictory with the invariability of the onset and i_0 before and after treatment, as the adsorption of oxygen is believed to strongly affect the kinetics of the ORR, as discussed in Chapter 4.

5.4.2. Evaluation of palladium-cobalt catalysts

Table 5-6 compares onset potential, exchange current density and Tafel slopes for palladium-cobalt catalysts with the same parameters for Pd/C-EG11 prepared catalyst and Pt/C from E-Tek. Every palladium-cobalt catalysts presented onset potentials and Tafel slopes close to Pd/C-EG11, onset potentials were equal or lower in every case. Tafel slopes values were all within the range of 60 ± 4 mV $decade^{-1}$.

Table 5-6: Onset potential, Tafel slope, transfer coefficient, exchange current density and mass activity for carbon-supported palladium-cobalt catalysts.

Catalyst	Onset potential (V *vs* NHE)	Tafel slope (mV dec^{-1})	Transfer coefficient	Exchange current density (A cm^{-2})	Mass activity at 0.75V (A g^{-2} Pd)
PdCo-EG11	0.89	58	0.99	9.7 x 10^{-12}	44.8
PdCo-EG11-300	0.84	57	1.03	2.8 x 10^{-13}	8.2
Pd_4Co-EG11	0.88	62	0.93	8.5 x 10^{-12}	19.2
Pd_4Co-EG11-300	0.88	63	0.90	1.4 x 10^{-11}	23.1
Pd(Co)-EG11	0.87	61	0.95	4.3 x 10^{-12}	10.4
Pd(Co)-EG11-300	0.86	61	0.96	2.7 x 10^{-12}	9.5
Pd_4(Co)-EG11	0.88	58	1.00	9.1 x 10^{-12}	26.2
Pd_4(Co)-EG11-300	0.88	63	0.92	7.5 x 10^{-12}	12.2
Pt	0.96	64 128	0.91 0.45	1.4 x 10^{-10} 6.1 x 10^{-8}	45.3
Pd	0.89	59	0.98	1.0 x 10^{-11}	29.7

From the XRD analyses we concluded that Pd-Co alloys were not formed without heat treatment in any case. Therefore this section will discuss differences in the activity ORR after treatment in H_2 at 300 ºC.

Catalysts with a Co content of ca. Pd:Co 1:0.6 or higher, PdCo-EG11 and Pd(Co)-EG11, exhibited a decrease in the exchange current density after H_2 treatment (Table 5-6). Untreated PdCo-EG11 and Pd(Co)-EG11 had i_0 values of 9.7 x 10^{-12} A cm^{-2} and 4.3 x 10^{-12} A cm^{-2}, respectively. These values fell after heat treatment by nearly two orders of magnitude for the co-deposited catalyst and approximately half when prepared on Pd/C, to 2.8 x 10^{-13} A cm^{-2} and 2.7 x 10^{-12} A cm^{-2} for PdCo-EG11-300 and Pd(Co)-EG11-300, respectively. All exchange current densities of Pd-Co catalysts were at least two orders of magnitude lower than the value reported by Savadogo et al. for palladium-cobalt 28% atomic cobalt, 5.1 x 10^{-9} A cm^{-2} [4].

Onset potentials of untreated high cobalt content catalysts, PdCo-EG11 and Pd(Co)-EG11 (Figure 5-23), were close to the onset value of Pd/C, 0.89 and 0.87 V, respectively. Both onset potentials decreased after heat treatment, to 0.84 and 0.86 V for PdCo-EG11-300 and Pd(Co)-EG11-300, respectively. The catalyst prepared by simultaneous co-deposition of palladium and cobalt at atomic ratio Pd:Co 1:0.9, PdCo-EG11, exhibited a decrease mass activity at 0.75 V vs NHE, in agreement with the decrease in onset potential and i_0, when heat treated. PdCo-EG11-300 mass activity decreased by more than 75%, from 244 to 61 A g Pd^{-1}, respectively. Unlike the small decrease recorded in their exchange current densities, catalysts synthesized by depositing Co on Pd/C at atomic ratio 1:0.6 Pd:Co, Pd(Co)-EG11 and Pd(Co)-EG11-300, did not show significant differences in mass activity before and after H_2 treatment. Mass activity remained ca. 10 A g Pd^{-1}.

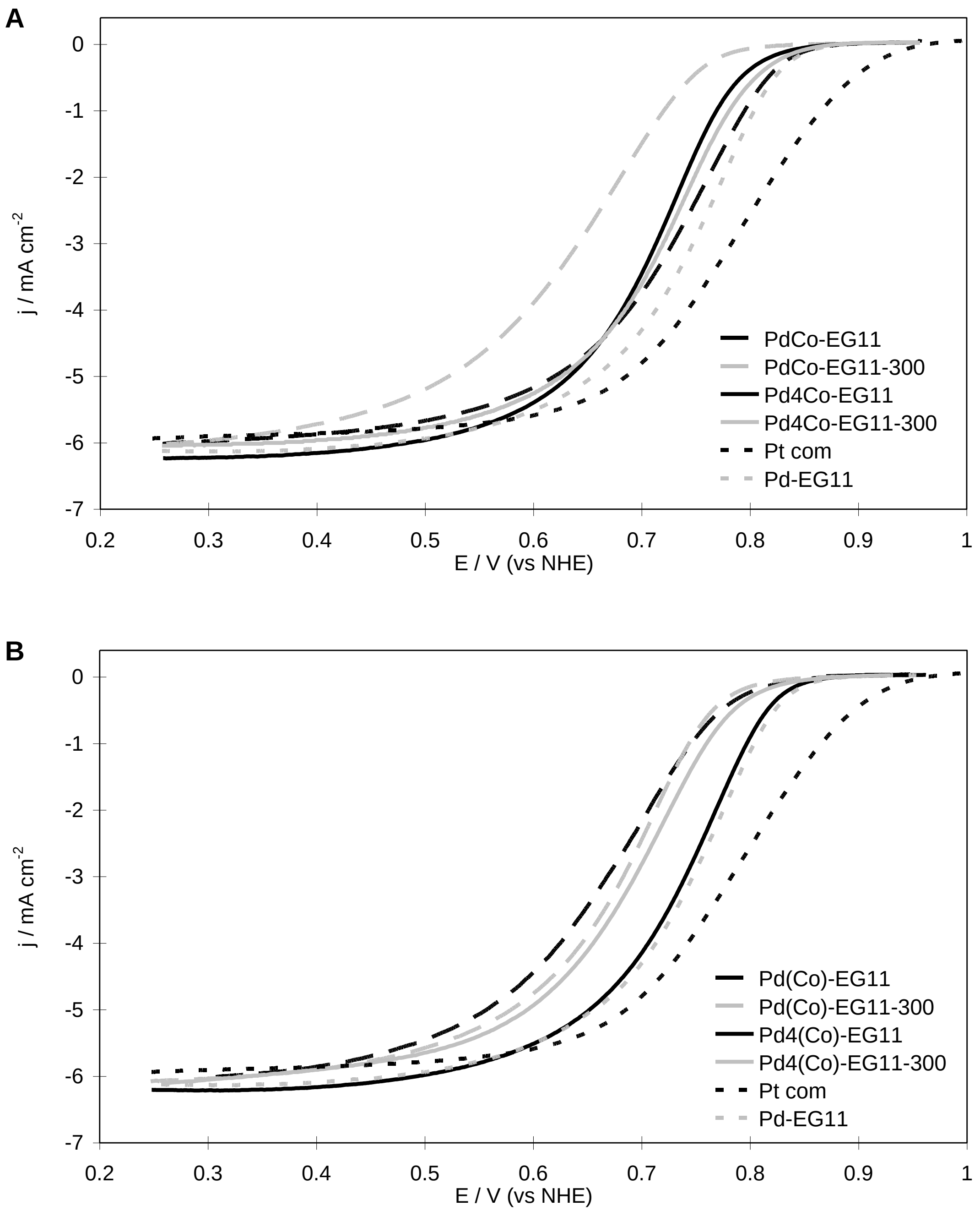

Figure 5-23: Linear sweep voltammograms of carbon-supported Pd-Co catalysts prepared by A) co-deposition of Pd and Co salts on carbon and B) on Pd/C.

For lower Co content, ca. Pd:Co 1:0.2, Pd_4Co-EG11 and Pd_4(Co)-EG11, exchange current densities were also close to those of Pd/C-EG11. After H_2 treatment i_0 increased for the co-deposited catalyst, from 8.5 x 10^{-12} to 1.4 x 10^{-11} A cm^{-2}, and hardly changed for the catalyst prepared on Pd/C, from 9.1 x 10^{-12} to 7.5 x 10^{-12} A cm^{-2}. Onset potentials were constant at 0.88 V, 10 mV lower than Pd/C, for both catalysts before and after heat treatment. In agreement with the improvement of the exchange current density after heat treating Pd_4Co-EG11, a rise from 19 to 23 A g^{-1} in the MA at 0.75 V was observed. When the catalyst with low Co content was prepared on Pd/C, the small i_0 decrease observed in Pd_4(Co)-EG11-300 with respect to Pd_4(Co)-EG11 was accompanied by a sharp decrease from 26 to 12 A g^{-1} in the MA at 0.75 V. Specific activity (current density per electrochemical surface area) reported by Savadogo et al. for palladium-cobalt 28% atomic cobalt, was considerably higher compared to the observed specific activity for Pd_4(Co)-EG11, 580 μA cm^{-2} at 0.80 V compared to 203 μA cm^{-2} at 0.75 V [4].

When cobalt was co-deposited with palladium and the catalysts were untreated, Co was present in an un-alloyed form according to the XRD analyses; its influence in the ORR activity of the Pd nanoparticles could not be determined. Onset potential, exchange current density and mass activity were close to Pd/C-EG11 (Table 5-6). This behavior was common to both untreated co-deposited catalysts with metal ratios Pd:Co 1:0.9 and 1:0.2, PdCo-EG11 and Pd_4Co-EG11, respectively. However, un-alloyed Co deposited on Pd/C seemed to have a detrimental effect on the catalyst ORR activity when the Co content was high, Pd:Co 1:0.6. The onset potential decreased by 20 mV and i_0 and MA at 0.75 V vs NHE were approximately half of the same parameters for Pd/C-EG11. For un-alloyed Co deposited on Pd/C present in a smaller amount, Pd:Co 1:0.2, the Co influence could again not be determined and all parameters were very close to those of Pd/C-EG11. The reason for this behavior remains unknown; it could be due to some amorphous cobalt phase blocking the Pd sites when deposited on Pd/C, and further studies would be necessary.

After treatment in H_2 at 300 ºC, co-deposited catalyst showed different effects depending on the Co content as mentioned above. The decrease in the ORR parameters presented by PdCo-EG11-300 was attributed to the introduction of a relatively large amount of Co atoms in the Pd lattice. As discussed in the physicochemical characterization section, the PdCo-EG11-300 Pd-Pd bond distance had the largest decrease compared to Pd/C, 0.2739 vs 0.2751 nm, respectively, which meant it had the largest alloy extension of all Pd-Co catalysts. Optimum distances for Pd-Co catalysts reported were for Pd_2Co, 0.272 nm [25] and 0.2726 nm [6], since the Pd-Pd bond distance was still far from these value, it was assumed that the degree of alloying was insufficient to increase the ORR activity; only sufficient Co was introduced to considerably depress the ORR activity of Pd. The increase from 8.5×10^{-12} to 1.4×10^{-11} A cm^{-2} in Pd_4Co-EG11-300 cannot be explained by the Pd-Pd bond distance (0.2747 nm) since, as previously discussed, the difference with Pd/C Pd-Pd bond distance could not be considered significant. It was assumed that the introduction of a small amount of Co in the lattice provoked a slight improvement in the ORR activity. The preparation and characterization of a wider range of Pd:Co atomic ratios could help to understand the effect of introducing different amounts of Co and would also provide a wider data collection to compare with the literature.

After heat treating both Pd-Co catalysts prepared on Pd/C in H_2 at 300 ºC a small decrease was observed in the onset potential and the exchange current density for Pd(Co)-EG11-300 and apparently invariability for Pd_4(Co)-EG11-300. When these changes were compared to the variation in the Pd-Pd bond distance, from 0.2748 to 0.2743 nm, it could be that, as in PdCo-EG11-300, the degree of alloying was insufficient to increase the ORR activity; only enough Co was introduced to depress the ORR of the untreated catalyst. Catalysts with low cobalt content, Pd_4(Co)-EG11-300, showed little change in the Pd-Pd bond distance, 0.2746 and 0.2745 nm before and after hydrogen treatment, respectively. Therefore it was understood that the treatment did not produce any important changes in the metal crystal structure, thus no important changes in the catalysts ORR activity were observed.

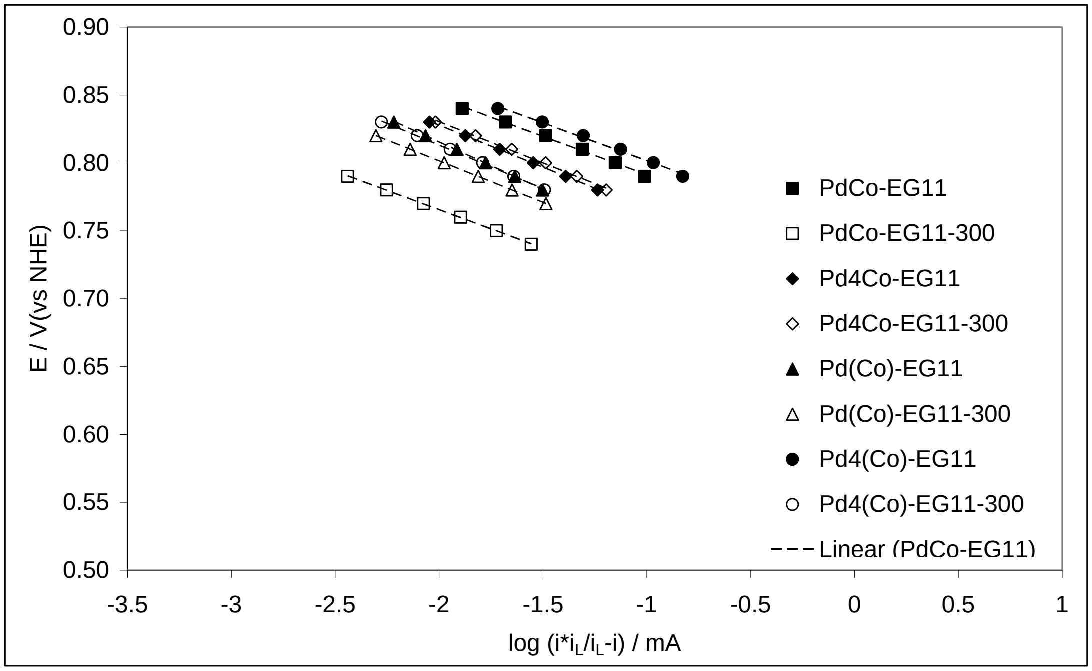

Figure 5-24: Tafel plots for palladium-cobalt catalysts.

5.4.3. Evaluation of palladium-iron catalysts

Table 5-7 compares onset potential, Tafel slopes and exchange current density values for palladium-iron catalysts with the same parameters for the prepared Pd/C-EG11 and Pt/C from E-Tek.

Table 5-7: Onset potential, Tafel slope, transfer coefficient, exchange current density and mass activity for several carbon-supported palladium-iron catalysts.

Catalyst	**Onset potential (V *vs* NHE)**	**Tafel slope (mV dec^{-1})**	**Transfer coefficient**	**Exchange current density (A cm^{-2})**	**Mass activity at 0.75V (A g^{-2} Pd)**
PdFe-EG11	0.86	65	0.89	1.3×10^{-11}	12.7
PdFe-EG11-300	0.81	60	0.97	4.7×10^{-13}	1.5
Pd_3Fe-EG11	0.88	61	0.95	1.7×10^{-11}	31.1
Pd_3Fe -EG11-300	0.87	62	0.92	1.3×10^{-11}	14.6
PdFe-H_2-500	0.78	63	0.92	2.5×10^{-13}	2.1
Pd(Fe)-H_2-500	0.86	62	0.94	4.3×10^{-12}	6.8
Pd_3Fe-H_2-500	0.84	57	1.02	3.1×10^{-13}	4.3
Pd_3(Fe)-H_2-500	0.87	60	0.97	4.2×10^{-12}	12.8
Pt	0.96	64 128	0.91 0.45	1.4×10^{-10} 6.1×10^{-8}	45.3
Pd	0.89	59	0.98	1.0×10^{-11}	29.7
PtFe 3:1[26]	0.94	45	1.29		

Onset potentials recorded for PdFe-EG11 and Pd_3Fe-EG11 (Figure 5-25) were 0.86 and 0.88 V, which were 30 and 10 mV lower than values for Pd/C, respectively. Because the decrease in the onset potential was higher for larger Fe content, this decrease was believed to be caused by the presence of iron, either by introduction of small amounts in the Pd lattice, unconfirmed by XRD, or by the presence of Fe^{2+} in the electrolyte or by the presence of Fe_2O_3 in the catalyst next to the Pd nanoparticles.

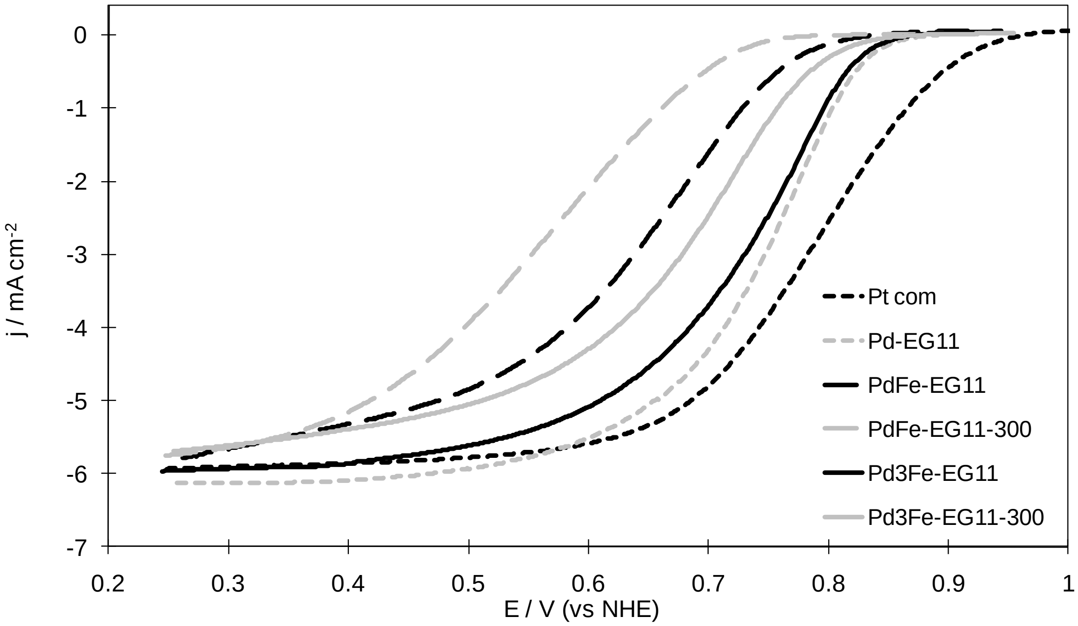

Figure 5-25: Linear sweep voltammograms of carbon-supported Pd-Fe catalysts prepared by ethylene glycol reduction.

Exchange current densities for PdFe-EG11 and Pd_3Fe-EG11 were of the same order of magnitude as for Pd/C, 1.3 x 10^{-11} and 1.7 x 10^{-11} A cm^{-2}, respectively. These i_0 values were slightly higher than for Pd/C (1.0 x 10^{-11} A cm^{-2}). This was believed to be due to the slightly higher Tafel slopes measured, despite being in the range 60 ± 4 mV $decade^{-1}$. Small variations in the Tafel slope, although within the 10% error allowed in this work, would be the cause of significant differences in exchange current densities. The reversible potential for the ORR in acid electrolyte corrected by Nernst is 1.21 V vs NHE, Tafel slopes were measured in a range where the minimum overpotential is 0.4 V. Therefore, when the straight line with the Tafel slope was extrapolated to zero overpotential to calculate i_0, the exchange current density will be influenced by the slope of the line. The influence of Fe or iron salts could not be determined for the two Pd-Fe catalysts from the kinetic parameters, although it is believed that the lower i_0 of PdFe-EG11 compared to Pd_3Fe-EG11 was in agreement with the lower onset potential, due to the higher Fe content of the first.

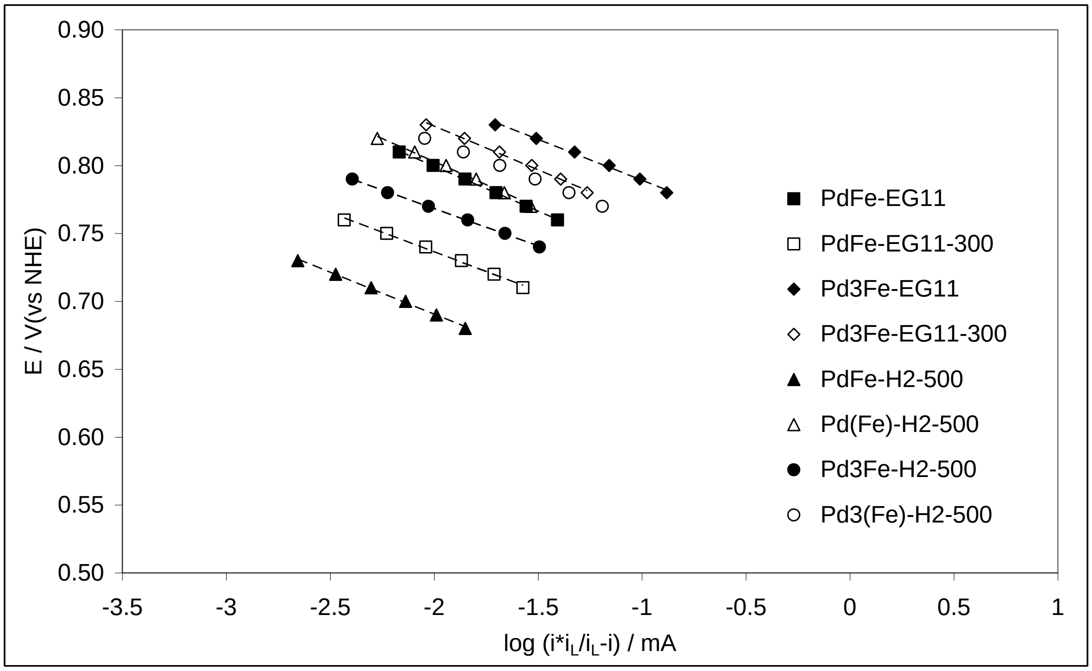

Figure 5-26: Tafel plots for palladium-iron catalysts.

When PdFe-EG11 and Pd_3Fe-EG11 were heat treated in H_2 at 300 ºC both onset potentials suffered a further decrease of approximately 50 and 10 mV for PdFe-EG11-300 and Pd_3Fe-EG11-300, respectively. The decrease in the onset agreed with the decrease in exchange current densities, i_0 for PdFe-EG11-300 and Pd_3Fe-EG11-300 were 4.7 x 10^{-13} and 1.3 x 10^{-11} A cm^{-2}, respectively. As previously discussed, the decrease in both parameters was believed to be caused by two factors; introduction of Fe in the Pd lattice and the presence of oxidized Fe species. Tafel slopes did not present significant changes before and after heat treatment.

Heat treated catalysts with atomic ratio Pd:Fe 1:0.7 exhibit important drops in both onset potential and i_0 compared to PdFe-EG11. The introduction of Fe in the Pd lattice could not be confirmed by XRD, as discussed in the physicochemical characterization; nevertheless, cyclic voltammograms presented in the previous section showed a small reduction peak overlapped with the Pd oxide reduction peak. This peak suggested the formation of some Pd-Fe phase. The iron in this phase could had been oxidized during the anodic sweep, from which we obtained kinetic parameters, shifting this way the onset towards the reduction potential of Fe_2O_3 to Fe^{2+}, ca.0.52 V vs NHE [21]. The presence of this un-characterised phase together with the presence of the Fe^{2+} in the electrolyte, Fe^{2+} that would have passed to the solution during the electrode conditioning, are believed to be the causes of the decrease, by over an order of magnitude of i_0.

Heat treated catalyst prepared by EG reduction with atomic ratio Pd:Fe 1:0.3 exhibited milder reductions in both onset potential and i_0 compared to PdFe-EG11-300. As discussed in the physicochemical characterization, the change in the Pd-Pd bond distance in Pd_3Fe-EG11-300 compared to Pd/C could be considered as proof of the introduction of Fe in the Pd lattice. Two carbon supported metal phases, Pd_2Fe/C and PdFe/C, were reported to have similar Pd-Pd bond distances [14] of ca. 0.2742 nm (Table 5-3). Cyclic voltammetries for Pd_3Fe-EG11-300 showed in the previous section presented a shift in the palladium oxide reduction peak of ca. 15 mV towards lower potentials. This shift was considered as a confirmation that changes observed in the XRD and the difference in the kinetic parameters were due to the introduction, in some extension, of Fe into the Pd lattice. The ORR activity of the phase or phases combination, Pd-Fe and Pd, in Pd_3Fe-EG11-300 was slightly lower than Pd/C.

Catalysts synthesized by reduction in H_2 at 500 ºC and co-deposition of both metals simultaneously, PdFe-H_2-500 and Pd_3Fe-H_2-500, exhibit onset potentials of 0.78 and 0.84 V, ca. 110 and 50 mV lower than Pd/C, respectively. From XRD analysis and voltammograms in N_2 saturated solution it was concluded that a Pd-Fe alloy was obtained, in some extension. Onset potentials suggested that the increase in the Fe content from 1:0.3 to ca. 1:1 Pd:Fe atomic ratio (Table 5-3) resulted in a poorer ORR activity. Tafel slopes were similar to Pd/C for both PdFe-H_2-500 and Pd_3Fe-H_2-500, within the 10% error allowed, 63 and 57 mV decade^{-1}, and exchange current densities were nearly two orders of magnitude lower than for Pd/C, 2.5×10^{-13} and 3.1×10^{-13} A cm^{-2}, respectively.

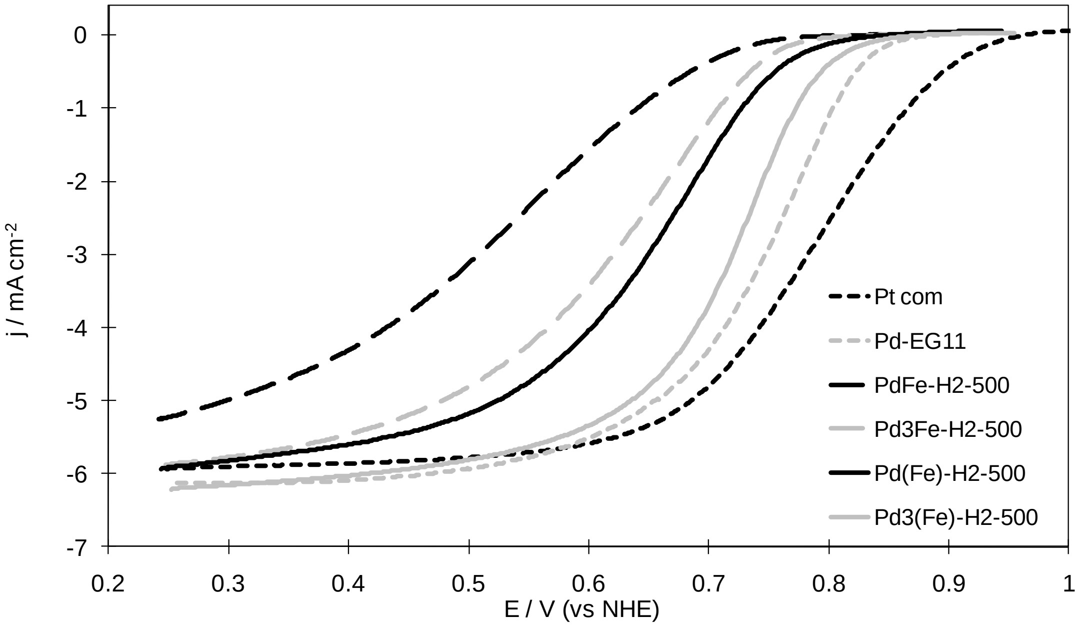

Figure 5-27: Linear sweep voltammograms of carbon-supported Pd-Fe catalysts prepared by reduction in H_2 at 500 °C.

When Fe was reduced on Pd/C by reduction in H_2 at 500 °C (Pd(Fe)-H_2-500 and Pd_3 (Fe)-H_2-500) both onset potentials and exchange current densities were higher than when Pd and Fe were co-deposited. Onset potentials recorded were 0.86 and 0.87 V, ca. 30 and 20 mV lower than Pd/C, respectively; again the larger decrease compared to Pd/C was for the higher Fe content, 1:0.9 vs 1:0.3 Pd:Fe atomic ratio. Tafel slopes were similar to Pd/C for both catalysts, 62 and 60 mV decade^{-1}, and exchange current densities were lower than i_0 for Pd/C, 4.3 x 10^{-12} and 4.2 x 10^{-12} A cm^{-2}, respectively. Thus it was concluded that for catalysts prepared on Pd/C, as for catalysts synthesized by co-deposition, in H_2 at 500 °C, an increase in the Fe content was detrimental for the ORR activity. It was also concluded that co-deposited metals produced catalysts with lower ORR activities than catalysts prepared on Pd/C, as previously observed by Shao et al. [14]

Mass activity agreed with the onset potential (Table 5-7), and was higher for catalysts with lower Fe content and for catalysts prepared on Pd/C. Mass activities for PdFe-H_2-500 and Pd(Fe)-H_2-500, 2 and 7 A g^{-2} Pd, were lower than these of Pd_3Fe-H_2-500 and Pd_3(Fe)-H_2-500, 4 and 13 A g^{-2} Pd, respectively. Mass activity reported by Shao et al. [14]

for carbon-supported Pd_3Fe, was ca. 500 A g^{-2} at 0.8 V, over an order of magnitude higher than for the synthesized $Pd_3(Fe)$-H_2-500.

From the comparison of mass activity it was concluded that co-deposition of Pd and Fe is detrimental for the ORR compared to the Fe deposition on Pd/C. This agreed with what was reported by Shao et al. [14]. However, no Pd-Fe catalysts showed an improvement in the ORR activity compared to Pd/C as was claimed by this group.

5.4.4. Evaluation of palladium- titanium catalysts

Table 5-8 compares onset potential, exchange current density and Tafel slope values for palladium-titanium catalysts with the same parameters for Pd/C-EG11 prepared catalysts and Pt/C from E-Tek. Every palladium-titanium catalyst presented Tafel slopes close to Pd/C-EG11, and all were within the range 60 ± 5 mV $decade^{-1}$.

Table 5-8: Onset potential, Tafel slope, transfer coefficient, exchange current density and mass activity for several carbon-supported palladium-titanium catalysts.

Catalyst	**Onset potential (V *vs* NHE)**	**Tafel slope ($mVdec^{-1}$)**	**Transfer coefficient**	**Exchange current density ($A\ cm^{-2}$)**	**Mass activity at 0.75V ($A\ g^{-2}$ Pd)**
PdTi-EG11	0.88	60	0.96	6.9×10^{-12}	19.3
PdTi-EG11-300	0.87	62	0.94	8.2×10^{-12}	14.2
Pd_9Ti-EG11	0.88	59	0.98	6.5×10^{-12}	27.0
Pd_9Ti -EG11-300	0.86	62	0.93	4.5×10^{-12}	5.9
PdTi-H_2-900	0.74	65	0.88	3.8×10^{-13}	0.0
Pd(Ti)-H_2-900	0.78	63	0.92	1.1×10^{-12}	0.3
Pd_9Ti-H_2-900	0.84	58	1.01	1.8×10^{-12}	3.1
Pd_9(Ti)-H_2-900	0.89	62	0.98	2.8×10^{-11}	11.2
Pt	0.96	64 128	0.91 0.45	1.4×10^{-10} 6.1×10^{-8}	45.3
Pd	0.89	59	0.98	1.0×10^{-11}	29.7

Voltammograms of catalysts prepared using ethylene glycol as the reducing agent are given in Table 5-8. Before heat treatment in H_2 at 300 ºC, both PdTi-EG11 and Pd_9Ti-EG11 showed onset potentials and exchange current densities slightly lower than Pd/C, 0.88 V and ca. 7.0×10^{-12} A cm^{-2}, respectively. Mass activity was also slightly lower compared to Pd/C, the values for PdTi-EG11 and Pd_9Ti-EG11 were 20 and 27 A g^{-2}, respectively, compared to 30 A g^{-2} (Table 5-8). The closest behavior to Pd/C was presented by the catalysts with atomic ratio Pd:Ti 1:0.14 before heat treatment. Lower mass activity for PdTi-EG11, Pd:Ti 1:0.7, was believed to be simply caused by the lower Pd content of the catalyst, 14% weight compared to 20% weight for PdTi-EG11 and Pd_9Ti-EG11, respectively; since no palladium-titanium catalyst prepared by ethylene glycol reduction showed any significant shift in the peak positions of XRD diffractions patterns (Section 5.2.4).

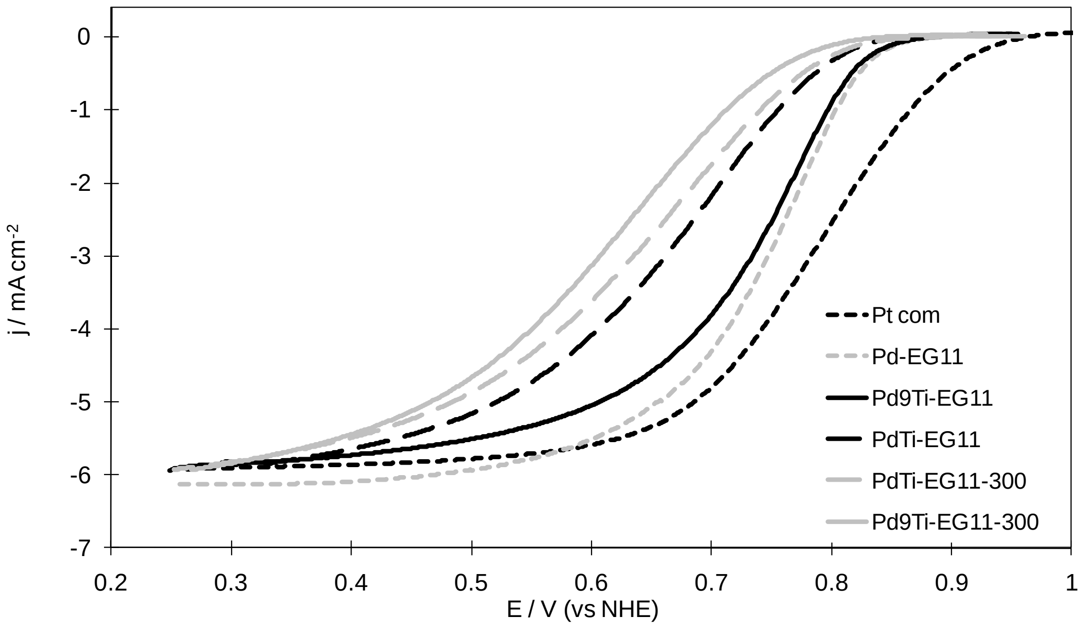

Figure 5-28: Linear sweep voltammograms of carbon-supported Pd-Ti catalysts prepared by ethylene glycol reduction.

After heat treatment in H_2 at 300 ºC, small reductions in onset potentials were observed of 10 and 20 mV in PdTi-EG11-300 and Pd_9Ti-EG11-300, respectively. This decrease in onset potentials was accompanied by a decrease in both mass activities, from 19 and 27 A g^{-2} to 14 and 6 A g^{-2}, respectively. Changes in mass activities were believed to be mainly a consequence of the increase in the particle size, which induced a significant reduction in the ECSA. Exchange current density did not exhibit significant changes for PdTi-EG11-300, 8.2 x 10^{-12} A cm^{-2}, and showed a small decrease in Pd_9Ti-EG11-300, 4.5 x 10^{-12} A cm^{-2}. The exchange current density did not show important changes before and after heat treatment for PdTi-EG11. By contrary, after treating Pd_9Ti-EG11 the exchange current density decreased, this was believed to be due to the introduction of small amounts of Ti in the Pd lattice. However no references supporting this hypothesis were found in the literature.

Voltammograms of catalysts prepared by reduction at 900 ºC in hydrogen are shown in Figure 5-29. These catalysts exhibit onset potentials and exchange current densities lower than Pd/C in every case but one (Table 5-8). Onset potentials and exchange current densities for PdTi-H_2-900, Pd(Ti)-H_2-900, Pd_9Ti-H_2-900 and Pd_9(Ti)-H_2-900 were 0.74, 0,78, 0.84 and 0.89 V, 3.8 x 10^{-13} A cm^{-2}, 1.1 x 10^{-12} A cm^{-2}, 1.8 x 10^{-12} A cm^{-2} and 2.8 x 10^{-11} A cm^{-2}, respectively.

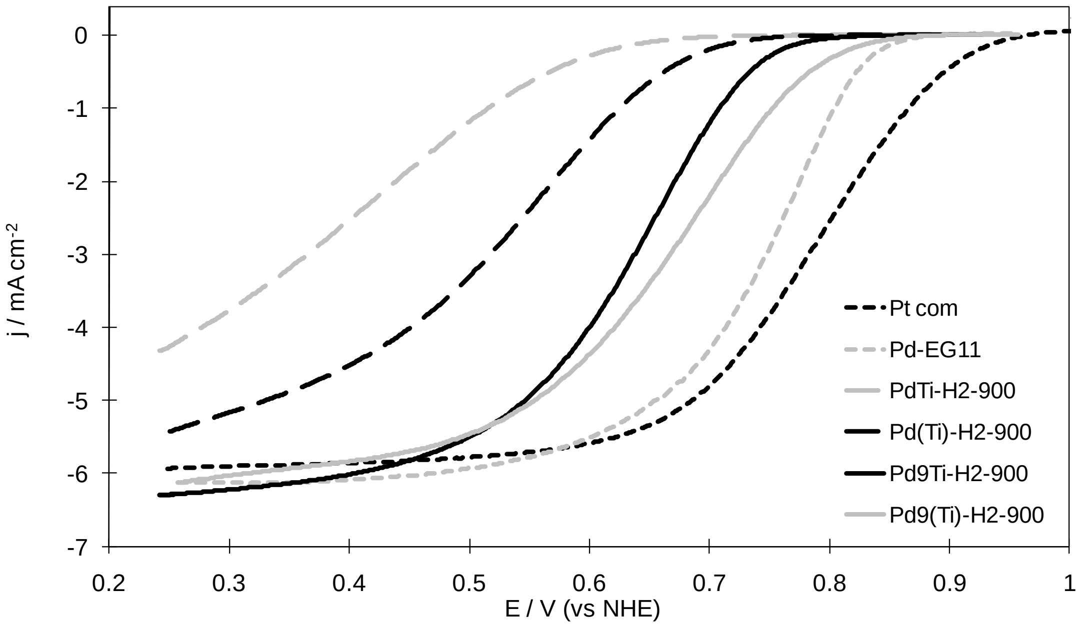

Figure 5-29: Linear sweep voltammograms of carbon-supported Pd-Ti catalysts prepared by reduction in H_2 at 900 ºC.

A negative effect of large amounts of TiO_2 when the catalyst is treated at high temperatures was seen in both PdTi-H2-900 and Pd(Ti)-H_2-900. The higher the titanium content, Pd:Ti 1:1.9 for PdTi-H_2-900 and 1:1.3 Pd(Ti)-H_2-900, the lower were the onset potential and i_0. Mass and activity was also extremely low for these catalysts with high titanium content. MA was reported as zero for both catalysts.

Results were surprising in catalysts prepared by reduction at 900 ºC in hydrogen with low Ti content. Pd_9Ti-H_2-900, prepared by co-deposition, exhibits a 50 mV decrease in onset potential and i_0 was one order of magnitude lower compared to the corresponding parameters for Pd/C. This behavior was somehow expected after studying Pd_9Ti-EG11-300, with similar Ti content, which also presented a depression in the ORR activity after heat treatment. The increase in heat treatment temperature seemed to stress the negative effect of heat treatment in H_2 when TiO_2 is present in an atomic percentage just above 10%. By contrary, when the catalyst was prepared on Pd/C at atomic ratio 1:0.13, it was observed that high temperatures induced a positive effect on the ORR activity. This catalyst, Pd_9(Ti)-H_2-900, presented the same onset potential as Pd/C and the exchange current density was more than the double the value calculated for the latter.

Reports of the influence of titanium oxide in the catalytic activity of Pd and other group VIII metals were found in the literature [22, 27]. For instance, Diebold reviewed the structure and properties of titanium oxide and stated that small additions of titania can modify metal-based catalysts in a profound way [27] due to the so-called Strong Metal-Support Interaction (SMSI). Traditional criterion for SMSI was a rapid reduction of H_2 or CO adsorption capacity, and this has been proved to occur in anatase supported Pd catalysts [28]. The effect of different amounts of anatase in the prepared catalysts was not studied in this piece of work.

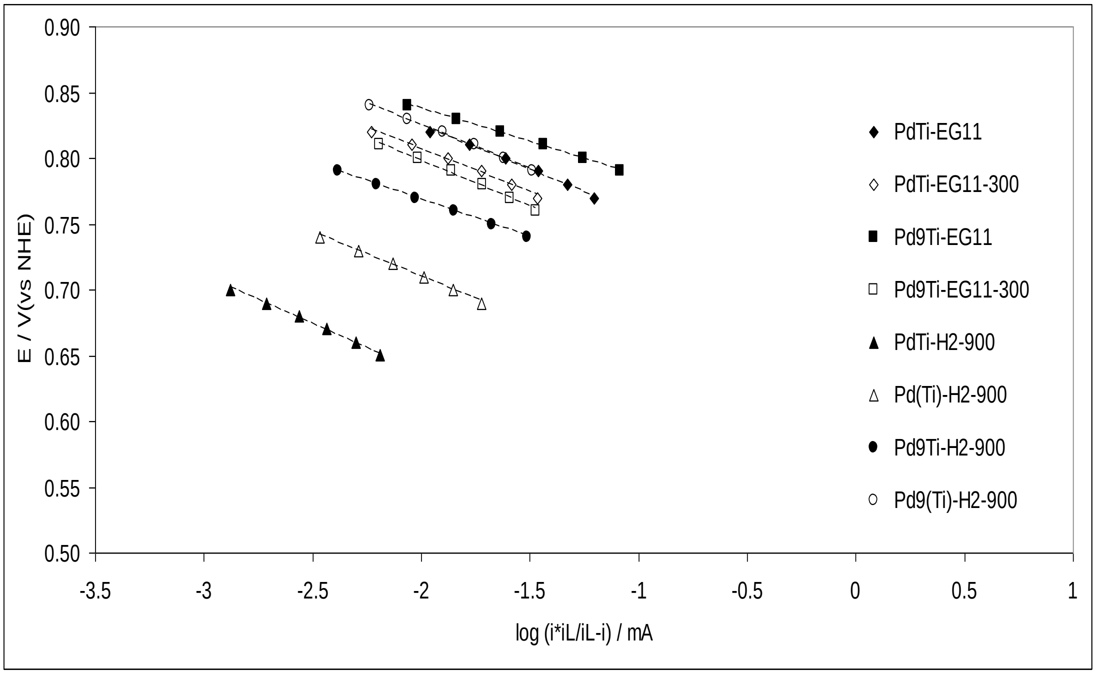

Figure 5-30: Tafel plots for palladium-titanium catalysts.

5.5. Conclusions

Pd-Pd bond distances were estimated from XRD patterns (Scherrer equation) and its values used to determine whether palladium-metal alloy had been formed. Introduction of any other metal atoms in the Pd lattice would cause distortion of the crystal structure since different atoms have different sizes. Pd-Pd bond length for pure carbon-supported Pd was estimated from a large number of samples and found to have an average value of 0.2751 nm, with an associated error of 0.0003 nm. A bond distance value outside the interval 0.2751 ± 0.0006 nm (200% of error) was the criterion used to consider weather palladium-metal alloy had been formed.

Palladium-gold alloys were formed when both metals were co-deposited and reduced in ethylene glycol at 110 ºC. Subsequent heat treatment 300 ºC under H_2 flow increased the extent of the alloy (more uniform composition). On the other hand, no alloy was obtained in any of the palladium-gold electrocatalysts prepared by depositing gold on Pd/C, before or after treating the catalysts at 300 ºC under H_2. The only observed difference in XRD patterns before and after heat treatment was a growth in the Pd particles size. The extent of the sintering of palladium particles undergoing heat treatment was lower compared to pure palladium, this was attributed to the presence of gold.

After electrochemical conditioning in acid electrolyte, gold-rich Pd-Au alloy electrodes present the electrochemical characteristic of a gold electrode. Gold-rich Pd-Au alloy electrodes exhibited Tafel slopes and onset potentials close to pure gold electrodes. The increase in the extent of the alloy by heat treatment led to a decrease of the ORR activity in any case. Also, the vicinity of large amounts of gold nanoparticles decreased the ORR activity of Pd nanoparticles.

No palladium-cobalt catalyst prepared by ethylene glycol reduction without subsequent heat treatment showed Pd-Co alloy formation. To form the Pd–Co alloy, heat treatment at 300 ºC under H_2 flow was necessary. When palladium and cobalt were co-deposited, the presence of different concentrations of cobalt salts did not affect the Pd particle size;

particle sizes were similar to those of pure Pd/C. On the other hand, the presence of cobalt depressed particle sintering during heat treatment at 300 ºC under H_2; smaller particle growth was observed for larger Co contents.

Catalysts with a Co content of ca. Pd:Co 1:0.6 or higher exhibit a decrease in the exchange current density after heat treatment under H_2. Alloying large amounts of Co has a negative impact in the ORR activity. For Co content of ca. Pd:Co 1:0.2, no significant differences in the activity after the alloying process were observed when the catalyst were prepared on Pd/C; however a slight improvement in the ORR activity was exhibited when both metals were co-deposited.

No palladium-iron catalysts prepared by reduction with ethylene glycol showed Pd-Fe alloy formation before heat treatment. Small amounts of Fe atoms are believed to have been introduced in the Pd lattice after heat treatment at 300 ºC under H_2 based on changes in the shape of the cyclic voltammograms compared to pure Pd and small changes in the Pd-Pd bond distance. All Pd-Fe catalysts prepared by reduction under H_2 at 500 ºC showed a typical face-centered cubic pattern with diffraction angles clearly shifted to higher positions compared to those of Pd/C, indicating the formation of Pd-Fe alloy. The presence of iron, likewise gold and cobalt, depressed particle sintering during heat treatment; smaller particle growth was recorded for larger Fe contents. A reduction peak with its maximum at ca. 0.36 V appeared in every Pd-Fe catalyst during the electrode conditioning, which according to the Poubaix diagram for iron in aqueous solution was caused by the reduction of Fe_2O_3 to Fe^{2+}. The area under the peak, and therefore the amount of Fe_2O_3, was larger in unalloyed catalysts.

All palladium-iron catalysts presented ORR activities lower than Pd/C. Introduction of iron in the palladium lattice was found to be detrimental to the ORR, contradicting work published by Shao et al. The highest activities within the Pd-Fe catalysts were exhibited by those prepared on Pd/C. The biggest drops in ORR activity compared to Pd/C where exhibited by catalysts with high iron content (Pd:Fe 3:1).

No significant changes in the Pd-Pd bond distance, compared to Pd/C, were observed for palladium-titanium catalyst prepared either by ethylene glycol reduction, before or after heat treatment at 300 ºC in H_2, or by reduction in H_2 at 900 ºC. However, the average Pd-Pd bond distance for catalysts synthesized by reduction in H_2 at 900 ºC was 0.2747 nm, lower than that of Pd/C by 0.0004 nm. Since Fernández et al. claimed the formation of Pd-Ti alloy based on small shifts in the XRD patterns, the presence of some Pd-Ti alloy could not be completely discarded. The presence of TiO_2 in its anatase form was easily identified from the XRD patters in all Pd-Ti catalysts with high titanium content; catalysts with lower Ti content are also believed to include small amounts of anatase. The presence of TiO_2 did not depress the sintering of Pd nanoparticles during heat treatment in H_2.

Pd-Ti catalysts prepared by EG reduction without heat treatment presented ORR activities close to Pd/C, independently of the amount of TiO_2 present. This activity decreased after heat treatment at 300 ºC in H_2, which was believed to introduce some Ti in the Pd lattice. Catalysts synthesized at high temperatures (900 ºC in H_2) presented lower ORR when the Ti content was high (Pd:Ti 1:1) compared to those with low Ti content (Pd:Ti 9:1). All Pd-Ti catalysts exhibited lower catalytic activity than Pd/C.

In summary, the presence of Au, Co and Fe decreased the degree of sintering of Pd nanoparticles; the presence of Ti did not affect Pd particle growth. Only Pd-Au and Pd-Co exhibited alloy formation using ethylene glycol as reducing agent, in the case of Co heat treatment at 300 ºC under H_2 flow was necessary to form the alloy. Pd-Fe, alloys were only identifiable after reduction at 500 ºC in H_2. No Pd-Ti catalysts exhibited clear alloy formation under any synthetic conditions. Only Pd-Co alloys with atomic ratio Pd:Co 4:1, synthesized by ethylene glycol reduction and after heat treatment at 300 ºC under H_2 flow, exhibited improved ORR activity compared to Pd/C.

References

1. Damjanovic, A., *Mechanism of oxygen reduction related to electronic structure of gold-palladium alloy.* Journal of Physical Chemistry, 1967. **71**(8): p. 2741-2742.

2. Obuchi, A., A. Ogata, K. Mizuno, A. Ohi, and H. Ohuchi, *Properties of Pd-Au and Pt-Cu alloy surfaces for the adsorption and catalytic reduction of O2 and NO by H2.* Colloids Surf., A Full Journal Title:Colloids and Surfaces, A: Physicochemical and Engineering Aspects, 1993. **80**(2-3): p. 121-6.

3. Fernández, J.L., V. Raghuveer, A. Manthiram, and A.J. Bard, *Pd-Ti and Pd-Co-Au Electrocatalysts as a Replacement for Platinum for Oxygen Reduction in Proton Exchange Membrane Fuel Cells.* Journal of the American Chemical Society, 2005. **127**(38): p. 13100-13101.

4. Savadogo, O., K. Lee, K. Oishi, S. Mitsushima, N. Kamiya, and K.I. Ota, *New palladium alloys catalyst for the oxygen reduction reaction in an acid medium.* Electrochemistry Communications, 2004. **6**(2): p. 105-109.

5. Mustain, W.E., K. Kepler, and J. Prakash, *CoPdx oxygen reduction electrocatalysts for polymer electrolyte membrane and direct methanol fuel cells.* Electrochimica Acta, 2006. **52**(5): p. 2102-2108.

6. Zhang, L., K. Lee, and J. Zhang, *Effect of synthetic reducing agents on morphology and ORR activity of carbon-supported nano-Pd-Co alloy electrocatalysts.* Electrochim. Acta Full Journal Title:Electrochimica Acta, 2007. **52**(28): p. 7964-7971.

7. Suo, Y., L. Zhuang, and J. Lu, *First-principles considerations in the design of Pd-alloy catalysts for oxygen reduction.* Angewandte Chemie - International Edition, 2007. **46**(16): p. 2862-2864.

8. Liu, H. and A. Manthiram, *Controlled synthesis and characterization of carbon-supported Pd 4Co nanoalloy electrocatalysts for oxygen reduction reaction in fuel cells.* Energy and Environmental Science, 2009. **2**(1): p. 124-132.

9. Fernández, J.L., D.A. Walsh, and A.J. Bard, *Thermodynamic Guidelines for the Design of Bimetallic Catalysts for Oxygen Electroreduction and Rapid Screening by Scanning Electrochemical Microscopy. M-Co (M: Pd, Ag, Au).* Journal of the American Chemical Society, 2004. **127**(1): p. 357-365.

10. Shao, M., P. Liu, J. Zhang, and R. Adzic, *Origin of enhanced activity in palladium alloy electrocatalysts for oxygen reduction reaction.* Journal of Physical Chemistry B, 2007. **111**(24): p. 6772-6775.

11. F*A*C*T and ChemSage/ChemApp, G., *Facility for the Analysis of Chemical Thermodynamics*

12. Tarasevich, M.R., G.V. Zhutaeva, V.A. Bogdanovskaya, M.V. Radina, M.R. Ehrenburg, and A.E. Chalykh, *Oxygen kinetics and mechanism at electrocatalysts on the base of palladium-iron system.* Electrochimica Acta, 2007. **52**(15): p. 5108-5118.

13. Cullity, B.D., *Elements of X-Ray Diffraction*. 1978: Addison-Wesley.

14. Shao, M.-H., K. Sasaki, and R.R. Adzic, *Pd-Fe Nanoparticles as Electrocatalysts for Oxygen Reduction.* Journal of the American Chemical Society, 2006. **128**(11): p. 3526-3527.

15. Celzard, A., J.F. Mareche, G. Furdin, V. Fierro, C. Sayag, and J. Pielaszek, *Preparation and catalytic activity of active carbon-supported Mo2C nanoparticles.* Green Chemistry, 2005. **7**(11): p. 784-792.

16. Mallát, T., É. Polyánszky, and J. Petró, *Electrochemical study of palladium powder catalysts.* Journal of Catalysis, 1976. **44**(3): p. 345-351.

17. Łukaszewski, M. and A. Czerwiński, *Electrochemical behavior of palladium-gold alloys.* Electrochimica Acta, 2003. **48**(17): p. 2435-2445.

18. Hoare, J.P., *A Cyclic Voltammetric Study of the Gold-Oxygen System.* Journal of The Electrochemical Society, 1984. **131**(8): p. 1808-1815.

19. Damjanovic, A. and V. Brusic, *Oxygen reduction at Pt-Au and Pd-Au alloy electrodes in acid solution.* Electrochimica Acta, 1967. **12**(9): p. 1171-1184.

20. Rand, D.A.J. and R. Woods, *A study of the dissolution of platinum, palladium, rhodium and gold electrodes in 1 m sulphuric acid by cyclic voltammetry.* Journal of Electroanalytical Chemistry, 1972. **35**(1): p. 209-218.

21. Pourbaix, M., *Atlas of Electrochemical Equilibria in Aqueous Solutions*. 2nd ed. 1974, Houston: National Association of Corrosion Engineers.

22. Kim, J.H., A. Ishihara, S. Mitsushima, N. Kamiya, and K.I. Ota, *Catalytic activity of titanium oxide for oxygen reduction reaction as a non-platinum catalyst for PEFC.* Electrochimica Acta, 2007. **52**(7): p. 2492-2497.

23. Gnanamuthu, D.S. and J.V. Petrocelli, *A Generalized Expression for the Tafel Slope and the Kinetics of Oxygen Reduction on Noble Metals and Alloys.* Journal of The Electrochemical Society, 1967. **114**(10): p. 1036-1041.

24. Bron, M., *Carbon black supported gold nanoparticles for oxygen electroreduction in acidic electrolyte solution.* Journal of Electroanalytical Chemistry, 2008. **624**(1-2): p. 64-68.

25. Shao, M.H., T. Huang, P. Liu, J. Zhang, K. Sasaki, M.B. Vukmirovic, and R.R. Adzic, *Palladium Monolayer and Palladium Alloy Electrocatalysts for Oxygen Reduction.* Langmuir, 2006. **22**(25): p. 10409-10415.

26. Xiong, L. and A. Manthiram, *Nanostructured Pt-M/C (M = Fe and Co) catalysts prepared by a microemulsion method for oxygen reduction in proton exchange membrane fuel cells.* Electrochimica Acta, 2005. **50**(11): p. 2323-2329.

27. Diebold, U., *Structure and properties of TiO_2 surfaces: A brief review.* Applied Physics A: Materials Science and Processing, 2003. **76**(5): p. 681-687.

28. Li, Y., Y. Fan, H. Yang, B. Xu, L. Feng, M. Yang, and Y. Chen, *Strong metal-support interaction and catalytic properties of anatase and rutile supported palladium catalyst Pd/TiO_2.* Chemical Physics Letters, 2003. **372**(1-2): p. 160-165.

Chapter 6: Hydrogen fuel cell tests

6.1. Introduction

Two of the synthesized catalysts reported in previous chapters were tested as cathode materials in a low temperature PEMFC using Nafion® at different temperatures with hydrogen. Two catalysts were chosen, the optimised carbon-supported palladium, Pd-EG11, and a palladium-cobalt catalyst, Pd_4Co-EG11-300. Commercial Pt/C from E-Tek was used as a benchmark.

Pd-EG11 was tested as cathode material at two different metal loadings, 0.6 and 1.0 mg cm^{-2}. Since palladium is considerably cheaper than platinum, the use of larger amounts of Pd in the cell cathode in order to match or surpass the performance of a Pt cathode would still be economically advantageous. The effect of the thickness of the catalyst layer was also discussed.

6.2. Low temperature polymer electrolyte membrane fuel cell tests

6.2.1. Evaluation of carbon-supported palladium nanoparticles

The optimized carbon-supported palladium, Pd-EG11, prepared by reduction of the palladium precursor with ethylene glycol on Vulcan XC-72R, was tested as a cathode catalyst in a low temperature hydrogen PEM fuel cell at 20, 40 and 60 ºC. Cathode loading was set to 0.6 mg cm^{-2} and its performance was compared to that of commercial Pt/C from E-tek.

Figure 6-1 shows polarization curves at scan rate 5 mV s^{-1} of the Pd MEA with air fed to the cathode. At 20 and 40 ºC potential losses due to catalyst activation (occurring in the low current densitity region) were hardly observed in the polarization curve. This kinetic region was believed to be masked by the overpotential caused by H_2 crossover, as discussed further on in this chapter. Open circuit potential (OCP) for the Pd MEA at 20 and 40 ºC was ca. 0.71 and 0.75 V, repectively. At 60 ºC the OCP decreased to ca. 0.68 V. This decrease in OCP was attributed to a lower oxygen concentration at the catalyst surface caused by smaller oxygen permeability in Nafion® with lower water content.

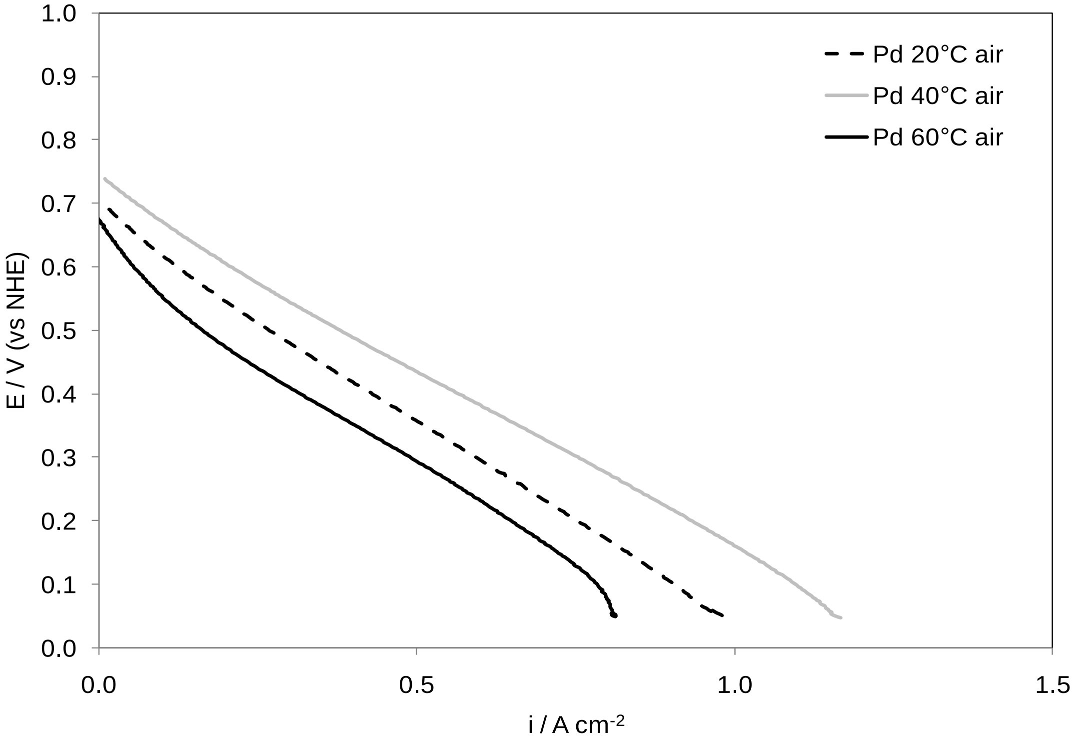

Figure 6-1: Polarization curves of a low temperature polymer electrolyte membrane fuel cell with carbon-supported Pd nanoparticles as cathode catalyst at 20, 40 and 60 ºC operating with air.

This lower oxygen permeability at 60 ºC compared to 20 and 40 ºC was suggested by the limiting current exhibited at 60 ºC. Limiting current density was not observed when tests were carried out at 20 and 40 ºC but was ca. 0.8 A cm^{-2} when the temperature was further increased to 60 ºC. The presence of a limiting current indicates oxygen starvation; this supports the hypothesis of lower water content in the electrode, which would affect the oxygen supply. While oxygen permeability in Nafion® increases with temperature up to 80 ºC for a given water content, it decreases sharply with decreasing water content, especially at higher temperatures (the dependence of oxygen permeability in Nafion® on water content increases with temperature) [1]. For a given relative humidity, water content in Nafion® decreases with increasing temperature [2] and for a given water vapor pressure, relative humidity decreases with increasing temperature [3]. Therefore the water content in Nafion® was lower at 60 ºC and as a consequence the oxygen permeability was lower.

Current densities exhibited by the Pd-EG11 MEA with air fed in the cathode (Table 6-1) increased when the fuel cell operating temperature was raised from 20 to 40 ºC, from 0.06 to 0.13 A cm^{-2} at 0.65 V. When the temperature was further increased to 60 ºC the current density decreased to 0.02 A cm^{-2} at 0.65 V.

Figure 6-2 shows polarization curves obtained with the Pd MEA, at scan rate 5 mV s^{-1}, with oxygen fed to the cathode. The effect of the temperature increase was different to the air fed cathode, the important performance loss at 60 ºC was not observed. In curves at 20 and 40 ºC the activation region was hardly observed. Open circuit potentials at 20, 40 and 60 ºC were ca. 0.75 and 0.80 and 0.79 V, respectively. The smaller decrease in the OCP and the slight increase in current density at low potentials when the temperature was increased from 40 to 60 ºC, compared to the air fed cathode, could be explained by a higher oxygen concentration when pure oxygen was used. Since dryness reduced the oxygen permeability through the Nafion® in the catalyst layer, and the permeability is proportional to the concentration [4], the effect would be more dramatic in air because the O_2 concentration is only 21%.

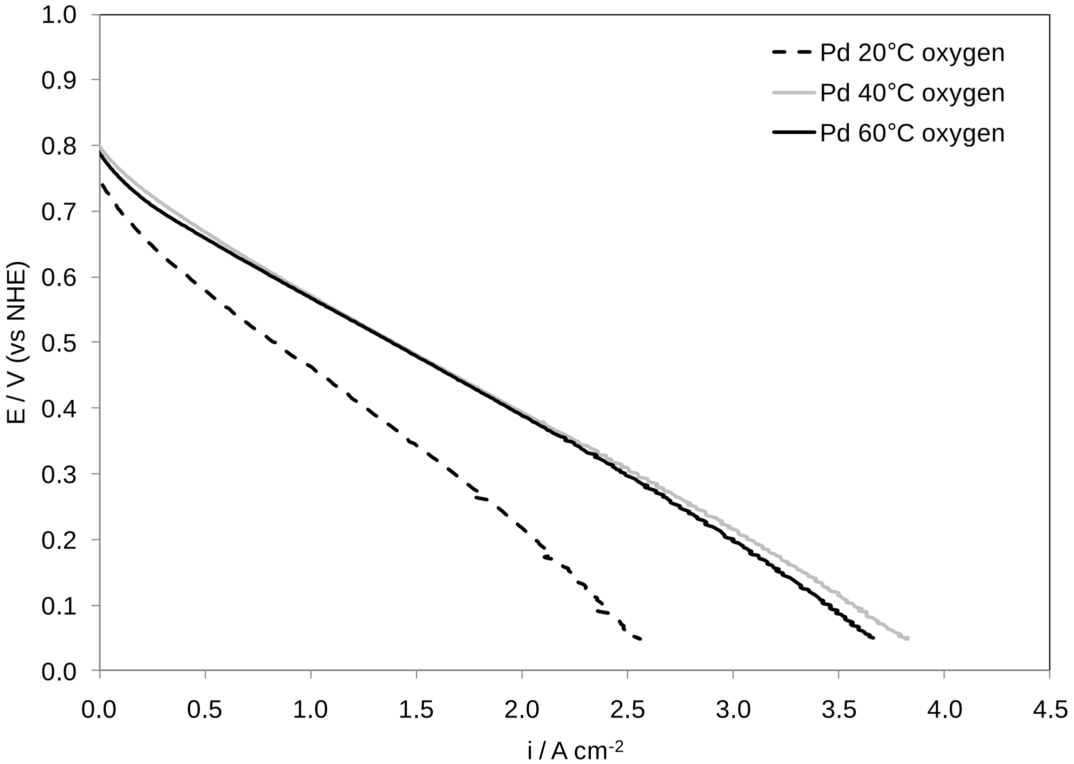

Figure 6-2: Polarization curves of a low temperature polymer electrolyte membrane fuel cell with carbon-supported Pd nanoparticles as cathode catalyst at 20, 40 and 60 ºC operating with oxygen.

With O_2 (Figure 6-2) current densities at 0.65 V increased when the cell temperature increased from 20 to 40 ºC from 0.24 to 0.59 A cm^{-2}, and when the temperature was further increased to 60 ºC the current density slightly decreased to 0.54 A cm^{-2}. Current densities exhibited by the different MEAs at 0.65 V are given in Table 6-1.

Table 6-1: Current densities at 0.65 V and peak power densities for low temperature PEMFC at different conditions and with different electrocatalysts in the cathode.

Cathode catalyst	**Temperature (ºC)**	**Cathode fed**	**Current density at 0.65 V (A cm^{-2})**	**Peak power density (mW cm^{-2})**
Pd-EG11	20	Air	0.06	182
Pd-EG11	20	O_2	0.24	516
Pd-EG11	40	Air	0.13	183
Pd-EG11	40	O_2	0.59	779
Pd-EG11	60	Air	0.02	147
Pd-EG11	60	O_2	0.54	782
Pd_4Co-EG11-300	20	Air	0.12	188
Pd_4Co-EG11-300	20	O_2	0.34	538
Pd_4Co-EG11-300	40	Air	0.21	233
Pd_4Co-EG11-300	40	O_2	0.65	790
Pd_4Co-EG11-300	60	Air	0.04	120
Pd_4Co-EG11-300	60	O_2	0.50	671
Pt/C-Etek	20	Air	0.20	255
Pt/C-Etek	20	O_2	0.66	667
Pt/C-Etek	40	Air	0.24	336
Pt/C-Etek	40	O_2	0.92	913
Pt/C-Etek	60	Air	0.16	255
Pt/C-Etek	60	O_2	1.08	1,040

Cell resistance values were measured, using an AC frequency response analyser, for the Pd-EG11 MEA at 20, 40 and 60 ºC were 92, 73 and 67 mΩ, respectively. Resistance decreased with increasing temperature as expected, which suggested the poor performance at 60 ºC was not a resistance issue, but oxygen mass transport.

Failure of the catalyst activity to increase with temperature after 40 ºC, with both air and oxygen, following Arrhenius behavior, was attributed to electrode dryness. Dryness would have reduced the oxygen concentration on the catalyst surface and that would counter the kinetic enhancement due to the temperature increase. Dryness (low water content) decreased oxygen permeability in Nafion®, and since this also depends on the oxygen concentration, the effect was more severe operating with low oxygen concentration (air). Since only the anode stream was humidified electrode dryness was uniquely affecting the cathode; the anode humidification provided enough water to humidify also the membrane, as concluded from the membrane resistance measurements (the conductivity of the membrane increased with temperature as expected in a fully hydrated membrane).

To confirm the hypothesis of the dryness a probe was introduced in the cell to measure the relative humidity. At 20 ºC (humidifier at 30 ºC), 40 ºC (humidifier at 50 ºC) and 60 ºC (humidifier at 70 ºC) relative humidity was 88, 94 and 73%, respectively. These measurements illustrated how relative humidity at 60 ºC was lower (causing electrolyte dryness). This shows the high sensitivity of Nafion® based systems to the system water management.

To confirm dryness as the cause of the performance loss at 60 ºC further tests were done. The humidifier temperature was increased from 70 to 80 ºC while the cell temperature was maintained at 60 ºC and a new polarization curve was recorded (Figure 6-3). The cell performance at 60 ºC with the humidifier at 80 ºC exhibited higher current densities compared to that with the humidifier at 70 ºC. The probe introduced to measure the humidity showed that the relative humidity with the humidifier at 80 ºC increased to 86% compared to 73%.

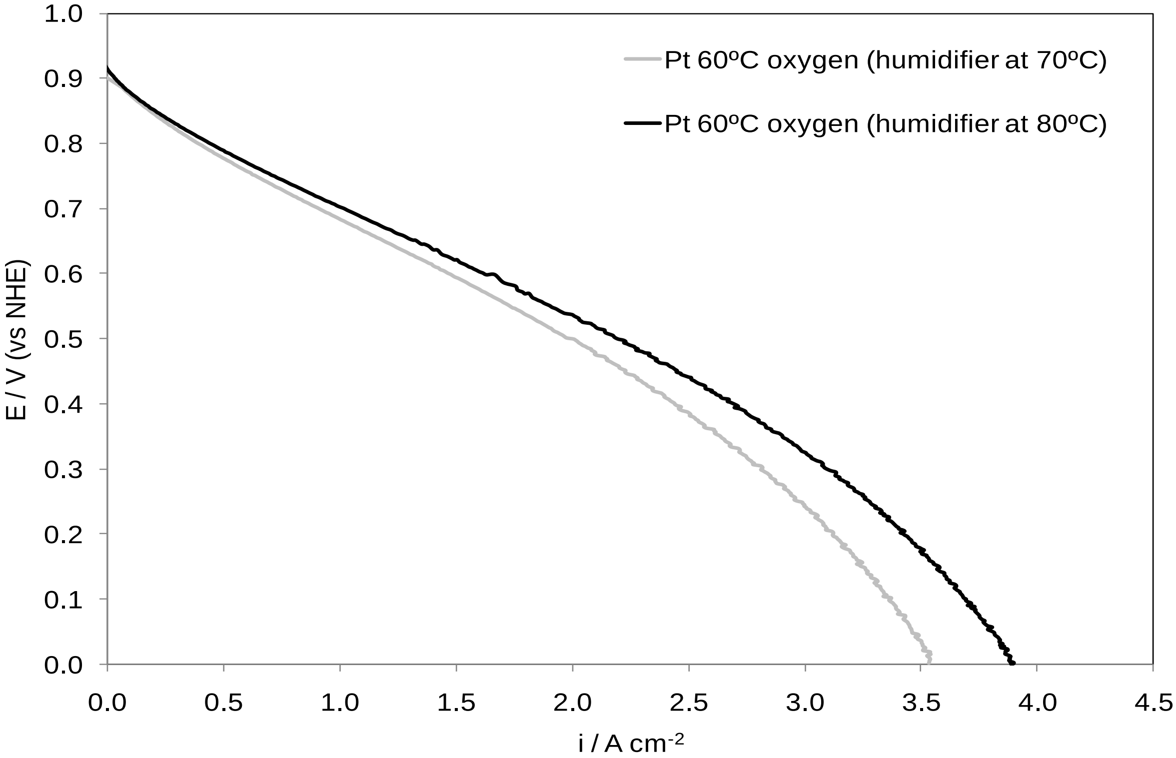

Figure 6-3: Polarization curves of a low temperature polymer electrolyte membrane fuel cell with Pt–Etek as cathode catalyst at 60 ºC operating with oxygen with the humidifier at 70 and 80 ºC.

Figure 6-4 shows cell polarization curves of the MEA prepared using commercial Pt/C as catalyst for the ORR (Pt/C-Etek MEA) with air fed to the cathode. In all three curves the activation region could be seen, unlike for the Pd MEA, the smallest activation losses were at 40 ºC. Open circuit potentials at 20 and 40 ºC were ca. 0.93 V. At 60 ºC the OCP fell to ca. 0.83 V, in a similar way observed with the Pd-EG11 MEA. The decrease in open circuit potential when increasing the temperature from 40 to 60 ºC was accompanied by a decreased performance in the low current density region. The polarization curve at 40 ºC showed some mass transport limitations at ca. 1.0 A cm^{-2} whilst at 60 ºC these limitations showed at ca. 0.8 A cm^{-2}. Decrease in the OCP and current density also occurred in the Pt/C-Etek MEA consistent with the hypothesis that the system was suffering from electrode dryness when operated at 60 ºC.

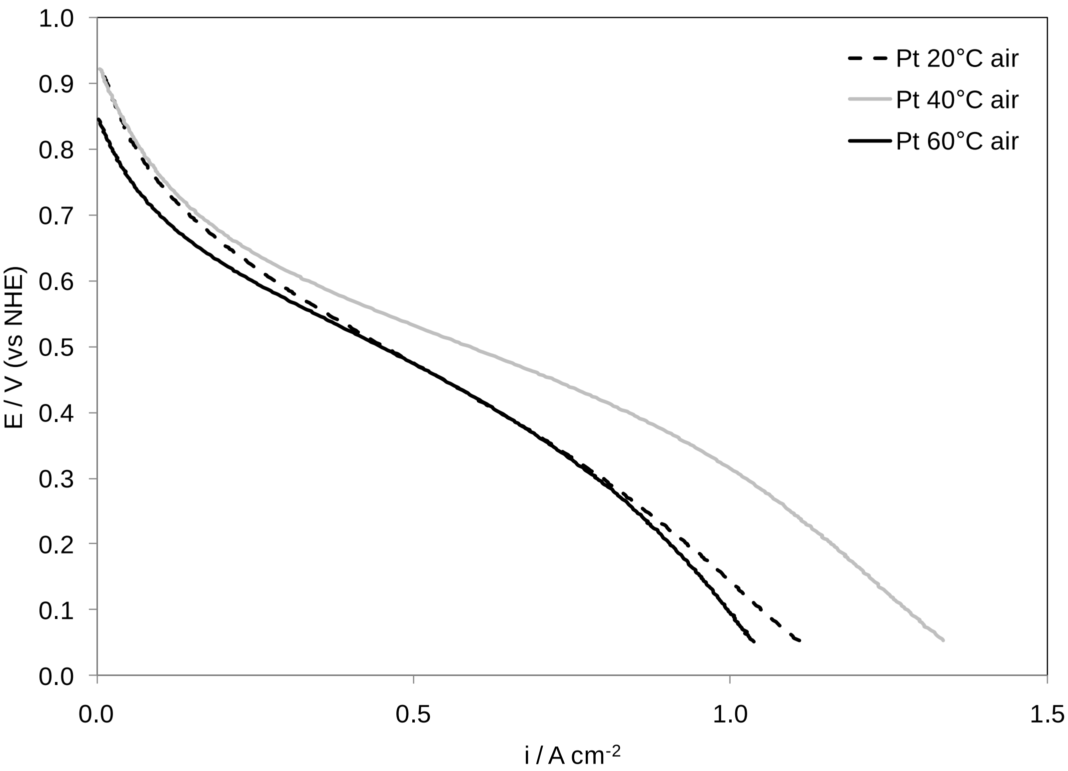

Figure 6-4: Polarization curves of a low temperature polymer electrolyte membrane fuel cell with commercial carbon-supported Pt as cathode catalyst at 20, 40 and 60 ºC operating with air.

Figure 6-5 shows polarization curves of the Pt MEA with oxygen fed to the cathode. In all three curves the activation region could be seen, here activation losses decreased with raising temperature as expected by the increase of the exchange current density with the temperature. Onset potentials at 20, 40 and 60 ºC were ca. 0.95, 0.96 and 0.95 V, respectively. Polarization curves of Pt/C-Etek MEA exhibited mass transport limitations at 20, 40 and 60 ºC from ca. 2.2, 3.0 and 3.4 A cm^{-2} with O_2, respectively. In both, air and O_2 current densities increased when the temperature was raised from 20 to 40 ºC. At 60 ºC, with air, current densities were lower than that exhibited at 20 ºC, the same behavior was observed for Pd-EG11 MEA. With O_2 current densities increased with each temperature rise, although the increase from 40 to 60 ºC was smaller than that from 20 ºC to 40 ºC. The failure of cell performance to increase with temperature from 20 ºC to 40 ºC, together with the observed low limiting current at 60 ºC, again suggested a decrease in oxygen supply to the cathode at 60 ºC compared with 40 ºC caused by electrode dryness.

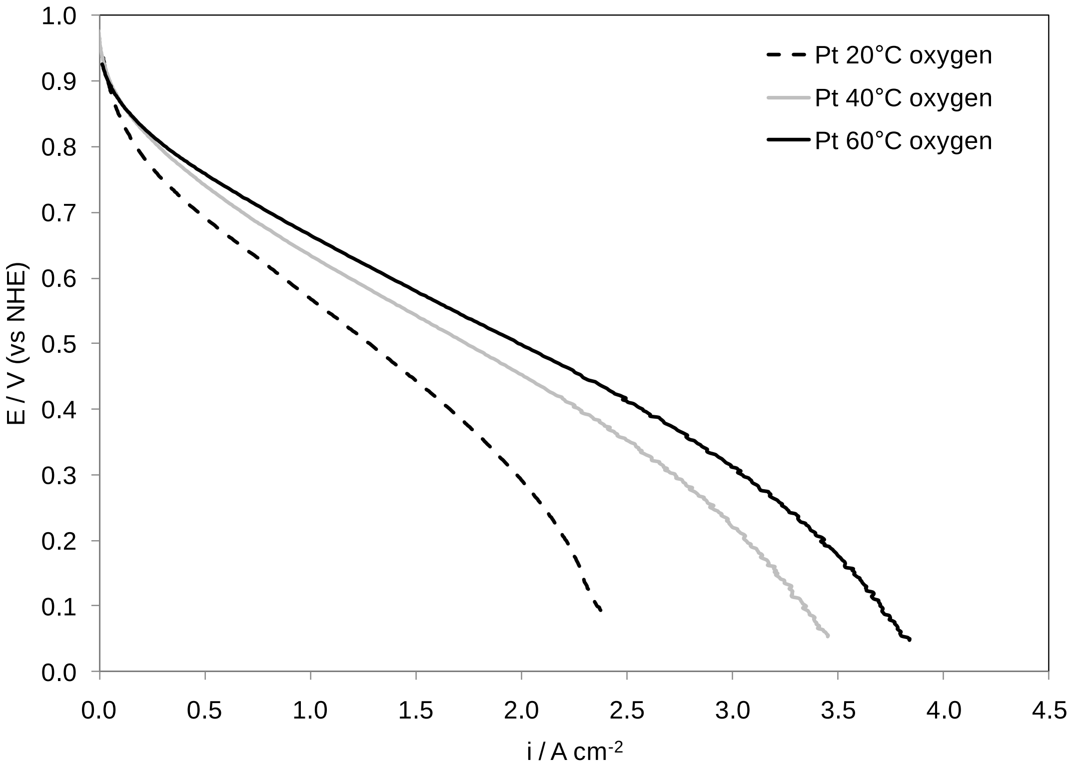

Figure 6-5: Polarization curves of a low temperature polymer electrolyte membrane fuel cell with commercial carbon-supported Pt as cathode catalyst at 20, 40 and 60 ºC operating with oxygen.

Figure 6-6 compares cell polarization curves of Pd-EG11 and Pt/C-Etek MEAs recorded at 20 ºC with oxygen and air. A difference of approximately 200 mV in the open circuit potential (OCP) between Pd and Pt was observed in both oxygen and air polarization curves at room temperature. In the three-electrode cell with liquid electrolyte Pd/C already presented an onset potential of 0.89 V vs NHE characterization, 70 mV lower than Pt/C from E-tek prior to any hydrogen crossover effects encountered in the fuel cell environment.

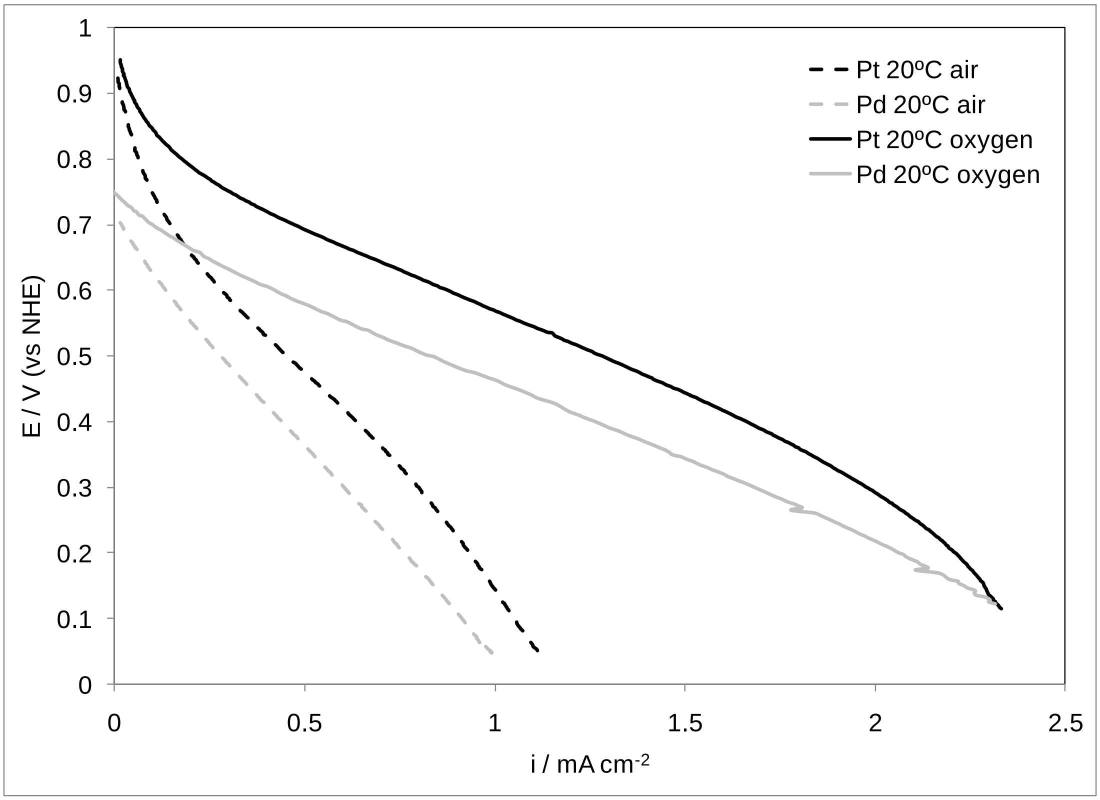

Figure 6-6: Comparison of polarization curves of a low temperature polymer electrolyte membrane fuel cell with carbon-supported Pd nanoparticles and commercial Pt/C from E-tek as cathode catalyst at 20 ºC.

The observed OCP in a fuel cell is always lower than the estimated value from the thermodynamics (1.23 V for oxygen reduction) due to the effect of crossover and other phenomena like carbon corrosion [5]. The increased difference in the OCP between Pd and Pt when tested in the PEM fuel cell compared to the half cell tests can be explained by H_2 crossover through the electrolyte membrane. The impact of this crossover was higher in Pd due to its lower exchange current density for ORR. This can be explained as follows:

The crossover effect on OCP has been accounted by modeling the flux of hydrogen through the membrane and by considering the total current as the sum of the two partial currents for hydrogen oxidation and oxygen reduction at the cathode:

$$i_C = i_{C,O_2} + i_{C,H_2} \tag{6.1}$$

Where $i_{C,O2}$ is the current density for oxygen reduction at the cathode and $i_{C,H2}$ is current density for (crossed-over) hydrogen oxidation in the cathode.

At open circuit conditions the current i_C is zero:

$$i_{C,O_2} + i_{C,H_2} = 0 \tag{6.2}$$

While $i_{C,H2}$ is limited by the hydrogen crossover rate through the membrane, adapting Fick's law for diffusion can be written:

$$\frac{i_{C,H_2}}{nFA} = \frac{Permeability}{\delta} \tag{6.3}$$

Where n is number of electrons involved in hydrogen oxidation (n=2), F faraday constant, A is cell geometric area (1 cm^2) and δ is the Nafion® membrane thickness (50µm). Using hydrogen permeability value of 1.8 x 10^{-11} mole cm^{-1} s^{-1} [6] a value of 0.7 mA cm^{-2} for $i_{C,H2}$ was obtained.

The over potential loss due to crossover, $\eta_{crossover}$, is the sum of losses of hydrogen oxidation overpotential, $\eta_{C,H2}$, and oxygen reduction overpotential, $\eta_{C,O2}$, at the cathode at current $i_{C,H2}$ = 0.7 mA cm^{-2}.

The relation between current density and potential loss can be expressed by the Butler-Volmer equation as:

$$i = i_0 \left[\exp\left(\frac{-\alpha_c F}{RT} \eta \right) - \exp\left(\frac{\alpha_a F}{RT} \eta \right) \right] \tag{6.4}$$

Where η is the overpotential, i is the current density, i_0 is the exchange current density and α_a and α_c are the transfer coefficients of the anodic and cathodic reactions, respectively. Assuming α_a=α_c=α, the hyperbolic sine function can be substituted in equation 6.1 yielding the following relationship:

$$i_{C,O_2} = 2i_{0,ORR}\sinh\left(\frac{-\alpha F}{RT}\eta_{C,O_2}\right) \tag{6.5}$$

$$i_{C,H_2} = 2i_{0,HOR}\sinh\left(\frac{-\alpha F}{RT}\eta_{C,H_2}\right) \tag{6.6}$$

Where $i_{C,H2}$= $i_{C,O2}$ at OCP, $i_{0,ORR}$ is the apparent oxygen reduction exchange current density and $i_{0,HOR}$ is the apparent hydrogen oxidation exchange current density at the cathode.

The apparent exchange current density for oxygen reduction, $i_{0,ORR}$, was calculated as the product of the exchange current density for ORR obtained from the half cell tests, 1.4 x 10^{-10} A cm^{-2}, the ECSA, 550 cm^2 mg^{-1}, and the metal loading, 0.6 mg cm^{-2}, and resulted 4.62 x 10^{-8} A cm^{-2} for platinum. The transfer coefficient α was also taken as 1 (see chapter 4). Similarly for palladium we can write the product of 7.7 x 10^{-12} A cm^{-2}, the ECSA, 150 cm^2 mg^{-1}, and the metal loading, 0.6 mg cm^{-2}, and was 6.93 x 10^{-10} A cm^{-2}.

Substituting the values above into Equation 6.5 obtained values of $\eta_{C,O2}$ were 260 and 373 mV for the Pt and Pd cathodes, respectively.

The hydrogen oxidation overpotential, $\eta_{C,H2,}$ could be ignored due to the high value of the exchange current density of hydrogen oxidation on Pt and Pd (1 and 1.28 mA.cm^{-2}, respectively [6]). $\eta_{C,H2}$ values calculated for these exchange current densities were 0.015 and 0.13 mV for Pt and Pd, respectively (considering Tafel slopes of 32 mV dec^{-1} for Pt and 100 mV dec^{-1} for Pd [7]). The calculated $\eta_{crossover}$ for the palladium MEA was 0.113 V larger than for platinum for the same crossover rate.

The high value of the overpotential losses caused by the crossover at low current densities (373 mV) masked the kinetic region of the polarization curve for Pd MEA were polarization curves started from low OCP of ca. 750 mV with oxygen. This is observed in Figure 6-6, Figure 6-7 and Figure 6-8, where the activation region could hardly be seen.

Polarization curves of Pd-EG11 and Pt-Etek MEAs have approximately the same slope in the ohmic region, indicating that the resistance and the transport of reactants are similar in both. At room temperature and operating with pure O_2, recorded current densities at 0.65 V for Pd and Pt MEAs were 0.24 and 0.66 A cm^{-2}, respectively. For a given current density of 1 A cm^{2}, cell potentials were 0.46 V for Pd and 0.57 V for Pt. This was translated into a constant difference of 110 mV in the ohmic region between Pd and Pt. When air was fed to the cathode, current densities for Pd and Pt MEAs at 0.65 V were 0.06 and 0.20 A cm^{-2} respectively. Cell potentials at 0.5 A cm^{-2} were 0.33 V for Pd and at 0.45 for Pt, respectively; therefore a 120 mV difference existed between the polarization curves.

Figure 6-7 shows cell polarization curves at 40 ºC. At this temperature operating with pure O_2 in the cathode, for Pd and Pt at 0.65 V, the cell exhibited current densities of 0.59 and 0.52 A cm^{-2}, respectively. For a given current density of 1 A cm^{-2}, cell potentials were 0.57 V for Pd and 0.63 for Pt. Thus, a constant difference of 60 mV was present in the ohmic region. When air was fed to the cathode, recorded current densities at 0.65 V were 0.13 and 0.24 A cm^{-2} for Pd and Pt MEAs. Cell potentials at 0.5 A cm^{-2} were 0.45 V for Pd and at 0.52 for Pt, respectively; therefore 70 mV difference existed between the polarization curves.

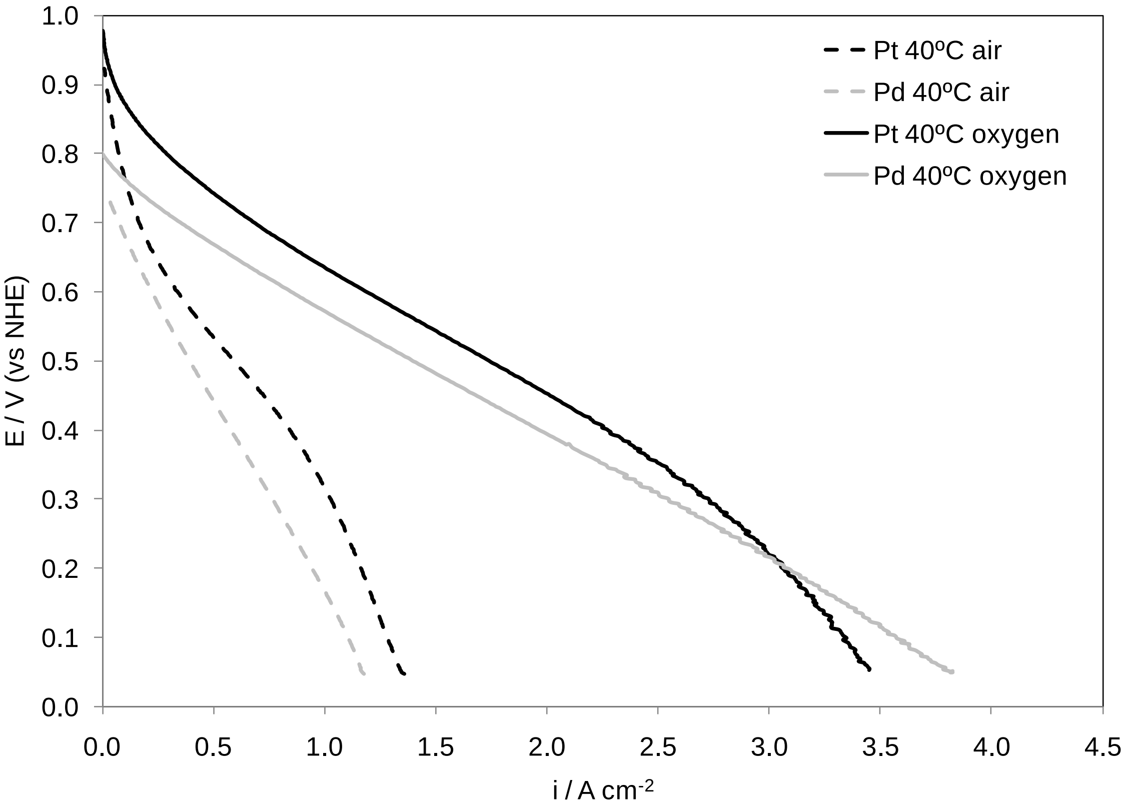

Figure 6-7: Comparison of polarization curves of a low temperature polymer electrolyte membrane fuel cell with carbon-supported Pd nanoparticles and commercial Pt/C from E-tek as cathode catalyst at 40 ºC.

The observed decrease in the difference between Pt and Pd performances with temperature, from 20 to 40 ºC, from 110 to 60 mV could be explained by the higher activation energy of oxygen reduction reaction on Pd/C, ca. 90 KJ mol^{-1} [8], compared to that on Pt, ca. 26 KJ mol^{-1} [9]. According to the Arrhenius equation (equation 6.1), the rate of a reaction with higher activation energy will be more dependent on the temperature. Therefore, for the same increase in the fuel cell temperature there would have been a larger increase in the activity of Pd, compared to Pt.

Figure 6-8 shows cell polarization curves of Pt and Pd MEAs at 60 ºC. At this temperature, operating with pure O_2 in the cathode, recorded current densities at 0.5 V were 1.38 and 1.98 A cm^{-2} for Pd and Pt, respectively. For a given current density, 2 A cm^{-2}, cell potentials were 0.39 V for Pd and 0.49 V for Pt. Thus, a constant difference of

100 mV was observed in the ohmic region (larger than the difference at 40 ºC). When air was fed to the cathode, recorded current densities at 0.5 V were, 0.16 and 0.45 A cm^{-2} for Pd and Pt MEAs, respectively. Cell potentials at 0.5 A cm^{-2} were 0.30 V for Pd and at 0.45 V for Pt, respectively; therefore 150 mV difference existed between the polarization curves. Peak power densities obtained from the Pd-EG11 and Pt-Etek MEAs when O_2 was fed to the cathode were 782 and 1040 mW cm^{-2}, respectively. The increased difference between Pd and Pt MEA at 60 ºC compared to 40 ºC is caused by concentration decrease of O_2 in the electrode causing higher losses in Pd than Pt because of its lower exchange current density. This also can be seen by larger difference between air and oxygen operation of Pd and Pt; the difference was 10 mVat 40 ºC (50 to 60 mV) and it increased to 50 mV at 60 ºC (100 to 150 mV).

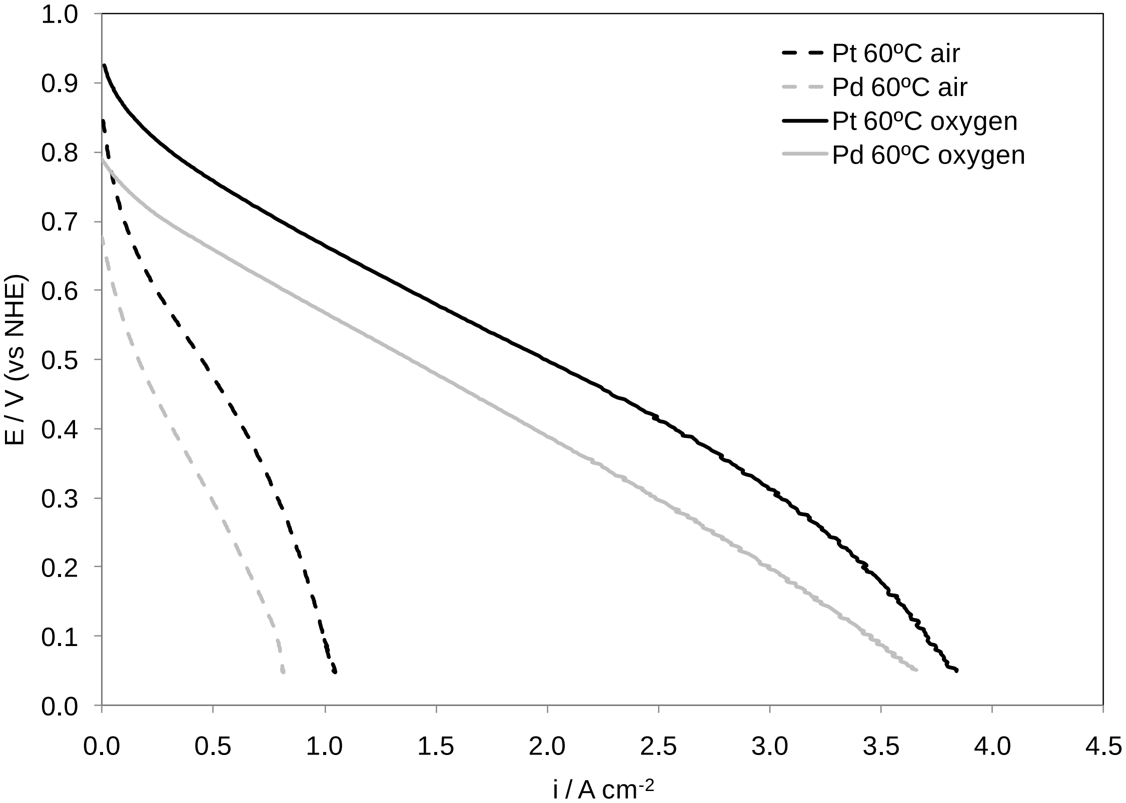

Figure 6-8: Comparison of polarization curves of a low temperature polymer electrolyte membrane fuel cell with carbon-supported Pd nanoparticles and commercial Pt/C from E-tek as cathode catalyst at 60 ºC.

In the literature, reported activities for Pt and Pd as cathode materials were lower than data collected during this study. For instance Fiçicilar et al. [10] reported activities of carbon-supported Pd and Pt nanometric particles, at 0.65 V current densities were ca. 0.02 and 0.18 A cm^{-2}, and cell potentials at 0.5 A cm^{-2} ca. 0.24 and 0.35 V, respectively. This performance was in a PEM operating with pure H_2 and O_2 at 70 ºC with a metal loading of 0.4 mg cm^{-2} in both anode and cathode. Homemade MEAs for Pd and Pt cathodes exhibited cell potentials of ca. 0.58 and 0.69 V at 0.5 A cm^{-2}, respectively. The potential difference between Pd/C and Pt/C is in both cases 110 mV, in Fiçicilar's and this study. Considerably lower activity for Pd on Vulcan was reported by Moreira et al. [11], with OCP lower than 0.6 V and current density values of ca. 0.04 A cm^{-2} at 0.5 V. This performance was in a PEM operating with pure H_2 and O_2 at room temperature with a metal loading of 0.4 mg cm^{-2} in the anode and 1 mg cm^{-2} in the cathode.

6.2.2. Evaluation of carbon supported bimetallic Pd-M nanoparticles

Polarization curves at scan rate 5 mV s^{-1} of the MEA prepared using carbon-supported Pd_4Co-EG11-300 as catalyst for the ORR (Pd-Co MEA) were recorded at 20, 40 and 60 ºC with air and oxygen fed to the cathode.

Figure 6-9 shows polarization curves of the Pd-Co MEA with air fed to the cathode. As for the Pd MEA, in the curves at 20 and 40 ºC the activation region, at low current densities, was hardly observed. In an analogous way to the Pd MEA, the kinetic region was believed to be masked by the overpotential caused by H_2 crossover. Onset potentials for the curves at 20 and 40 ºC were ca. 0.78 and 0.80 V, once again a decrease in the onset potential at 60 ºC was recorded, to ca. 0.73 V. Limiting current densities were ca. 1.05 A cm^{-2} at 40 ºC, 0.7 A cm^{-2} at 60 ºC and approached 0.95 at 20 ºC.

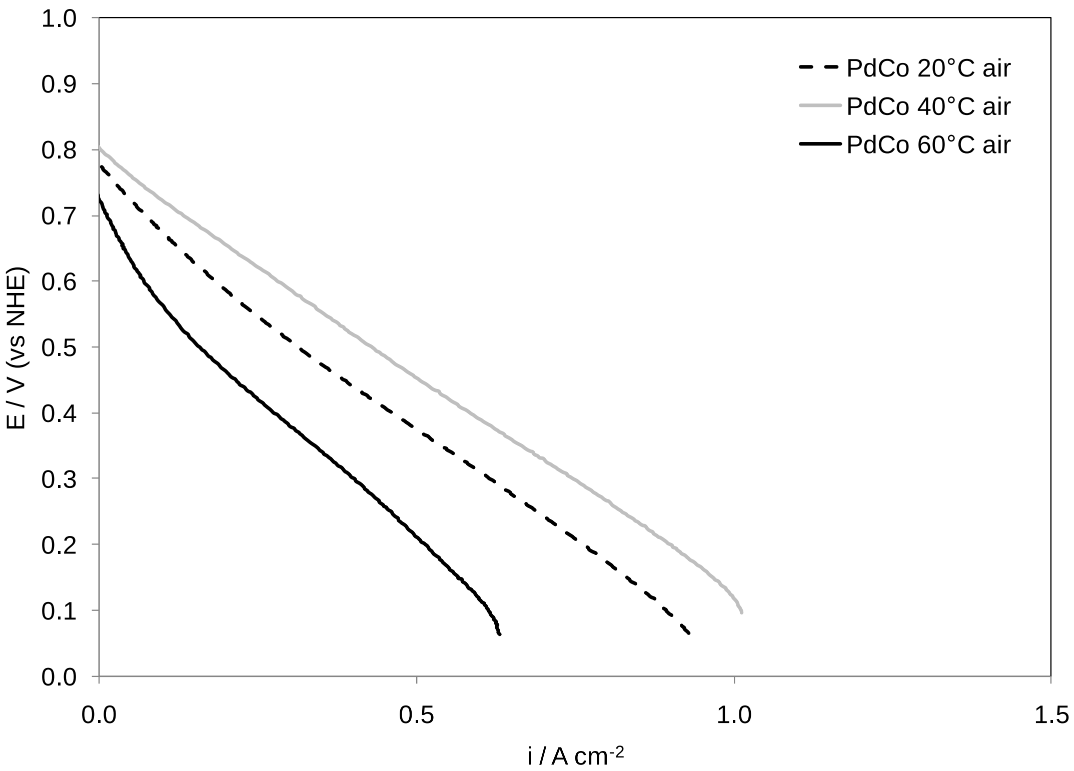

Figure 6-9: Polarization curves of a low temperature polymer electrolyte membrane fuel cell with carbon-supported Pd-Co nanoparticles as cathode catalyst at 20, 40 and 60 ºC operating with air.

In Figure 6-10 polarization curves of the Pd-Co MEA with O_2 fed to the cathode are shown. At 20 and 40 ºC the activation region was again hardly observed, only some activation was observed at 60 ºC. Onset potentials for the curves at 20, 40 and 60 ºC were ca. 0.75 and 0.80 V and 0.79, respectively.

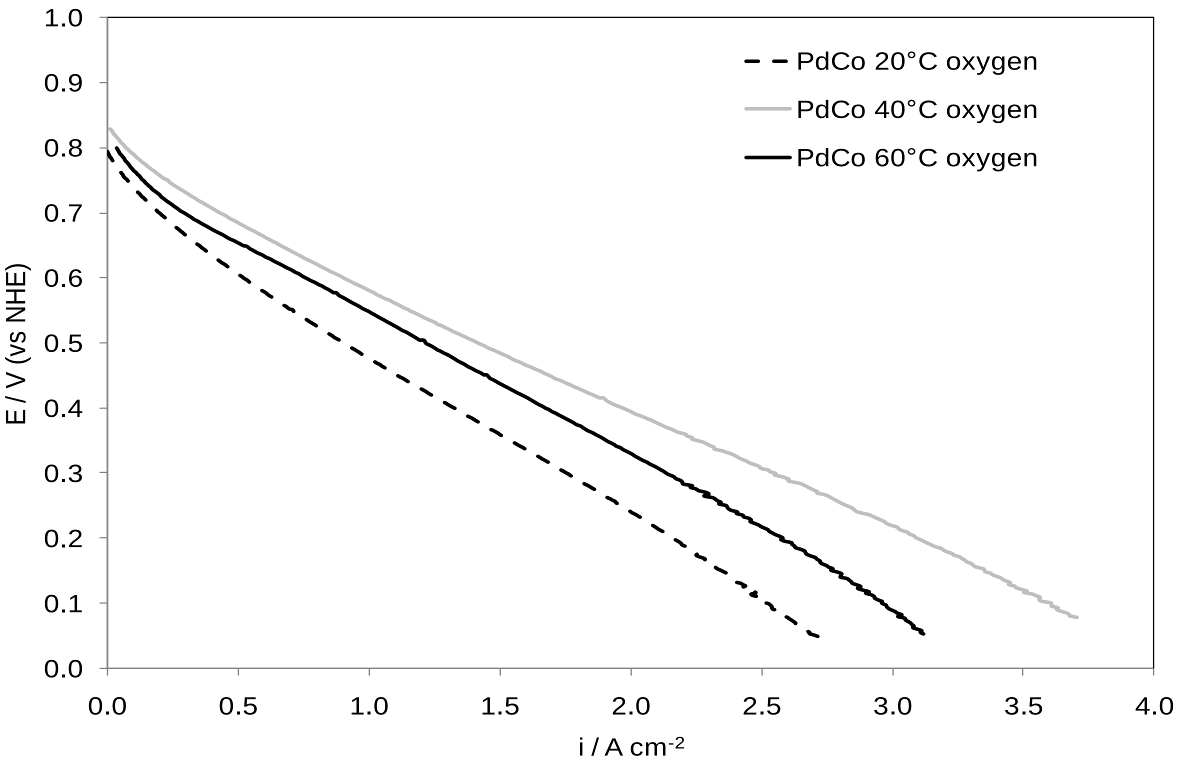

Figure 6-10: Polarization curves of a low temperature polymer electrolyte membrane fuel cell with carbon-supported Pd-Co nanoparticles as cathode catalyst at 20, 40 and 60 ºC operating with oxygen.

Current densities exhibited by the Pd-Co MEA with air fed in the cathode (Figure 6-9) at 0.65 V operating at 20 and 40 ºC were 0.12 and 0.21 A cm^{-2}. When the temperature was further increased to 60 ºC the observed current density decreased to 0.04 A cm^{-2} at 0.65 V.

Current densities at 0.65 V increased from 0.34 to 0.65 A cm^{-2} when the fuel cell operating temperature was raised from 20 to 40 ºC. When the temperature was further increased to 60 ºC the current density decreased to 0.50 A cm^{-2} at 0.65 V. The behavior of this MEA was very similar to that of Pd-EG11 MEA, and by analogy, this lack of improvement with temperature, following Arrhenius behavior, was attributed to electrode dryness.

Figure 6-11 compares cell polarization curves of Pd-Co and Pd MEAs at 20 ºC. Open circuit potentials were higher for Pd-Co MEA in air, by ca. 70 mV, and oxygen, by ca. 50

mV. Kinetic losses were also slightly lower for Pd-Co and, as a consequence differences in the ohmic region were only 30 mV for air and 10 mV for oxygen. At 20 ºC operating with pure O_2 current densities at 0.65 V were 0.24 and 0.34 A cm^{-2} for Pd and Pd-Co, respectively. For a given current density of 1 A cm^{-2}, cell potentials were 0.46 V for Pd and 0.47 V for Pd-Co MEA, respectively. With air current densities at 0.65 V were double for Pd-Co than for pure Pd, 0.06 and 0.12 A cm^{-2} for Pd and Pd-Co MEAs, respectively. Cell potentials at 0.5 A cm^{-2} were 0.36 V for Pd and at 0.37 for Pd-Co, respectively. Therefore, it could be stated that the addition of Co improved the catalytic activity of Pd, especially in the kinetic region, as catalyst for oxygen reduction in acidic media at room temperature.

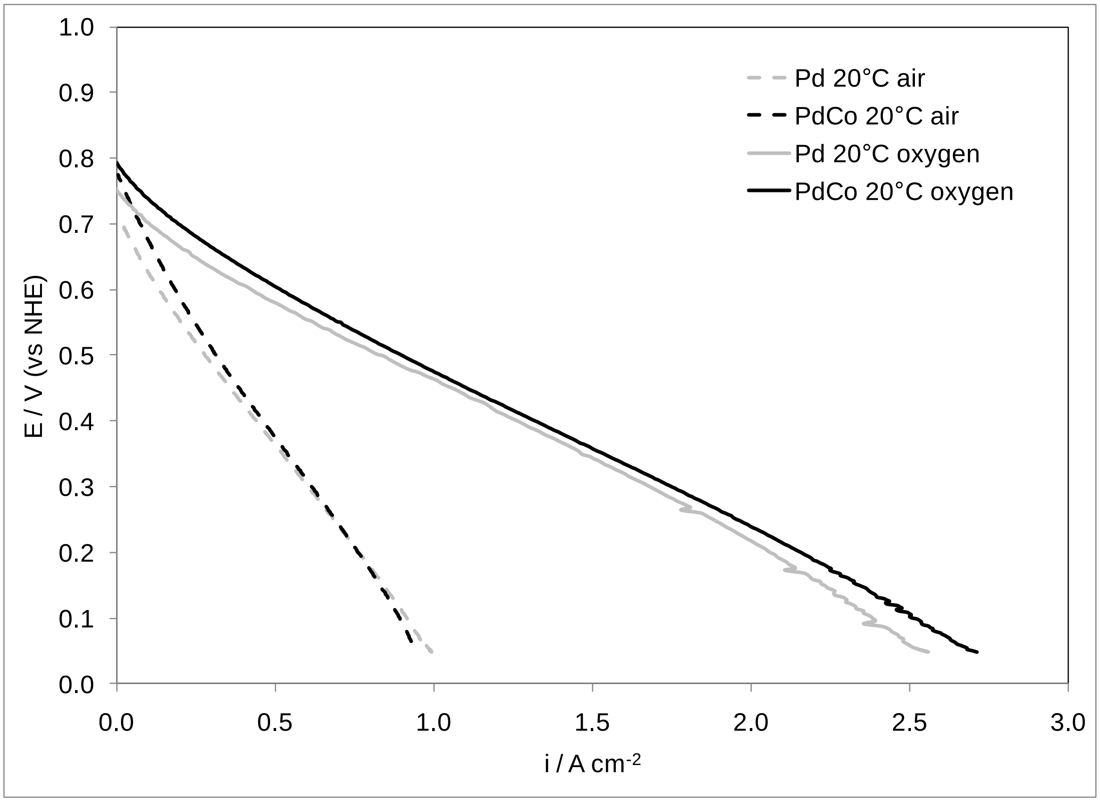

Figure 6-11: Comparison of polarization curves of a low temperature polymer electrolyte membrane fuel cell with carbon-supported Pd nanoparticles and carbon-supported Pd-Co nanoparticles as cathode catalyst at 20 ºC.

Figure 6-12 shows cell polarization curves of Pd-Co and Pd MEAs at 40 ºC. At this temperature, operating with pure O_2 in the cathode, current densities at 0.65 V were 0.59

and 0.65 A cm^{-2} for Pd and Pd-Co, respectively. For a given current density of 2 mA cm^{-2}, cell potentials were 0.39 V for both Pd and Pd-Co MEAs. When air was fed to the cathode, recorded current densities at 0.65 V were, 0.13 and 0.21 A cm^{-2} for Pd and Pd-Co MEAs, respectively. Cell potentials at 0.5 A cm^{-2} were 0.44 V for Pd and at 0.45 for Pd-Co. Similarly to 20 ºC, an improvement in cell performance, especially in the low current density region was observed with Pd-Co over pure Pd.

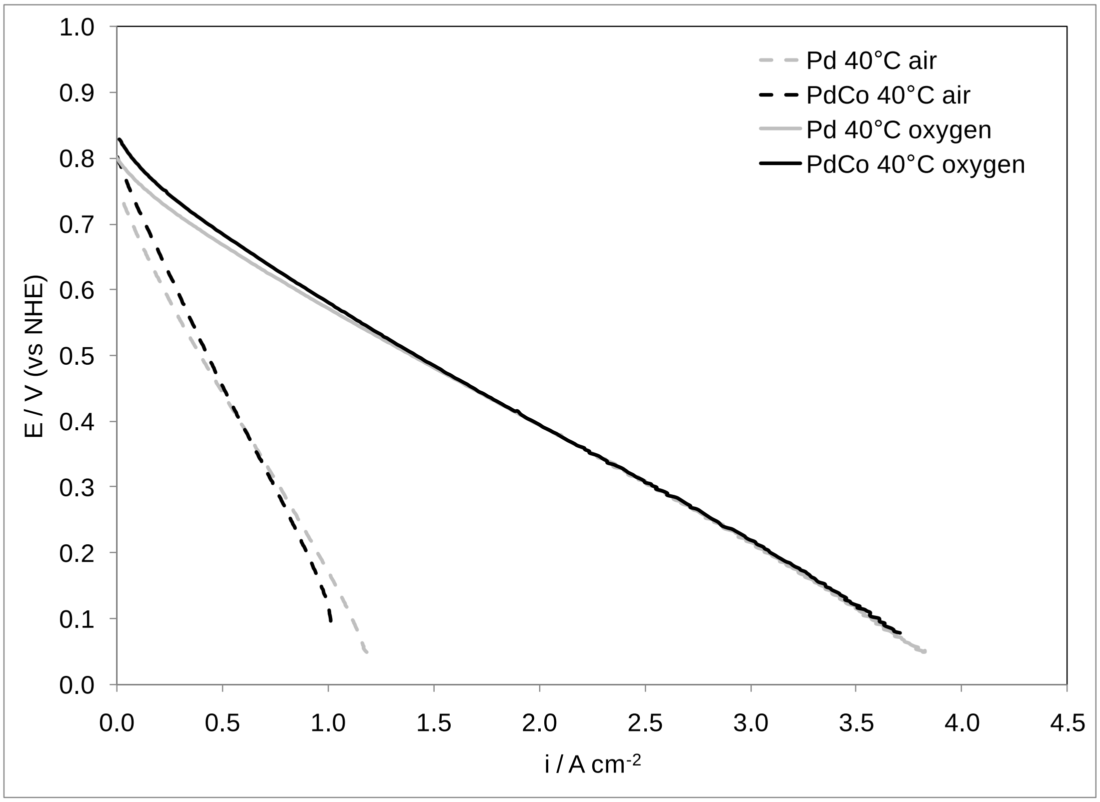

Figure 6-12: Comparison of polarization curves of a low temperature polymer electrolyte membrane fuel cell with carbon-supported Pd nanoparticles and carbon-supported Pd-Co nanoparticles as cathode catalyst at 40 ºC.

Figure 6-13 compares polarization curves of Pd-Co and Pd MEAs at 60 ºC. Operating with pure O_2 in the cathode current densities at 0.65 V were 0.54 and 0.50 A cm^{-2} for Pd and Pd-Co, respectively. For a given current density of 2 mA cm^{-2}, cell potentials were 0.38 V for Pd and 0.33 V for Pd-Co MEA, respectively. When air was fed to the cathode, current densities at 0.65 V were 0.02 and 0.04 A cm^{-2} for Pd and Pd-Co MEAs, respectively. Cell potentials at 0.5 A cm^{-2} were 0.29 V for Pd and at 0.21 V for Pd-Co.

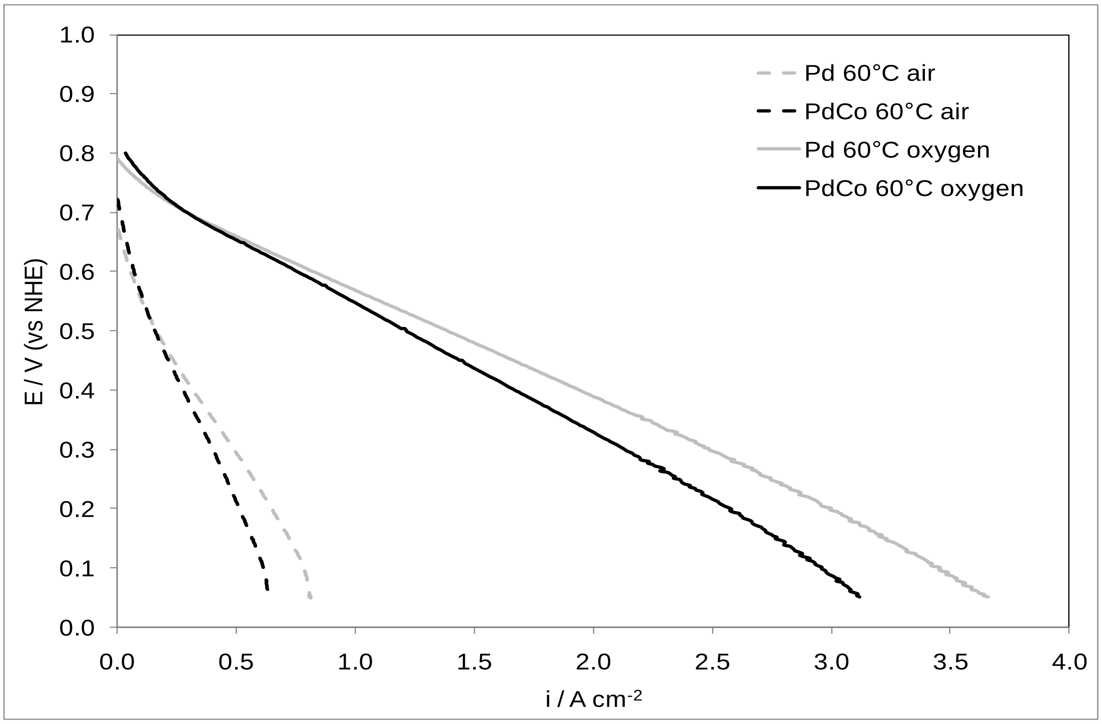

Figure 6-13: Comparison of polarization curves of a low temperature polymer electrolyte membrane fuel cell with carbon-supported Pd nanoparticles and carbon-supported Pd-Co nanoparticles as cathode catalyst at 60 ºC.

Figure 6-14 compares polarization curves of Pd-Co and commercial Pt MEAs operating with air at 40 ºC. Current densities at 0.70 V were 0.14 and 0.16 A cm^{-2} for Pd-Co and Pt, respectively. Peak power densities were 336 and 234 mW cm^{-2} for Pd-Co and Pt MEAs, respectively.

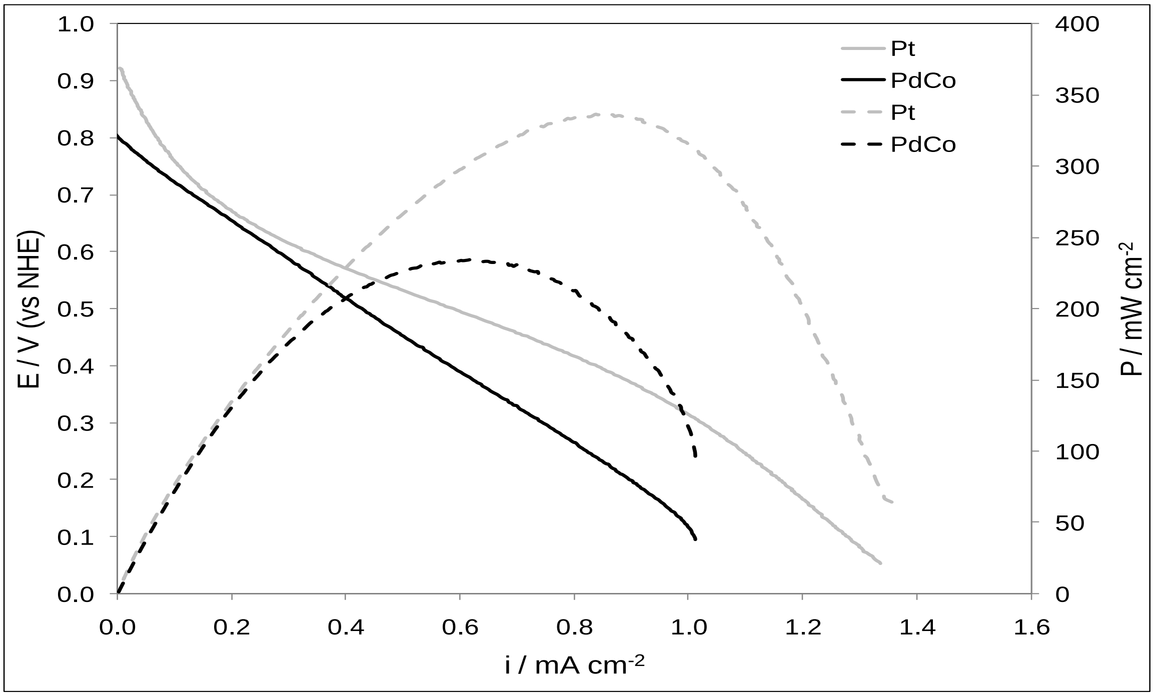

Figure 6-14: Comparison of polarization curves of a low temperature polymer electrolyte membrane fuel cell with carbon-supported Pd-Co nanoparticles and commercial Pt/C as cathode catalyst operating with air at 40 ºC.

Several publications reported characterization of Pd-Co catalysts for ORR in half cells, few PEM fuel cells with Pd-Co cathodes has been reported. Mustain et al. [12] showed polarization curves of a PEM fuel cell with commercial Pt/C and Pd_3Co/C cathodes both producing ca. 0.25 and 0.21 A cm^{-2} at 0.65 V, respectively, with pure H_2 and O_2, at 60 ºC and with 0.2 mg cm^{-2} of metal in both anode and cathode. Is not possible to directly compare with our catalyst due to the lack of information. No Pd-Pd distances were provided for comparison with Pd_4Co-EG11-300. In a later publication [13], the same group reported the cathodic polarization curves of a cell with Pd_5Co/C as catalysts for ORR. Current densities reported at 0.65 V were A cm^{-2} at 60 ºC.

Table 6-2: Comparison of Pd-Co catalysts performance with published data.

Catalyst	Output	Operating Conditions	Reference
Pd_3Co/C	0.21 A cm^{-2} (cathode)	0.65 V, 60 ºC, H_2/O_2 0.2 mg cm^{-2} cathode	[12]
Pt/C	0.25 A cm^{-2} (cathode)	0.65 V, 60 ºC, H_2/O_2 0.2 mg cm^{-2} cathode	[12]
Pd_5Co/C	0.15 A cm^{-2} (single cell)	0.65 V, 60 ºC, H_2/O_2 0.2 mg cm^{-2} cathode	[13]
Pt/C	0.15 A cm^{-2} (single cell)	0.65 V, 60 ºC, H_2/O_2 0.2 mg cm^{-2} cathode	[13]
Pd_4Co/C	0.50 A cm^{-2} (single cell)	0.65 V, 60 ºC, H_2/O_2 0.6 mg cm^{-2} cathode	This work
Pt/C	1.1 A cm^{-2}	0.65 V, 60 ºC, H_2/O_2 0.6 mg cm^{-2} cathode	This work

6.2.3. Evaluation of higher loading palladium electrodes

Since palladium is approximately four times cheaper than platinum (Johnson Matthey prices), the use of larger amounts of Pd in the cell cathode in order to match or overtake the performance of a Pt cathode would still be economically advantageous. In this section a MEA with cathode loading 1.0 mg cm^{-2} of Pd was compared with MEAs with cathode loadings of 0.6 mg cm^{-2} of Pd or Pt.

Figure 6-15 and Figure 6-16 compare polarization curves of palladium MEAs with different cathode metal loadings at 20 and 40 ºC, respectively. The increase of the cathode metal loading from 0.6 to 1.0 mg cm^{-2} produced a large increase in current density in the kinetic region (low current densities). At 20 ºC operating with air the open circuit voltage increased by 0.14 V, from ca. 0.71 to 0.85 V. Operating with oxygen at 20 ºC the OCP increase was also 0.14 V. When the operating temperature was 40 ºC a similar effect was observed in the cell OCP. Cathode metal loading 1.0 mg cm^{-2} exhibited an OCP 0.15 and 0.13 V higher than loading 0.6 mg cm^{-2}, with air and oxygen, respectively. This is in accord with the previous analysis of the crossover impact on Pd, increasing the loading will increase the ECSA and i_0 accordingly leading to a smaller impact of crossover.

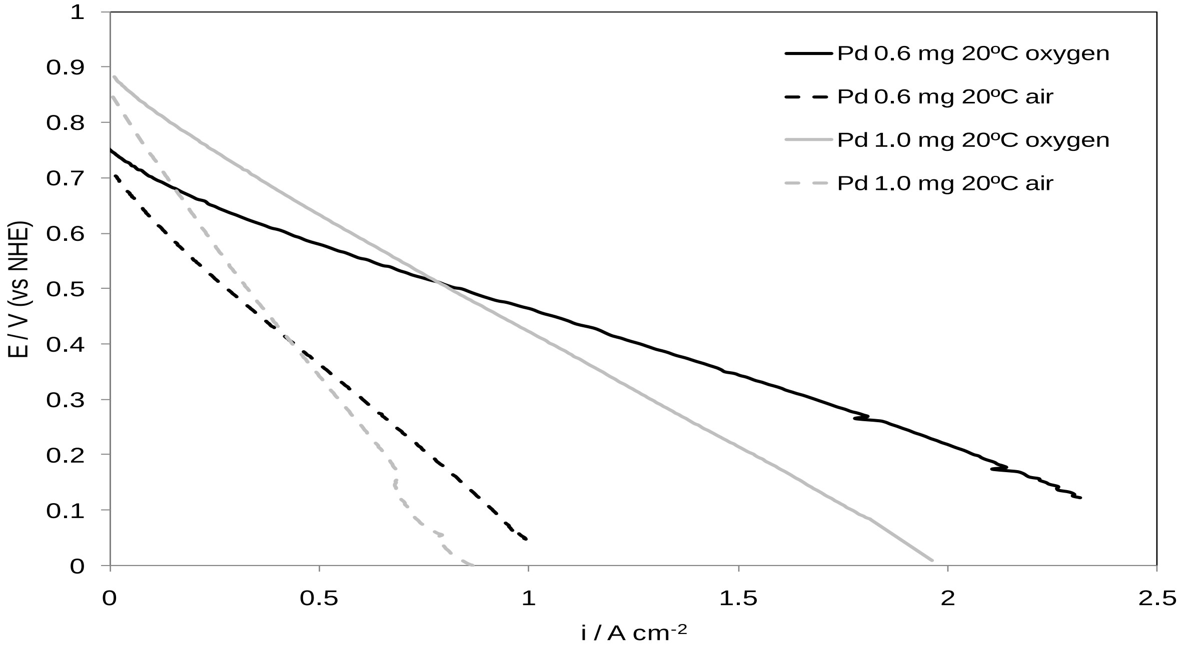

Figure 6-15: Comparison of polarization curves of a low temperature PEMFC with cathode catalyst Pd/C-EG11 and loadings 0.6 and 1.0 mg cm^{-2} at 20 ºC.

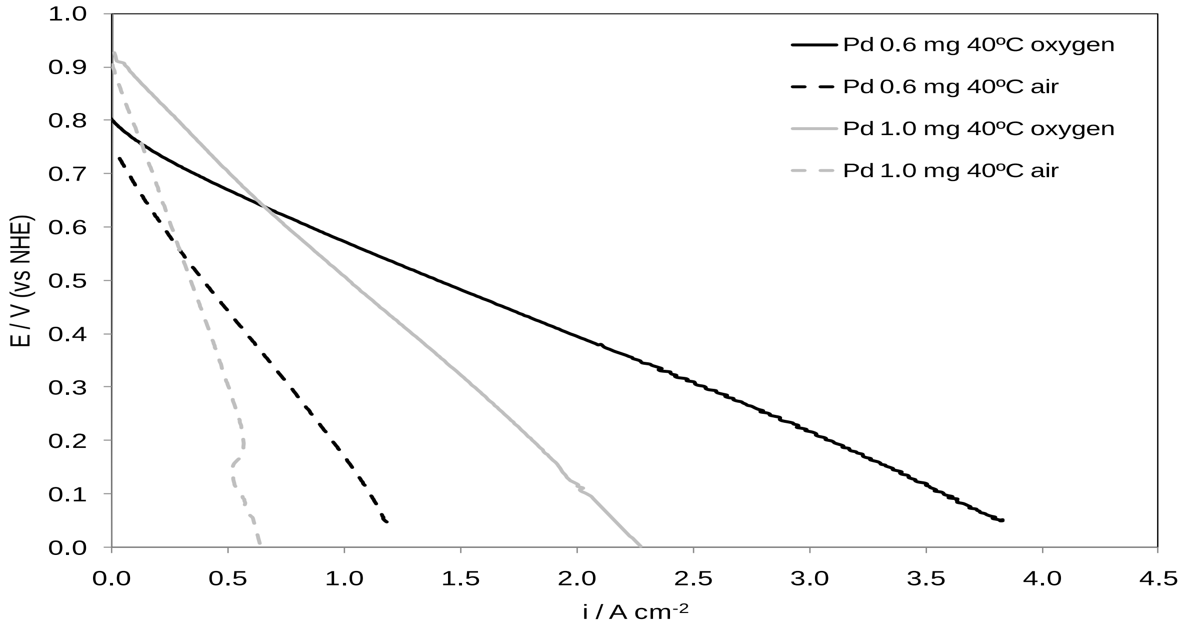

Figure 6-16: Comparison of polarization curves of a low temperature PEMFC with cathode catalyst Pd/C-EG11 and loadings 0.6 and 1.0 mg cm^{-2} at 40 ºC.

On the other hand, in the high current density region the MEA with lower cathode metal loading exhibited higher cell potentials. This phenomenon was attributed to mass transport effects. Differences in the slopes between polarization curves of the two MEAs (Figure 6-15 and Figure 6-16) indicated that the MEA with larger cathode loading was suffering from mass transport problems, since membrane and operating conditions were the same for both MEAs. This also can be seen from the difference between oxygen and air operation for a given current density is significantly higher in the double loading than the single loading MEA. To illustrate this, the thickness of the catalysts layer was estimated for both cathode metal loadings.

The thickness of the catalyst layer can be estimated from the volume of the different components in the catalysts layer, this volume was calculated from their mass and density. It can be expressed as:

$$\delta = \frac{V}{A} \qquad (6.16)$$

Where δ is the thickness of the catalyst layer and V is its total volume and A is the geometric area. The total volume of the catalyst layer can be expressed as:

$$V = V_{Pd} + V_{Naf} + V_C + V_{por} \tag{6.17}$$

Where V_{Pd}, $V_{Naf,}$ V_C and V_{por} are the volumes of the palladium, Nafion®, carbon and porous parts in the catalyst layer, respectively. The porosity of the catalyst layer was considered 30% volume, as reported by Jaouen et al. [14], metal loading was 20% wt and Nafion® content was 20% weight of Pd/C. Density of carbon was taken as 1.8 g cm^{-3} (for Vulcan XC-72R [15]), Nafion® density was taken as 2.1 g cm^{-3} [16] and Pd density is 12.0 cm^{-3} with all three at 25 ºC.

The calculated thickness for cathodes with 0.6 and 1.0 mg cm^{-2} of Pd were 24 and 40 µm, respectively. This shows how the catalysts layer thickness with 1.0 mgPt cm^{-2} was almost twice that with 0.6 mgPt cm^{-2}, this would cause worse oxygen mass transport and greater potential losses (ohmic losses). It must be also pointed out that both values are greatly larger than those considered as optimal in low temperature PEMFC: Jeng et al. used a 5 µm catalyst layer in their study of the oxygen mass transport [17] and Jaouen et al. used a 10 µm thick catalyst layer [14]. Thus future investigations on Pd electrocatalysts would look into the synthesis of Pd/C with higher metal content in order to reduce the thickness of the catalyst layer. The effect of catalyst layer thickness and oxygen mass transport losses was further discussed in section.

Figure 6-17 and Figure 6-18 compare polarization curves of palladium MEA with cathode metal loading 1.0 mg cm^{-2} with the Pt MEA with cathode loading 0.6 mg cm^{-2} at 20 and 40 ºC, respectively. The same behavior discussed earlier for the two Pd MEAs is also seen, in the high current densities region the lower loading MEAs exhibited considerably higher potential, whilst in the kinetic region (low current density) the Pd MEAs matched and sometimes even surpassed the performance of the Pt MEA.

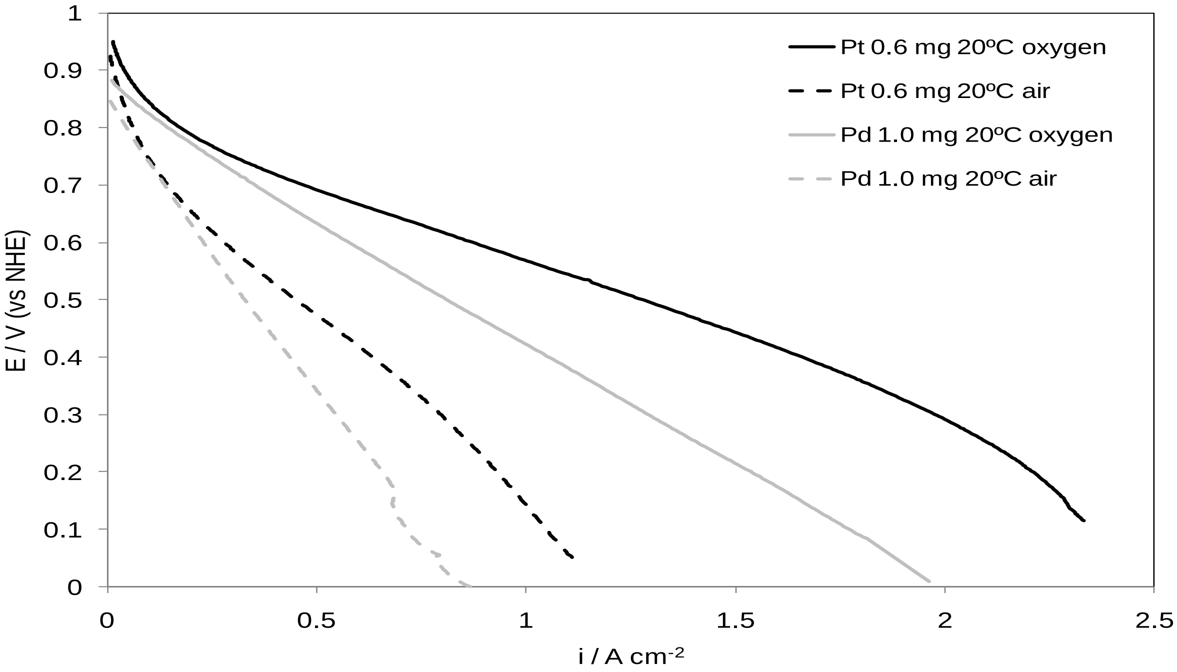

Figure 6-17: Comparison of polarization curves of a low temperature PEMFC with cathode loadings 1 mg cm^{-2} of Pd/C-EG11 and 0.6 mg cm^{-2} Pt/C-Etek at 20 ºC.

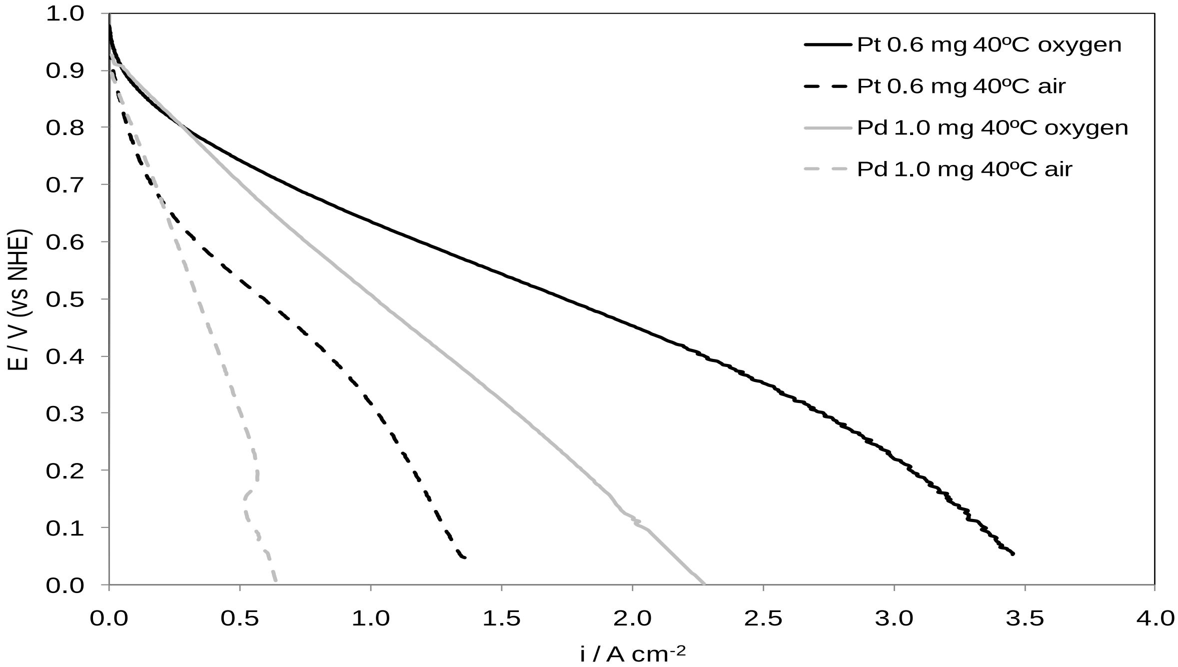

Figure 6-18: Comparison of polarization curves of a low temperature PEMFC with cathode loadings 1 mg cm^{-2} of Pd/C-EG11 and 0.6 mg cm^{-2} Pt/C-Etek at 40 ºC.

With the cell operating with air at 20 ºC at 0.75 V (ca. 60% efficiency) both platinum and palladium produced current densities of 0.10 A cm^{-2}. When the cell operating temperature was raised to 40 ºC Pd overtook Pt, with a current density of 0.14 compared to 0.12 A cm^{-2}, respectively. These operating conditions are favourable for economic and practical reasons (it is easier and cheaper to operate the cell with air than with pure oxygen). Therefore, the use of Pd, four times cheaper than platinum, even on a higher loading is highly desirable; the price of the novel metal for the cathode would be approximately 2.4 times cheaper.

6.3. High temperature polymer electrolyte membrane fuel cell tests

High temperature PEMFC tests were conducted at 120, 150 and 175 ºC with Pd-EG11 as cathode catalyst and compared with those with a 20% weight commercial Pt/C. Membrane Electrode Assemblies (MEA) were prepared using the phosphoric acid doped PBI. Metal loading on the electrodes was 0.2 mg cm^{-2} of Pt in the anode and 0.3 mg cm^{-2} of Pd or Pt in the cathode.

Figure 6-19 compares polarization curves at 120 ºC for Pd and Pt MEAs operating with oxygen and air. In all four polarization curves, potential loses due to the catalyst activation in the low current density region can be observed. This activation region was not observed in low temperature PEMFC for the Pd MEA. Exchange current densities for the ORR depend on the oxygen concentration at the catalyst surface. No PBI was added to the catalyst layer, polytetrafluoroethylene (PTFE) was used as a binder as this was found to provide higher oxygen permeability as reported by Mamlouk and Scott [18]; therefore the oxygen concentration at the catalyst surface can be taken as the oxygen concentration in pure phosphoric acid. Oxygen solubility in Nafion® at 30 ºC was reported to be 9.3×10^{-3} mol dm^{-3} [19] whilst oxygen solubility in phosphoric acid at 125 ºC was reported to be 9.7×10^{-5} mol dm^{-3} [20]. Thus the oxygen concentration in the PBI based cell would be approximately two orders of magnitude lower at high temperature conditions as reported by Mamlouk and Scott [21].

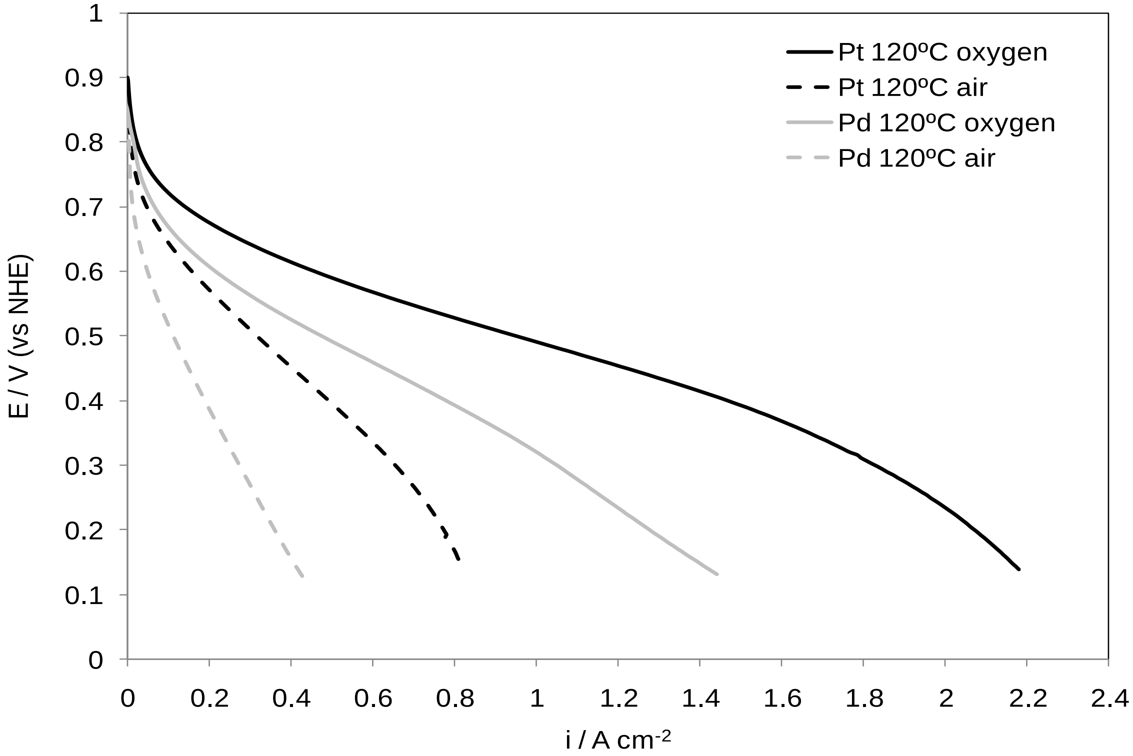

Figure 6-19: Comparison of polarization curves of a high temperature PEMFC with cathode catalysts Pd/C-EG11 and Pt/C-Etek at 120 ºC.

At 120 ºC current densities at 0.65 V with oxygen fed to the cathode for Pd and Pt MEAs were 0.12 and 0.27 A cm^{-2}, respectively. Operating with air current densities for Pd and Pt MEAs were 0.04 and 0.09 A cm^{-2}, respectively. Cell potentials compared at 0.2 A cm^{-2} were ca. 70 mV higher for Pt than Pd when the cell was operated with oxygen and approximately 140 mV when air was used (Table 6-3).

Table 6-3: Current densities at 0.65 V and cell potentials at 0.2 A cm^{-2} for high temperature PEM fuel cell at different conditions and with different electrocatalysts in the cathode.

Cathode Catalyst	Temperature (ºC)	Cathode fed	Current density at 0.65 V (A cm^{-2})	Cell potential at 0.2 A cm^{-2} (V)
Pd-EG11	120	Air	0.035	424
Pd-EG11	120	O_2	0.123	606
Pd-EG11	150	Air	0.026	385
Pd-EG11	150	O_2	0.081	568
Pd-EG11	175	Air	0.009	341
Pd-EG11	175	O_2	0.048	530
Pt/C-Etek	120	Air	0.089	570
Pt/C-Etek	120	O_2	0.274	674
Pt/C-Etek	150	Air	0.089	572
Pt/C-Etek	150	O_2	0.258	667
Pt/C-Etek	175	Air	0.089	571
Pt/C-Etek	175	O_2	0.267	675

Figure 6-20 compares polarization curves at 150 ºC for Pd and Pt MEAs operating with oxygen and air. Current densities exhibited by the Pt MEA at 0.65 V were almost identical to those at 150 ºC (0.09 and 0.26 A cm^{-2} for air and oxygen, respectively). On the other hand, current densities showed by the Pd MEA at 0.65 V were lower than at 120 ºC (0.03 and 0.08 A cm^{-2} for air and oxygen, respectively). Similar behavior was observed when the operating temperature was further increased to 175 ºC: the performance of the Pt MEA did not increase with temperature and Pd MEA showed lower current densities at higher operating temperatures (Table 6-3).

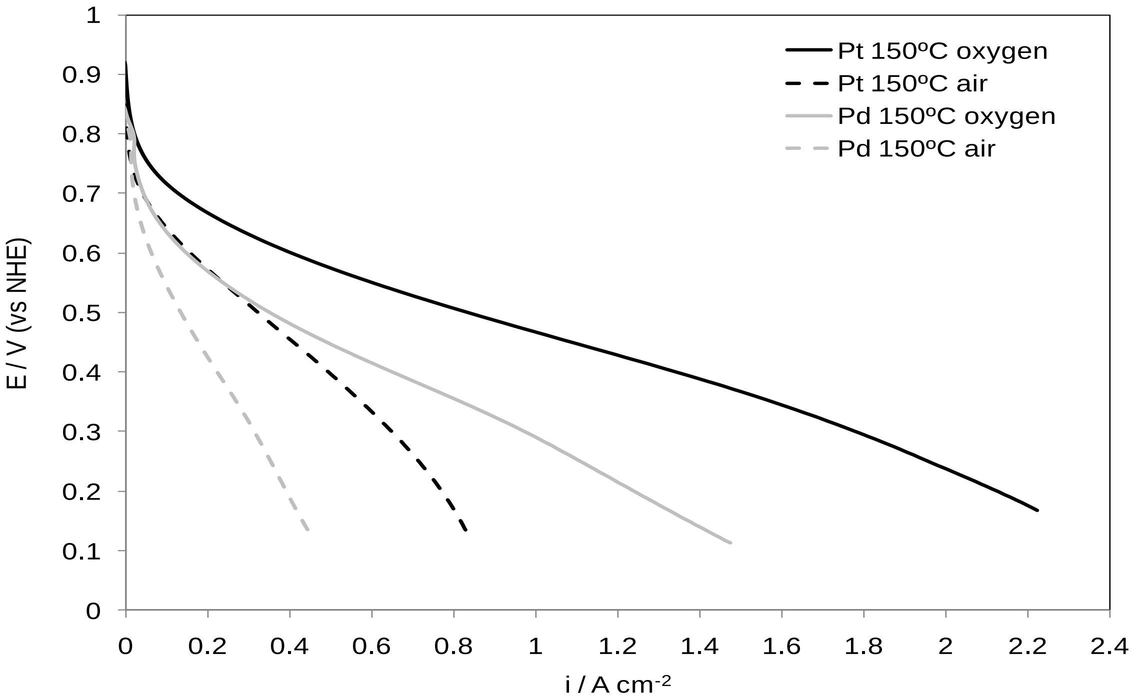

Figure 6-20: Comparison of polarization curves of a high temperature PEMFC with cathode catalysts Pd/C-EG11 and Pt/C-Etek at 150 ºC.

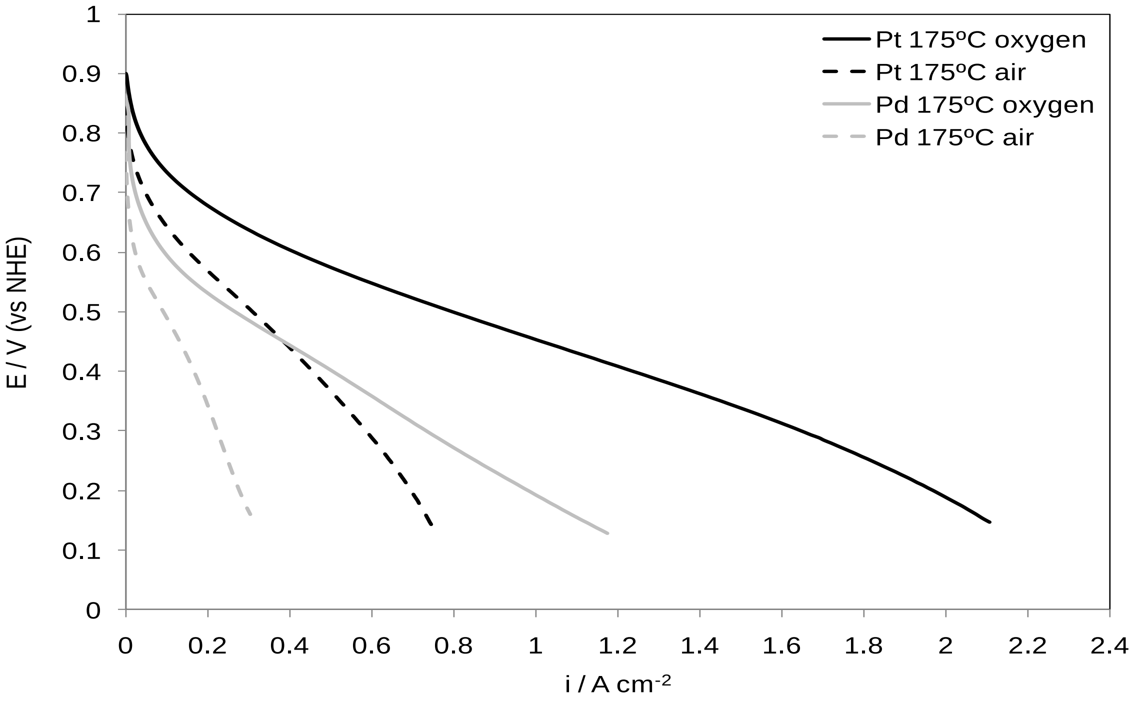

Figure 6-21: Comparison of polarization curves of a high temperature PEMFC with cathode catalysts Pd/C-EG11 and Pt/C-Etek at 175 ºC.

Operating at high temperatures leads to a lower solubility of oxygen in phosphoric acid [22] (therefore the oxygen concentration at the catalyst surface is lower) and lower oxygen diffusion due to increases in the viscosity of phosphoric acid due to dehydration [23]. Both factors impact on oxygen mass transport and its effect on cell performance. This effect was previously reported by Mamlouk in MEAs with no PBI in the catalyst layer [5]. The lower solubility of oxygen and higher viscosity of phosphoric acid counters the kinetics enhancement at higher temperature. This explains why performance of the Pt MEA did not markedly change in the temperature range 120 to 175 ºC.

Palladium MEAs however showed poorer performance at higher temperature (Table 6-3). This was attributed to instability of Pd nanoparticles in these harsh operating conditions (hot phosphoric acid) based on the studies published by Stonehart [24, 25] on phosphoric acid fuel cells; losses in electrochemical surface area were observed in hot phosphoric acid environment.

Current densities at 0.65 V at 120 ºC operating in air for Pd and Pt MEAs were 0.04 and 0.09 A cm^{-2}; at 40 ºC they were 0.13 and 0.24 A cm^{-2}, respectively. At high temperature performance for both MEAs was approximately one third of that at low temperature for two main reasons: firstly the loading was 0.3 mg cm^{-2} instead of 0.6 mg cm^{-2} and secondly Nafion® is a better environment for ORR than H_3PO_4 (where other processes such as phosphate adsorption take place), oxygen concentration in the latter is two orders of magnitude lower than in Nafion® [19, 20]. This can be clearly seen from much lower limiting current values with air and oxygen in the PBI based cell in comparison to nafion cell despite the much higher operating temperatures.

Increasing palladium metal loading in the cathode would possibly close the gap in cell performance with the Pt MEA (as occurred in low temperature, discussed in Section 6.2). However, these tests were not carried out due to the instability exhibited by the Pd MEA when. The Pd MEA with 0.3 mg cm^{-2} Pd in the cathode showed decreasing performance when temperature was raised from 120 to 150 to 175 ºC (Table 6-3) with both oxygen and air. This behavior was attributed to the loss of electrochemical surface area in hot phosphoric acid environment, as discussed above.

6.4. Conclusions

Carbon supported Pd nanoparticles prepared by reduction by ethylene glycol at pH 11 were tested in a low temperature fuel cell as cathode material and its performance compared to the state of the art commercial Pt/C. For the same metal loading, Pt cathode performed better than Pd, although due to its higher activation energy Pd performance was closer to Pt at higher temperature. Operating with air at 40 ºC current densities at 0.65 V (53% efficiency) for Pd and Pt MEAs were 0.13 and 0.24 A cm^{-2}, respectively.

Since Pd is considerably cheaper than platinum, the use of larger amounts of Pd in the cathode would still be economically advantageous. MEA with Pd loading in the cathode of 1.0 mg cm^{-2} was prepared and compared with MEAs with cathode loadings of 0.6 mg cm^{-2} of Pd and Pt. The increase of the catalyst loading led to a sharp increase on the kinetics of the ORR and therefore of the cell performance, although severe mass transport effects were observed in the high current density region due to the thickness of the catalyst layer. At feasible operating conditions, 40 ºC and operating with air, Pd MEA (1.0 mg cm^{-2}) overtook Pt MEA (0.6 mg cm^{-2}), showing current densities at 0.65 V of 0.14 and 0.12 A cm^{-2}, respectively.

Pd$_4$Co-EG11-300, presented an increased OCP and smaller kinetic losses compared to the Pd-EG11 when it was used as cathode material. Overall, the Pd-Co MEA presented improved performance at 20 and 40 ºC compared to the Pd MEA. Operating with air at 40 ºC current densities at 0.65 V for Pd and PdCo MEAs were 0.13 and 0.21 A cm^{-2}, respectively.

Pd/C prepared by reduction by ethylene glycol at pH 11 was also tested as the cathode catalyst in a high temperature fuel cell and its performance compared to commercial Pt/C.

Operating with air at 120 ºC current densities at 0.65 V for Pd and Pt MEAs were 0.04 and 0.09 A cm^{-2}, respectively. In the temperature range from 120 to 175 ºC the Pt MEA performance failed to increase due to phosphoric acid properties: decrease of the oxygen solubility and increase of its viscosity. Pd MEA showed declining performance in the same temperature range due to instability of palladium nanoparticles in these harsh operating conditions.

References

1. Sakai, T., H. Takenaka, N. Wakabayashi, Y. Kawami, and E. Torikai, *Gas Permeation Properties of Solid Polymer Electrolyte (SPE) Membranes.* Journal of The Electrochemical Society, 1985. **132**(6): p. 1328-1332.

2. Broka, K. and P. Ekdunge, *Oxygen and hydrogen permeation properties and water uptake of Nafion® 117 membrane and recast film for PEM fuel cell.* Journal of Applied Electrochemistry, 1997. **27**(2): p. 117-124.

3. *Steam Tables*. Smith son Ian 2006 [cited; Available from: www.knovel.com.

4. Ayad, A., J. Bouet, and J.F. Fauvarque, *Comparative study of protonic conducting polymers incorporated in the oxygen electrode of the PEMFC.* Journal of Power Sources, 2005. **149**(1-2): p. 66-71.

5. Mamlouk, M., *Investigation of High Temperature Polymer Electrolyte Membrane Fuel Cells*, in *Chemical Engineering and Advanced Materials*. 2008, Newcastle University: Newcastle upon Tyne.

6. Broka, K. and P. Ekdunge, *Oxygen and hydrogen permeation properties and water uptake of Nafion® 117 membrane and recast film for PEM fuel cell.* Journal of Applied Electrochemistry, 1997. **27**(2): p. 117-123.

7. Conway, B.E. and B.V. Tilak, *Interfacial processes involving electrocatalytic evolution and oxidation of H2, and the role of chemisorbed H.* Electrochimica Acta, 2002. **47**(22-23): p. 3571-3594.

8. Mustain, W.E. and J. Prakash, *Kinetics and mechanism for the oxygen reduction reaction on polycrystalline cobalt-palladium electrocatalysts in acid media.* Journal of Power Sources, 2007. **170**(1): p. 28-37.

9. Paulus, U.A., T.J. Schmidt, H.A. Gasteiger, and R.J. Behm, *Oxygen reduction on a high-surface area Pt/Vulcan carbon catalyst: a thin-film rotating ring-disk electrode study.* Journal of Electroanalytical Chemistry, 2001. **495**(2): p. 134-145.

10. Ficicilar, B., A. Bayrakceken, and I. Eroglu, *Effect of Pd loading in Pd-Pt bimetallic catalysts doped into hollow core mesoporous shell carbon on performance of proton exchange membrane fuel cells.* Journal of Power Sources, 2009. **193**(1): p. 17-23.

11. Moreira, J., P. del Angel, A.L. Ocampo, P.J. Sebastian, J.A. Montoya, and R.H. Castellanos, *Synthesis, characterization and application of a Pd/Vulcan and Pd/C catalyst in a PEM fuel cell.* International Journal of Hydrogen Energy, 2004. **29**(9): p. 915-920.

12. Mustain, W.E., K. Kepler, and J. Prakash, *Investigations of carbon-supported CoPd3 catalysts as oxygen cathodes in PEM fuel cells.* Electrochemistry Communications, 2006. **8**(3): p. 406-410.

13. Mustain, W.E., K. Kepler, and J. Prakash, *CoPdx oxygen reduction electrocatalysts for polymer electrolyte membrane and direct methanol fuel cells.* Electrochimica Acta, 2007. **52**(5): p. 2102-2108.

14. Jaouen, F., S. Marcotte, J.-P. Dodelet, and G. Lindbergh, *Oxygen Reduction Catalysts for Polymer Electrolyte Fuel Cells from the Pyrolysis of Iron Acetate Adsorbed on Various Carbon Supports.* Journal of Physical Chemistry B, 2003. **107**(6): p. 1376-1386.

15. Cabot. [cited; Available from: http://www.cabot-corp.com/Specialty-Carbon-Blacks.

16. Ma, Y.L., J.S. Wainright, M.H. Litt, and R.F. Savinell, *Conductivity of PBI membranes for high-temperature polymer electrolyte fuel cells.* Journal of the Electrochemical Society, 2004. **151**(1).

17. Jeng, K.T., S.F. Lee, G.F. Tsai, and C.H. Wang, *Oxygen mass transfer in PEM fuel cell gas diffusion layers.* Journal of Power Sources, 2004. **138**(1-2): p. 41-50.

18. Mamlouk, M. and K. Scott, *Phosphoric acid-doped electrodes for a PBI polymer membrane fuel cell.* International Journal of Energy Research, 2010.

19. Parthasarathy, A., C.R. Martin, and S. Srinivasan, *Investigations of the O2 reduction reaction at the platinum Nafion interface using a solid-state electrochemical cell.* Journal of The Electrochemical Society, 1991. **138**(4): p. 916-921.

20. McBreen, J., W.E.O. Grady, and R. Richter, *A Rotating Disk Electrode Apparatus for the Study of Fuel Cell Reactions at Elevated Temperatures and Pressures.* Journal of the Electrochemical Society, 1984. **131**(5): p. 1215-1216.

21. Mamlouk, M. and K. Scott, *The effect of electrode parameters on performance of a phosphoric acid-doped PBI membrane fuel cell.* International Journal of Hydrogen Energy. **35**(2): p. 784-793.

22. Klinedinst, K., J.A.S. Bett, J. Macdonald, and P. Stonehart, *Oxygen solubility and diffusivity in hot concentrated H3PO4.* Journal of Electroanalytical Chemistry, 1974. **57**(3): p. 281-289.

23. Ma, Y.L., *The Fundamental Studies of Polybenzimidazole/Phosphoric Acid Polymer Electrolyte For Fuel Cells*, in *Case Western Reserve University*. 2004.

24. Stonehart, P., *Development of alloy electrocatalysts for phosphoric acid fuel cells (PAFC).* Journal of Applied Electrochemistry, 1992. **22**(11): p. 995-1001.

25. Stonehart, P., *ldquoDevelopment of Advanced Noble Metal-Alloy Electrocatalysts for Phosphoric Acid Fuel Cells (PAFC)rdquo.* Berichte der Bunsengesellschaft für physikalische Chemie, 1990. **94**(9): p. 913-921.

Chapter 7: Direct methanol fuel cell

7.1. Introduction

Optimized carbon-supported palladium catalyst, Pd-EG11, was considered as a candidate because of its high activity towards oxygen reduction. Pd-EG11 was tested as a cathode catalyst in a direct methanol fuel cell. Cell performance with Pd/C in the cathode was compared with the performance when using commercial Pt/C as cathode catalyst. Cell potentials at low current densities were compared (5 mA cm^{-2}) and current densities at 400 mV were chosen for the purpose. A constant methanol flow rate of 7 mL min^{-1} was used in every test; this flow rate was chosen for being the optimum for 1M methanol [1]. The effect of methanol concentration on cell performance was studied using methanol solutions of 1 to 7 M. Temperature was studied in the range of 20, 40 and 60 ºC.

Measured exchange current densities at room temperature for the oxygen reduction reaction (ORR) on platinum and palladium electrodes were 1.4×10^{-10} and $7.7 \text{ X } 10^{-12}$ A cm^{-2}_{metal} (Chapter 4). Considering the activation energy of the oxygen reduction reaction on Pd/C, ca. 90 KJ mol^{-1} [2], and on Pt/C, ca. 26 KJ mol^{-1} [3], the exchange current density for ORR at 50 ºC on platinum can be estimated to be 3.2×10^{-10} in comparison to 1.3×10^{-10} A cm^{-2}_{ESA} for palladium. In other words, at 50 ºC platinum is 2.5 times more active than palladium for ORR. On the other hand, the exchange current density for the methanol oxidation reaction (MOR) at 50 ºC is reported [4] to be ca. 3×10^{-8} A.cm^{-2}_{metal} on platinum and ca. 10^{-11} A.cm^{-2}_{metal} on palladium. This means at 50 ºC platinum is approximately 3000 times more active than palladium for the methanol oxidation reaction. Calculating the ratio of $i_{0(MOR)}/i_{0(ORR)}$ for both catalyst at 50 ºC, we obtain ca. 100 and 0.1 for Pt and Pd, respectively. This suggests that platinum is approximately 100 times more active (o more selective) for methanol oxidation than for oxygen reduction, and therefore the effects of any crossed-over methanol would be severe. On the contrary, palladium is approximately 10 times less active for MOR in comparison to ORR, thus palladium is a more selective catalyst for ORR than MOR. Therefore it can be concluded that palladium is a good candidate for methanol fuel cell cathodes (DMFCs) especially at higher methanol concentration and higher operating temperatures.

7.2. Effect of methanol concentration on fuel cell performance

7.2.1. Cell polarizations

Figure 7-1, Figure 7-2 and Figure 7-3 compare potential-current curves for the palladium electrocatalyst and commercial Pt/C cathode materials using 1M methanol fed to the cathode at 20, 40 and 60 ºC, respectively, operating with air and oxygen. The discussion of the experimental data is mainly focused on the low current density region because it is the region where the effect of methanol crossover is more evident and because fuel cells would be ideally operating in this range, at high efficiency.

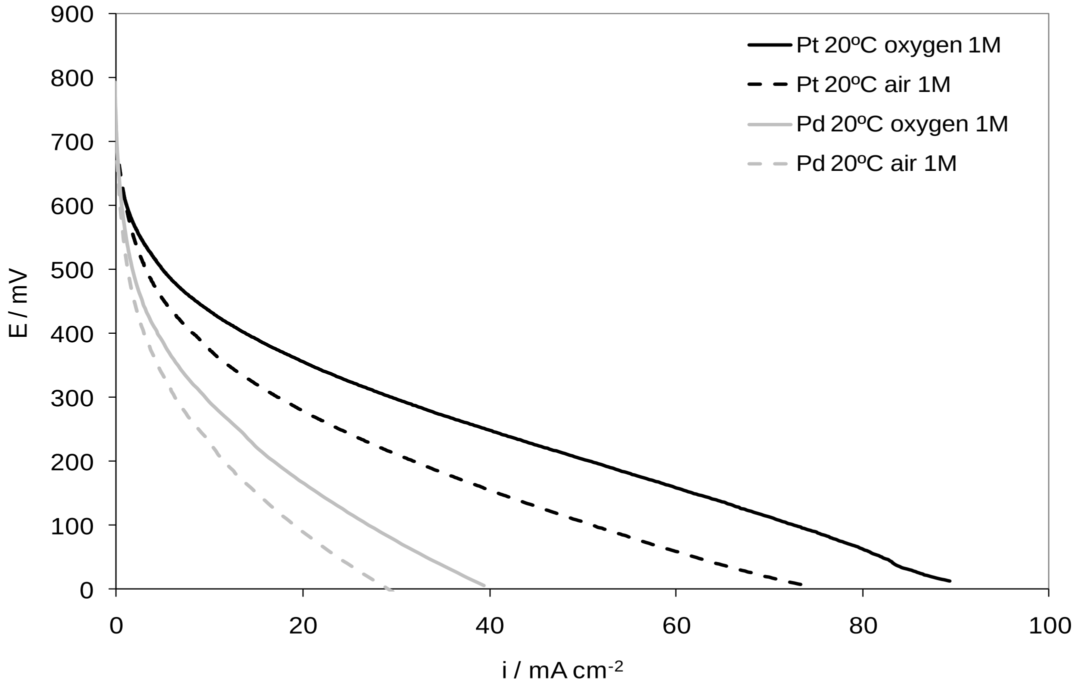

Figure 7-1: Comparison of polarization curves of a direct methanol fuel cell with Pd/C and commercial Pt/C from E-tek as cathode catalyst at 20 ºC and 1M methanol.

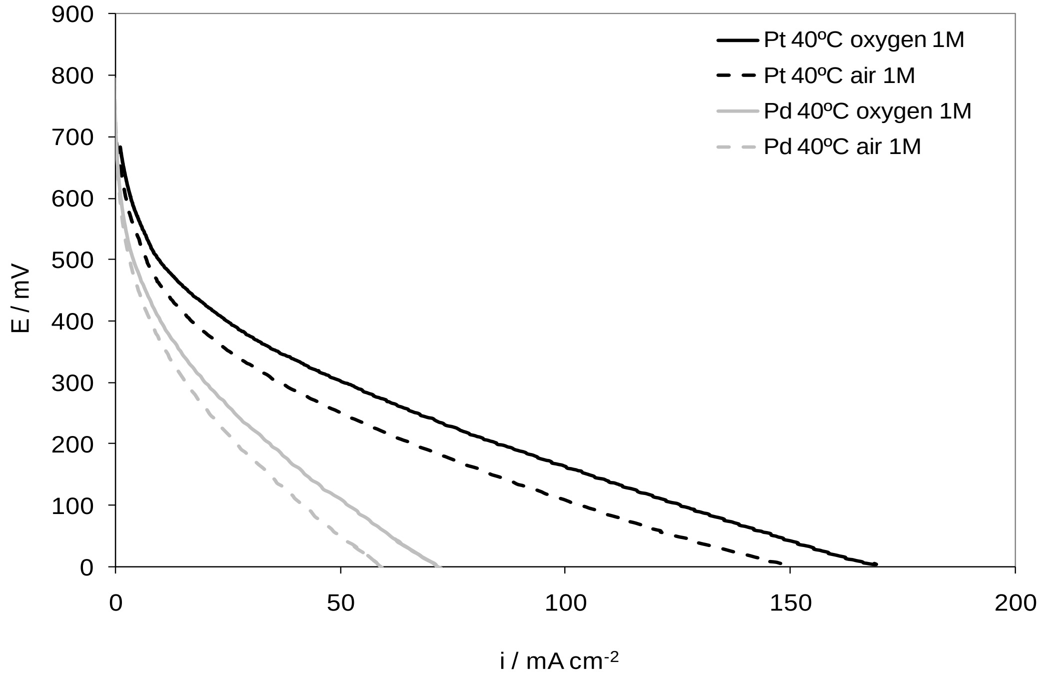

Figure 7-2: Comparison of polarization curves of a direct methanol fuel cell with Pd/C and commercial Pt/C from E-tek as cathode catalyst at 40 ºC and 1M methanol.

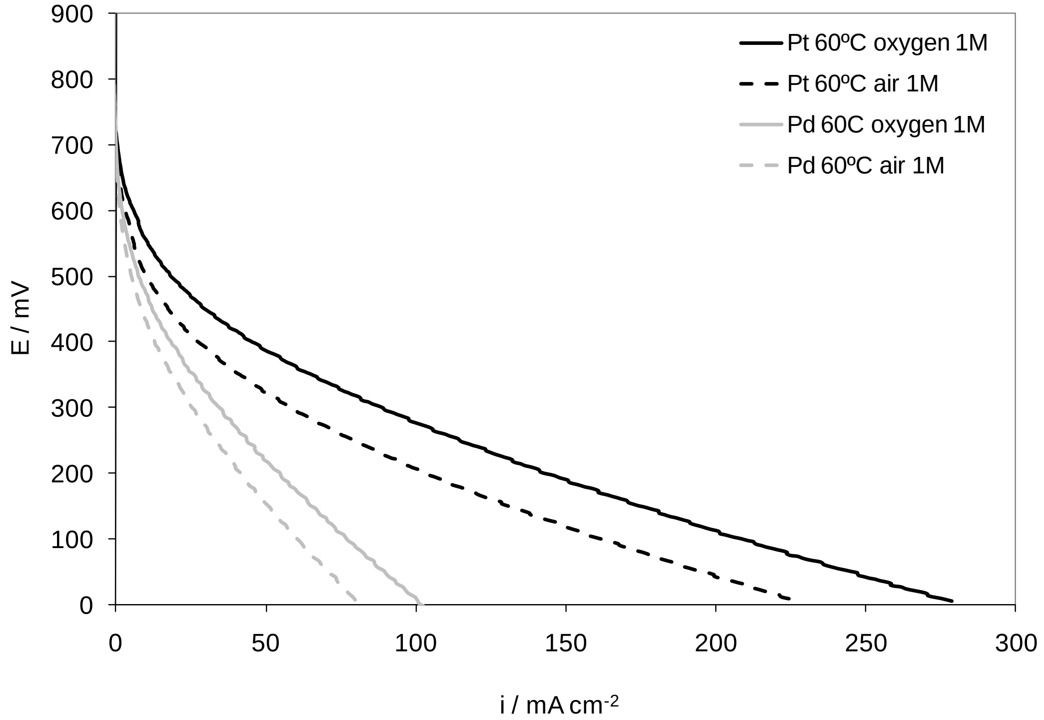

Figure 7-3: Comparison of polarization curves of a direct methanol fuel cell with Pd/C and commercial Pt/C from E-tek as cathode catalyst at 60 ºC and 1M methanol.

Cell voltages at 5 mA cm^{-2} in different conditions, summarised in Table 7-1, were larger for the Pt MEA in every case. The difference in cell voltage between Pt and Pd MEAs was similar when the cell was operating with air or oxygen. For example, at 20 ºC the difference was 116 mV for air and 107 mV for oxygen, decreasing to 88 mV for air and 81 mV for oxygen at 40 ºC and 67 mV for air and 63 mV for oxygen at 60 ºC. This tendency was also observed at higher current densities; comparing cell potentials at 20 mA cm^{-2}, at 20 ºC the difference between Pt and Pd was 188 mV for air and 187 mV for oxygen, decreasing to 124 mV for air both air and oxygen at 40 ºC and 95 mV for air and 101 mV for oxygen at 60 ºC. The decreasing difference with increasing temperature between Pd and Pt cell potentials at low current densities would indicate that the activation energy of the oxygen reduction reaction on Pd is higher than on Pt; which was already shown for hydrogen PEM fuel cells (chapter 6).

Table 7-1: Current densities at 0.4 V, cell voltage at 5 mA cm^{-2} and peak power densities for a direct methanol fuel cell with 1 M methanol solution fed to the anode.

Cathode catalyst	**Temperature (ºC)**	**Cathode fed**	**Voltage at 5 mA cm^{-2} (mV)**	**Current density at 0.4 V (mA cm^{-2})**	**Peak power density (mW cm^{-2})**
Pd-EG11	20	Air	335	3.0	2.3
Pt/C-Etek	20	Air	451	8.2	6.4
Pd-EG11	20	O_2	390	4.5	3.4
Pt/C-Etek	20	O_2	497	13.8	10.0
Pd-EG11	40	Air	448	7.6	5.4
Pt/C-Etek	40	Air	536	16.8	13.2
Pd-EG11	40	O_2	482	10.0	6.9
Pt/C-Etek	40	O_2	563	25.5	17.0
Pd-EG11	60	Air	500	12.8	8.3

Pt/C-Etek	60	Air	567	27.0	20.6
Pd-EG11	60	O_2	542	18.4	11.1
Pt/C-Etek	60	O_2	605	45.6	29.1

The difference between air and oxygen operation on cell voltage for a given operating current density is dependent on oxygen mass transport in the cathode and methanol crossover effects. The methanol crossover effect will be more pronounced at lower oxygen concentration, which can be illustrated as follows:

The total current density on the cathode is the sum of two partial currents, for methanol oxidation and oxygen reduction:

$$i = i_{O2} + i_{CH_3OH} \tag{7.1}$$

At open circuit conditions current density is zero and the open circuit potential can be expressed as:

$$i_{O2} + i_{CH_3OH} = 0 \tag{7.2}$$

Where i_{CH3OH} is the current generated by the oxidation of the crossed-over methanol to the cathode which is governed by the flux of methanol through membrane N_{CH3OH}:

$$N_{CH_3OH} = \frac{-i_{CH_3OH}}{nF} \tag{7.3}$$

The potential loss with air (lower oxygen concentration) therefore will be significantly higher than that with oxygen for considerable values of N_{CH3OH} and negligible for small values of N_{CH3OH}. The small difference between air and oxygen operation shows that the methanol cross-over effect on the cathode is not very significant given the low concentration of methanol used.

No reports for pure Pd cathodes in direct methanol fuel cells were found in the literature; however some palladium alloys have been tested as cathode materials in DMFC. Mustain et al. tested a DMFC with a Pd_3Co cathode and Pt anode at 60 ºC operating with oxygen and 0.5M methanol solution [5]. They observed current densities of ca. 20 mA cm^{-2} in these conditions, close to the 18 mA cm^{-2} exhibited with Pd-EG11 with 1M methanol.

Figure 7-4 and Figure 7-5 show cell polarization curves for a DMFC with Pd and Pt cathode catalysts fed with 3M methanol solution, operating with air and oxygen, respectively. The performance with Pd as with Pt cathodes improved significantly with an increase in temperature. The performance of the Pd MEA improved more with temperature increase than Pt when operating with air or oxygen due to combined effect of larger activation energy and higher methanol tolerance (methanol permeability increases with temperature).

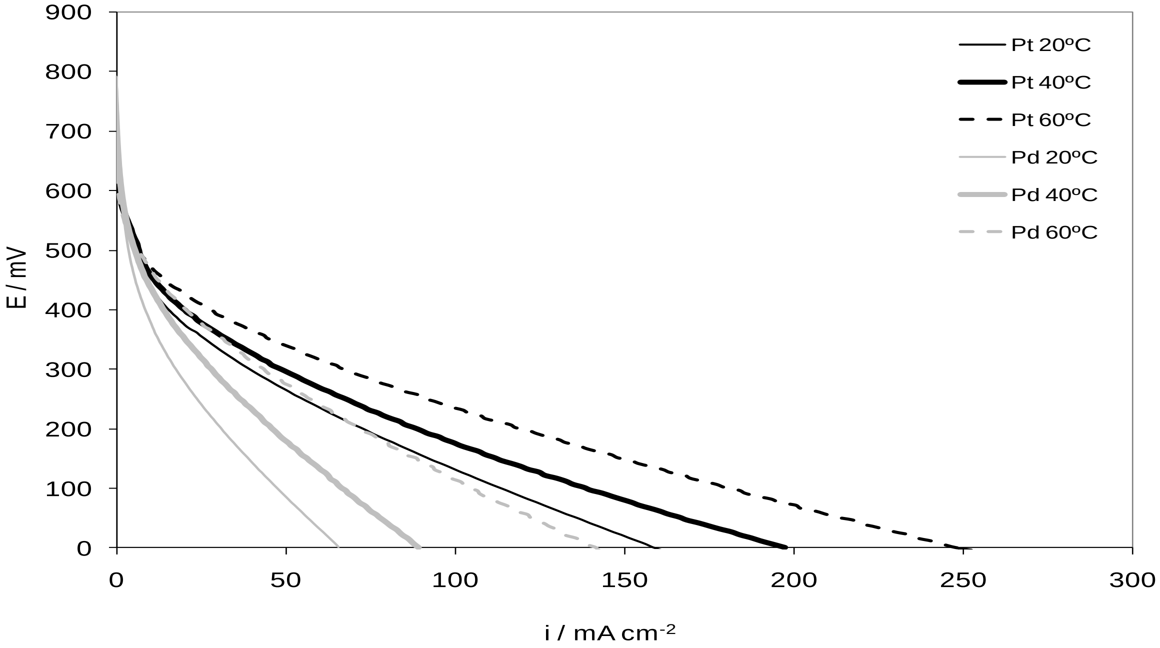

Figure 7-4: Comparison of polarization curves of a direct methanol fuel cell operating with air and 3M methanol with Pd/C and commercial Pt/C from E-tek as cathode catalyst at 20, 40 and 60 ºC.

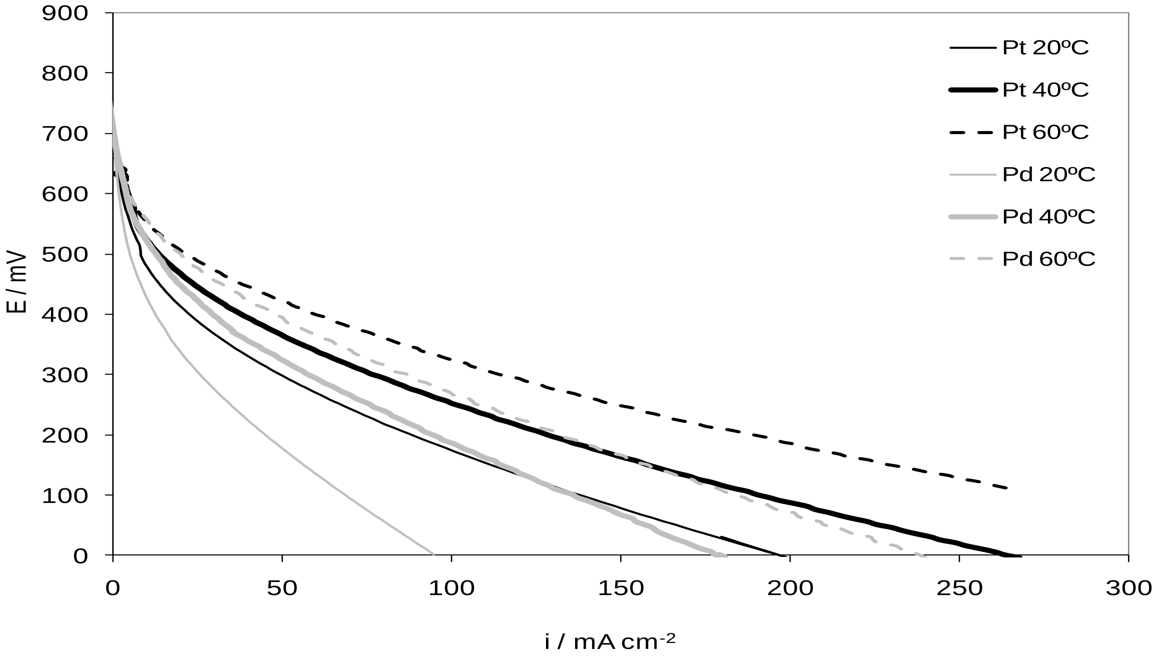

Figure 7-5: Comparison of polarization curves of a direct methanol fuel cell operating on oxygen and 3M methanol with Pd/C and commercial Pt/C from E-tek as cathode catalyst at 20, 40 and 60 ºC.

Table 7-2 summarizes current densities at 0.4 V and cell voltage at 5 mA cm^{-2} for the polarization curves in Figure 7-4 and Figure 7-5. Cell voltages at 5 mA cm^{-2} were larger for the Pt MEA in every case; however, the difference between Pd and Pt performance decreased compared to when using 1M methanol solution. Using 3M methanol solution the difference in cell voltage between Pt and Pd MEAs was smaller with air operation, whilst no differences between air and oxygen where observed when the cell was operating with 1M methanol. For example, with 3M methanol solution at 20 ºC the difference was 35 mV for air and 75 mV for oxygen whilst at 60 ºC it was only 12 mV for air and 24 mV for oxygen. This more pronounced increase in difference between air and oxygen operation, compared to 1M methanol, with increasing temperature between Pd and Pt cell potentials at low current densities would indicate that the higher methanol concentration has a more negative effect on the Pt cathode performance (higher concentration causes higher crossover rate) than in the Pd. On the other hand, at high current densities differences between Pd and Pt increase again due to the improvement in the Pt cathode performance caused by the consumption of the crossed-over methanol when the cell is polarized [6] discussed further in this chapter (Section 6.2).

Table 7-2: Current densities at 0.4 V, cell voltage at 5 mA cm^{-2} and peak power densities for a direct methanol fuel cell with 3M methanol solution fed to the anode at 20, 40 and 60 ºC.

Cathode catalyst	**Temperature (ºC)**	**Cathode fed**	**Voltage at 5 mA cm^{-2} (mV)**	**Current density at 0.4 V (mA cm^{-2})**	**Peak power density (mW cm^{-2})**
Pd-EG11	20	Air	455	8.7	6.2
Pt/C-Etek	20	Air	490	14.8	14.2
Pd-EG11	20	O_2	472	9.4	6.9
Pt/C-Etek	20	O_2	547	22.2	17.6
Pd-EG11	40	Air	485	11.5	9.3
Pt/C-Etek	40	Air	514	23	26.6
Pd-EG11	40	O_2	503	14.5	10.3
Pt/C-Etek	40	O_2	590	38	25.8
Pd-EG11	60	Air	507	16.7	19.1
Pt/C-Etek	60	Air	519	26.4	25.7

Pd-EG11	60	O_2	566	40	26
Pt/C-Etek	60	O_2	590	59.4	37.8

Figure 7-6 and Figure 7-7 show polarization curves for a DMFC with Pd and Pt cathode catalysts fed with 5M methanol solution, operating with air and oxygen, respectively. When 5M methanol was fed to the anode the advantage of using Pd instead of Pt in the cathode, with lower activity towards the methanol oxidation reaction, became evident. DMFC would be ideally operating at 60 ºC or higher, to enhance both anode and cathode reactions, and with air at atmospheric pressure, to reduce operating cost and energy consumption. On these operating conditions Pd advantaged Pt as cathode catalyst.

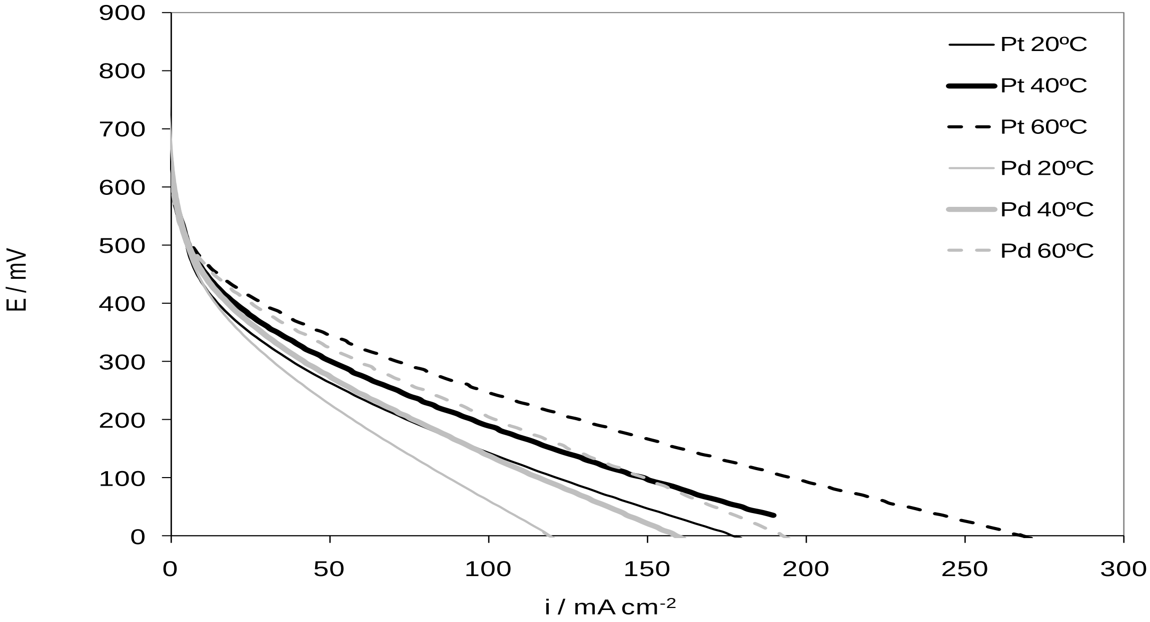

Figure 7-6: Comparison of polarization curves of a direct methanol fuel cell operating with air and 5M methanol with Pd/C and commercial Pt/C from E-tek as cathode catalyst at 20, 40 and 60 ºC.

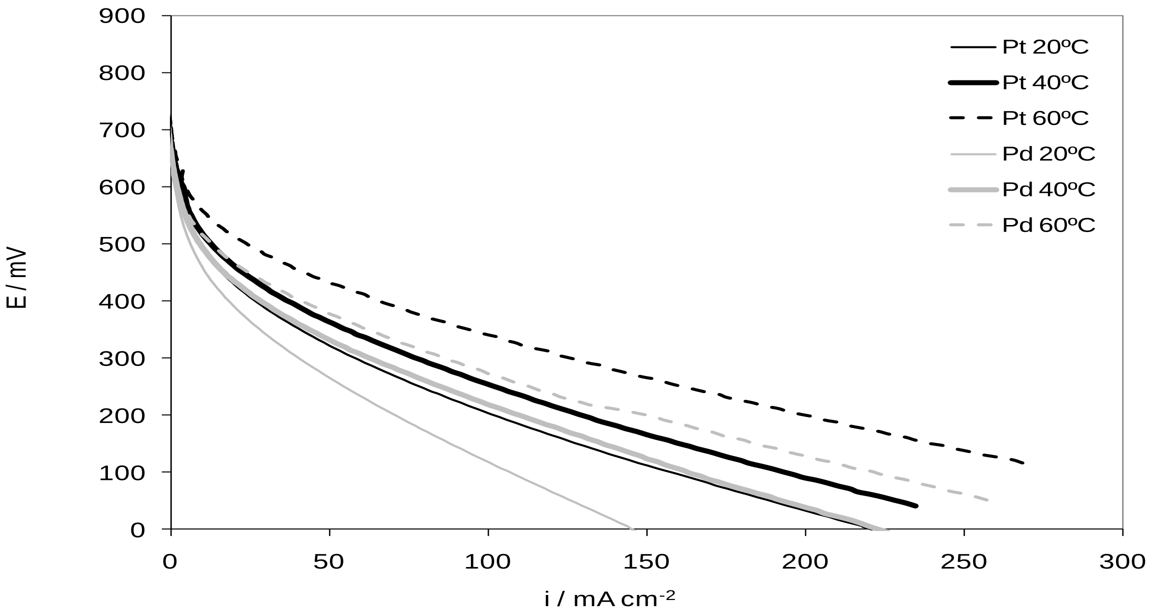

Figure 7-7: Comparison of polarization curves of a direct methanol fuel cell operating with oxygen and 5M methanol with Pd/C and commercial Pt/C from E-tek as cathode catalyst at 20, 40 and 60 ºC.

At low current densities with 5M methanol the palladium MEA exhibited slightly enhanced performance with increasing temperature with both oxygen and air, as expected. However, the performance of the Pt MEA only increased with the temperature operating with oxygen; with air current densities decreased in the kinetic region when the temperature was raised from 40 to 60 ºC. At 5 mA cm^{-2} with air operation at 20, 40 and 60 ºC cell potentials for the Pd MEA were virtually identical to those corresponding to the Pt MEA. However, with oxygen operation Pt exhibited slightly higher cell potentials than Pd at 20, 40 and 60 ºC (42, 26 and 29 mV). On the other hand, at larger current densities, larger than ca. 20 mA cm^{-2}, the Pt MEA also showed improved performance with the temperature. This effect is caused, as discussed for the 3M methanol solution, by the methanol crossed-over to the cathode, which decreases the cathode performance at low current densities but is consumed during the polarization decreasing this way its effect as the current density increases.

Table 7-3: Current densities at 0.4 V, cell voltage at 5 mA cm^{-2} and peak power densities for a direct methanol fuel cell with 5M methanol solution fed to the anode at 20, 40 and 60 ºC.

Cathode catalyst	**Temperature (ºC)**	**Cathode fed**	**Voltage at 5 mA cm^{-2} (mV)**	**Current density at 0.4 V (mA cm^{-2})**	**Peak power density (mW cm^{-2})**
Pd-EG11	20	Air	498	14	11.5
Pt/C-Etek	20	Air	497	14.5	14.9
Pd-EG11	20	O_2	510	28.7	26.5
Pt/C-Etek	20	O_2	562	26.2	20.3
Pd-EG11	40	Air	505	18	15.3
Pt/C-Etek	40	Air	514	24	26.6
Pd-EG11	40	O_2	540	35.1	22
Pt/C-Etek	40	O_2	566	36.3	26
Pd-EG11	60	Air	507	25.2	20.6
Pt/C-Etek	60	Air	508	19.6	19
Pd-EG11	60	O_2	559	43.8	30
Pt/C-Etek	60	O_2	588	65.1	40.5

At 60 ºC and with air fed to the cathode (suitable operating conditions for a DMFC) current density using Pt in the cathode decreased from 26 to 20 mA cm^{-2} when methanol concentration was increased from 3 to 5M. The opposite effect was exhibited by the MEA with Pd in the cathode, which performance was enhanced from 17 to 25 mA cm^{-2}.

Figures 7-8 and 7-9 compare polarization curves of Pd and Pt MEAs at 60 ºC using methanol concentrations of 3, 5 and 7 M using air and oxygen, respectively. When the cell was operating with air, platinum exhibited a small decrease in current density when changing from methanol 1M to 3M to 5M (from 27 to 26 to 20 mA cm^{-2} at 400 mV) and its performance fell sharply with a concentration of 7 M; to 5 mA cm^{-2}. However, when the platinum MEA was operated with oxygen, the current density increased by 12.5 and 6 mA cm^{-2} at 400 mV when changing from 1M to 3M and from 3M to 5M, respectively. While with O_2 the current density decreased at 7M less dramatically than air (from 65 to 50 mA cm^{-2}). The overall cell performance is a balance between improved anode kinetics and greater methanol crossover causing greater cathode losses, when methanol feed concentration is increased. The cross-over influence is more evident with air due to the lower O_2 concentration as discussed earlier.

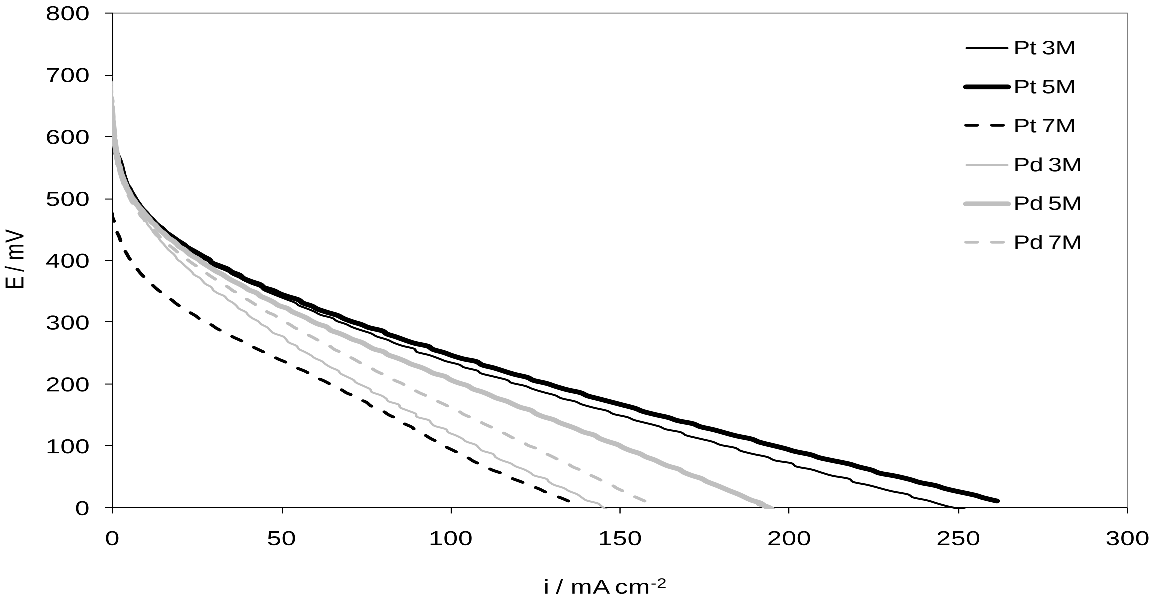

Figure 7-8: Comparison of polarization curves of a direct methanol fuel cell operating with air with Pd/C and commercial Pt/C from E-tek as cathode catalyst at 60 ºC and 3, 5 and 7M methanol.

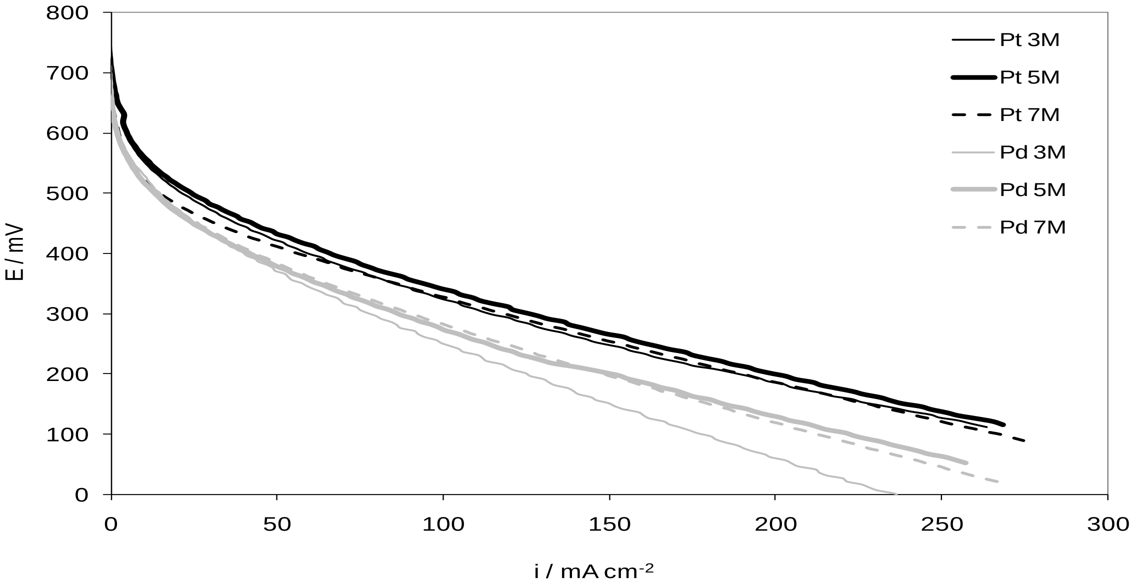

Figure 7-9: Comparison of polarization curves of a direct methanol fuel cell operating with oxygen with Pd/C and commercial Pt/C from E-tek as cathode catalyst at 60 ºC and 3, 5 and 7M methanol.

Table 7-4: Current densities at 0.4 V, cell voltage at 5 mA cm^{-2} and peak power densities for a direct methanol fuel cell with 3, 5 and 7M methanol solution fed to the anode at 60 ºC.

Cathode catalyst	**Methanol concentration (mol L^{-1})**	**Cathode fed**	**Voltage at 5 mA cm^{-2} (mV)**	**Current density at 0.4 V (mA cm^{-2})**	**Peak power density (mW cm^{-2})**
Pd-EG11	3	Air	503	14.7	19.1
Pt/C-Etek	3	Air	519	26.4	25.7
Pd-EG11	3	O_2	566	40	26
Pt/C-Etek	3	O_2	590	59.4	37.8
Pd-EG11	5	Air	507	25.2	20.6
Pt/C-Etek	5	Air	508	19.6	19
Pd-EG11	5	O_2	559	43.8	30
Pt/C-Etek	5	O_2	588	65.1	40.5
Pd-EG11	7	Air	503	24.9	17.2
Pt/C-Etek	7	Air	400	5.0	12.8
Pd-EG11	7	O_2	558	44.6	30.9
Pt/C-Etek	7	O_2	556	50.1	38.5

7.2.2. Cathode polarizations

The amount of methanol crossing from anode to cathode through the electrolyte membrane (methanol cross-over) in a DMFC, increases with increasing methanol concentration and temperature. The presence of methanol in the cathode decreases its performance by hindering the access of the oxygen molecules to the catalyst sites and, in some cases, by the “mixed potential” effect [7]. On the other hand, methanol oxidation reaction improves with increasing methanol concentration and temperature. Therefore the overall cell performance is a balance of the two factors. In this section the influence of the methanol concentration on the cathode performance was studied at 60 ºC.

Cathode polarization curves were obtained by adding cell (operating with oxygen) and anode potential-current curves; since a cell potential-current curve can be obtained by subtracting the anode from the cathode polarization curve [8]. To record anodic polarization curves H_2 flowed through the cathode, this way the latter behaves like a Normal Hydrogen Electrode (NHE) [7]. The obtained cathode data were IR-free since the anode data inherently includes the IR losses in it. Figure 7-10 shows anode polarization curves at 60 ºC with different methanol concentrations fed to the anode. Anodic current densities increased as expected with increasing methanol concentration. Currents densities produced by the anode at 400 mV and 60 ºC for 1, 3, 5 and 7M methanol concentration were 23.2, 26.1, 30.2 and 38.5 mA cm^{-2}, respectively.

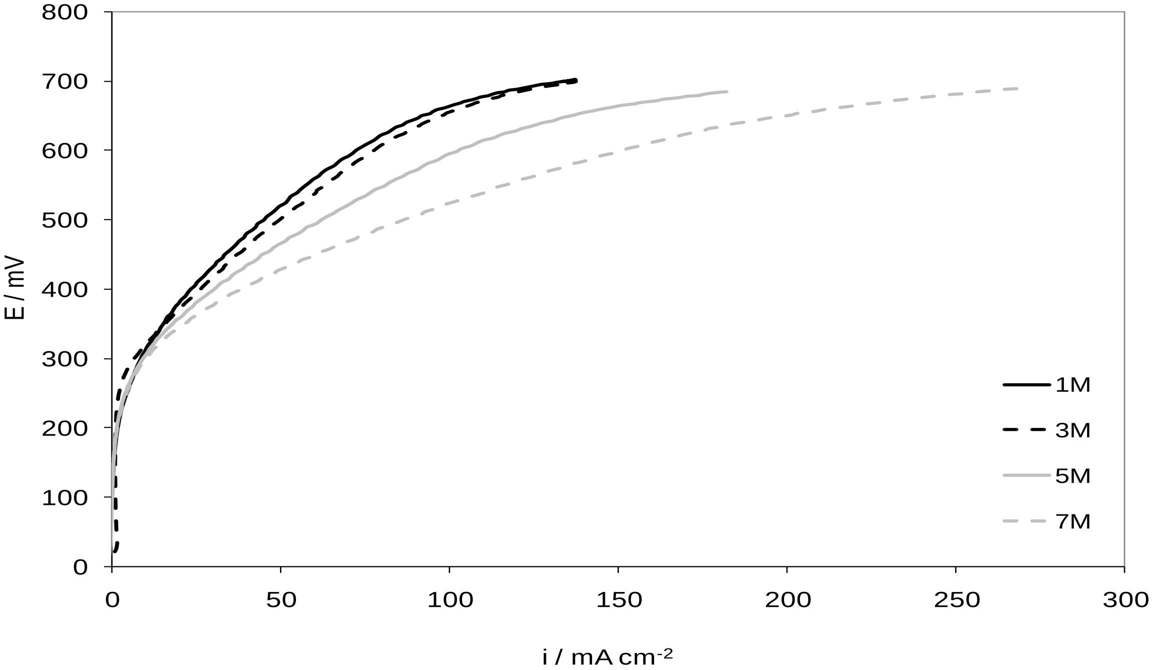

Figure 7-10: Anode polarization curves for a fuel cell with PtRu/C from E-tek anode catalyst and Pd-EG11 cathode catalyst at 60 ºC fed with methanol 1, 3, 5 and 7M with air operation.

These anode polarization curves demonstrated how anode performance increased with fuel concentration. However this does not apply to the overall cell performance mainly due to the effect of methanol crossover. There is an optimum methanol concentration at which the cell would exhibit its maximum performance. This optimum methanol concentration depends on various parameters, including temperature and cathode catalyst. Ko et al. built a dynamic model to study the influence of different parameters on cell performance, and according to their model, the optimal methanol concentration using

Pt/C in the cathode and at 60 ºC was ca. 1M [9]. Since the activity of Pd/C towards the methanol oxidation reaction is lower than that of Pt/C, the optimal methanol concentration when using Pd/C as cathode material is expected to be higher.

Figure 7-11 shows cathode polarization curves for the Pt MEA at different methanol concentration. Data is compared to polarization curves, in the corresponding current range, obtained from a hydrogen PEM fuel cell. Cathode polarization curves with 1, 3 and 5M methanol solution exhibited a raising potential with increasing current densities; this behavior is attributed to the improvement of cell performance with the oxidation of the methanol present in the cathode (methanol crossed-over is oxidized when the cell is polarized), as discussed in the work of Gurau et al. [6]. Using 7M methanol there was a sharp decrease in the rest potential (i = 0), of approximately 150 mV, compared to 5M. A great decrease at low current densities (10 mA cm^{-2}), of ca. 150 mV, in the cathode potential was observed when the methanol concentration was further increased to 7M. This confirms the decreased cathode performance with increased methanol concentration.

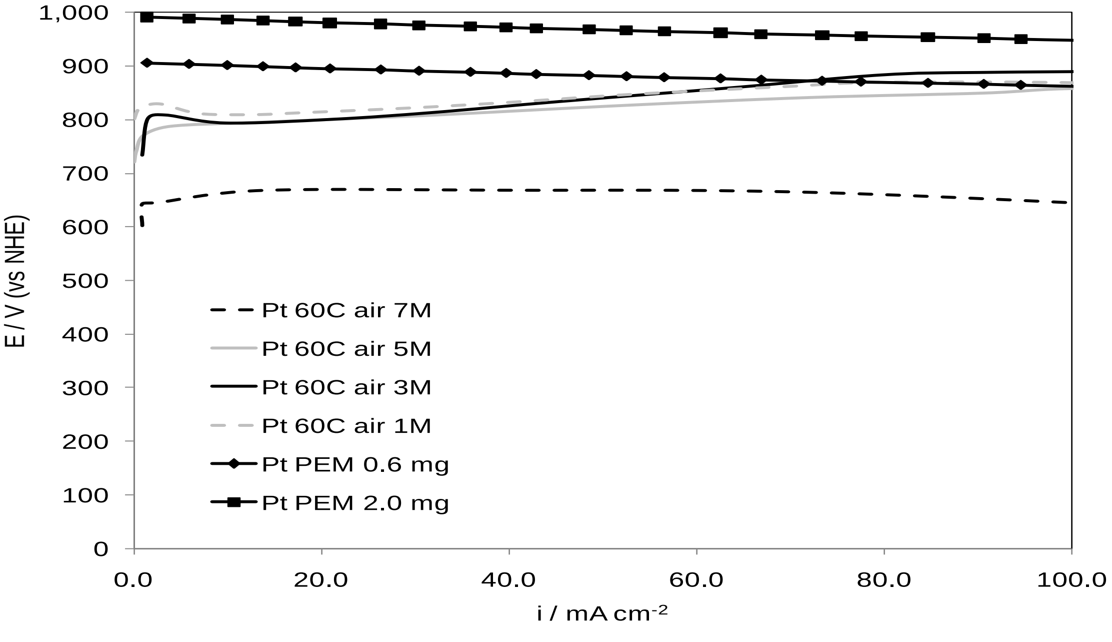

Figure 7-11: Cathode polarization curves for Pt MEA for a DMFC at 60 ºC fed with 1, 3, 5 and 7M methanol solution with air operation compared to experimental (0.6 mg) and predicted (2.0 mg) data from a H_2 PEM fuel cell.

DMFC data in Figure 7-11 is compared with data from a hydrogen fuel cell. At low current densities (under 10 mA cm^{-2}) there is a difference of ca. 200 mV between the DMFC (using methanol 1, 3 and 5M) and the hydrogen fuel cell with the same metal loading. At larger current densities, 10 mA cm^{-2}, this difference decreases up to ca. 100 mV for 1, 3 and 5 M methanol solution. This illustrates how when the cell is polarized (the methanol present in the cathode is consumed) the behavior of both cathodes gets closer. Also, as current was drawn the crossover of methanol fell and thus the cathode partially recovered.

Since the Pt loading in the cathode of the DMFC was approximately 3.3 times larger than the loading in the hydrogen fuel cell, an estimation of the performance of the hydrogen fuel cell with higher loading.

From Tafel equation we can write:

$$\eta_1 = \frac{RT}{\alpha nF}\ln i + \frac{RT}{\alpha nF}\ln i_0 \tag{7.4}$$

$$\eta_2 = \frac{RT}{\alpha nF}\ln i + \frac{RT}{\alpha nF}\ln i_0^* \tag{7.5}$$

Where i is current density, η_1 and η_2 are cell overpotentials and i_0 and i_0^* are apparent exchange current densities with cathode metal loadings of 2.0 and 0.6 mg cm^{-2}, respectively. Since apparent exchange current density is proportional to the electrochemically active surface area (See equation 8.26) and this is proportional to the catalyst load $3.3 \times i_0^* = i_0$; substracting equations 7.5 from 7.4:

$$\eta_1 - \eta_2 = \frac{RT}{\alpha nF}\ln 3.3 \tag{7.6}$$

Solving equation 7.6 the difference η_1 - η_2 equals 69 mV. This amount was added to the potential on the data corresponding to loading 0.6 mg cm^{-2} to obtain the estimated curve for loading 2.0 mg cm^{-2}.

Figure 7-12 compares cathode polarization curves for the Pd MEA at different methanol concentration with data obtained from a hydrogen PEM fuel cell. It is clear that whilst Pd cathode data with methanol free cathode exhibited lower rest potential (or onset) than Pt by 120mV (ca. 1000 vs 880 mV). Pd cathode potential losses due to the mixed potential cause by the methanol cross over were significantly lower; for example at 5M it was approx 100 mV for Pd compared to 200 for Pt, therefore the overall difference between the two cathodes (with air operation) using 5M methanol becomes negligible. At higher concentrations Pd becomes more advantaged than Pt. The effect of crossover would be even more severe at lower cathode loading (equation 7.2) because the current generated from the oxygen reduction would be lower and therefore Pd would surpass Pd at even lower methanol concentrations.

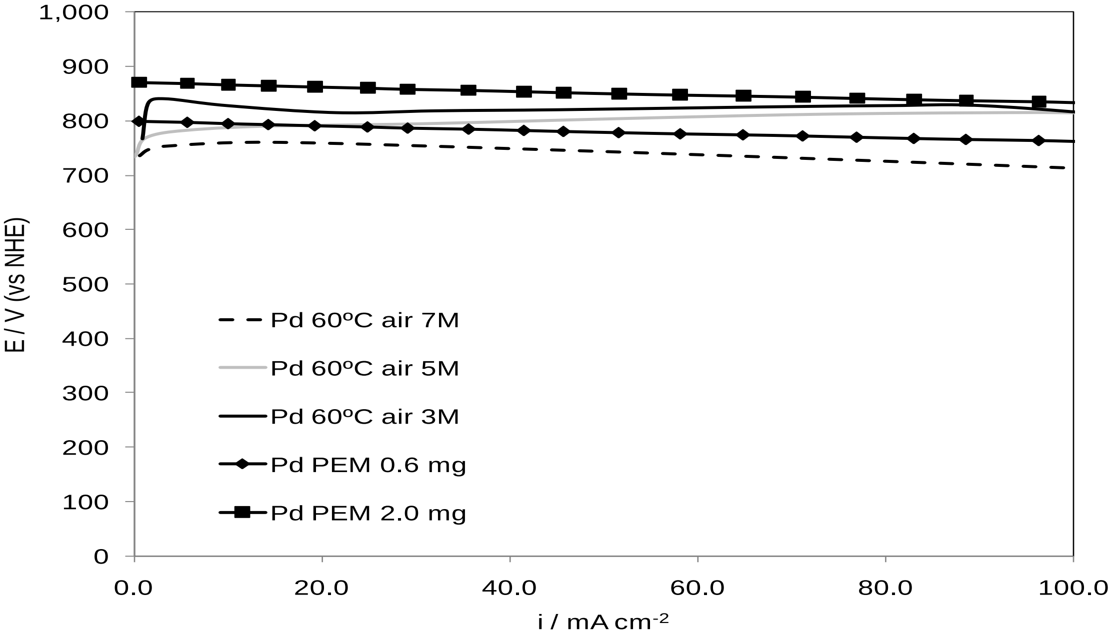

Figure 7-12: Cathode polarization curves for Pd MEA for a DMFC at 60 ºC fed with 3, 5 and 7M methanol solution compared to data from a H_2 PEM fuel cell.

Experimental results agreed with studies published by McGrath [10], where it was shown how the partial substitution of Pt by Pd in the cathode led to higher cell performance at high methanol concentrations, even with lower total metal loading. Comparison data from this study could not be drawn due to the use of different operating conditions; some DMFC from the literature and from this work is summarised in Table 7-5.

Table 7-5: Comparison of Pd catalysts performance with published data.

Catalyst	Output	Operating Conditions	Reference
Pd/C + Pt/C	20 mA cm^{-2}	0.4 V, 30 ºC, 5M methanol, 0.5L/min air, 2 mg cm^{-2} Pt + 1 mg cm^{-2} Pd	[10]
Pt/C	9 mA cm^{-2}	0.4 V, 30 ºC, 5M methanol, 0.5L/min air, 4 mg cm^{-2} Pt	[10]
Pd_3Co/C	20 mA cm^{-2}	0.4 V, 60 ºC, 0.5M methanol, oxygen, 0.2 mg cm^{-2} Pd_3Co	[5]
Pd/C	18 mA cm^{-2}	0.4 V, 40 ºC, 5M methanol, 0.3 L/min air, 2 mg cm^{-2} Pd	This work
Pt/C	24 mA cm^{-2}	0.4 V, 40 ºC, 5M methanol, 0.3 L/min air, 2 mg cm^{-2} Pt	This work
Pd/C	25 mA cm^{-2}	0.4 V, 60 ºC, 5M methanol, 0.3 L/min air, 2 mg cm^{-2} Pd	This work
Pt/C	20 mA cm^{-2}	0.4 V, 60 ºC, 5M methanol, 0.3 L/min air, 2 mg cm^{-2} Pt	This work

7.3. Effect of temperature on fuel cell performance

Anode polarization curves at different temperatures for a fuel cell with PtRu/C from E-tek in the anode and fed with 5M methanol solution are compared in Figure 7-13. The increase of temperature increased the anode performance by increasing the kinetics of the methanol oxidation reaction. Anodic currents at 400 mV at 20, 40 and 60 ºC were 10.2, 17.8 and 30.2 mA cm^{-2}, respectively.

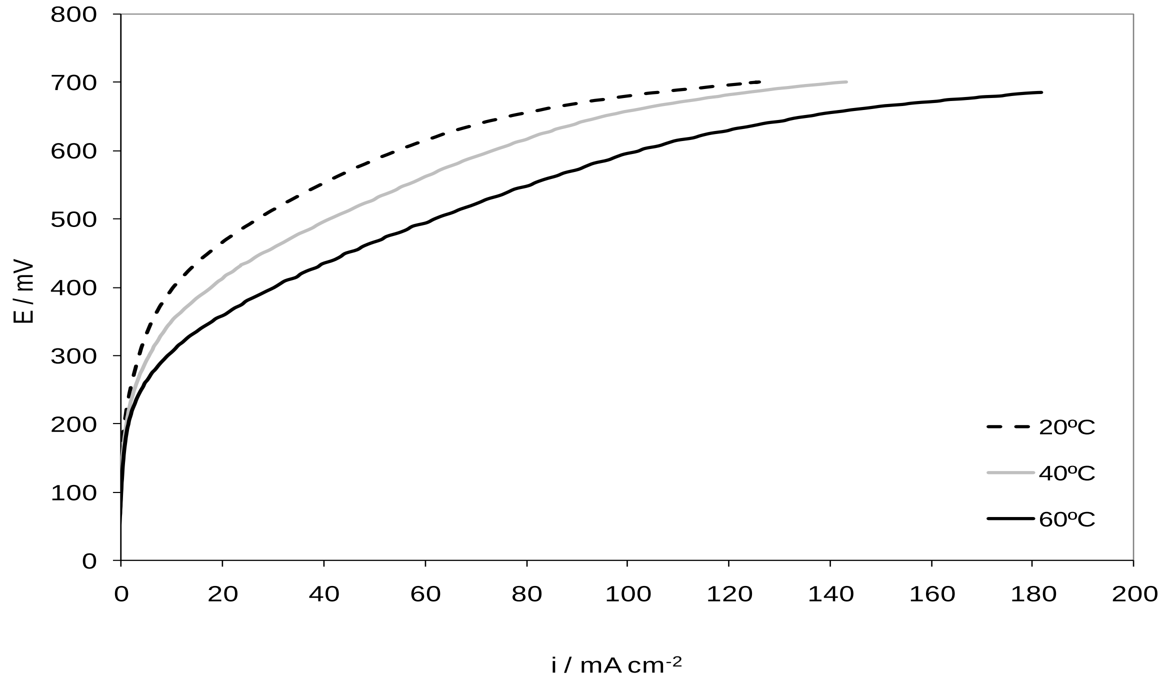

Figure 7-13: Anode polarization curves for a fuel cell with PtRu/C from E-tek anode catalyst and Pd-EG11 cathode catalyst at 20, 40 and 60 ºC fed with methanol 5M.

Anode performance increased with temperature; however, with an increase in temperature methanol crossover to the cathode may increase due to faster diffusion. The dependence of methanol permeability on temperature through Nafion® has been reported to follow Arrhenius behavior: for Nafion® 117 at 20, 40 and 60 ºC values were ca. 14 x 10^{-7}, 22 x 10^{-7} and 34 x 10^{-7} cm^{2} s^{-1}, respectively [11]. A greater crossover rate when the temperature was increased from 40 to 60 ºC is the main cause of the lack of significant increase in cell performance with temperature at low current densities.

Figure 7-14 shows cathode polarization curves for the Pt MEA fed with 5M methanol solution at 20, 40 and 60 ºC. The highest cathode potential at low current densities (10 mA cm^{-2}) was exhibited at 20 ºC, ca. 830 mV, and remained constant up to 100 mA cm^{-2}. When the temperature was raised to 40 ºC, the cathode potential at low current densities decreased to ca. 800 mV, despite the enhancement of the ORR by the temperature; it remained also constant up to 100 mA cm^{-2}. At 60 ºC cathode potential decreased further at low current densities, to ca. 780 mV, but increased with the current density due to the consumption of the crossed over methanol (discussed in section 6.1.2). Data was compared with data from a hydrogen fuel cell, all Pt cathode polarizations using 5M methanol are at least 200 mV lower that that predicted for a hydrogen fuel cell with the same loading.

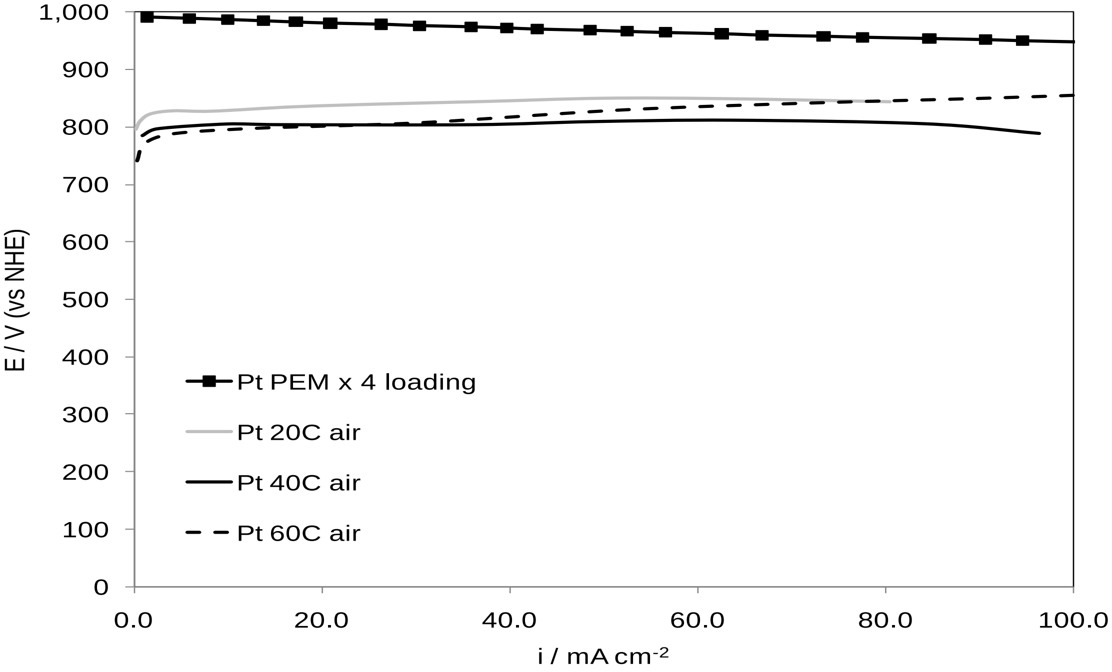

Figure 7-14: Cathode polarization curves for Pt MEA for a DMFC at 20, 40 and 60 ºC fed with 5M methanol solution compared to data from a H_2 PEM fuel cell.

Figure 7-15 shows cathode polarization curves for the Pd MEA fed with 5M methanol solution at 20, 40 and 60 ºC. The trend with increasing temperature is similar to that of Pt in the low current density region, the cathode potential decreases slightly with the temperature. However, the difference with hydrogen fuel cell data is under 60 mV at any operating temperature.

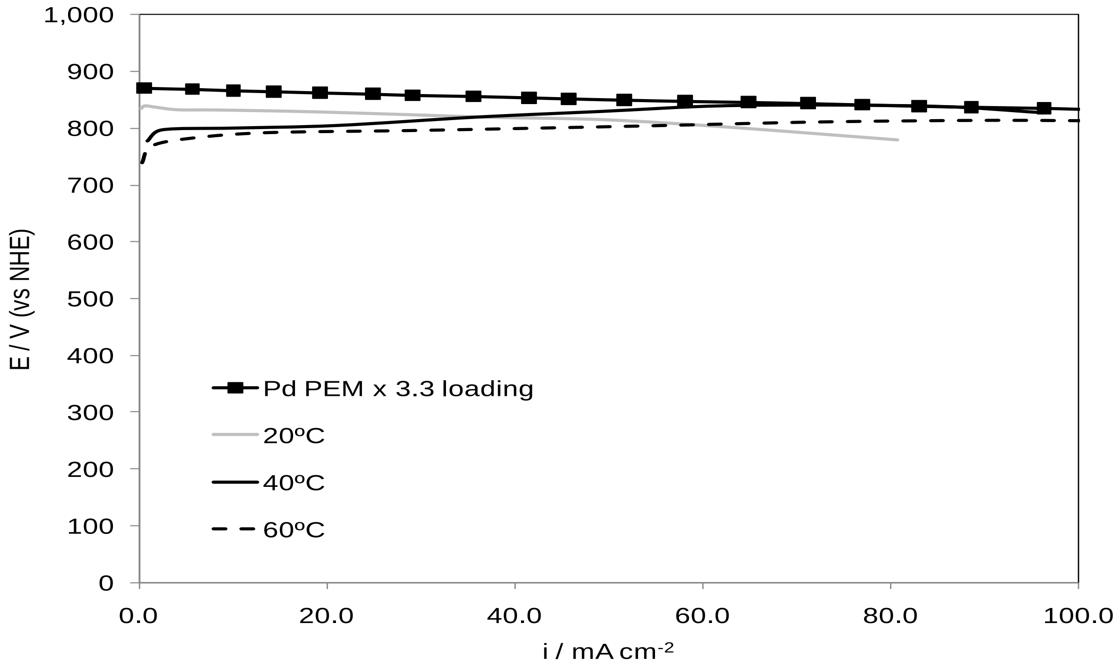

Figure 7-15: Cathode polarization curves for Pd MEA for a DMFC at 20, 40 and 60 ºC fed with 5M methanol solution compared to data from a H_2 PEM fuel cell.

At 60 ºC with air operation (suitable operating conditions for a DMFC), and at low current densities Pd cathodes match the performance of a Pt cathode with the same metal loading when 5M methanol is fed to the anode.

7.4. Conclusions

Pd-EG11 was tested as a cathode catalyst in a direct methanol fuel cell and its performance was compared to a commercial Pt/C. Cell performance was compared at methanol concentrations of 1, 3, 5 and 7M and at temperatures 20, 40 and 60 ºC.

Anode potential vs current density curves showed how anode performance increased with increasing temperature and methanol concentration. This did not always reflect on the overall cell performance due to methanol crossover to the cathode. The effect of methanol crossover was more severe for the Pt cathode due to its higher activity towards the methanol oxidation reaction.

Despite its lower electrochemical surface area palladium overtook platinum as cathode catalyst at high methanol concentrations. Current densities at 400 mV exhibited by the palladium MEA were higher than for platinum at 60 ºC with methanol concentrations 5M or higher, suitable operating conditions for DMFC. This makes Pd an adequate substitute to Pt due to its lower price. Moreover, since the effect of crossover would be more severe for Pt at lower cathode loadings (lower ORR current) the performance of a Pd cathode would be higher than that of a Pt cathode even lower than 5M (equal performance at low current densities with 2 mg cm^{-1} cathode loading).

References

1. Lin, J., A. Trivisonno, R. Wycisk, and P.N. Pintauro, *Optimized DMFC Performance Comparison for Modified and Unmodified Nafion Membranes*. ECS 210th Meeting.

2. Mustain, W.E. and J. Prakash, *Kinetics and mechanism for the oxygen reduction reaction on polycrystalline cobalt-palladium electrocatalysts in acid media*. Journal of Power Sources, 2007. 170(1): p. 28-37.

3. Paulus, U.A., T.J. Schmidt, H.A. Gasteiger, and R.J. Behm, *Oxygen reduction on a high-surface area Pt/Vulcan carbon catalyst: a thin-film rotating ring-disk electrode study.* Journal of Electroanalytical Chemistry, 2001. 495(2): p. 134-145.

4. Kadirgan, J.F., Beden, B., Leger, J.M. and Lamy, *Synergistic effect in the electrocatalytic oxidation of methanol on platinum+palladium alloy electrode.* Journal of Electroanalytical Chemistry, 1981. **125**(1): p. 89-103.

5. Mustain, W.E., K. Kepler, and J. Prakash, *CoPdx oxygen reduction electrocatalysts for polymer electrolyte membrane and direct methanol fuel cells.* Electrochimica Acta, 2007. **52**(5): p. 2102-2108.

6. Gurau, B. and E.S. Smotkin, *Methanol crossover in direct methanol fuel cells: A link between power and energy density.* Journal of Power Sources, 2002. **112**(2): p. 339-352.

7. *Electrocatalysis of Direct Methanol Fuel Cells*, ed. H. Liu and J. Zhang. 2009, Weinheim: WILEY-VCH.

8. Vielstich, W., H. Gasteiger, and A. Lamm, *Handbook of fuel cells : fundamentals, technology and applications*. 2003, Chichester: Wiley. 4 v.

9. Ko, D., M. Lee, W.H. Jang, and U. Krewer, *Non-isothermal dynamic modelling and optimization of a direct methanol fuel cell.* Journal of Power Sources, 2008. **180**(1): p. 71-83.

10. McGrath, K., *High Concentration Direct Methanol Fuel Cell Using QSI-Nano® Pd.* Energy Research Laboratory, QuantumSphere Inc., 2008.

11. Tricoli, V., N. Carretta, and M. Bartolozzi, *A Comparative Investigation of Proton and Methanol Transport in Fluorinated Ionomeric Membranes.* Journal of the Electrochemical Society, 2000. **147**(4): p. 1286-1290.

Chapter 8: Modeling of low temperature polymer electrolyte membrane fuel cell

8.1. Introduction

A model for low temperature hydrogen polymer electrolyte membrane fuel cells (PEMFCs) has been developed using thermodynamics, transport and kinetic equations. The model considers mass transport through a thin film electrolyte and through porous media. Available experimental physical and chemical properties data for PEMFCs have been used, when appropriated, in the construction of this model. In this chapter a pseudo one dimensional model is described for a fuel cell made up of a Nafion® membrane sandwiched between two gas diffusion electrodes. The model is used to simulate the influence of cathode catalyst loading, thickness and materials and the operating conditions on the cell voltage and current density output.

8.2. Mathematical model

The mathematical model built in this study was a pseudo one dimensional model since the gas flow channels of the cell were not considered. The parts of the fuel cell considered for the construction of the model were a Nafion® membrane, cathode catalyst layer with gas diffusion layer. Assumptions made in the model were:

- Single vapor phase operation, i.e. no liquid water formation in the pores of the catalyst layer [1, 2, 3].
- Steady state and isothermal operation of the system.
- Ideal gas behavior.
- Mass transport is solely due to diffusion, convection effect is negligible.
- Negligible contact resistances between components.

- No membrane swelling.
- Isotropic macro-homogeneous porous regions.
- Catalyst layer treated as interface rather than a region (zero dimensional).
- Anode losses in PEMFCs with the loading used are negligible and therefore not considered.

Since the cell temperature is controlled by electrical heaters during tests, the isothermal operation was considered a realistic assumption. Ideal gas behavior was suitable because the fuel cell was not pressurised. The conditions at the boundary between flow channels and the diffusion layer were taken as those of the feed gas, this assumption was justified by the excess of gas flow applied.

The macrohomogeneous model was used for the catalyst layer [4]. This model considers the porous electrode as an 'average' of the solid electrode and the electrolyte. Thus, the effective conductivity of the porous electrode is the weighted volume average of the respective conductivities. Diffusion coefficients and other properties are similarly averaged.

The objective of this model is to determine the effect of cathode catalyst and operating conditions on the cell voltage of the Nafion® based low temperature PEMFC. The overall cell voltage is obtained by subtracting from the thermodynamic cell potential (reversible potential) voltage losses, associated with ohmic resistances through membrane and electrodes, and kinetic losses at the cathode.

$$E_{cell} = E_{rev} - |\eta_c| - iR \qquad (8.1)$$

Where E_{cell} is the overall cell voltage, E_{rev} is the reversible cell potential, η is the potential losses induced by the polarization and iR is the ohmic resistance losses.

8.3. Thermodynamic equilibrium potential

The overall electrochemical reaction in a low temperature polymer electrolyte membrane fuel cell operating with H_2 as fuel and O_2 as oxidant can be expressed as:

$$H_{2(g)} + \frac{1}{2} O_{2(g)} \rightarrow H_2O_{(l)} \tag{8.2}$$

The thermodynamic equilibrium potential for the above stated reaction can be determined by the Nernst equation:

$$E_{T,P}^{rev} = -\left(\frac{\Delta G_T^0}{nF}\right) + \frac{RT}{nF} \ln\left[\frac{P_{H_2}\left(P_{O_2}\right)^{0.5}}{\alpha_{H_2O}} \frac{\alpha_{H_2O}^0}{P_{H_2}^0\left(P_{O_2}^0\right)^{0.5}}\right] \tag{8.3}$$

Where P_X is the partial pressure of the species X. ΔH^0 is the standard enthalpy and ΔS^0 is the standard entropy of the reaction at temperature T and activity 1. α_{H2O} is the water activity at temperature T. P^0_{O2}, P^0_{H2} and α^0_{H2O} are the standard values of oxygen and hydrogen partial pressure and water activity, respectively, at temperature T. The last three values equal 1.

In order to calculate the change in the standard Gibbs free energy with temperature, ΔG^0_T, for Equation 8.3 the following equation was proposed by Scharifker et al. [5]:

$$\Delta G_T^0\ kJ.mol^{-1} = -0.0000487792\mathrm{T}^2 + 0.1934130924\mathrm{T} - 290.039925263 \tag{8.4}$$

The cell reversal potential calculated from Equation 8.3 would diverge from the standard reversal potential depending on the water activity and oxygen and hydrogen partial pressures.

The water activity is given by [6]:

$$a_{H_2O} = P_{H_2O} / P^{*}_{H_2O} = \frac{RH\%}{100} \tag{8.5}$$

Where P_{H2O} is the water vapor pressure in equilibrium with the acid electrolyte, P^{*}_{H2O} is the saturation vapor pressure of pure water at the same temperature.

Saturated water vapor pressures were obtained from steam tables [7]. To present water vapor pressures in the temperature range of 273-500 K, data was plotted and the following function was build:

$$P^{sat*}_{H_2O} = \begin{pmatrix} 142.07682T^4 - 171026.12676T^3 + 78013638.11584T^2 \\ -15953375633.8471T + 1231888491801.45 \end{pmatrix} \times 10^{-10} \tag{8.6}$$

Where P is in atmospheres and T is in kelvin.

This model considers the catalyst surface covered by a thin electrolyte film; therefore partial pressures were replaced by activities in the electrolyte. Activities of hydrogen and oxygen could be replaced by their concentration in the thin film by considering their activity coefficients to be close to 1 (applicable at low concentrations). Thus Equation 8.3 can be expressed as:

$$E_{rev} = E^{0}_{rev} + \frac{RT}{nF} \ln \left[\frac{(RT)^{1.5} C_{H_2} \left(C_{O_2}\right)^{0.5}}{a_{H_2O}} \frac{a^{0}_{H_2O}}{P^{0}_{H_2} \left(P^{0}_{O_2}\right)^{0.5}} \right] \tag{8.7}$$

Where the solubility (concentration) of the reactants was obtained using Henry's law:

$$C_{H_2} = \frac{P_{H_2}}{H^{H_2}_{T,C_{Nafion}}} \tag{8.8}$$

$$C_{O_2} = \frac{P_{O_2}}{H^{O_2}_{T,C_{Nafion}}} \tag{8.9}$$

Where C_{H2}, C_{O2} are the concentration of dissolved hydrogen and oxygen Nafion®**,** P_x is the equilibrium partial pressure of species x in atmosphere H^x is Henry's constant for species x in Nafion® electrolyte in atmosphere cm^3 mol^{-1} at a given temperature T. The term RT included in the logarithm in Equation 8.7 was introduced in order to convert the concentration, C_x, into pressure units (atmosphere).

The observed open circuit potential (OCP) for the cell was lower than the value estimated from thermodynamics, E_{rev}, this is due to the effect of cross-over and other phenomena such as carbon corrosion, etc. The hydrogen crossover through the membrane leads to an overvoltage, $\eta_{cross\text{-}over}$, which can be expressed as:

$$\eta_{cross-over} = \frac{-RT}{\alpha F}\ln\left[\frac{i_{cross-over}}{2i_{0,c}} + \sqrt{1+\left(\frac{i_{cross-over}}{2i_{0,c}}\right)^2}\right] \tag{8.10}$$

Where α is the transfer coefficient and i_o is the exchange current density.

The observed OCP would be lower than the theoretical E_{rev}, 1.23 V, by $\eta_{cross\text{-}over}$. The effect of cross-over on polarization curves is only important at small current densities and becomes negligible, i is much larger than $i_{cross\text{-}over}$ (Equation 8.11):

$$\eta_{cross-over} = \frac{-RT}{\alpha F}\ln\left[\frac{\dfrac{i+i_{cross-over}}{2i_{0,c}} + \sqrt{1+\left(\dfrac{i+i_{cross-over}}{2i_{0,c}}\right)^2}}{\dfrac{i}{2i_{0,c}} + \sqrt{1+\left(\dfrac{i}{2i_{0,c}}\right)^2}}\right] \tag{8.11}$$

8.4. Gas transport through porous media

Since the cathode is normally the limiting electrode in hydrogen polymer electrolyte membrane fuel cells, due to the fast kinetics of the hydrogen oxidation reaction [8], the anode was not considered in the construction of this model.

To build this model a one-dimensional diffusion, perpendicular to the electrode surface, was considered. The diffusion of multi-component gas streams (three species are present in the cathode gas stream: O_2, N_2 and H_2O) through the porous carbon electrode can be described by the Stefan-Maxwell equation:

$$\frac{\partial X_i}{\partial z} = \frac{RT}{P} \sum_j \frac{X_i N_j - X_j N_i}{D_{ij}^{eff}} \tag{8.12}$$

Where X_i is the molar fraction of species i, N_i is the molar flux of species i and $D_{ij}{}^{eff}$ is the effective binary diffusion coefficient for the pair i-j in the porous medium.

$D_{ij}{}^{eff}$ was calculated using the Slattery-Bird [9] correlation and corrected afterwards to take into account porosity and tortuosity effects as in the work published by Scott et al. [10].

$$D_{ij}^{eff} = \frac{a}{P} \left(\frac{T}{\sqrt{T_{c,i} T_{c,j}}} \right)^b \left(P_{c,i} P_{c,j} \right)^{1/3} \left(T_{c,i} T_{c,j} \right)^{5/12} \left(\frac{1}{M_i} + \frac{1}{M_j} \right)^{1/2} \varepsilon^{\tau} \tag{8.13}$$

Where T_c and P_c are gas critical temperature and pressure, respectively, M is the gas molecular weight, ε is the porosity, τ is the tortuosity and a and b are constants. a is 0.0002745 for di-atomic gases and 0.000364 for water vapor and b is 1.832 for di-atomic gases and 2.334 for water vapor.

The following equations describe the flux of species. Nitrogen is an inert species therefore its flow can be expressed as:

$$N_{N_2,g} = 0 \tag{8.14}$$

Applying mass balance:

$$N_{O_2,g} = \frac{j}{4F} \tag{8.15}$$

$$N_{H_2O,g} = \frac{-j}{2F} \tag{8.16}$$

Where j is the current density per geometric electrode area and F is Faraday constant. The flux direction is determined by its sign: N_{H2O} is negative because H_2O is produced, N_{O2} is positive because O_2 is consumed.

Expressions for flux were substituted in Equation 8.12. The resulting expression was integrated with boundary conditions at the electrode channel interface $z = 0$, $X_{N2} = X^0_{N2}$ (0.79 for air) and at the catalyst layer $z = Z$, $X_{N2} = X_{N2}$ where Z is thickness of the gas diffusion electrode:

$$X_{N_2} = X^0_{N_2} e^{\left[\frac{RT}{p}\left(\frac{N_{O_2,g}}{D^{eff}_{N_2,O_2}} + \frac{N_{H_2O,g}}{D^{eff}_{N_2,H_2O}}\right)Z\right]} \tag{8.17}$$

$$X_{H_2O} = \left[\begin{array}{l} e^{\frac{-jRT}{4FP\,D^{eff}_{O_2,H_2O}}Z}\left(X^0_{H_2O} - X^0_{N_2}\dfrac{2D^{eff}_{N_2,O_2}\left(D^{eff}_{O_2,H_2O} - D^{eff}_{N_2,H_2O}\right)}{D^{eff}_{N_2,H_2O}\left(D^{eff}_{N_2,H_2O}D^{eff}_{O_2,H_2O} - 2D^{eff}_{N_2,O_2}D^{eff}_{O_2,H_2O} + D^{eff}_{N_2,H_2O}D^{eff}_{N_2,O_2}\right)} - 2\right) \\ + X^0_{N_2}\dfrac{2D^{eff}_{N_2,O_2}\left(D^{eff}_{O_2,H_2O} - D^{eff}_{N_2,H_2O}\right)}{D^{eff}_{N_2,H_2O}\left(D^{eff}_{N_2,H_2O}D^{eff}_{O_2,H_2O} - 2D^{eff}_{N_2,O_2}D^{eff}_{O_2,H_2O} + D^{eff}_{N_2,H_2O}D^{eff}_{N_2,O_2}\right)} e^{\frac{RTj}{4FP}\frac{D^{eff}_{N_2,H_2O} - 2D^{eff}_{N_2,O_2}}{D^{eff}_{N_2,H_2O}D^{eff}_{N_2,O_2}}Z} + 2 \end{array}\right] \tag{8.18}$$

The oxygen molar fraction is given by:

$$X_{O_2} = 1 - X_{N_2} - X_{H_2O} \tag{8.19}$$

8.5. Gas transport through thin film electrolyte

The macro-homogeneous model for the catalyst layer assumes that each catalytic site or specific area in the catalyst layer is an 'average' of the whole electrolyte and solid electrode. Accordingly, the effective diffusion coefficient through the catalyst layer was calculated as the pondered volume average of the respective diffusion coefficients.

Oxygen transport from the porous layer to the catalyst surface occurs through a thin polymer electrolyte film covering the catalyst particles. The oxygen dissolves at the boundary gaseous phase-thin film, and then diffuses through the thin electrolyte film to reach the catalytic site. The film also allows protons to move from the catalytic active sites to the membrane and vice versa. The average film thickness, δ, can be estimated by the following expression:

$$\delta = \frac{m_{Nafion} - \rho_{Nafion}}{S_C + S_{Pt}} \tag{8.20}$$

Where m_{Nafion} is the mass of Nafion® per unit area, ρ is the density of Nafion® and S_c and S_{Pt} are the specific surface area of carbon and platinum (or other metallic electrocatalyst), respectively, per unit area.

The concentration of oxygen at the catalyst surface was determined by deriving from Fick's law for diffusion:

$$\frac{N_{O_2}}{S_{Pt,cathode}} = \frac{-D_{O_2}^{Nafion}\left(C_{O_2,Pt} - C_{O_2,(dissolved)}\right)}{\delta_{cathode}} \tag{8.21}$$

Where N is the molar flux, C_{Pt} is the reactant concentration on the catalyst surface and $C_{dissolved}$ is the equilibrium reactant concentration in the polymer electrolyte thin film at a given temperature.

Concentration values of oxygen in the electrolyte (solubility) were obtained using Henry's law for solubility (Equation 8.8 and Equation 8.9).

Parthasarathy et al. studied variation of oxygen solubility and diffusion with temperature in Nafion® [11]. Two first order polynomials were built to fit their data for oxygen diffusion (Equation 8.22) and concentration in the thin film layer (Equation 8.23). Plots of T^{-1} (K^{-1}) vs $ln\ C_{O2}$ (in mol dm^{-3}) and T^{-1} (K^{-1}) vs $ln\ D_{O2}$ (in $m^2\ s^{-1}$) are shown in Figure 8-1 and the respective polynomial functions displayed in the plots.

$$C = -2983.6 \, {}^{1}\!/_{T} - 12.442 \tag{8.23}$$

$$\ln D = 662.50 \, {}^{1}\!/_{T} - 7.2805 \tag{8.24}$$

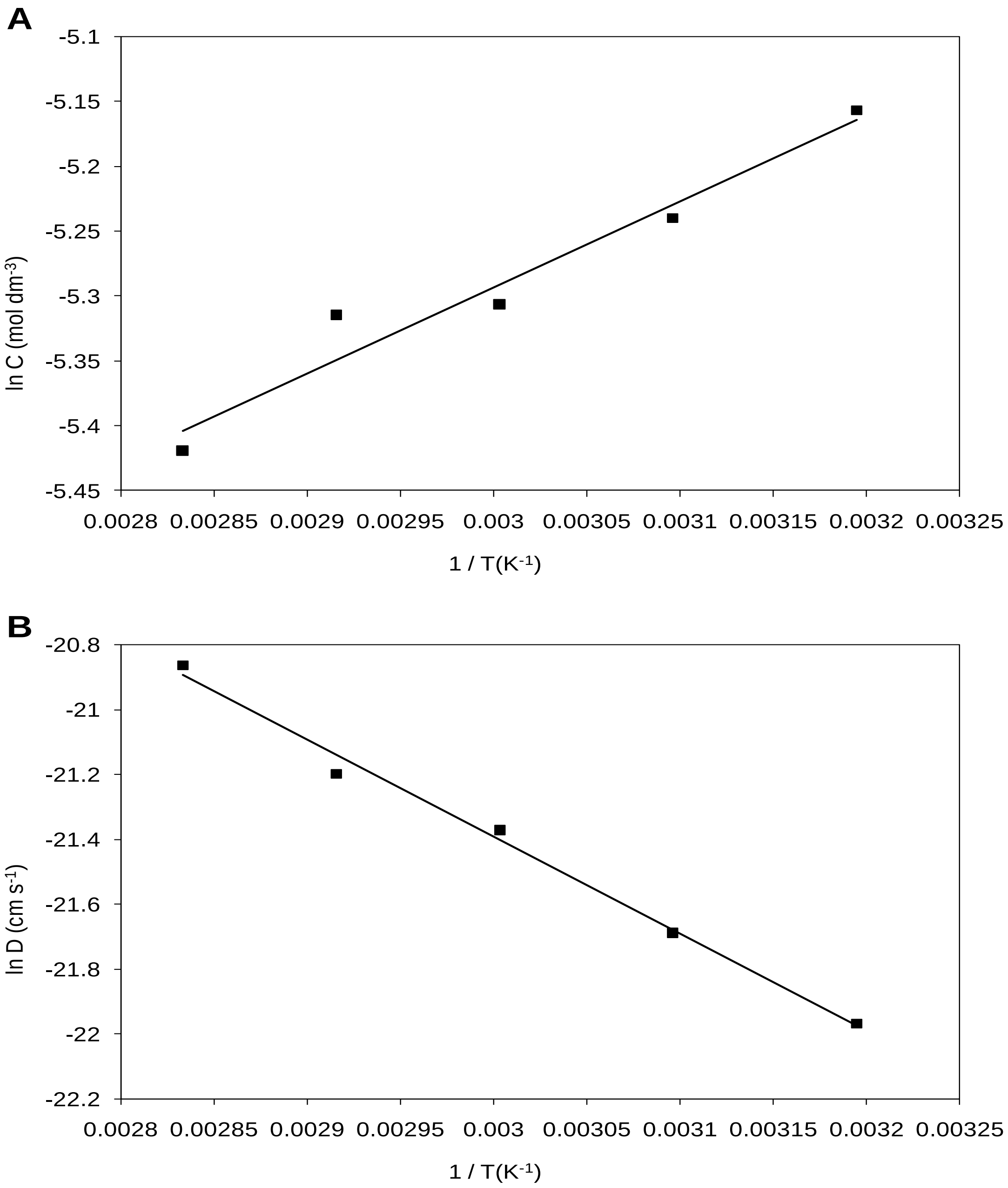

Figure 8-1: Plots of A) inverse of temperature versus natural logarithm of oxygen solubility and B) inverse of temperature versus natural logarithm of oxygen diffusivity in Nafion®.

The values of C_{O2} and D_{O2} were substituted in Equation 8.21 for a given temperature to obtain $C_{O2,Pt}$, the oxygen concentration on the catalyst surface necessary to solve the Butler-Volmer kinetic equation.

8.6. Kinetics

The relation between current density and potential loss can be expressed by the widely known Butler-Volmer equation as:

$$i = i_0 \left[\exp\left(\frac{-\alpha_c F}{RT} \eta \right) - \exp\left(\frac{\alpha_a F}{RT} \eta \right) \right] \tag{8.25}$$

Where η is the overpotential, i is the current density, i_0 is the exchange current density and α_a and α_c are the transfer coefficients of the anodic and cathodic reactions, respectively. Assuming $\alpha_a = \alpha_c = \alpha$, the hyperbolic sine function can be substituted in Equation 8.25 yielding the following relationship:

$$i = 2 i_0 \sinh\left(\frac{-\alpha F}{RT} \eta \right) \tag{8.26}$$

The transfer coefficient calculated from half cell tests (Chapter 4) for Pt was 0.45 in the high current density region. This value was used in the construction of the model as it is close to 0.5 employed in most models such as the ones from Liu, Min and Wang [12-14].

Exchange current density was calculated from the following equation:

$$i_0 = i_0^{ref} a_c L_c \left(\frac{C_{Pt}}{C_{Pt}^{ref}} \right)^{\gamma} \exp\left[-\frac{E_C}{RT} \left(1 - \frac{T}{T_{ref}} \right) \right] \tag{8.27}$$

Where i_0 is the apparent exchange current density in A cm^{-2} (current density per electrode geometric area), i_0^{ref} is the exchange current density in A cm$_{Pt}^{-2}$ measured at a reference temperature, T_{ref}, and at a reference dissolved oxygen concentration, C_{ref}, and E_C is the activation energy. C_{Pt} is the oxygen concentration on the catalyst surface calculated from equation 8.21 and a_c is the catalyst electrochemical surface area in m^2 g^{-1} of Pt, measured using cyclic voltammetry (Chapter 4). L_c is the catalyst loading in mg cm^{-2} and the product a_c x L_c is the roughness factor, which is the Pt electrochemical surface area divided by the electrode geometric area. γ is the reaction order with respect to oxygen in acid media, reported as 1 in the literature by Paulus et al. [15] and Mukerjee et al. [16]. However, different values of γ were used to fit experimental data in the range from 1 to 2, as discussed in Section 8.8.2. Kinetic parameters employed in the construction of this model were obtained from this work, or if unavailable, were taken from the literature; these parameters are summarised in Table 8.6.

Table 8-6: Kinetic parameters used in the construction of the model.

Parameter	**Pt/C-Etek**	**Pd/C-EG11**	**Reference**
α	0.45	0.45	This work
i_o^{ref} (A cm^{-2})	1.4 x 10^{-10}	1.0 x 10^{-11}	This work
L_c (g metal cm^{-2})	0.6	0.6, 1.0, 1.8	This work
C_{Pt}^{ref} (mol dm^{-3})	2.03 x 10^{-4}	2.03 x 10^{-4}	[17]
γ	1, 1.75, 2	1, 1.75, 2	[15, 18] and this work
ε	0.3	0.3	[19]
τ	1.5	1.5	[20]
Z (µm)	200	200	[21]

8.7. Conductivity and IR losses

To calculate the proton conductivity of Nafion® 112 at different temperatures the following expression has been suggested by Sun et al. [22]:

$$\sigma = (0.005139\lambda - 0.00326)\exp\left[1268\left(\frac{1}{303} - \frac{1}{T}\right)\right] \tag{8.28}$$

Where σ is the conductivity in S cm^{-1}, T is the operating temperature and λ is the water content (number of water molecules per sulfonic acid group in the membrane). To calculate the water content Zawodzinski et al. [23] suggested the expression:

$$\lambda = 0.043 + 17.18a - 39.85a^2 + 36a^3 \quad (8.29)$$

Where a is the water activity, defined as *RH%/100* i, where *RH* is the relative humidity at given temperature. It was assumed that the vapor phase was fully saturated; therefore water activity was considered as 1.

Nafion® resistance was obtained from conductivity using Equations 8.30 and 8.31:

$$\sigma = \frac{1}{\rho} \quad (8.30)$$

$$\rho = R\frac{A}{l} \quad (8.31)$$

Where σ is the conductivity in S cm^{-1}, ρ is the resistivity in Ω cm, R is the resistance in Ω, A is cross-section area of the electrode (1 cm^2) and l is the thickness of the membrane (50 µm for Nafion® 112).

The overall cell voltage is given by:

$$U_{cell} = E_{rev} - |\eta_c| - IR \quad (8.32)$$

The *iR* potential losses were calculated from Equations 8.28, 8.30 and 8.31 using Ohm's law, cathode potential losses were calculated from Equation 8.25, and thermodynamic cell reversible potential from Equation 8.3.

8.8. Results and discussion

Matlab® V.7.3 and Simulink® V.6.5 equipped with Ordinary Differential Equation solver (ODE 45) were used to solve the model governing equations. The results predicted by the model are compared to experimental data obtained from a low temperature polymer electrolyte membrane fuel cell. Experimental data include tests using Pd/C-EG11 and commercial Pt/C as cathode catalysts; metal loadings were 0.6 and 1.0 mg cm^{-2} in cathode and 0.2 mg cm^{-2} Pt/C in the anode. Model predictions are compared to the anodic sweep at 5 mV s^{-1}.

8.8.1. Mass transport losses

This model considers mass transport through a thin film electrolyte as well as through the porous media. This assumption was necessary for the model to predict the mass transport limitations with air operation observed in the experimental results. In this section diffusion through the porous media and through the electrolyte thin film are analyzed.

8.8.1.1. Mass transport in porous media

Figure 8-2 shows the effect of current density on oxygen, water and nitrogen gas partial pressures at the catalysts surface for 30% porosity [19] and diffusion length of 200 μm [21]; the existence of the electrolyte thin film was not taken into account. Limiting current would be observed when the oxygen partial pressure reaches zero ($P_{O2} = 0$), this did not occurred even at high current densities of 4 A cm^{-2} using air. This confirms what was previously discussed in the literature review (Chapter 2), concerning the failure of models with no electrolyte thin film consideration to explain experimentally observed limiting current densities (below 1.5 A cm^{-2}) with air operation.

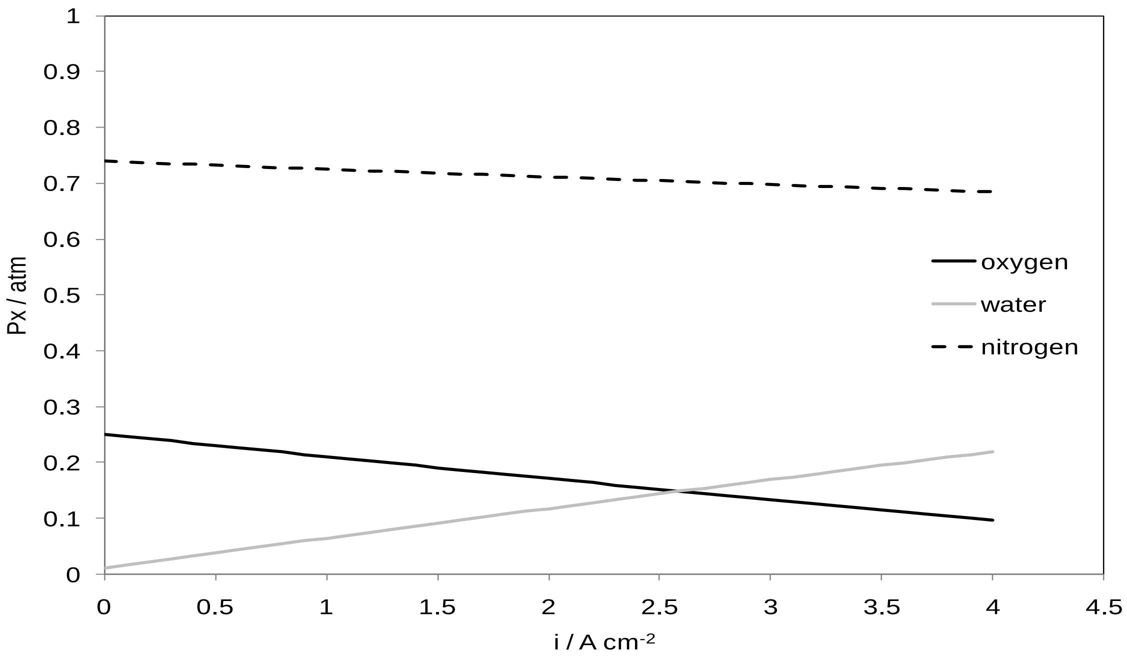

Figure 8-2: Predicted effect of operating current density on the cathode gas mixture operating with air at 40 ºC.

This illustrates why considering that mass transport occurs only through the porous media fails to predict mass transport limitations with air operation and consequently over estimates the cell performance at high current densities.

8.8.1.2. Mass transport in thin film

In reality, in the catalyst layer, a thin film of electrolyte surrounds the catalyst nanoparticles and mass transport of reactants through this phase needs to be considered. Reactants have to dissolve in this phase and diffuse through it to reach the catalytic sites. Diffusion through the porous media is faster than through the polymer electrolyte and this explains the experimentally observed mass transport behavior.

Figure 8-3 shows the effect of current density on oxygen concentration at the catalysts surface with air and oxygen operation. In this case the presence of an electrolyte thin film has been considered. When O_2 diffusion through the electrolyte thin film was considered, the model predicted limiting current (oxygen concentration equal to zero) of ca. 1.5 A cm^{-2} at 40 ºC with air operation. This value is close to the limiting currents observed in fuel cell tests and therefore supports the addition of the electrolyte thin film to the model.

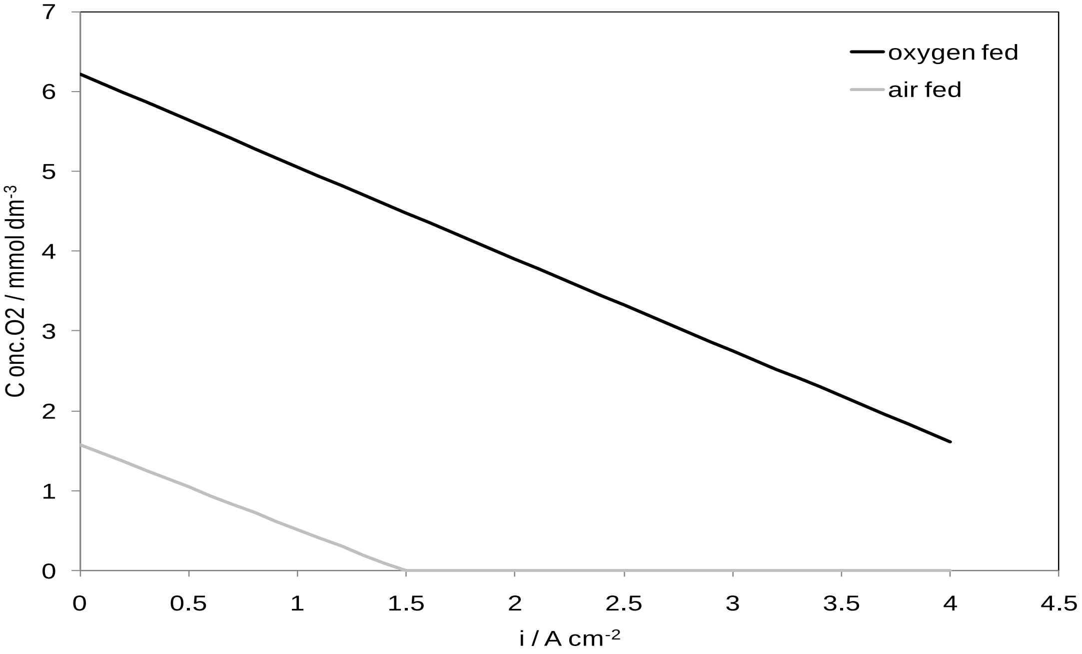

Figure 8-3: Predicted effect of operating current density on the oxygen concentration in the thin film with air and oxygen at 40 ºC.

8.8.2. Model predictions and limitations

Figures 8-4 and 8-5 compare current-potential curves obtained from fuel cell tests with model predictions. For both Pt and Pd model predictions matched closely fuel cell experimental data for oxygen, however, it overestimated performance with air operation, especially at high current densities. This limitation was attributed to oxygen starvation, which was not considered in simple one-dimensional models like the macro-homogenous model used. On a thick electrode (using a catalysts with low metal to carbon ratio and relatively high metal loadings, 0.6 mg cm^{-2}) the oxygen concentration will decrease sharply as the cell is polarized, as illustrated in Figure 8-3.

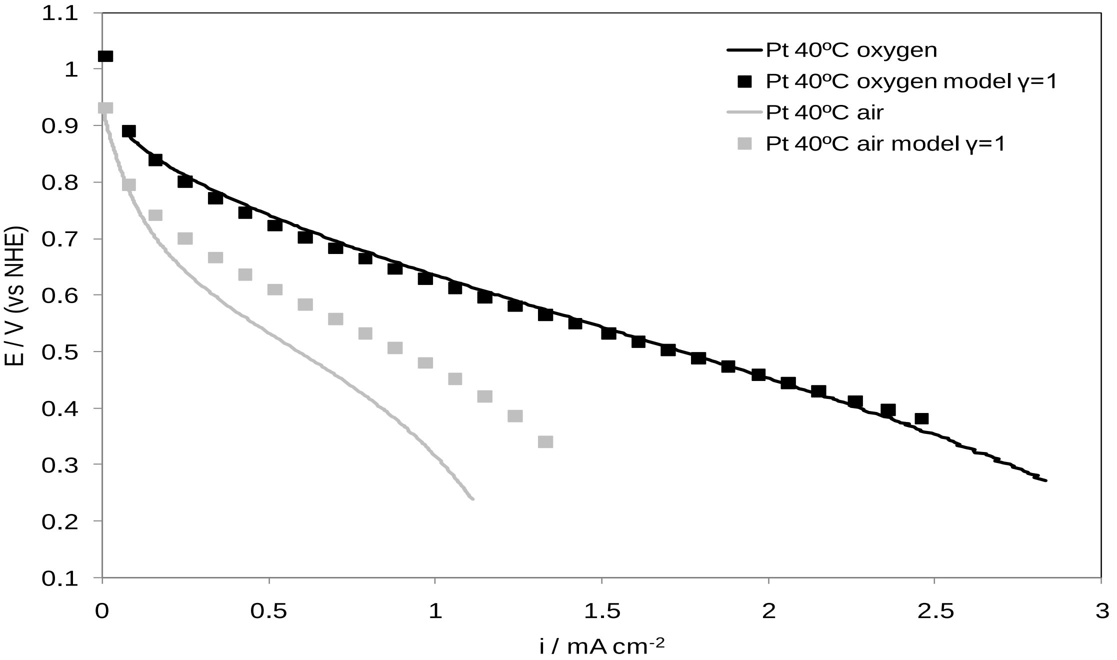

Figure 8-4: Comparison between experimental and predicted polarization curves for a low temperature PEMFC at 40 ºC using commercial Pt/C at the cathode with reaction order γ=1.

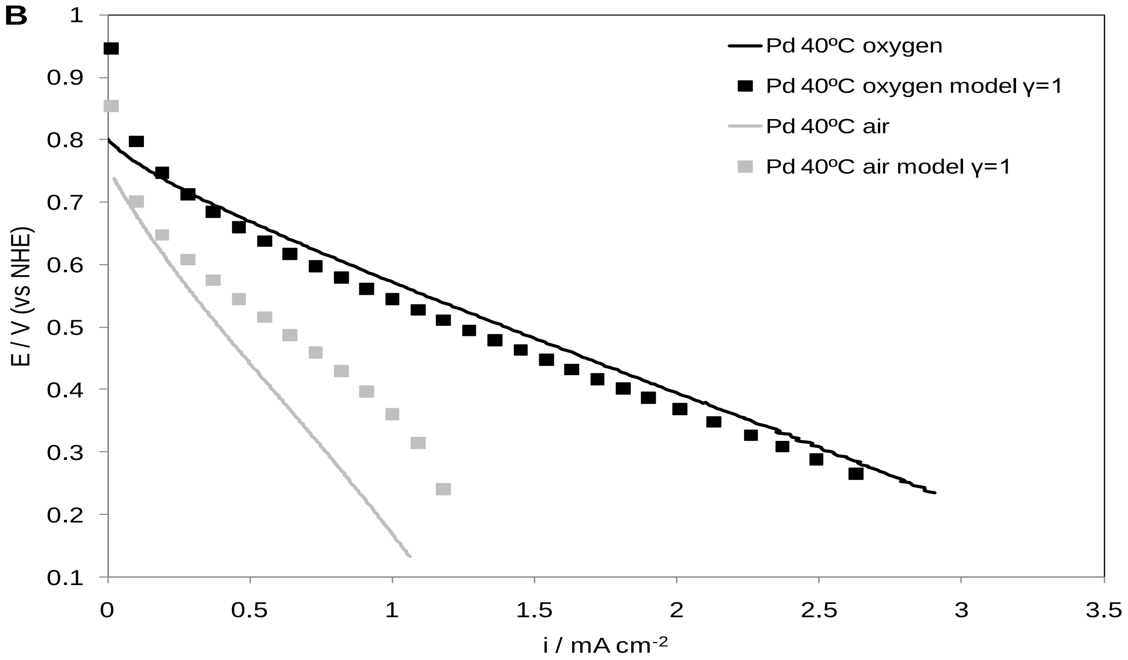

Figure 8-5: Comparison between experimental and predicted polarization curves for a low temperature PEMFC at 40 ºC using Pd/C-EG11 at the cathode with reaction order γ=1.

The following expression relates exchange current density, i_0, with the reaction order, γ, as described in Section 8.6:

$$i_0 = i_0^{ref} a_c L_c \left(\frac{C_{Pt}}{C_{Pt}^{ref}} \right)^{\gamma} \exp\left[-\frac{E_C}{RT} \left(1 - \frac{T}{T_{ref}} \right) \right] \tag{8.33}$$

For a given catalysts and a given temperature can be expressed as:

$$i_0 = i_{0,T}^{ref} a_c L_c \left(\frac{C_{Pt}}{C_{Pt}^{ref}} \right)^{\gamma} \tag{8.34}$$

Substituting i_0 in the well known Tafel equation:

$$\eta = \frac{RT}{\alpha F} \ln \frac{i}{i_{0,T}^{ref} a_c L_c \left(\frac{C_{Pt}}{C_{Pt}^{ref}} \right)^{\gamma}} \tag{8.35}$$

rearranging:

$$\eta = \frac{RT}{\alpha F} \left(\ln i - \ln \left(i_{0,T}^{ref} a_c L_c \left(\frac{C_{Pt}}{C_{Pt}^{ref}} \right)^{\gamma} \right) \right) \tag{8.36}$$

Losses in the accessible active electrochemical surface area or effective catalyst utilization might occur due to oxygen starvation, where at very low concentrations, oxygen will not be able to reach parts of the catalyst surface even though they are available for reaction (covered with electrolyte). This effect would lead to a further decline in performance at high current densities and low oxygen concentrations (in comparison to γ=1). Unfortunately, such an effect is not accounted for in this model and is one of the limitations of the macro-homogeneous model, where it is assumed that the average accessible catalyst layer is constant. However if such effects are present then the ESA can be written as function of ln (C_{O2}/C^{0}_{O2}) which would effectively cause an increase in the apparent reaction order.

This explains why in air operation (low oxygen concentration) a value of gamma higher than 1 was necessary to fit the experimental results. This new gamma value was increased with temperature to counter the effect of the lower solubility of oxygen at in Nafion® at higher temperatures.

Figures 8-6 and 8-7 show polarization curves for Pt and Pd membrane electrodes assemblies operating with air and oxygen at 40 ºC, experimental results are compared with model predictions using gamma values of 1 and 1.75. As discussed above using a higher apparent gamma value of 1.75 to account for oxygen starvation (air operation) would enhance greatly the model fitting to the experimental data (air operation at current densities higher than ca. 0.2 A cm^{-2}). When the cell was operating with oxygen (Figure 17) there was no significant difference in the current-potential curve predicted by the model between γ=1 and γ=1.75; both fitted closely experimental data probing this way the oxygen starvation is not important when operating with pure O_2.

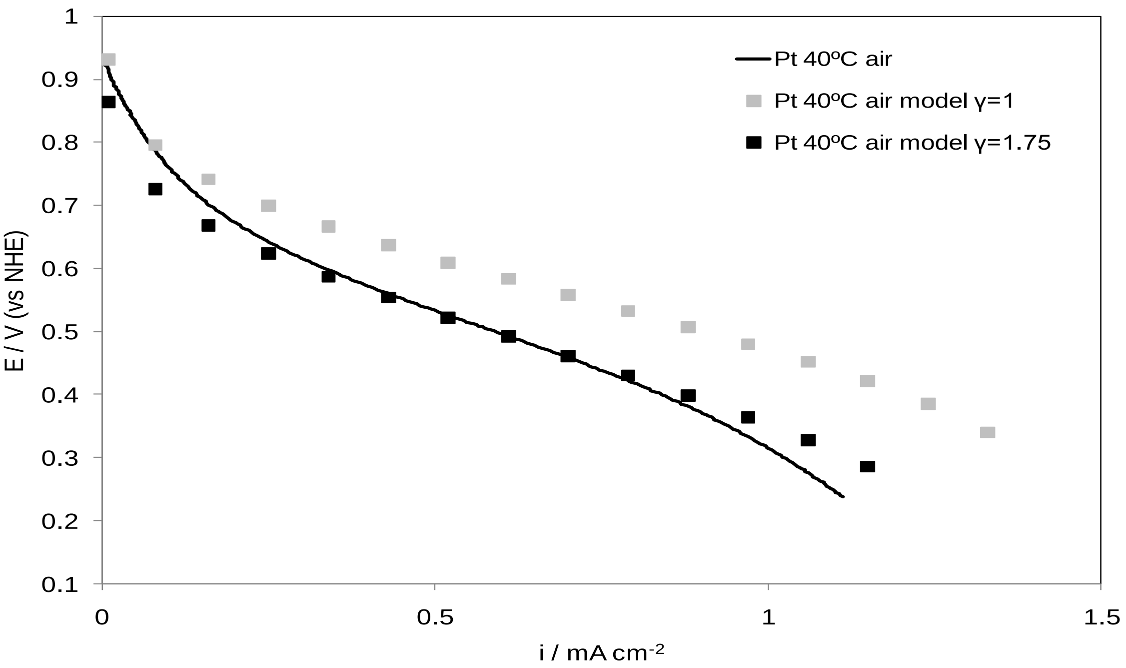

Figure 8-6: Comparison between predicted polarization curves for a low temperature PEMFC operating on air at 40 ºC using commercial Pt/C at the cathode with reaction orders γ=1 and γ=1.75.

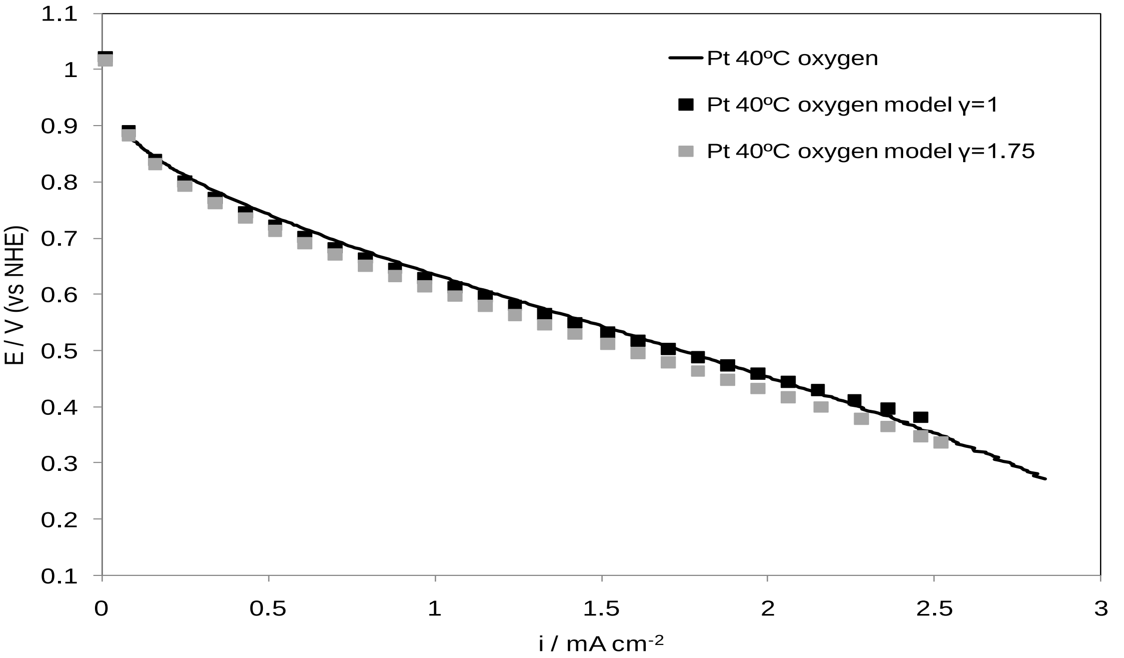

Figure 8-7: Comparison between predicted polarization curves for a low temperature PEMFC operating with oxygen at 40 ºC using Pt/C at the cathode with reaction orders γ=1 and γ=1.75.

8.8.3. Temperature effect

Figures 8-8 and 8-9 compare model predictions and polarization curves for Pt and Pd membrane electrodes assemblies operating with air and oxygen at 20 and 40 ºC, respectively. At both temperatures the model fits closely with the obtained fuel cell data for the two electrocatalysts.

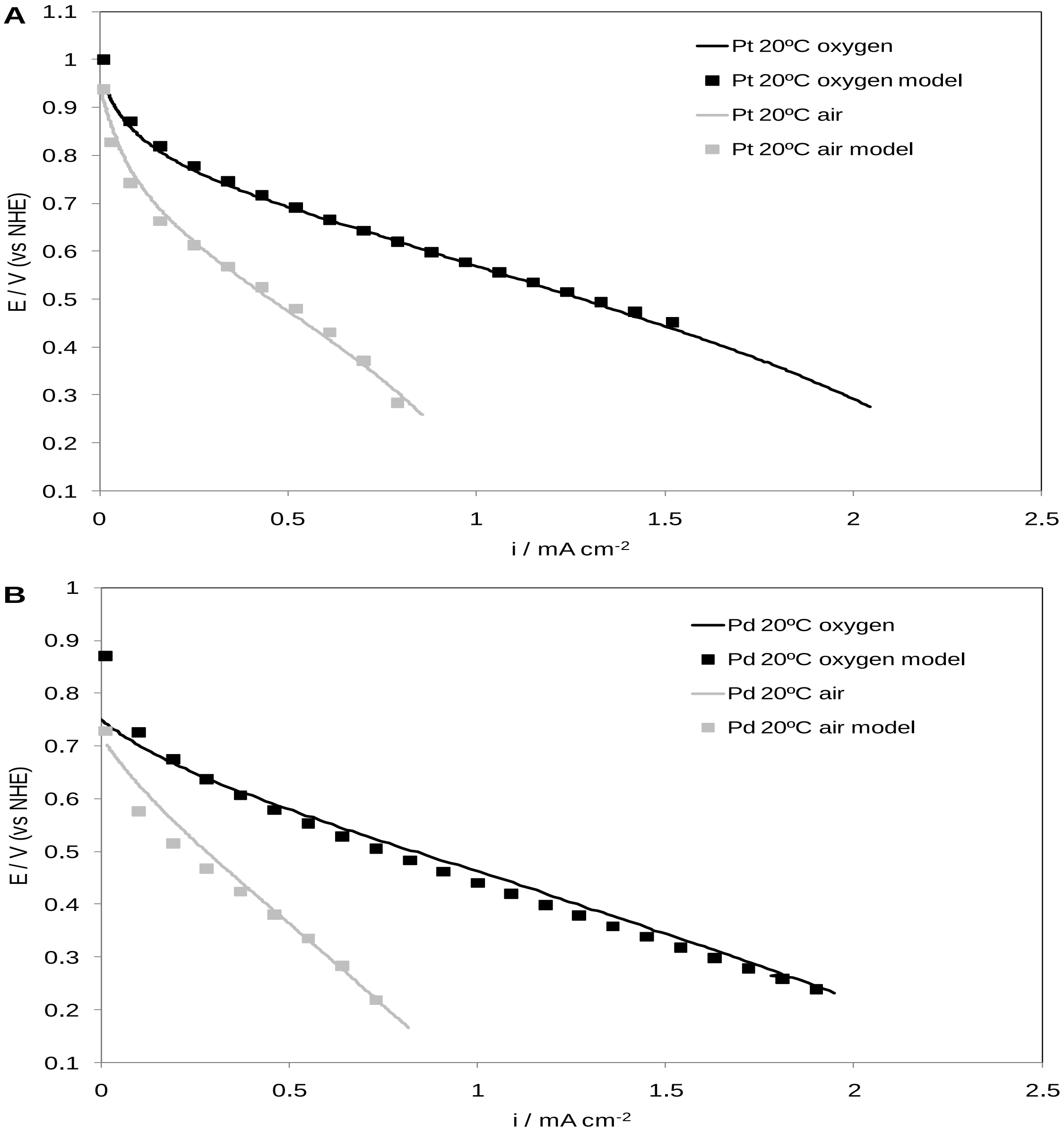

Figure 8-8: Comparison between predicted and experimental data for a low temperature PEMFC operating with air (γ=1.5) and O_2 (γ=1) at 20 ºC using A) commercial Pt/C and B) Pd/C-EG11 as cathode catalysts.

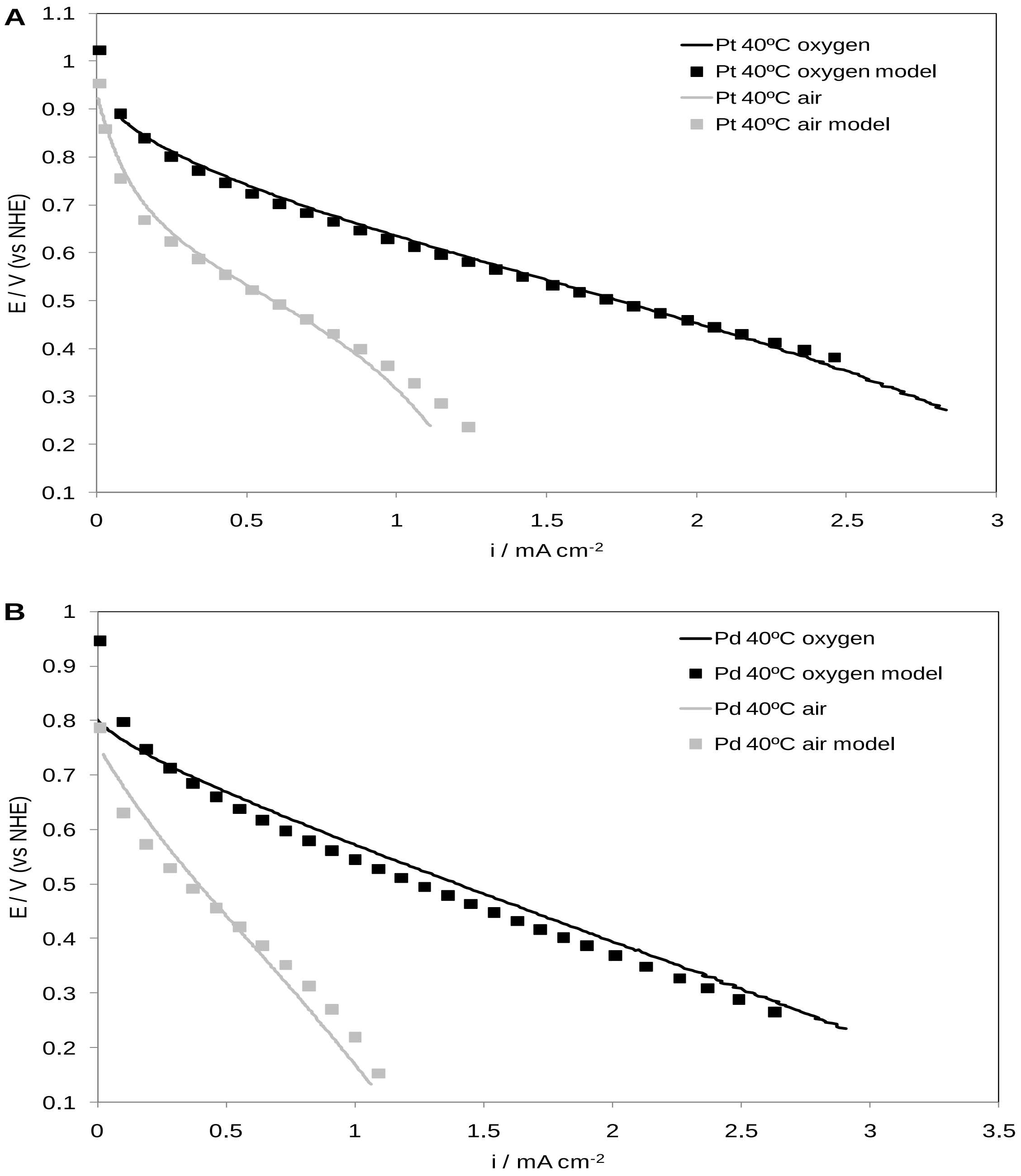

Figure 8-9: Comparison between predicted and experimental data for a low temperature PEMFC operating with air (γ=1. 75) and O_2 (γ=1) at 40 ºC using A) commercial Pt/C and B) Pd/C-EG11 as cathode catalysts.

Oxygen solubility in Nafion® decreases with increasing temperature as shown in Section 8.6 [24] and this was taken into account in the construction of the model. Oxygen permeability in Nafion® also depends on the water content. Measured cathode relative humidity values were close to 100% at 20, 40 ºC and only 73% at 60 ºC (Chapter 6). Takamura et al. studied the influence of the relative humidity on the oxygen permeability through Nafion® [25]. They found that oxygen permeability at 70% relative humidity was approximately half of that at 100% relative humidity at 50 ºC, ca 1.3 and 2.5 x 10^{-12} mol cm^{-1} s^{-1}. At 60 ºC oxygen permeability for a 90% relative humidity was ca. 3.0 x 10^{-12} mol cm^{-1} s^{-1}. Since permeability decreases with decreasing water content [26] and for a given relative humidity water content decreases with increasing temperature [27], the difference between oxygen permeability at 100% and at 70% relative humidity will be higher at 60 ºC than at 50 ºC. Oxygen permeability therefore was considered 2.5 times lower at 70% RH in comparison to 100% RH at 60 ºC. This assumption seems reasonable as the estimated limiting current from the model with air operation is very close to that obtained from the experimental data.

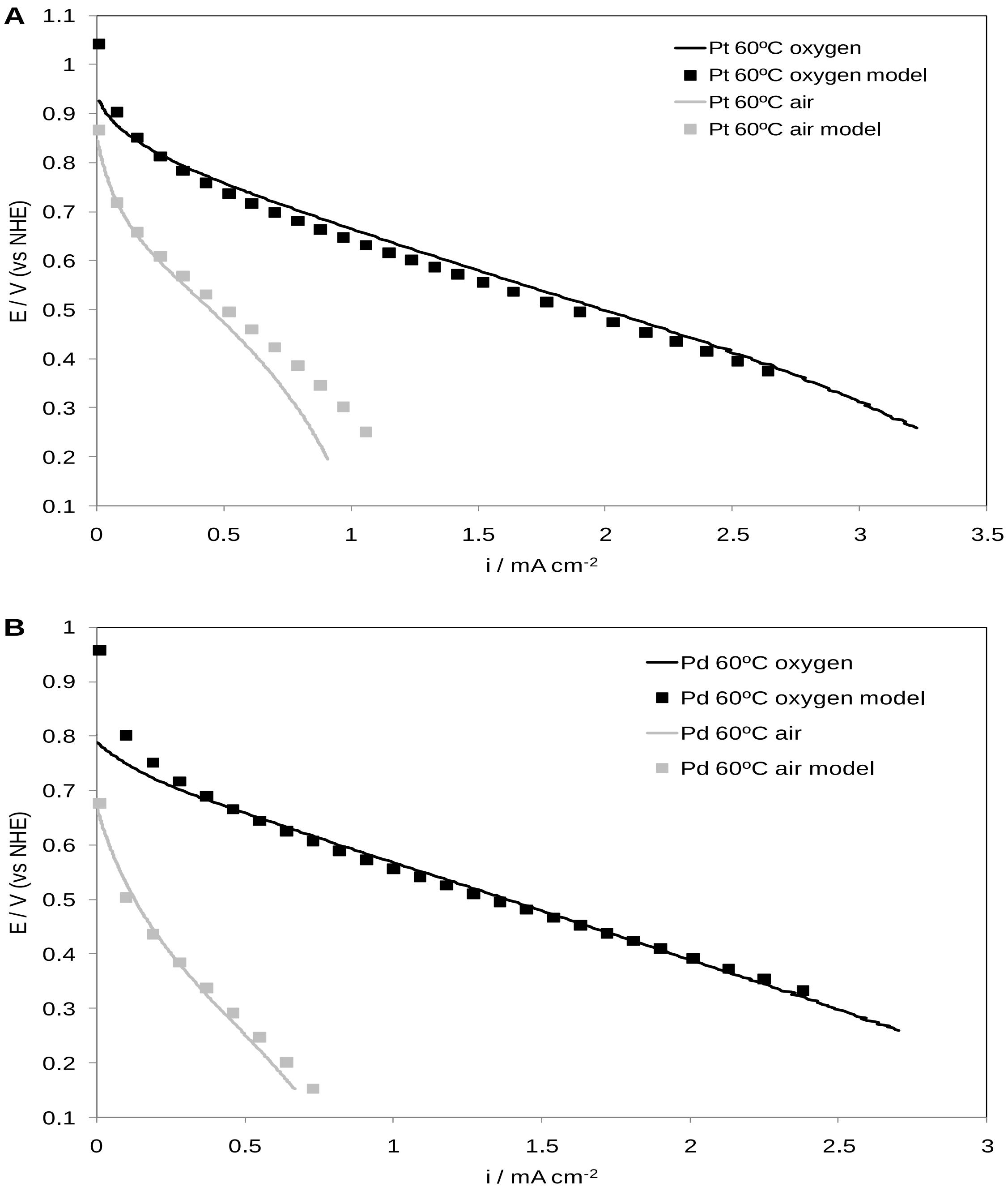

Figure 8-10: Comparison between predicted and experimental data for a low temperature PEMFC operating with air (γ=2) and O_2 (γ=1) at 60 ºC using A) commercial Pt/C and B) Pd/C-EG11 as cathode catalysts.

To illustrate how the oxygen concentration at the catalysts surface is affected by the decrease in oxygen permeability through Nafion®, predicted oxygen concentration in the cathode versus current density were plotted for Pt with air operation at 40 and 60 ºC

(Figure 8-11). Oxygen concentration at 60 ºC (lower oxygen permeability) is zero at 1.4 A cm^{-2} whilst at 40 ºC the oxygen is totally consumed when current density reaches 1.5 A cm^{-2}. This reduction in oxygen concentration would counter any improvement from the kinetics caused by the temperature increase from 40 to 60 ºC; this explained why no improvement in performance was observed experimentally.

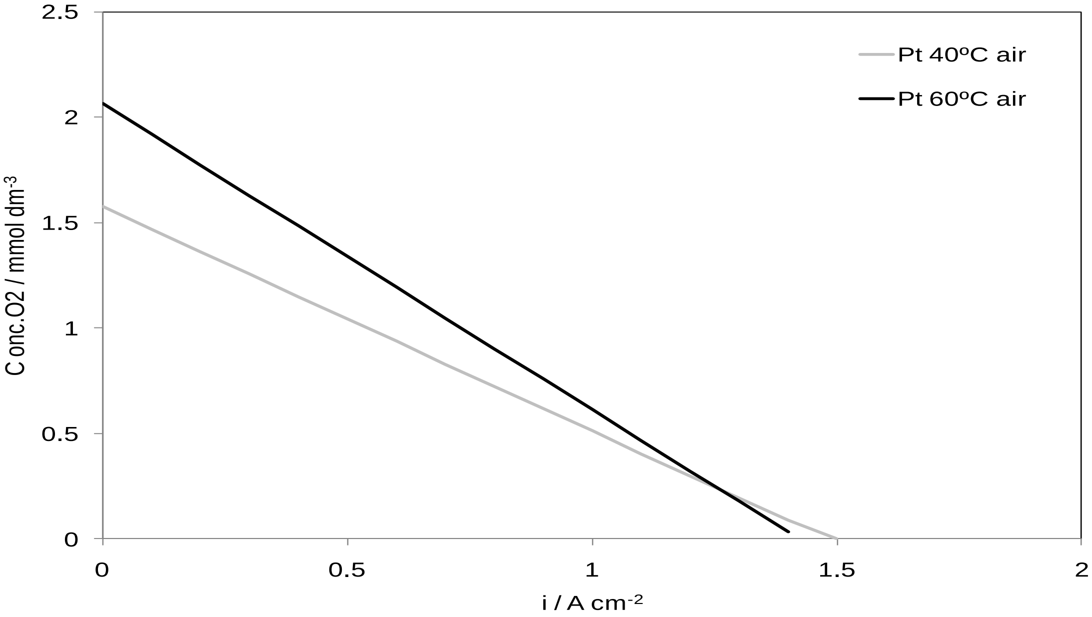

Figure 8-11: Predicted effect of operating current density with the cathode oxygen concentration operating with air at 40 and 60 ºC.

8.8.4. Catalyst loading effect

Figure 8-12 compares model predictions and polarization curves for a Pd membrane electrode assembly with 1 mg cm^{-2} of Pd/C-EG11 in the cathode operating with air and oxygen at 40 ºC. To predict this higher loading the thickness of the catalysts layer was increased accordingly to the loading in the model. Although the increase in the metal loading enhanced the kinetic region of the polarization curve, the raise in the amount of catalyst enlarged the amount of carbon in the catalyst layer (20% Pd/C), making the gas transport through this phase more difficult. This increase in the catalysts layer thickness imposed larger mass transport limitations in the gaseous phase which agrees with the experimental data. Figure 8-13 shows the effect of current density on oxygen, water and nitrogen gas partial pressures at the catalyst surface when the catalyst layer is doubled, respect to that calculated for a 0.6 mg cm^{-2} metal loading.

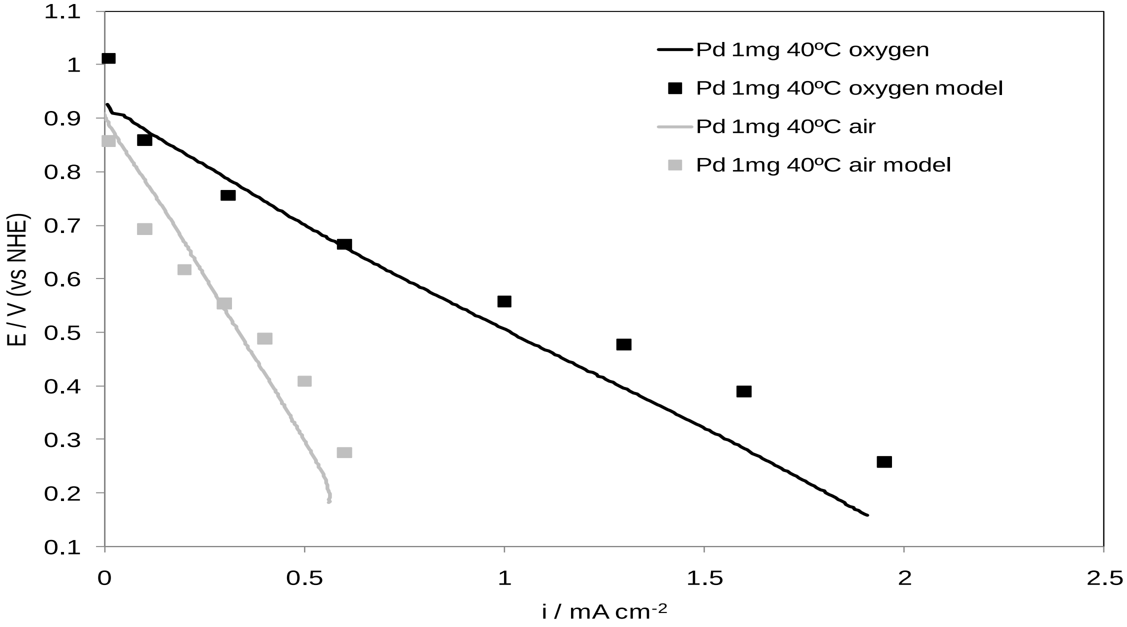

Figure 8-12: Comparison between predicted and experimental data for a low temperature PEMFC operating with air (γ=1.75) and O_2 at 40 ºC using 1mg cm^{-2} of Pd in the cathode.

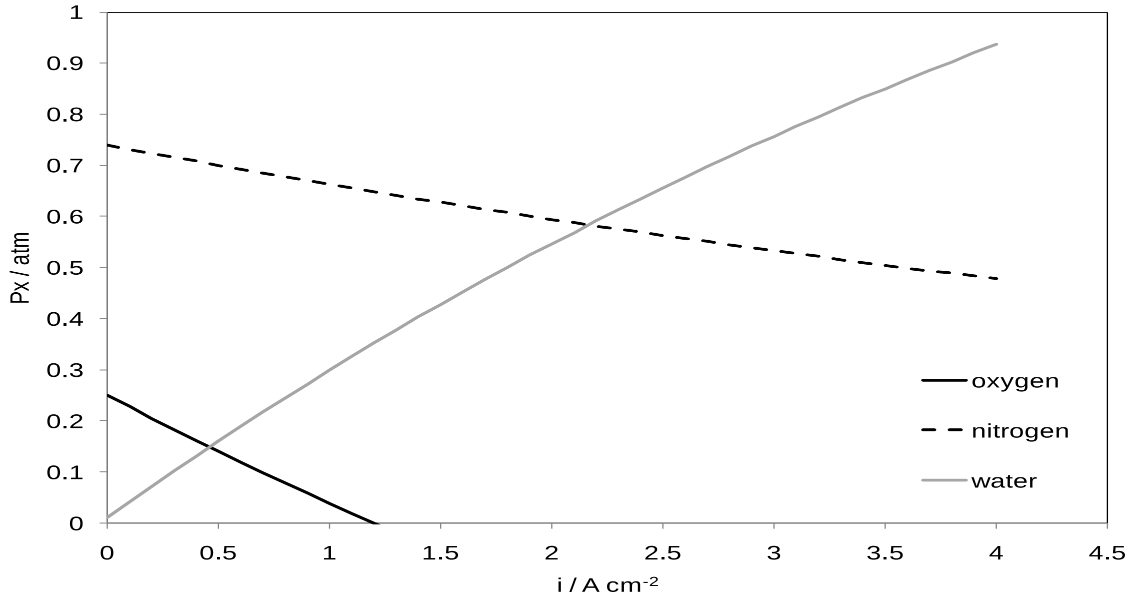

Figure 8-13: Predicted effect of operating current density on the cathode gas mixture operating with air at 40 ºC for a catalyst load of 1.2 mg cm^{-2}.

Increasing the catalyst loading showed enhancement in the kinetic region of the polarization curves. With 1 mg cm^{-2} Pd the performance in the low current density region matches that of commercial Pt/C, as discussed in Chapter 6. The model seems to provide a close estimate to that of the experimental data when higher loading was used. Model predictions were also obtained with a cathode loading of 1.8 mg cm^{-2} Pd (Figure 8-14). The model predicts an enhanced performance in the low current density region (overtaking that of Pt) but also shows severe mass transport, with limiting currents close to 1 A cm^{-2} with oxygen operation.

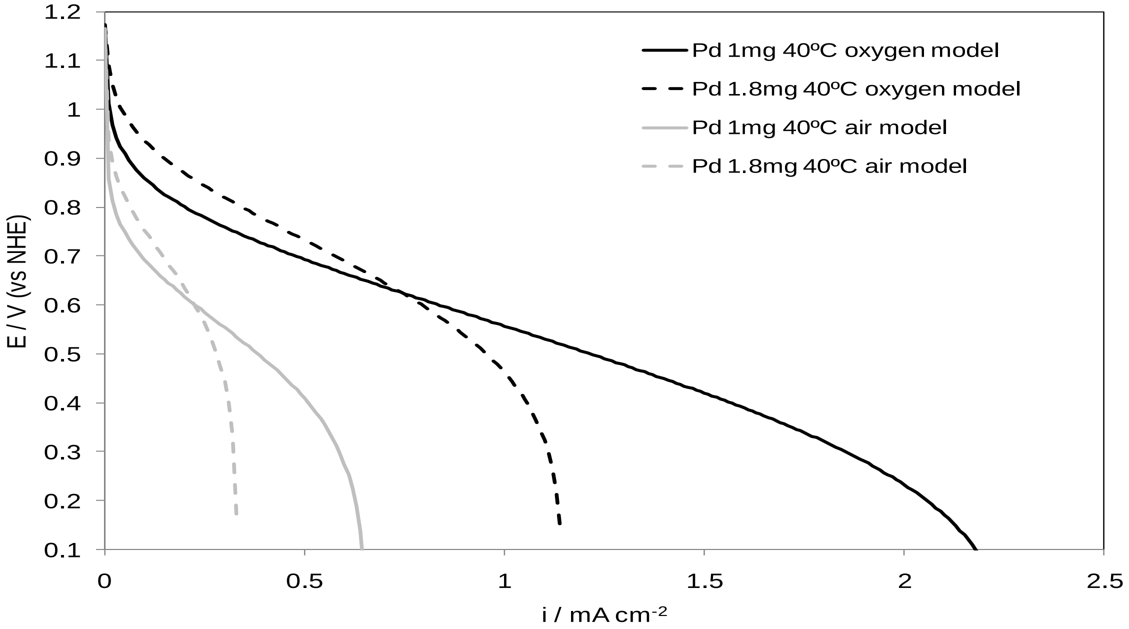

Figure 8-14: Comparison between predicted polarization curves for a low temperature PEMFC operating with air (γ=1.75) and O_2 at 40 ºC with 1.0 and 1.8 mg Pd in the cathode.

Since the main issue with using high metal loading was the gas diffusion through the porous media a possible solution would be to increase the metal percentage in the carbon-supported palladium nanoparticles. To support this idea, model predictions were obtained with metal loadings of 1 mg cm^{-2} Pd/C but catalyst layer thickness corresponding to a loading of 0.6 mg cm^{-2} Pd/C of Pd/C 20% was considered (Figure 8-15). This way the enhancement in the low current density region was accompanied by a raised performance in the high current density region. While it is necessary to use 1 mg cm^{-2} for Pd/C to be good substitute to Pt, a higher metal loading would be required (40% weight Pd/C) to overcome mass transport losses (and worse oxygen starvation) at high current densities.

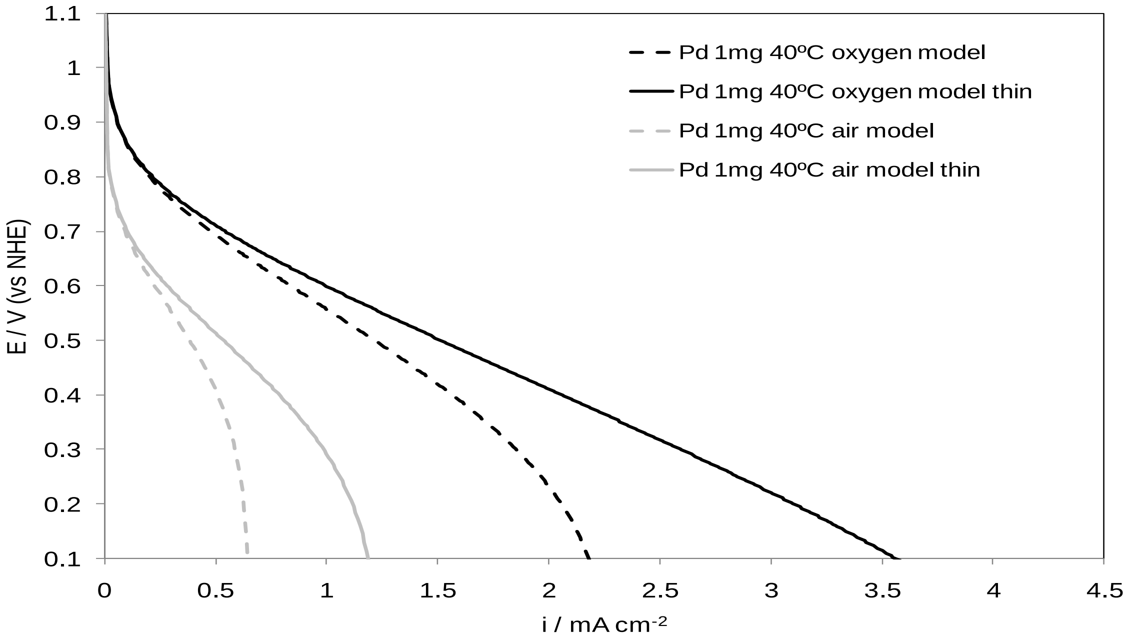

Figure 8-15: Comparison between predicted polarization curves for a low temperature PEMFC operating with air (γ=1.75) and O_2 at 40 ºC with different catalysts layer thickness.

8.9. Conclusions

A model of a low temperature PEMFc has been applied to low temperature hydrogen polymer electrolyte membrane fuel cells to simulate the influence of cathode catalyst loading, thickness and materials and the operating conditions on the cell voltage and current density. The assumption of the existence of an electrolyte thin film was necessary for the model to predict the mass transport limitations with air operation observed in the experimental results.

The model closely matched the fuel cell experimental data with oxygen operation; however it overestimated performance with air, especially at high current densities. This failure of the model was attributed to oxygen starvation, and was explained by losses in the active electrochemical surface area. To enhance the model accuracy a new concept, the apparent reaction order (Γ), was introduced to explain the need of a higher reaction order to fit experimental data. Apparent reaction order was taken for air operation at 20, 40 and 60 ºC as 1.5, 1.75 and 2, respectively.

The model predicted closely experimental results at 20 and 40 ºC. At 60 ºC, a lower permeability value was employed according with the lower humidity measured experimentally. Above 40 ºC cell performance did not improve experimentally and this was predicted by the model. This lack of improvement was attributed to the decrease of oxygen permeability through Nafion® and the consequent decrease of the oxygen concentration at the catalyst surface, which countered any kinetic enhancement with the temperature increase.

The increase of the metal loading in the cathode enhanced fuel cell performance in the low current density range; however severe mass transport limitation appeared. Predicted results showed that this could be solved by increasing the loading without increasing the catalyst layer thickness, which can be practically achieved by increasing the metal content of the carbon-supported catalyst.

References

1. Yi, J. and T. Nguyen, *Multicomponent transport in porous electrodes of proton exchange membrane fuel cells using the interdigitated gas distributors.* Journal of The Electrochemical Society, 1999. **146** (1): p. 38-45. |

2. A. Kazim, H. Liu and P. Forges, *Modelling of performance of PEM fuel cells with conventional and interdigitated flow fields.* Journal of Applied Electrochemistry, 1999. **29** (12): p. 1409-1416.

3. A. Kulikovsky, J. Divisek and A. Kornyshev. *Modeling the cathode compartment of polymer electrolyte fuel cells: Dead and active reaction zones.* Journal of The Electrochemical Society, 1999. **146** (1): p. 3981-3991.

4. Hampson, N.A.a.A.J.S.M., *The Electrochemistry of Porous Electrodes: Flooded, Static (Natural) Electrodes, in Electrochemistry*, ed. D. Pletcher. 1983, London: Royal Society of Chemistry (RSC).

5. Scharifker, B.R., P. Zelenay, and J.O.M. Bockris, *The Kinetics of Oxygen Reduction in Molten Phosphoric Acid at High Temperatures.* Journal of The Electrochemical Society, 1987. **134**(11): p. 2714-2725.

6. Weng, D., J.S. Wainright, U. Landau, and R.F. Savinell, *Electro-osmotic drag coefficient of water and methanol in polymer electrolytes at elevated temperatures.* Journal of The Electrochemical Society, 1996. **143**(4): p. 1260-1263.

7. *Steam Tables*. Smith son Ian 2006 [cited; Available from: www.knovel.com.

8. Vielstich, W., H. Gasteiger, and A. Lamm, *Handbook of fuel cells : fundamentals, technology and applications*. 2003, Chichester: Wiley. 4 v.

9. Slattery, J.C. and R.B. Bird, *Calculation of the Diffusion Coefficient of Dilute Gases and of the Self-diffusion Coefficient of Dense Gases.* J. A.I.Ch.E, 1958. **4**(2): p. 137-142.

10. Scott, K., S. Pilditch, and M. Mamlouk, *Modelling and experimental validation of a high temperature polymer electrolyte fuel cell.* Journal of Applied Electrochemistry, 2007. **37**(11): p. 1245-1259.

11. Parthasarathy, A., S. Srinivasan, A.J. Appleby, and C.R. Martin, *Temperature dependence of the electrode kinetics of oxygen reduction at the platinum/nafion®*

interface - a microelectrode investigation. Journal of The Electrochemical Society, 1992. **139**(9): p. 2530-2537.

12. Liu, Z., Z. Mao, and C. Wang, *A two dimensional partial flooding model for PEMFC.* Journal of Power Sources, 2006. **158**(2 SPEC. ISS.): p. 1229-1239.

13. Min, C.H., Y.L. He, X.L. Liu, B.H. Yin, W. Jiang, and W.Q. Tao, *Parameter sensitivity examination and discussion of PEM fuel cell simulation model validation. Part II: Results of sensitivity analysis and validation of the model.* Journal of Power Sources, 2006. **160**(1): p. 374-385.

14. Wang, H., P. Cao, and Y. Wang, *Monte Carlo simulation of the PEMFC catalyst layer.* Frontiers of Chemical Engineering in China, 2007. **1**(2): p. 146-150.

15. Paulus, U.A., T.J. Schmidt, H.A. Gasteiger, and R.J. Behm, *Oxygen reduction on a high-surface area Pt/Vulcan carbon catalyst: a thin-film rotating ring-disk electrode study.* Journal of Electroanalytical Chemistry, 2001. **495**(2): p. 134-145.

16. Mukerjee, S. and S. Srinivasan, *Enhanced electrocatalysis of oxygen reduction on platinum alloys in proton exchange membrane fuel cells.* Journal of Electroanalytical Chemistry, 1993. **357**(1-2): p. 201-224.

17. McBreen, J., W.E.O. Grady, and R. Richter, *A Rotating Disk Electrode Apparatus for the Study of Fuel Cell Reactions at Elevated Temperatures and Pressures.* Journal of the Electrochemical Society, 1984. **131**(5): p. 1215-1216.

18. Mukerjee, S. and J. McBreen, *Effect of particle size on the electrocatalysis by carbon-supported Pt electrocatalysts: An in situ XAS investigation.* Journal of Electroanalytical Chemistry, 1998. **448**(2): p. 163-171.

19. Jaouen, F., G. Lindbergh, and G. Sundholm, *Investigation of mass-transport limitations in the solid polymer fuel cell cathode. I. Mathematical model.* Journal of The Electrochemical Society, 2002. **149**(4): p. A437-A447.

20. Barbir, F., *PEM Fuel Cells:Theory and Practice*, ed. R.C. Dorf. 2005.

21. Sousa, T., M. Mamlouk, and K. Scott, *An isothermal model of a laboratory intermediate temperature fuel cell using PBI doped phosphoric acid membranes.* Chemical Engineering Science. **65**(8): p. 2513-2530.

22. Sun, Y.-P. and K. Scott, *An analysis of the influence of mass transfer on porous electrode performance.* Chemical Engineering Journal, 2004. **102**(1): p. 83-91.

23. Zawodzinski Jr, T.A., T.E. Springer, J. Davey, R. Jestel, C. Lopez, J. Valerio, and S. Gottesfeld, *Comparative study of water uptake by and transport through ionomeric fuel cell membranes.* Journal of the Electrochemical Society, 1993. **140**(7): p. 1981-1985.

24. Parthasarathy, A., B. Dave, S. Srinivasan, A. Appleby, and C. Martin, *Platinum microelectrode/Nafion interface: an electrochemical impedance spectroscopic analysis of oxygen reduction kinetics and Nafion characteristics.* Journal of The Electrochemical Society, 1992. **139**(6): p. 1634-1641.

25. Takamura, Y., E. Nakashima, H. Yamada, A. Tasaka, and M. Inaba. *Effects of temperature and relative humidity on Oxygen permeation in nationÂ® and sulfonated poly(arylene ether sulfone)*. in *ECS Transactions*. 2008.

26. Sakai, T., H. Takenaka, N. Wakabayashi, Y. Kawami, and E. Torikai, *Gas Permeation Properties of Solid Polymer Electrolyte (SPE) Membranes.* Journal of The Electrochemical Society, 1985. **132**(6): p. 1328-1332.

27. Broka, K. and P. Ekdunge, *Oxygen and hydrogen permeation properties and water uptake of Nafion® 117 membrane and recast film for PEM fuel cell.* Journal of Applied Electrochemistry, 1997. **27**(2): p. 117-124.

Chapter 9: Conclusions and future work

9.1. Conclusions

A systematic study of the synthesis and optimization of carbon-supported palladium and palladium alloys nanoparticles is reported. A comprehensive comparative study of Pd and state of the art Pt catalyst for ORR in polymer electrolyte membrane fuel cells is reported in this piece of work: low and high temperature hydrogen PEMFCs and direct methanol fuel cells.

Palladium nanoparticles supported on pre-treated Vulcan XC-72R synthesized by reduction of ammonium tetrachloropalladate (II) with ethylene glycol in alkaline conditions, between 10 and 13 pH units, yielded Pd particles of approximately 6 nm. The pH, within this alkaline region, had no apparent effect on the Pd particle size. Nanoparticles synthesized without pH control had an average size of 11 nm. Exchange current densities estimated for all Pd/C catalysts prepared by EG reduction were all similar and were in the interval 7.7 x 10^{-12} to 1.0 x 10^{-11} A cm^{-2} Pd. Therefore, it was concluded that the particle size, within the studied range, did not affect the ORR activity of Pd nanoparticles prepared by EG reduction.

On the other hand, the pH of the reaction system induced a change in the dispersion of palladium nanoparticles on the carbon surface. Dispersion of the Pd nanoparticles was higher in basic pH, as indicated by higher ECSA and mass activity values. TEM analysis showed particle agglomeration for all the Pd/C catalysts analysed. The least severe agglomeration was observed for Pd/C-EG11 as evidenced in its higher mass activity, 20 A g^{-2} Pd, than for Pd/C-EG, Pd/C-EG10, Pd/C-EG12 or Pd/C-EG13. A pH value of 11 was chosen in further catalyst preparations by EG reduction, both for Pd or palladium-based bimetallic catalysts. Carbon-supported palladium nanoparticles were also prepared on as-received Vulcan XC-72R using ethylene glycol as a reducing agent at pH 11.

Characterization of this catalyst, Pd/C-untr, showed that its particle size of 7 nm its ECSA of 15 m^2 g^{-1} and its exchange current density of 1.0 x 10^{-11} A cm^{-2} Pd were similar to those calculated for Pd/C-EG11.

All carbon-supported palladium catalysts exhibited only one Tafel slope, in the low current density region, with values ranging from 59 to 64 mV $decade^{-1}$. In the high current density region a constantly changing Tafel slope was observed. This change in Tafel slope was believed to be due to the change of the oxygen coverage of the catalyst surface with the potential.

Heat treatment in H_2 at 300 ºC caused particle growth on all carbon-supported palladium nanocatalysts. The extension of the sintering increased with increasing temperature, in the range from room temperature to 300 ºC, and it was more severe for smaller palladium particles. Heat treatment caused an important loss of ECSA in each catalyst and therefore a decrease in its mass activity. Heat treatment did not affect the activity towards ORR of the Pd catalyst: kinetic parameters calculated for Pd/C-EG-300 did not differ significantly from those of Pd/C-EG.

The Pd-Pd bond distance was estimated from XRD patterns (Scherrer equation) and its values used to determine whether a palladium-metal alloy had been formed. Introduction of any other metal atoms in the Pd lattice would cause distortion of the crystal structure since different atoms have different sizes. The Pd-Pd bond length for pure carbon-supported Pd was estimate from a large number of samples and found to have an average value of 0.2751 nm, with an associated error of 0.0003 nm. A bond distance value outside the interval 0.2751 ± 0.0006 nm (200% of error) was the criterion used to consider that palladium-metal alloy was formed.

Palladium-gold alloys were formed only when both metals were co-deposited and reduced in ethylene glycol at 110 ºC, no when Au was reduced on Pd/C. Subsequent heat treatment at 300 ºC under H_2 flow increased the extent of the alloy in co-deposited catalysts. In electrocatalysts prepared by depositing gold on Pd/C, it was observed that the extent of the Pd particle growth was significantly larger compared to pure palladium. The presence of gold inhibited the sintering of Pd nanoparticles when heat treated under H_2 flow. After electrochemical conditioning in acid electrolyte, gold-rich Pd-Au alloy electrodes present the electrochemical characteristic of a gold electrode. Gold-rich Pd-Au alloy electrodes exhibited Tafel slopes and onset potentials close to pure gold electrodes. The increase in the extent of the alloy by heat treatment led to a decrease of the ORR activity in any case. Also, the vicinity of large amounts of gold nanoparticles decreased the ORR activity of Pd nanoparticles. Every palladium-gold catalyst prepared presented an ORR activity lower than pure Pd.

Palladium-cobalt catalysts prepared by ethylene glycol reduction required heat treatment under H_2 flow in order to form an alloy. And, as with Au, the presence of cobalt depressed particle sintering during heat treatment at 300 ºC under H_2; smaller particle growth was observed for larger Co contents. Alloying large amounts of Co (Pd:Co 1:0.6 or higher) has a negative impact on the ORR activity. For Co content of ca. Pd:Co 1:0.2, no significant differences in the activity after the alloying process were observed when the catalysts were prepared on Pd/C; and a slight improvement in the ORR activity was exhibited when both metals were co-deposited.

Small amounts of Fe atoms are believed to have been introduced in the Pd lattice after reduction with ethylene glycol and heat treatment at 300 ºC under H_2 based on changes in the shape of the cyclic voltammograms compared to pure Pd and small changes in the Pd-Pd bond distance. All Pd-Fe catalysts prepared by reduction under H_2 at 500 ºC showed a typical face-centered cubic pattern with diffraction angles clearly shifted to higher positions compared to those of Pd/C, indicating the formation of a Pd-Fe alloy. The presence of iron, likewise gold and cobalt, depressed particle sintering during heat treatment; smaller particle growth was recorded for larger Fe contents. A reduction peak with its maximum at ca. 0.36 V appeared in every Pd-Fe catalyst during the electrode conditioning, which according to the Poubaix diagram for iron in aqueous solution was caused by the reduction of Fe_2O_3 to Fe^{2+}. The area under the peak, and therefore the amount of Fe_2O_3, was larger in unalloyed catalysts. This indicated leaching of the iron under potential cycling conditions.

All palladium-iron catalysts presented ORR activities lower than Pd/C. Introduction of iron in the palladium lattice was found to be detrimental to the ORR, contradicting work published by Shao et al. The highest activities within the Pd-Fe catalysts were exhibited by those prepared on Pd/C. The biggest losses in ORR activity compared to Pd/C where exhibited by catalysts with high iron content (Pd:Fe 3:1).

No significant changes in the Pd-Pd bond distance, compared to Pd/C, were observed for palladium-titanium catalyst prepared either by ethylene glycol reduction, before or after heat treatment at 300 ºC in H_2, or by reduction in H_2 at 900 ºC. However, the average Pd-Pd bond distance for catalysts synthesized by reduction in H_2 at 900 ºC was 0.2747 nm, lower than that of Pd/C by 0.0004 nm. Since Fernández et al. claimed the formation of Pd-Ti alloy based on small shifts in the XRD patterns, the presence of some Pd-Ti alloy could not be completely discarded. The presence of TiO_2 in its anatase form was easily identified from the XRD patters in all Pd-Ti catalysts with high titanium content; catalysts with lower Ti content are also believed to include small amounts of anatase. The presence of TiO_2 did not depress the sintering of Pd nanoparticles during heat treatment in H_2.

Pd-Ti catalysts prepared by EG reduction without heat treatment presented ORR activities close to Pd/C, independently of the amount of TiO_2 present. This activity decreased after heat treatment at 300 ºC in H_2, which was believed to introduce some Ti in the Pd lattice. Catalysts synthesized at high temperatures (900 ºC in H_2) presented lower ORR when the Ti content was high (Pd:Ti 1:1) compared to those with low Ti content (Pd:Ti 9:1). All Pd-Ti catalysts exhibited lower catalytic activity than Pd/C.

In summary, the presence of Au, Co and Fe decrease the degree of sintering of Pd nanoparticles; the present of Ti did not affect Pd particle growth. Only Pd-Au and Pd-Co exhibited alloy formation using ethylene glycol as the reducing agent, in the case of Co heat treatment at 300 ºC under H_2 flow was necessary to form the alloy. Pd-Fe alloys were only identifiable after reduction at 500 ºC in H_2. No Pd-Ti catalysts exhibited clear alloy formation with any synthetic conditions. Only Pd-Co alloys with atomic ratio Pd:Co 4:1, synthesized by ethylene glycol reduction and after heat treatment at 300 ºC under H_2 flow, exhibited improved ORR activity compared to Pd/C.

Carbon supported Pd nanoparticles prepared by reduction by ethylene glycol at pH 11 were tested in a low temperature fuel cell as cathode material and its performance compared to the state of the art commercial Pt/C. For the same metal loading, the Pt cathode performed better than the Pd, although due to its higher activation energy Pd performance was closer to Pt at higher temperature. Operating on air at 40 ºC the current densities at 0.65 V (53% efficiency) for Pd and Pt MEAs were 0.13 and 0.24 A cm^{-2}, respectively.

Since Pd is considerably cheaper than platinum, the use of larger amounts of Pd in the cathode would still be economically advantageous. MEA with Pd loading in the cathode of 1.0 mg cm^{-2} was prepared and compared with MEAs with cathode loadings of 0.6 mg cm^{-2} of Pd and Pt. The increase of the catalyst loading led to a sharp increase on the kinetics of the ORR and therefore of the cell performance, although severe mass transport effects were observed in the high current density region due to the thickness of the catalyst layer. At feasible operating conditions, 40 ºC and operating on air, Pd MEA (1.0 mg cm^{-2}) overtook Pt MEA (0.6 mg cm^{-2}), showing current densities at 0.65 V of 0.14 and 0.12 A cm^{-2}, respectively.

Pd_4Co-EG11-300, presented an increased OCP and smaller kinetic losses compared to the Pd-EG11 when it was used as cathode material. Overall, the Pd-Co MEA presented improved performance at 20 and 40 ºC compared to the Pd MEA. Operating on air at 40 ºC current densities at 0.65 V for Pd and PdCo MEAs were 0.13 and 0.21 A cm^{-2}, respectively.

Pd/C prepared by reduction by ethylene glycol at pH 11 was also tested as the cathode catalyst in a high temperature fuel cell and its performance compared to commercial Pt/C. Operating on air at 120 ºC current densities at 0.65 V for Pd and Pt MEAs were 0.04 and 0.09 A cm^{-2}, respectively. In the temperature range from 120 to 175 ºC the Pt MEA performance failed to increase due to phosphoric acid properties: decrease of the oxygen solubility and increase of its viscosity. Pd MEA showed declining performance in the same temperature range due to instability of palladium nanoparticles in these harsh operating conditions.

Pd-EG11 was tested as a cathode catalyst in a direct methanol fuel cell and its performance was compared to a commercial Pt/C. Cell performance was compared at methanol concentrations of 1, 3, 5 and 7M and temperatures 20, 40 and 60 ºC.

Anode potential vs current density curves showed how anode performance increased with increasing temperature and methanol concentration. This did not always reflect on the overall cell performance due to methanol crossover to the cathode. The effect of methanol crossover was more severe for the Pt cathode due to its higher activity towards the methanol oxidation reaction.

Despite its lower electrochemical surface area palladium overtook platinum as cathode catalyst at suitable operating conditions for a DMFC. Current densities at 400 mV exhibited by the palladium MEA were higher than for platinum at 60 ºC with a methanol concentration 5M or higher. This makes Pd an adequate substitute to Pt due to its lower price. Moreover, since the effect of crossover would be more severe for Pt at lower cathode loadings (lower ORR current) Pd would advantage Pt at methanol concentrations even lower than 5M obtained (equal performance at low current densities with 2 mg cm^{-1} cathode loading).

The assumption of the existence of an electrolyte thin film was necessary for the model to predict the mass transport limitations with air operation observed in the experimental results.

The model closely matched fuel cell experimental data with oxygen operation; however it overestimated performance with air operation, especially at high current densities. This failure of the model was attributed to oxygen starvation, and was explained by losses in the active electrochemical surface area. To enhance the model accuracy a new concept, apparent reaction order (Γ), was introduced to explain the need of a higher reaction order to fit experimental data. Apparent reaction order was taken for air operation at 20, 40 and 60 ºC as 1.5, 1.75 and 2, respectively.

The model closely predicted experimental results at 20 and 40 ºC. At 60 ºC a lower permeability value was employed according with the lower humidity measured experimentally. Above 40 ºC cell performance did not improve experimentally and that was predicted by the model. This lack of improvement was attributed to the decrease of oxygen permeability through Nafion® and consequent reduced oxygen concentration at the catalyst surface, which countered any kinetic enhancement with the temperature increase.

The increase of the metal loading in the cathode enhanced fuel cell performance in the low current density range; however, severe mass transport limitation appeared. Predicted results showed that this could be solved by increasing the loading without increasing the catalyst layer thickness, which can be practically achieved by increasing the metal content of the carbon-supported catalyst.

In summary, Pd/C prepared by ethylene glycol reduction at pH 11 is a suitable substitute for Pt in low temperature PEMFC and in DMFC applications. In PEMFCs a higher cathode loading is required to match Pt performance, however, this is still advantageous due to the significant lower cost of Pd. In DMFCs Pd cathodes overtake Pt cathodes with the same loading at methanol concentrations equal or higher than 5M with air operation at 60 ºC.

9.2. Future work

Palladium is a very promising cathode catalyst for DMFC since the effect of crossover is less severe than in platinum. Pd has shown advantage over Pt at methanol concentrations of 5M and above with metal loading of 2 mg cm^{-2}. At lower metal loading the methanol crossover effect would become more severe and palladium should outperform Pt at methanol concentrations lower than 5M.

While studies on palladium used as a membrane composite for DMFC to reduce crossover through the membrane have been published [1, 2], there is no solid study of its use as DMFC cathode materials. Future comparative studies of Pd and Pt cathodes with lower metal content and long term stability would be beneficial to support Palladium use in DMFC. Numerous studies investigated the use of platinum bimetallic alloys in DMFC cathodes and reported higher methanol tolerance in comparison with pure platinum [3], however, there is a limited amount of literature available on the use of palladium alloys for DMFC [4, 5] and therefore further studies are needed to investigate their potential and methanol tolerance.

The use of alternative Pd precursors, e.g. $PdCl_2$, might lead to a better dispersion of Pd nanoparticles on the carbon support and thus to a higher catalytic active area. The investigation might lead to a substitute to ammonium tetrachloropalladate (II) resulting in Pd nanoparticles with less agglomeration on the carbon surface. The effect of catalyst support should also be considered (different carbon, carbon pre-treatment, alternative materials, etc), since catalyst-support interaction influences its catalytic activity, and support type affects Pd crystallography and particle size.

Based on the model predictions for low temperature PEMFC, a thinner cathode catalyst layer would provide higher cell performance over a wider current range when high metal loading was used. This can be achieved by using a catalyst with a higher metal to carbon ratio. It would therefore be interesting to explore the synthesis and characterization of carbon-supported Pd nanoparticles with higher metal content, 40 or 50% weight metal.

Pd activity towards the ORR did not always increase with deceasing particle size, rather it showed instability at particle sizes of approximately 3 nm (Pd/C commercial). An optimum particle size is believed to exist for electrocatalysts, this has already been reported for Pt to be ca. 3.5 nm for ORR [6], a future study would be needed to determine similar value for Pd. It also would be important to determine which crystal type is the most active for the ORR in palladium in acid media (for Pt crystal (110) has been reported to have the highest activity in sulphuric and phosphoric acid solutions [7, 8]).

Carbon-supported Pd nanoparticles could also be tested in other types of fuel cells such as alkaline or microbial fuel cells.

References

1. Choi, W.C., J.D. Kim, and S.I. Woo, *Modification of proton conducting membrane for reducing methanol crossover in a direct-methanol fuel cell.* Journal of Power Sources, 2001. **96**(2): p. 411-414.

2. Ma, Z.Q., P. Cheng, and T.S. Zhao, *A palladium-alloy deposited Nafion membrane for direct methanol fuel cells.* Journal of Membrane Science, 2003. **215**(1-2): p. 327-336.

3. Baglio, V., A. Stassi, A. Di Blasi, C. D'Urso, V. Antonucci, and A.S. Aricò, *Investigation of bimetallic Pt-M/C as DMFC cathode catalysts.* Electrochimica Acta, 2007. **53**(3): p. 1360-1364.

4. Mustain, W.E., K. Kepler, and J. Prakash, *CoPdx oxygen reduction electrocatalysts for polymer electrolyte membrane and direct methanol fuel cells.* Electrochimica Acta, 2007. **52**(5): p. 2102-2108.

5. Sarkar, A., A.V. Murugan, and A. Manthiram, *Synthesis and Characterization of Nanostructured Pdâˆ'Mo Electrocatalysts for Oxygen Reduction Reaction in Fuel Cells.* The Journal of Physical Chemistry C, 2008. **112**(31): p. 12037-12043.

6. Sattler, M.L. and P.N. Ross, *The surface structure of Pt crystallites supported on carbon black.* Ultramicroscopy, 1986. **20**(1-2): p. 21-28.

7. El Kadiri, F., R. Faure, and R. Durand, *Electrochemical reduction of molecular oxygen on platinum single crystals.* Journal of Electroanalytical Chemistry, 1991. **301**(1-2): p. 177-188.

8. Gasteiger, H.A. and P.N. Ross, *Oxygen Reduction on Platinum Low-Index Single-Crystal Surfaces in Alkaline Solution: Rotating Ring DiskPt(hkl) Studies.* The Journal of Physical Chemistry, 1996. **100**(16): p. 6715-6721.

Appendix A

Carbon-supported Pd-Co-Au was prepared by a reverse microemulsion method following the synthetic method reported in the publication of Fernández et al. [1]. The catalyst was used to prepare a gas diffusion electrode which was evaluated for oxygen reduction reaction in O_2 saturated 0.5M H_2SO_4 solution. The catalyst layer was sprayed on a commercial gas diffusion layer, a low temperature microporous layer (GDL LT 1200-W, from E-Tek). The catalyst ink was prepared by mixing in an ultrasonic bath the carbon-supported catalyst with Nafion® in a water-ethanol (66% volume of ethanol) solution for 0.5 hours. The amount of Nafion® in the catalyst ink was 20% of the catalyst weight. 0.5 mg of metal where deposited per cm^2 of electrode. A gas diffusion electrode with commercial Pt/C as catalysts was prepared following the same procedure; potential-current curves exhibited by both electrodes are compared in Figure A-31.

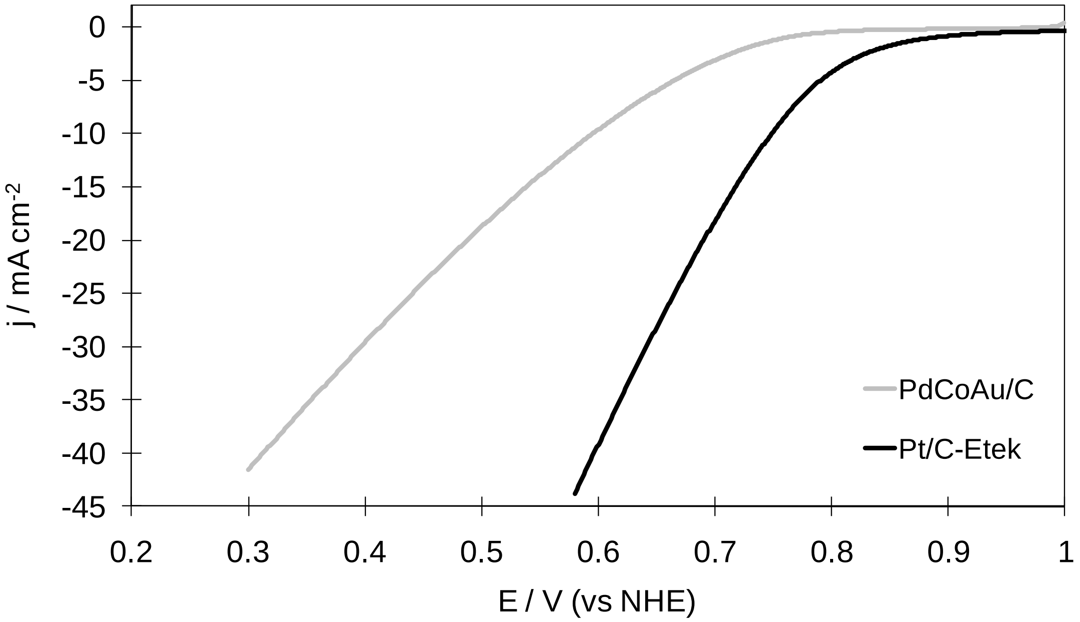

Figure A-31: Linear sweep voltammograms of gas diffusion electrodes of commercial Pt/C from E-tek and homemade PdCoAu/C.

Onset potentials were 0.97 V for commercial Pt/C and 0.83 V vs NHE for PdCoAu/C. Current density compared at 0.6 V was four times bigger for commercial Pt/C than for

PdCoAu/C (ca. 40 and 10 mA cm^{-2}, respectively). These results contradicted their published data. At least three catalysts were prepared to confirm the results shown in Figure A-31. Figure A-2 shows the great degradation rate of the Pd-Co-Au cathode over 5 consecutive days immersed in 0.5M H_2SO_4 solution.

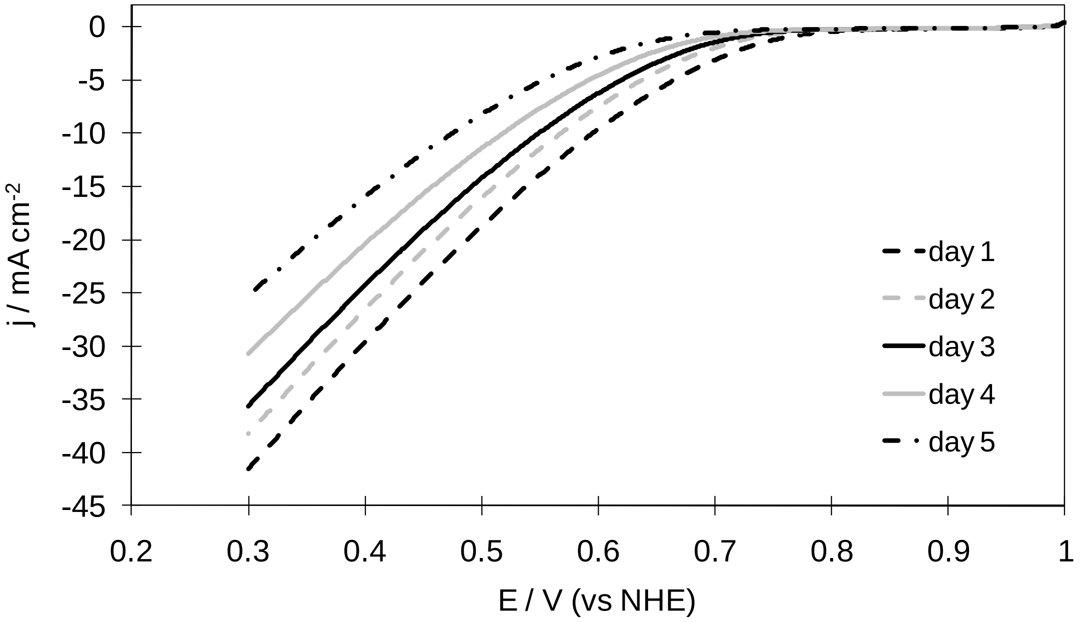

Figure A-32: Linear sweep voltammograms of a gas diffusion electrode with homemade PdCoAu/C tested over five consecutive days.

Carbon-supported Pd-Ti was prepared by an impregnation method also following the experimental procedure stated in the publication of Fernández et al. [1]. Figure A-3 compares Pt-Ti and Pt/C commercial tested for ORR in O_2 saturated 0.5M H_2SO_4 solution using a rotating disc electrode (electrode preparation described in Section 3.2). Onset potentials were 0.96 V for Pt/C commercial and ca. 0.70 for Pd-Ti. Again activity towards ORR of the palladium-based catalysts was far from that claimed in the literature. No further studies by this or another research group were subsequently published.

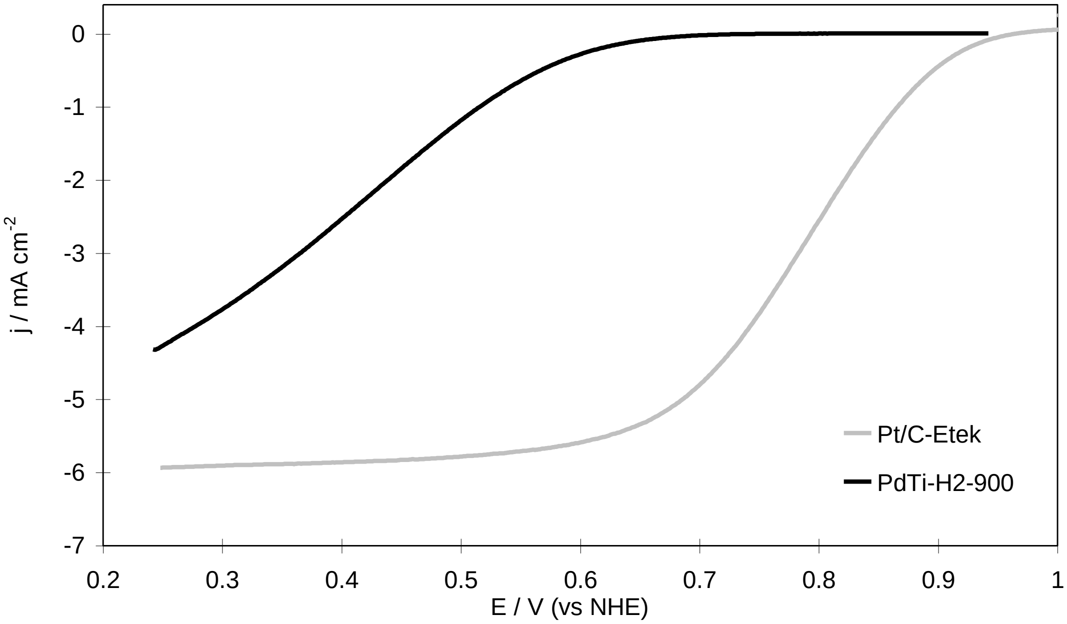

Figure A-33: Linear sweep voltammograms of a rotating disk electrode with commercial Pt/C and PdTi-H_2-900.

References

1. Fernández, J.L., V. Raghuveer, A. Manthiram, and A.J. Bard, *Pd-Ti and Pd-Co-Au Electrocatalysts as a Replacement for Platinum for Oxygen Reduction in Proton Exchange Membrane Fuel Cells.* Journal of the American Chemical Society, 2005. **127**(38): p. 13100-13101.

Appendix B

List of publications

Oral presentations:

1. Scientific Advances in Fuel Cell Systems, Confederation of Danish Industries, Copenhagen, Denmark, 8-9 October 2008
2. International Energy Agency Meeting, ICT Pfinztal, Germany, 8-9 December 2008
3. Supergen Fuel Cell Symposium, Notingham University, UK, 13 November 2008
4. Postgraduate Research Conference, Newcastle University, UK 10-11 April 2008
5. International Energy Agency Meeting, TU Graz, Austria, 22-23 November 2007
6. Supergen Fuel Cell Annual Meeting, St. Andrews University, UK, 12-13 November 2007
7. Supergen Fuel Cell Symposium, Notingham University, UK, April 2007
8. Supergen Fuel Cell Symposium, Imperial College London, UK, 13 November 2006

Poster presentations:

9. Sustainable Energy UK: Meeting the science and engineering challenge, St Anne's College, Oxford, UK, 13 May 2008
10. Hydrogen and fuel cells: for a low carbon future, National Exhibition Centre, Birmingham, UK, 2 April 2008
11. Industrial Advisory Board Meeting, Newcastle University, UK, 30 October 2007
12. Electrochem 07, Imperial College London, UK, 3-4 September 2007